Modèle hybride pour simuler l'écoulement à travers un birotor éolien caréné et sa validation expérimentale

Michal Lipian

ParisTech
INSTITUT DES SCIENCES ET TECHNOLOGIES
PARIS INSTITUTE OF TECHNOLOGY

ARTS ET MÉTIERS ParisTech

2018-ENAM-0073

École doctorale n° 432 : Science des Métiers de l'ingénieur

Doctorat ParisTech

T H È S E

pour obtenir le grade de docteur délivré par

l'École Nationale Supérieure d'Arts et Métiers

Spécialité " Génie énergétique "

présentée et soutenue publiquement par

Michal LIPIAN

17 Décembre 2018

The hybrid simulation model for a twin-rotor diffuser-augmented wind turbine and its experimental validation

Directeur de thèse : **Fawaz MASSOUH, Krzysztof JOZWIK (directeur cotutelle)**
Co-encadrement de la thèse : **Ivan DOBREV, Maciej KARCZEWSKI (co-encadrant cotutelle)**

Jury

M. Michael TODOROV, Professeur, Technical University of Sofia	Président
M. Piotr DOERFFER, Professeur, Polish Academy of Sciences	Rapporteur
M. Frank RUCKERT, Professeur, Saarland University of Applied Sciences	Rapporteur
M. Farid BAKIR, Professeur, Arts et Métiers ParisTech	Examinateur
M. Krzysztof JOZWIK, Professeur, Lodz University of Technology	Examinateur
M. Fawaz MASSOUH, Professeur Emérite, Arts et Métiers ParisTech	Examinateur
M. Ivan DOBREV, Docteur, Arts et Métiers ParisTech	Invité
M. Maciej KARCZEWSKI, Docteur, Lodz University of Technology	Invité

T H È S E

Arts et Métiers ParisTech - Campus de Paris
DynFluid – Laboratoire de dynamique des fluides

What's past is prologue

William Shakespeare, The Tempest, Act 2, Scene I

Ad astra

Publius Vergilius Maro, Aeneid, book IX, line 641

Acknowledgments

The crafting process of what has become my PhD thesis wouldn't be possible without people around me. To all those who helped me along the way I wish to forward my deepest thanks.

First and most of all I want to thank my parents and grandparents. I value the moral support You gave me during my long path of studies as the most precious assistance I got and could get from anybody.

My very warm wishes go to my supervisors, prof. Krzysztof Jozwik and prof. Fawaz Massouh. Your doors were always opened for me and my ideas, no matter how backbreaking they would be. Your assistance and wisdom were soothing, Your help fighting the bureaucracy in Poland and in France – reassuring. Thank You for guiding me all the way to the end.

The work I have done would not be possible without the substantive support of my co-supervisors, Maciej Karczewski, PhD, and Ivan Dobrev, PhD. My especially warm sentiment goes to the latter, whom I consider a researcher *au sens propre*. Sir, I admire Your expertise and marvel Your workshop. It's an honour to work with and learn from You.

To M. You came into my life when I didn't expect, gave me what I didn't seek and made me ask for more. You gave a new direction to my life and a new world to explore. Thank You for all Your help, interruptions, questions and answers. Thank You for making Your way through the walls around me.

To M. Far or close, early in the morning or late in the evening - I can always count on Your assistance and council. Thank You for Your support of my actions and smart criticism when needed. Thank You for soothing conflicts and helping with burdens when they were pushing me down.

To my friends Filip and Philippe. Both of You are extraordinary characters of extraordinary intelligence. Thank You for Your straightforwardness and advice. A man is always in need of a good friend, and friends like You are a true blessing.

To all my friends and colleagues from the Institute of Turbomachinery. My special thanks go to Krzysiek, Piotr, Mateusz, Zbyszek and Grzesiek. Working with a self-proclaimed genius on a daily basis is a hard job. Thank You for bringing me back to Earth whenever my ego was surpassing my actions.

To all those whom I met and worked with at Arts et Metiers ParisTech. I especially acknowledge the assistance of prof. Farid Bakir and prof. Patrick Kuszla. Your understanding and calmness always gave me hope for a positive end of my studies.

To the entire GUST team. We've been through ups and downs, as a team and as a group of individuals. Working with You for several years, watching You evolve and achieve targets impossible for others is the most precious gift that any tutor can get.

And finally – to every person reading this thesis. Whether it is need, order or pleasure that drives You, I hope You will share the joy that accompanied me during my work.

Table of contents

Funding

The research was carried with funding of the following projects:

Okanałowana turbina wiatrowa w układzie tandem dla polskiej mikroenergetyki (Diamentowy Grant DI2013 011843)

Small Wind Turbine Optimized for Wind Low Speed Conditions (Polish-Norwegian Research Programme 200957)

Le programme d'excellence Eiffel

Symbols and notations

AoA	Angle of attack (also α)
ADM	Actuator Disk Model
ALM	Actuator Line Model
BEM	Blade-Element Momentum theory
BET	Blade-Element Theory
SRWT	Single-Rotor Wind Turbine
CROR	Counter-Rotating Open Rotor
CRWT	Counter-Rotating Wind Turbine
DAWT	Diffuser-Augmented Wind Turbine
EU	European Union
FDM	Fused Deposition Modelling
FFT	Fast Fourier Transform
FRM	Fully-resolved Rotor Model
LES	Large Eddy Simulation
PoR	Plane of Rotation
RES	Renewable Energy Sources
SWT	Small Wind Turbine
TKE	Turbulent Kinetic Energy (also k)
TSR	Tip-Speed Ratio (also λ)
UDF	User-Defined Function (ANSYS Fluent routine)
WT	Wind Turbine

A	m^2	Area
B	-	Number of blades
Cd	-	Drag coefficient
Cl	-	Lift coefficient
Cp	-	Power coefficient (wind power extraction efficiency)
Ct	-	Thrust coefficient
D	m	Wind turbine diameter
F_d	N	Drag force
F_t	N	Thrust force
Ma	-	Mach number
P	W	Power
Q	Nm	Torque
R	m	Rotor radius
Re	-	Reynolds number
RH	%	Relative humidity
St	-	Strouhal number
T	K, ^oC	Temperature
U	$m \cdot s^{-1}$	Streamwise velocity component
U_∞	$m \cdot s^{-1}$	Freestream wind velocity
V	$m \cdot s^{-1}$	Velocity
W	$m \cdot s^{-1}$	Inflow velocity

a	-	Axial induction factor
a’	-	Tangential induction factor
c	m	Chord
cp	-	Pressure coefficient
d	$N \cdot m^{-1}$	Drag force per unit blade length
dt	s	Timestep
f	Hz	Frequency
k	$m^2 \cdot s^{-2}$	Turbulent Kinetic Energy (also TKE)
l	$N \cdot m^{-1}$	Lift force per unit blade length
m	kg	Mass
n	-	Wind turbine-to-diffuser exit area ratio, A/A_e
p	Pa	Pressure (notably static)
q	Pa	Dynamic pressure
r	$J \cdot kg^{-1} \cdot K^{-1}$	Individual gas constant
t	s	Time
α	deg	Angle of attack (also AoA)
β	deg	Pitch angle
γ	-	Power coefficient based on the diffuser exit
ε	-	Air flow momentum loss factor
ζ	deg	Diffuser cone half-angle
η	-	Diffuser pressure recovery efficiency
λ	-	Tip-Speed Ratio (also TSR)
μ	Pa·s	Dynamic viscosity
ν	$m^2 \cdot s$	Kinematic viscosity
ρ	$kg \cdot m^{-3}$	Density
ϕ	deg	Inflow angle
ω	$rad \cdot s^{-1}$	Rotational velocity

Subscripts:

u	upstream
d	downstream
e	(diffuser) exit
n	normal
t	tangential
tot	total
w	wake
∞	reference value
+	(immediately) upstream rotor
-	(immediately) downstream rotor

Frames of reference:

(x,y,z)	Coordinates in rectangular frame of reference
X, Y, Z	Directions (axes) of rectangular frame of reference
(r,φ,z)	Coordinates in cylindrical frame of reference

1. Introduction

According to the European Commission directive "20 20 by 2020" [1], the countries of European Union (EU) have to, by year 2020, limit the greenhouse gas emissions by 20%, increment energy efficiency by 20% comparing to 1990 levels, and increase energy production from Renewable Energy Sources (RES) to 20% of the energy mix Europe-wise (15% for Poland, 23% for France).

According to the former European Wind Energy Association (EWEA), in 2015 1266 MW in wind turbine (WT) power was installed in Poland. A number surpassed only by Germany, it accounted for 9.9% of all power installed in wind turbines in the EU in this period [2]. Thus, as of the end of 2017, wind turbines remain the most important converters of RES in the Polish market: 5858 MW, that is about 68% of all RES installed power [3]. The structure of the Polish wind market concentrates currently on the multi-megawatt machines condensed in wind farms. Unfortunately, the current legislation in force in Poland significantly curbs new investments of this type [4]. In the meantime Polish wind resources (see ex. [5]) seem to address the localized power harvesting, where each energy consumer may become a prosumer, addressing own electricity needs produced by Small Wind Turbines (SWTs). High efficiency is a key factor in such constructions, to economically justify their use.

In France, the nuclear energy has been a well-established leader of the market for several decades. In 2017 the nuclear power plants accounted for 71.6% of total annual electric energy production, followed by hydroelectric (10.1%) and natural gas (7.7%) power plants [6]. Installed power of wind turbines in France grew in 2017 by 15.3% but, alike in Poland, this was mainly concentrated in wind farms. Access to relatively cheap electrical energy from nuclear power plants, along with shortage of precise wind resource data at low heights make small wind turbines hardly rentable in the continental France [7]. This situation changes, however, if Overseas France is taken into account, where SWTs may answer the needs of isolated locations. Efficient and reliable operation is a key factor in this case.

SWTs usually operate at low wind speeds and adverse range of Reynolds number values. This significantly limits the possibility of aerodynamic blade optimisation and promotes research towards more sophisticated solutions. The promising ideas include Diffuser-Augmented Wind Turbine (DAWT), previously studied at the Institute of Turbomachinery, Lodz University of Technology (IMP TUL), and Counter-Rotating Rotors (CRR). The diffuser promotes an increase in the wind mass flow rate through the rotor, which translates into higher wind turbine power and energy outcome. This solution also has an advantage of protecting against blade breakage and potential to damp the wind turbine noise. The CRR explores possibility of extracting the kinetic energy of wind in the wake. This concerns most of all the axial component of wind speed, but may also apply to the tangential component, which is normally lost in the form of a rotating wake.

To answer the above challenges the project *Twin-rotor Diffuser-Augmented Wind Turbine for Polish wind speed conditions* was proposed. It combines the concepts of DAWT and twin-rotor. The DAWT is already commercialized i.a. in Japan and United States, which proves its purposefulness. At the same time it is tempting (and not yet exploited) to profit further on from the wind velocity increase due to diffuser, by placing the second rotor in the augmented velocity region(s). This novel idea is hoped to rise the overall efficiency of the system, thus decreasing the effective price of electrical energy per kWh and further on – making the investment in RES economically reasoned.

The main objective of the thesis *The hybrid simulation model for a twin-rotor diffuser-augmented wind turbine and its experimental validation* is to investigate the functioning of a twin-rotor shrouded wind

turbine and to analyse the flow through this kind of a device. This task requires advanced tools of flow analysis, both numerical and experimental. However, due to the complex nature of the flow, experimental methods have only limited applicability. For example, PIV measurements techniques would be very hard to apply due to technical reasons. Experimental tests are also limited by the scale effects, which would occur for testing relatively small models, and who is not present a priori in the case of simulations. Hence, and owing to a multitude of functional parameters of the concerned system, the main focus of the thesis will be put on the simulation tools. This is due to the fact that they enable a relatively facile modification of parameters such as the geometry of rotors and/or their relative position. The complicated character of the problem, however, makes complete modelling of the rotors (FRM, Fully-resolved Rotor Model) prohibitively resource-consuming (due to mesh size, time of calculations, etc.). Thus the idea to employ a simplified, hybrid model seems to be reasonable. Such approach represents the wind rotor by source terms in Navier-Stokes equations. These source terms can be applied within a thin disk which represents the entire rotor (ADM, Actuator Disk Model), or around lines representing the blades separately (Actuator Line Model - ALM).

An important added value will be due to the dedicated experimental campaign, performed at the IMP TUL wind tunnel. The results will be used for model validation and further flow analysis.

The following hypothesis has been forwarded:

Creation of a hybrid simulation model of a twin-rotor diffuser-augmented wind turbine will enable a sterling analysis of this system's functioning.

The following scientific objectives were assumed:

- creation of a hybrid simulation model for two counter-rotating shrouded wind turbine rotors,
- creation of experimental apparatus of the above mentioned system in the wind tunnel for functional analysis of the system and validation of the hybrid simulation model basing on the experiment-simulation integration approach.

The thesis is composed of 8 chapters and 3 appendices.

Chapter 1 presents the motivation for the proposed work and discusses the content of the thesis. presents the scientific formulation of the problem, defines the thesis' argument and scientific goals.

Chapter 2 gives an introduction into the subject of wind energy. Wind usage history and practical aspects are discussed, followed by the State of the Art analysis in the subject of both ducted- and twin-rotor wind turbine systems.

Chapter 3 provides the essential physical concepts and mathematical formulations used in the current thesis. This includes the main principles of a flow through wind turbines of various construction, the dimensionless analysis principles, governing equations.

Chapter 4 presents the experimental study performed in frames of the thesis. Measurement methodology is presented and evaluated. The results obtained for 4 cases: bare- are shrouded wind turbines in both single- and twin-rotor configurations are presented.

Chapter 5 evaluates the first of the proposed numerical models, that is Fully-resolved Rotor Model. Model validation and verification are performed, followed by the presentation and discussion of

results for selected wind turbine configurations. An evaluation of results is performed towards their further use in a hybrid model validation process.

Chapter 6 presents the developed hybrid model. General information concerning the aerofoil data and in-house-developed code are given, so as to explain its principles. Model description is then presented, followed by its verification and validation.

Chapter 7 compares the outcomes of 3 different employed research paths. Results for a Counter-Rotating Shrouded Rotor (CRSR) are compared, where applicable. A discussion then follows concerning the examined structure, in which the complementing results are used to evaluate the system's performance and eventual further development paths.

Chapter 8 is a summary of the performed works, conclusions and recommendations for future works.

Appendix 1 shows the research pertaining to flow evaluation in subsonic wind tunnel of the Institute of Turbomachinery, Lodz University of Technology, in which experimental study for the thesis was performed.

Appendix 2 evaluates on the practical aspects of the measurement campaign, such as preparation and diagnostics of the test stand and model.

Appendix 3 presents the information concerning the wind nature and assessment, basing on a dedicated experimental campaign.

2. Background and the State of the Art

This chapter starts with overview of wind energy aspects from the historic and statistic points of view. It then proceeds to technical aspects pertaining to wind energy exploitation, from wind resource assessment, through different types of wind turbines, to finish with the State of the Art analysis.

2.1. Wind energy over the centuries

Wind is among the earliest energy sources discovered and adopted by human beings. This Section presents the evolution of wind harvesting, its present state and future perspectives.

2.1.1. History

There is no general consensus over the time and place where the mankind began harvesting the wind energy. Ancient China and Egypt are usually named as the pioneering civilisations to use a sail for riverine and deep-water vessels as early as 4000 BC – 3400 BC [8]. Wind-propelled ships were to dominate the rivers for the next millennia, until the successful application of a steam engine at the turn of 18th and 19th century [9]. Even then the sails were often maintained as an auxiliary source of propulsion.

Where and when the first windmill was installed is a question open to interpretation. Babylonian ruler Hammurabi is said to have wanted to employ windmills for irrigation purposes in Mesopotamia as early as 1700 BC, although no accounts exist of actual operating installations [10]. Some interpretations of the ancient Hindu texts suggest that windmills were commonplace in India for similar usage around 400 BC [11]. Both Heron of Alexandria and Vitruvius mention the use of "wind-vanes" in the 1st and 2nd century Europe, although these were proved to be musical organs, rather than windmills. In China, windmills might have existed during the Eastern Han Dynasty (25-220), as proved by the paintings in tombs unearthed near Liaoyang City near the Yellow Sea [8].

The first fully confirmed use of vertical-axis windmills (panemones) was at the Persian-Afghan borders circa 200 BC. The rotors were shrouded, with slotted circular walls enabling the wind passage through rotor. These primitive windmills were used to pump water and grind grain [12]. Gradual expansion of these constructions towards India, China and Arab countries followed, most probably thanks to merchants and sailors. In England, the horizontal-axis windmills emerged, when in 1137 William of Almoner constructed such a "post-mill" in Leicester. The devices were placed on a vertical post (hence the name), and manually-positioned towards wind. Primitive as they were, these machines were lift-operated, and thus significantly more efficient than the Persian drag-operated vertical-axis constructions. This and substantial technical differences suggest that there was little, if any, connection between the two concepts [13]. As the windmill was popularised in continental Europe, the pole was replaced with a more elaborate construction of stone or brick, thus creating a (typically 4-bladed) tower mill. This construction has become a common landmark in Western Europe, notably the Netherlands. The Dutch extended the traditional use of windmills to propulsion of sawmills, paper factories, grinding machines. They are also credited for transporting the technology to the New World, around 1750. By that time in Europe there were an estimated number of 10 000 wind-powered devices in UK and German States, 8 000 in The Netherlands, 5 000 in Denmark [12]. However, a quick decline in these numbers in Europe was at the doorstep, with arrival of more reliable and mobile steam engine. Still, an estimated number of 6 million "American farm windmills" operated between 1850 and 1900 in the American Great Plains, becoming eventually an USA interior icon. These machines were

characterised by relatively large number of blades, compact construction, easy maintenance, self-regulation and low price [13]. Examples of the discussed constructions one can find in Fig. 1.

Fig. 1 Evolution of windmills: a) panemone (modern) [14], b) post mill [15], c) tower mill [16], d) American windmill [17]

The great comeback of windmills arrived once they were married with the new technical innovation - electricity. Thus was created a wind *turbine* (Fig. 2), enabling to separate the energy production and consumption places. Claimed to be the first practical construction of this type, a 12 kW, 144-bladed HAWT (Horizontal-Axis Wind Turbine) of rotor diameter 17.1 m (56 feet) was installed in 1888 in Cleveland, Ohio, by Charles Brush [13]. This model was never duplicated or commercialised, contrarily to works of Poul la Cour in Denmark. He developed a wind turbine experimental station at Askov, about 30 km from the North Sea coast. Rotors of diameter up to 23 m were usually connected with DC dynamos and had electric output in the range of 5 and 25 kW.

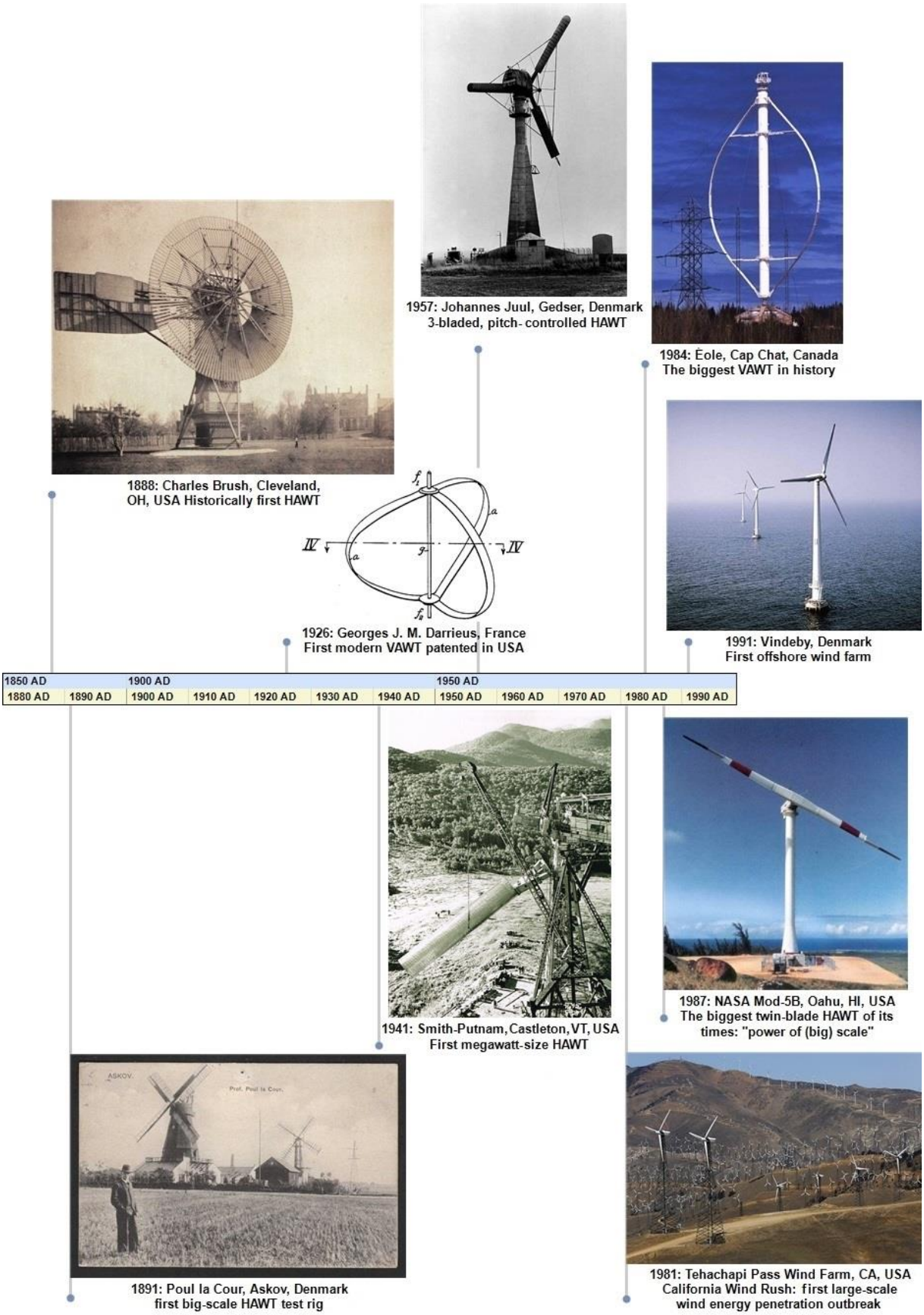

Fig. 2 Wind turbine history in images [18], [19], [20], [21], [22], [23], [24], [25], [26]

By 1920 several hundreds of HAWTs were operating in Denmark nationwide, generating a total power of as much as 120 – 150 MW. They were a significant relief to the population struck by fossil-fuels shortage during WWI and later WWII. This observation was not left unnoticed abroad and the interwar period saw a worldwide development of modern wind turbines. USA (Jacobs, Putman), USSR (Kranovsky), France (Darrieus), Germany (Kumme) may be given as examples of both domestic and bigger-scale wind turbine projects [12]. The American Smith-Putnam project was possibly the most significant of the above mentioned. Palmer Cosslett Putnam erected a two-bladed wind turbine of 53 m diameter on Grandpa's Knob in Castleton, VT, USA. The rotor, rated 1 - 1.25 MW (at wind velocity of 13.2 m/s), operated from 1941 to 1945, when one of the blades separated from the hub and crashed. Apart from the project being recognized as the first megawatt-size wind turbine, it is also acclaimed for the way it was conducted. It was financed by the private industry (S. Morgan Smith Company) and included a set of prominent scientists and energy companies of the time. As stated by Pasqualetti [13] "What is most remarkable about the Smith-Putnam project is not its successful operation but rather the fact that it happened at all".

The arrival of a modern wind turbine is usually associated with the Gedser model constructed by Johannes Juul for electricity company SEAS (Sydsjællands Elektricitets Aktieselskab) in 1957. The 3-bladed, stall-regulated upwind rotor of 24 m diameter was connected to asynchronous generator. Rated power was equal to 200 kW at wind velocity of 15 m/s. After the 1973 oil crisis numerous government-funded programs for development of wind turbines were launched, resulting in a significant increase in nominal power of wind turbines. Notable examples include American Mod-5B (97.5 m rotor diameter, 2.5 MW, 2 blades, HAWT) and Canadian Éole (110 m-high height, 4 MW, Darrieus rotor). The Gedser wind turbine architecture, dubbed the "Danish concept" was successfully used for wind turbines as big as 60 m diameter and nominal power of 1.5 MW. This was finally the concept that dominated the way we think about wind turbines today [13], [27].

The second oil crisis in 1979 led the governments (e.g. Denmark, USA) to reconsider their energy policies. At that time the state of California decided to subsidise the conversion of renewable energy sources. What's more, the state started measuring wind resources and sharing the information publicly. This came along with the opening of the state utilities and energy market. All these pieces formed a massive development of wind turbine installations and wind farms all over the state. They totalled to an estimated number on 11 000 units (mainly of order 50 – 200 kW per machine) by the end of 1980s, when the rush began to fade away due to citizens' complaints, subsidies' ceasing and increasing regulation. The California example provided experience and warnings necessary when considering future wind project policies [13], [25].

Back in 1984 Musgrove [28], [12] predicted, basing on the then-actual research, that medium-sized (15 m – 20 m diameter) wind turbines could harness, during the same period, the same amount of wind energy less expensively than large, multi-megawatt-scale rotors. The development of new materials and technologies had proven this theory to be wrong, as scaling-up the rotor enabled to increase the wind turbine capacity factors. From 1983 to 2016 the average global wind turbine diameter rose from 17 m to 101 m, and the capacity factor from 20% to 28% [29].

The scale-factor was to be crucial especially for the emerging offshore wind farms. In 1991 the first structure of this type was installed in Vindeby, 3 km offshore the coast of Denmark. Wind turbines of total power of 11 450 kW, adapted for offshore wind conditions, were operating until final

decommissioning in 2017, after having produced a total energy of 243 GWh in their lifetime. The technology has advanced significantly since that pioneering undertaking. London Array, the biggest offshore wind farm in the world (by capacity: 630 MW, as of July 2018), comprises of 175 3.6 MW SWT-3.6-120 HAWTs produced by Siemens Wind Power. Placed 20 km offshore United Kingdom, it has annual energy output of 2500 GWh (2015).

Over the centuries wind turbines have grown in size, their technology has matured, their applications have diversified. The nature of the wind remains unpredictable, but the humankind has developed tools to extract its energy in an easier and more practical way than ever before.

2.1.2. Present state

According to Burton [27], the interest in development of wind turbines back in 1970s was the oil crisis. In 1990s this shifted towards increasing concerns about greenhouse emissions. Currently, wind energy is also seen as a means for diversification of energy sources, thus securing the energy market.

The above consideration is a very important aspect for example in EU, struggling lately to decrease energy market dependence on foreign sources. WindEurope (former EWEA, European Wind Energy Agency) states in its *Wind in power 2017* report [30] that 15.6 GW in wind power (55% of all new power) was installed in EU in 2017. 20% accounted for offshore installations. As of 2017, wind turbines are the second-largest installed capacity in EU (18.0%, after gas – 20.1%), covering 11.6% of EU annual electricity demand (see Fig. 3).

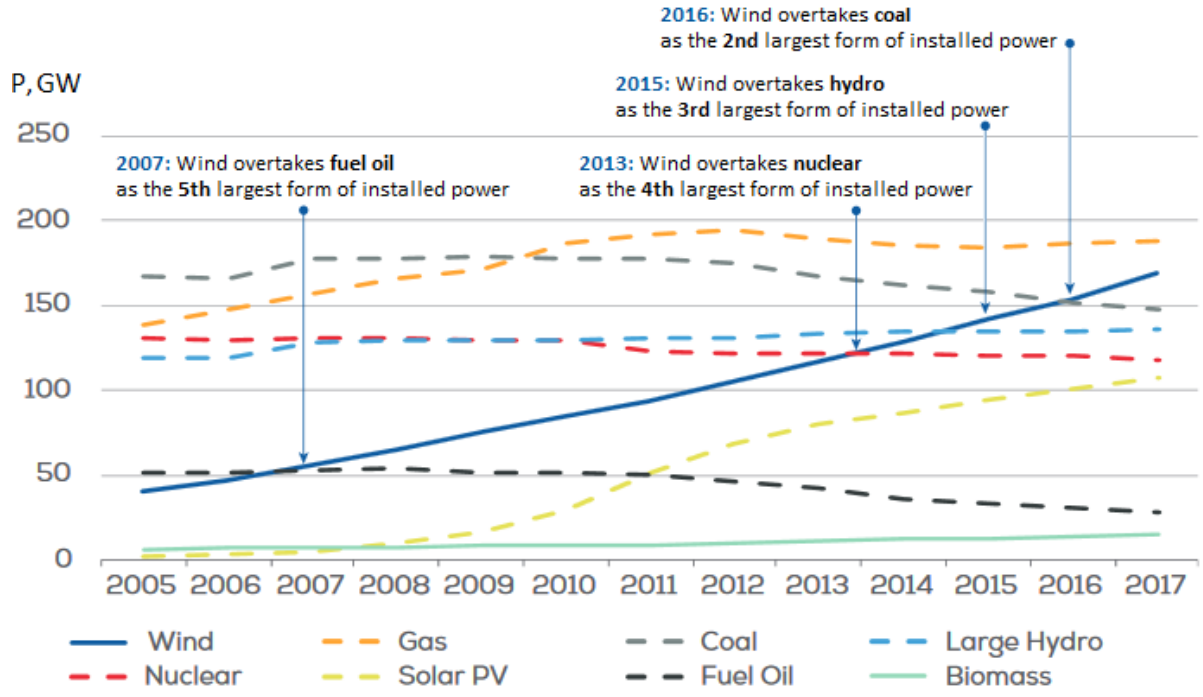

Fig. 3 2005-2017 evolution of installed power generation capacity in the EU [30]

In Poland, as of the end of 2017, power of 5858 MW installed in wind turbines accounted for 13.5% of the entire national energy mix [3]. The wind turbines in Poland are mainly grouped in wind farms, although the current legislation concerning RES ([4] and amendments) is heavily against this kind of installations. Thus construction of the new (and replacement of the old) megawatt-range wind turbines has virtually stopped since 2016, when new laws were introduced. This, however, has given field to alternative approach to RES, with increasing role of prosumers. According to the statistics presented

in Fig. 4 for year 2017, about 56% of new RES power capacity was installed in sources of power lower than 50 kW. Average power size of these installations was about 6.5 kW, while for the bigger systems it was about 880 kW. To put this statistics into perspective, power of 225 kW in 35 new small RESes was installed each day in Poland in 2017. Even though an important part of these systems was in solar power, this statistic is an important indicator of increasingly positive sentiment towards prosumer, small-size RES, and hence the need for development of this kind of installations.

As for France, the metropolitan electrical energy market has been dominated by two sectors: nuclear power (72% market share, 398.4 TWh generated in 2017) and hydraulic power (9%, 49.2 TWh). At 24 TWh produced in 2017, wind turbines account for approximately 5% of the total energy market and 1.8 GW of new power was installed in wind turbines in 2018 (Fig. 5) [31], [32]. These are mainly big-scale wind turbines, both onshore and offshore. According to the analyses by ADEME (l'Agence de l'Environnement et de la Maîtrise de l'Energie) there is little interest in implementing SWTs in the French metropolitan electric grid to balance the national energy demand-supply, due to scale effect. It is the difficult since no reliable wind assessment data is available for SWT height range. However, the same report underlines the potential of SWTs in two contexts: prosumer approach (noting the importance of feed-in tariffs) and isolated sites [7]. The latter may be especially interesting, having in mind the French overseas territories.

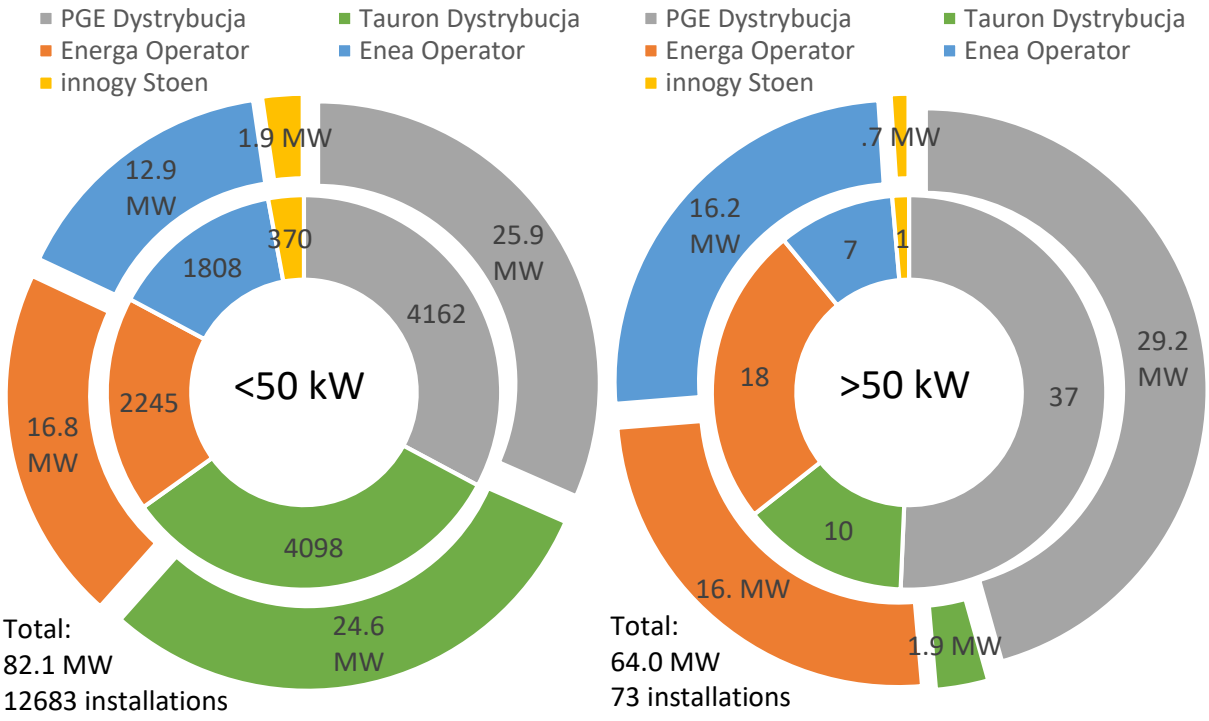

Fig. 4 RES power installed in Poland in 2017 in small (<50 kW, left) and big (>50 kW, right) scale systems: data from 5 biggest Poland's electricity providers (99% of market share by power), data source: [3], [33]

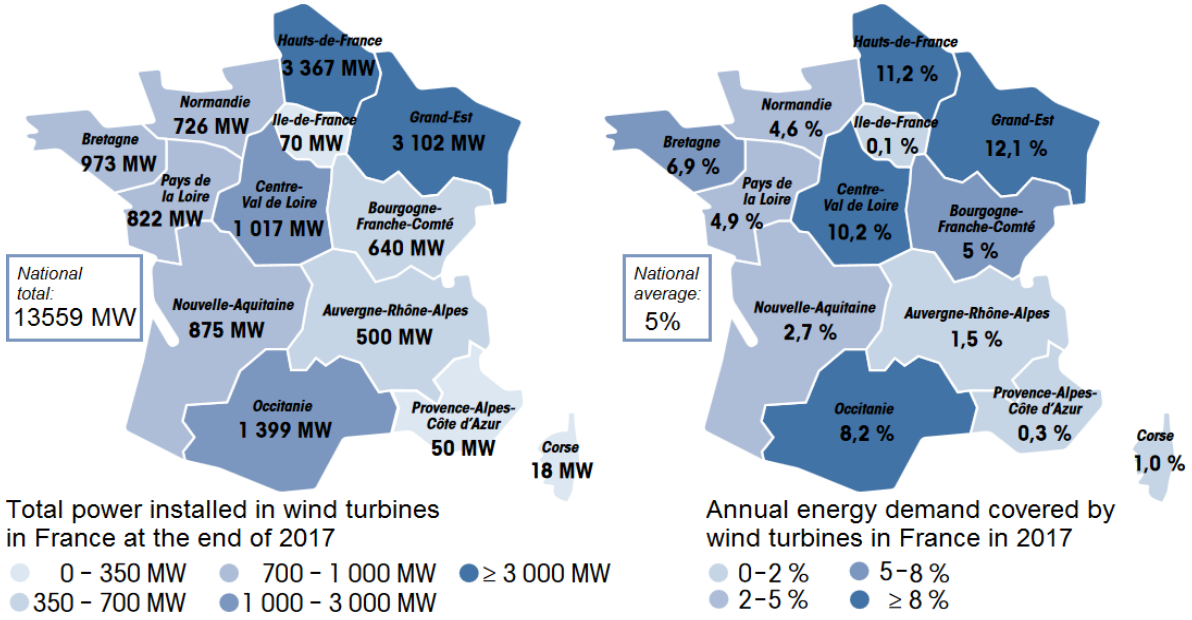

Fig. 5 2017 wind energy statistics per regions of metropolitan France: installed power (left) and annual electric energy demand covered (right) [32]

2.1.3. Future

From the engineering point of view, development of wind turbines towards larger rated powers and rotor diameters is the general tendency. Especially the offshore applications call for ever bigger and more powerful wind turbines. The leading model up to date (July 2018) is Vestas V164 platform, with 9.5 MW (rated wind speed of 13 m/s) model being the most powerful serially produced wind turbine. Each of three blades of the 164 m diameter rotor is of the mass 33 000 – 35 000 kg [34]. GE Haliade-X 12 MW wind turbine (rated wind speed not yet specified) is currently under development. With 107 m long blades the total height of the wind turbine will be 260 m [35]. These wind turbines are mainly targeted towards offshore wind energy, expected to grow rapidly in the upcoming years.

A completely different direction of wind turbine design lies at the basis of development and application of Small Wind Turbines (SWTs). In this approach the wind turbine user is usually a so-called prosumer (person/institution being at the same time both producer and consumer of energy). The prosumer energy generation permits to produce electric energy directly in the place of its consumption (distributed energy generation) and sell the possible surplus. The concept has been evolving in the EU to become a part of its official energy policy. According to the Polish law the small RES (also known as RES microscale installation) has a power no higher than 50 kW, while for example in USA this limit is equal to 100 kW. Taking this country as an example, 1.6 MW (3200 units) of SWTs was installed in 2017 at a cost of about 10 M USD. This is a decline compared with 2016. However, the SWT market is expected to rise significantly in years to come, due to increasing standardisation and certification, and a bipartisan agreement for financial aids for this type of installations [36]. This thesis will concentrate on a concept of a small wind turbine of a twin-rotor, shrouded construction.

A so-called “third way” has emerged lately, that is “community wind”, seen especially often in Denmark and Germany. In this approach a community or group of citizens would install collectively a small wind turbine cluster or a single megawatt-range wind turbine to produce electrical energy for common needs. The modular nature of wind energy makes it possible to scale the wind energy source for the needs of decentralized consumer network. According to Gipe [25] “[Wind turbines] may be owned

individually, cooperatively or mutually through numerous mechanisms. The key is for the community to identify the turbines as its own". It might be said that the community wind promotes wind energy by bringing it directly to them, as a common good. Samsø island in Denmark is a good example of this approach. A community of about 3700 people is energetically fully self-sufficient thanks to wind turbines and biomass combustion [25]. In USA in 2017 the community wind approach constitutes 2.5% of installed wind power, with 15 new installations (48.5 MW in total) installed that year, ranging from 750 kW to 1.5 MW. This suggests an increasing interest in this form of operation in the near future [36].

The future of wind energy in EU is generally given in a favourable manner. Regardless of source, the steady development is envisaged in the years to come, with development of all the aforementioned branches of wind energy generation (Fig. 6). The main questions for the future include the Europe-wise strategies introduced by EU, rate of wind energy market development in the Western Europe and local policies introduced in Eastern Europe. Nevertheless, wind energy is expected to cover as much as 20 – 30% of EU's energy demand in 2030 [37].

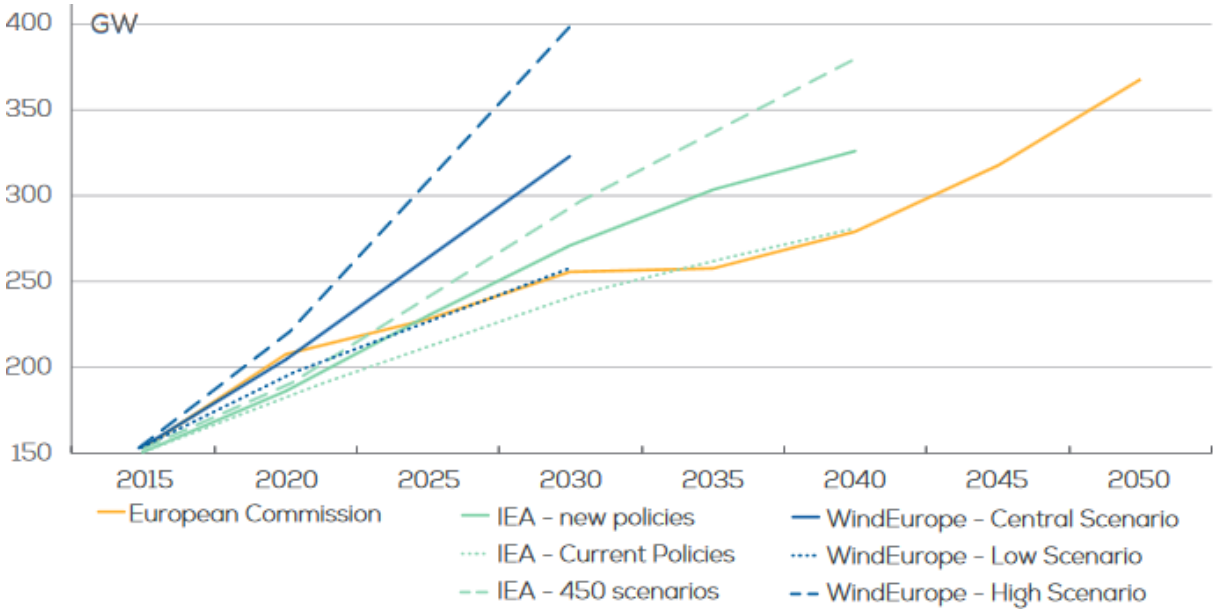

Fig. 6 Scenarios for cumulative wind power capacity development in the EU 2016 – 2050; IEA 450 scenarios – International Energy Agency plan to curb the global temperature increase in 2100 to 2°C above pre-industrial levels [37]

2.2. Systematics of wind turbines

Although technically the concepts described in this and further sections stand correct for all types of windmills, from now the text will refer to wind turbines, being a connection of a windmill and generator, and thus producing electricity. Although technically fitting this definition, emerging technologies such as kite wind turbines are not included in this study.

The orientation of wind turbine axis of rotation is possibly the most apparent means to categorise these machines. Thus the HAWTs and Vertical-Axis Wind Turbines (VAWTs) may be distinguished [25]. This distinction is, however, not as precise as it may seem - a VAWT may also operate efficiently if placed horizontally [38]. Thus it might be more proper to divide the wind turbines by the direction of their axis with respect to that of wind. By this definition the parallel direction would refer to the

HAWTs, while transverse – to all types of VAWTs, regardless of whether the axis is placed horizontally or vertically. Although this definition was used for example in the original US patent by Darrieus [26], it has not caught on.

A majority of the traditional VAWTs falls into one of two categories: Darrieus- and Savonius-type (Fig. 7). The Darrieus rotor consists of slender blades fixed to a rotating shaft. In the most common design the blades of a constant cross-section are curved and fixed to the mast in two places, at its top and bottom, similar to a Greek letter phi (Φ). The aforementioned Éole wind turbine is a two-bladed wind turbine of this configuration. It was only used very briefly, due to significant vibrations. Today the parked rotor serves mostly as a tourist attraction [39]. Variants of Darrieus wind turbines exist, of which H-rotor (giromill) is the most notable. In this design the blades are supported to the shaft via additional beams. In its simplest design the straight, constant-section blades are placed parallel to the axis of rotation. Despite its simplicity, the Darrieus rotor has gained a limited practical use, mainly due to its inability to self-start. This disadvantage may, however, be overcome, for example by special pitch-control systems or an additional start-up device, like Savonius VAWT [25]. The Savonius rotors consist usually of two opposed, hollow semi-cylindrical blades, giving an S-shaped cross-section if seen from above. Due to its curvature, the blade experiences less drag when moving against the wind than when moving with the wind, causing the Savonius to spin. Their ancestors may be assumed to be the above mentioned historic Persian rotors.

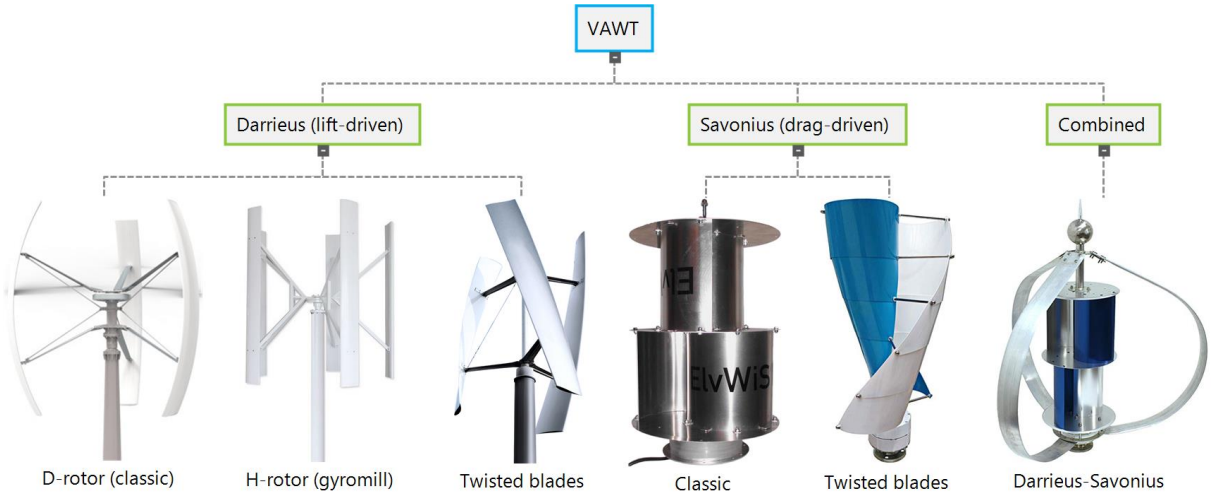

Fig. 7 Examples of typical domestic-size VAWTs [40], [41], [42], [43], [44], [45]

From the aerodynamic point of view, the Darrieus rotor is a lift-driven, while the Savonius is a drag-driven device. This makes the Savonius rotor less efficient, but also more appropriate for placement at low heights. Despite their obvious advantage of omnidirectionality without yawing and ability to operate at lower wind speeds/rotational velocities, field tests prove VAWTs to be generally less cost-efficient than HAWTs. This may, however, change in future, as features such as twisted blades become more common in VAWT design [25].

In case of HAWTs, the most common approach is to divide them by the number of blades (Fig. 8). Wind turbine needs only one blade to harvest the wind energy. The single-bladed rotor operates at relatively high rotational velocities. Thus it normally does not require a gearbox to assure high rotational velocity for the generator to work efficiently. This, along with the lower number of blades, results in a reduced price. However, a single-sided loading introduces significant cyclic loads in the shaft and bearings, thus

a counter-weight is necessary. The blade must also be stronger than in multiple-blade designs to sustain aerodynamic and mechanic loads. Higher rotational velocity also means a higher level of noise emission. In all, no single-blades HAWT has withstood the test of time, despite notable examples coming from Germany (MBB, up to 640 kW) and Italy (Riva Calzoni, up to 300 kW) [25].

The two-bladed HAWT design was particularly popular in the 1970s and 1980s. The design offers much better dynamic behaviour compared to a single-bladed rotor, facilitating the rotor balancing. However, the aerodynamic efforts on the blades still require a relief system, practically realised by means of teetering (movement of the rotor back and forth with respect to principal plane of rotation). Gipe [25] estimates that, as of 2016, at most 250 twin-bladed HAWTs operated worldwide, accounting for no more than 0.1% of wind turbines globally.

As it follows from the classic 1D flow theory (see Subsection 3.1.1) an ideal HAWT rotor should have an infinite number of (infinitely thin) blades. The increase of number of blades is, however, practically limited. This comes from factors such as elevated price of rotor (due to high number of blades), blades material (providing enough stiffness at low cross-section), difficulty in gearbox/generator design (generators generally need to be provided with a sufficiently high rotational speed shaft), complex design of rotor hub. Thus the multi-blade HAWT rotors, although historically significant, are encountered today almost exclusively in special applications, such as micro-wind turbines installed on yachts (e.g. Rutland Windcharger [46]).

Having the above in mind it becomes clearer why a majority of today's HAWTs possesses a three-bladed rotor. It offers the best compromise between efficiency, mechanical properties (blade loading) and environmental impact (noise, visual aspects). Hence the three-bladed design is found in both most powerful large wind turbines in the world, and most popular small ones (e.g. Bergey WindPower [47]).

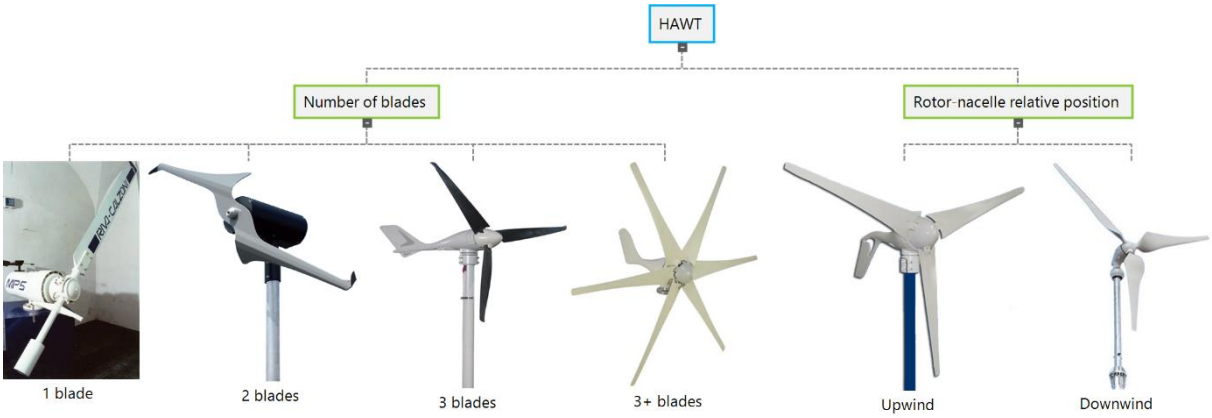

Fig. 8 Examples of domestic-size HAWTs, divided by number of blades (left) or rotor-nacelle relative position [48], [49], [50], [51], [52], [53]

HAWTs may also be classified basing on the relative position of the rotor with respect to the nacelle, that is upwind (the most common design) or downwind type. The latter design has an important advantage of self-orientation towards wind (passive yaw). To increase this effect the blades may be coned, by about 1° - 10°, depending on the blades size. However, as proven by the experiments (Section A2.5 in Appendix 2), the tower's aerodynamic shadow decreases the obtained power. It may also increase the level of noise emission. The downwind HAWTs also tend to operate less steadily than

upwind rotors, notably in high wind conditions. Consequently, the upwind HAWTs (equipped with tail vanes or active yaw control systems) remain the most common designs [25].

To sum up, wind turbines may be classified as of either VAWT or HAWT type. The latter type, in three-bladed upwind rotor configuration, is the most basic design of a contemporary wind turbine. This thesis will concentrate on a three-bladed HAWT exclusively.

2.3. DAWT and its performance

Although the concept of a stator-equipped wind turbine was studied back at the beginning of the 20th century, the first practically realisable solutions were presented around the 1980s. Igra [54] was studying diffusers of a long form, inspired by the turbomachines. Gilbert and Foreman [55] proposed a construction based on an aerodynamic profile (Fig. 9). The drawback of these early solutions was their big size and mass - thus also the cost. There was little practical interest in the solution, due to its financial inefficiency. The concept remained unexplored until the addition of a flange (or a brim) at the diffuser exit (Fig. 10), as proposed by Abe and Ohya [56].

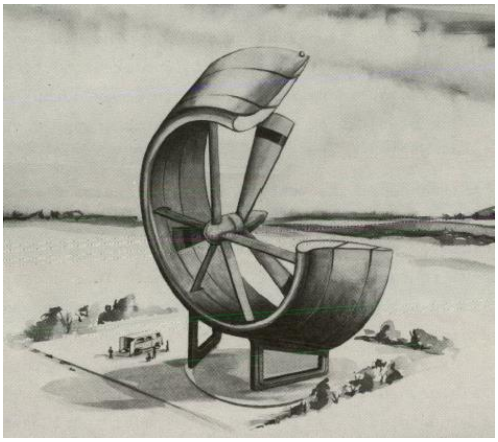

Fig. 9 Artist's impression of an early, 60 m-diameter DAWT [57]

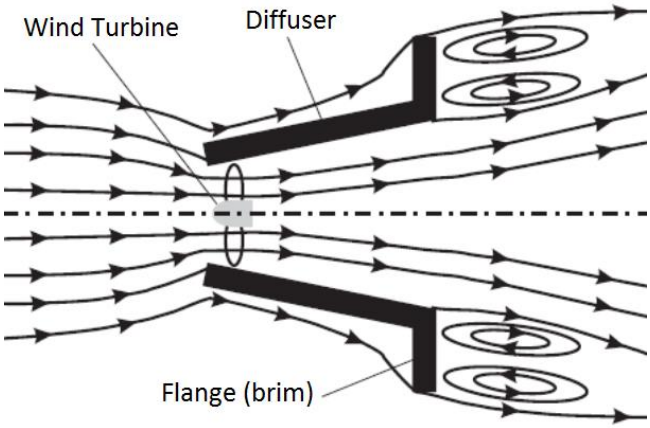

Fig. 10 Streamwise sectional view of a modern DAWT [56]

The research pertaining to DAWTs is currently most advanced in Japan, where DAWTs, born by the name "Wind Lens", are already commercially available. The Wind Lens Turbine WL5000 collects up to 5 kW of power from a wind in wind speed range 12-17 m/s. Its three-bladed rotor has a diameter of 2.5 m, the outer flange diameter is 3.4 m. The structure is 4.24 m high of the mass of 650 kg and may be installed either on a pole or a rooftop [58]. In parallel, the researchers investigate the possibility of larger DAWTs (100 kW, 12.8 m - diameter test turbines operate at Ito campus of Kyushu University, [59]), and use of this technology in offshore applications (on floating hexagonal platforms collecting also solar and tidal energy).

As stated by Igra [54], in the case of an open rotor the entire flow field is typified by atmospheric pressure. The shroud, in the other hand, may support sub-atmospheric pressures in the vicinity of the turbine, thus increasing the role of dynamic pressure in that region. As stated by the mass continuity, the increase in cross sectional area of the diffuser decreases the axial velocity, producing a corresponding increase in pressure. Hence, the diffuser inlet is at a significantly lower pressure than its exit. When a wind turbine is placed at the diffuser inlet, the shroud increases significantly the mass flow and total pressure drop across the turbine. The power available to the turbine is proportional to this product [60].

In a profound analytical study, Lilley and Rainbird [61] compared the performance of an open-rotor and a ducted wind turbine. The authors performed calculations employing the 1D flow theory, as well as the vortex theory. They were able to estimate that the shrouding may result in an increase in a power outcome of an ideal wind turbine by 65%, but pointed out that the calculations would have to be benchmarked with experimental study.

Foreman et al. [62], after a study performed for Grumman Aerospace Corporation, identified the static pressure decrease at the diffuser exit (well below atmospheric pressure) as the factor responsible for flow velocity augmentation in DAWT. The authors stated that an efficient way to increase the performance would be to increase the outlet-to-inlet area ratio. This can be achieved by elongating the diffuser (which is economically inefficient) or increasing the cone angle. The latter solution provokes, however, occurrence of boundary layer separation inside the diffuser – the main reason of efficiency drop. To address this issue, the authors proposed two solutions: slots, that would permit boundary layer mixing and regeneration inside the diffuser, thus reenergizing it and preventing separations, and construction of the diffuser from short aerofoil sections of optimal pressure distribution. The authors claimed that by employing both solutions they were able to double the WT (wind turbine) efficiency. They concluded that the DAWT solution may be a competitive way of increasing the WT power outcome with respect to elongating the blades for small (diameter D < 20 m) and large (D < 50 m) turbines.

A different approach is proposed by Abe and Ohya [56], where the diffuser is brimmed. The authors proposed a 2D actuator model of a flow through DAWT, in which the presence of a wind turbine is modelled by inserting additional source terms to the Navier-Stokes equations in the axial (streamwise) direction. The thrust force was computed using dynamic pressure at the diffuser inlet (with no precision whether it is an averaged or local value), and a constant load coefficient. The force thus determined was applied in a rectangular zone at the diffuser inlet. Reynolds number computed basing on the rotor diameter is equal to Re = 20 000. The study shows that, for increased performance of WT, its loading coefficient should be lower than that for an open rotor (due to higher flow velocity at which ducted WT operates). It is once again underlined that the performance of a DAWT depends on the occurrence of separation inside diffuser. The increased loading may provoke the occurrence of separations, which in turn would decrease the performance.

In a more advanced study by the same team (Abe et al., [63]) the WT load was estimated using the Blade Element-Momentum theory (BEM), thus accounting for the actual profile characteristics and blade geometry. The study compared bare and ducted three-blade wind turbines, by means of 2D simulation (Re = 20 000) and experiment ($Re_{ducted} \approx 200\,000$, $Re_{bare} \approx 300\,000$). The experimental investigation included hot wire anemometry and power determination (by measuring the torque Q and rotational velocity ω). Despite the coarseness of the applied numerical model, a satisfying agreement with experiment was observed for turbine operation conditions that do not provoke flow separation at the blade surface. However, for low and very high rotational velocities (i.e. outside the usual operating range) the model lacked proper prediction of the flow character and predicts incorrect results. Hot wire measurements permitted also to reconstruct the velocity field around bare and shrouded WT. Flow immediately downstream blades was similar in both cases, with only minor differences in the tip region. In return, strong dissimilarities were observed further on, with a rapid destruction of vortex wake in case of DAWT, credited to the damping effect of diffuser.

Finally, in [64] and [65], the same research team proposed a yet more refined numerical 3D models. By applying respectively Actuator Disk (ADM) and Fully-resolved Rotor (FRM) approach they tried to capture the 3D phenomena downstream three-blade rotor. The ADM was firstly examined with no actuator force applied (empty diffuser), then with source terms calculated by the BEM code. In both cases the model was capable of catching properly the time-averaged flow structure inside diffuser, namely the flow velocity and static pressure. The authors proposed an in-house, empirical tip loss correction that assumes linear decrease of actuator force near the blade tip for shrouding of compact form (where diffuser damping effect is less evident). Meanwhile, the FRM approach employed a non-stationary, 3D moving boundary Large-Eddy Simulation (LES). The authors were able to identify what they claim to be an "induced blade tip vortex": a twin structure appearing between the blade tip and duct's inner surface, rotating in the opposite direction to the "normal" blade tip vortex. Its generation is explained by the interaction of blade tip and diffuser inner surface boundary layer. The role of induced blade tip vortex is to thin the boundary layer of diffuser inner surface, and decrease the possibility of flow separation downstream the rotor. As a result, pressure recovery from the diffuser entrance to the exit improves, owing to increased performance. The interaction and mutual weakening between induced and "normal" blade tip vortex is also credited for damping effect of the diffuser.

IMP PL also performed own experimental research in the low wind speed wind tunnel of the institute [66]. The experiment involved PIV flow imaging of an empty diffuser, pneumatic measurements and wind turbine model power determination.

2.4. Twin-rotor wind turbine systems

Following the classical 1D momentum theory by Betz (see ex. [67]) the wind turbine power coefficient (ratio of WT shaft power and wind power) Cp is limited by a value of Cpmax = 16/27 ≈ 59% (a so-called *Betz limit*). Achieving this value would require drop of the axial velocity across the rotor by 2/3. The limit is altered further on when the rotational phenomena are taken into account (see Subsection 3.1.1).

In the case of "classic" turbines (ex. vapour turbines) Charles Gordon Curtis addressed this issue by patenting [68] an impulse turbine composed of a series of stages. This design takes advantage of the so-called velocity compounding, which enables one to decompose the energy extraction process into several nozzle-rotor series. The rotor blades would be installed on a common rotating shaft. This construction's smaller size, as compared to the contemporary solutions, was its main advantage.

Due to a lack of nozzle blades, in the case of wind turbine the two rotors are usually counter-rotating. Appa [69] proposed a twin-rotor counter-rotating wind turbine composed of two rotors of the same geometry (diameter D = 4 m and tip-speed ratio $\lambda = 6$). The rotor separation distance was not explicitly given by the authors, but may be estimated at D/4. Authors estimated by calculations that the theoretical overall Cp of the system could attain values even up to 85%. The study also incorporated the prototype fabrication and tests. Each one of two-blade rotors was mounted directly on a permanent magnet drum, turning around a stationary armature and thus forming an alternator. The prototype was tested in atmospheric conditions for 5 days a month, over 5 consecutive months. Mechanical power and wind speed measurements permit to estimate the turbine efficiency, as seen in Fig. 11. The researchers managed to increase the system Cp by 25 - 40%, as compared with single-rotor, and this gain was most visible for low rotation velocities. The authors also claimed that the buffeting phenomenon (high-frequency instability, caused by airflow separation phenomenon) was

not observed. They concluded that the solution might be suitable for retrofitting of existing wind turbine units, with estimated cost return time of approximately 3 to 5 years.

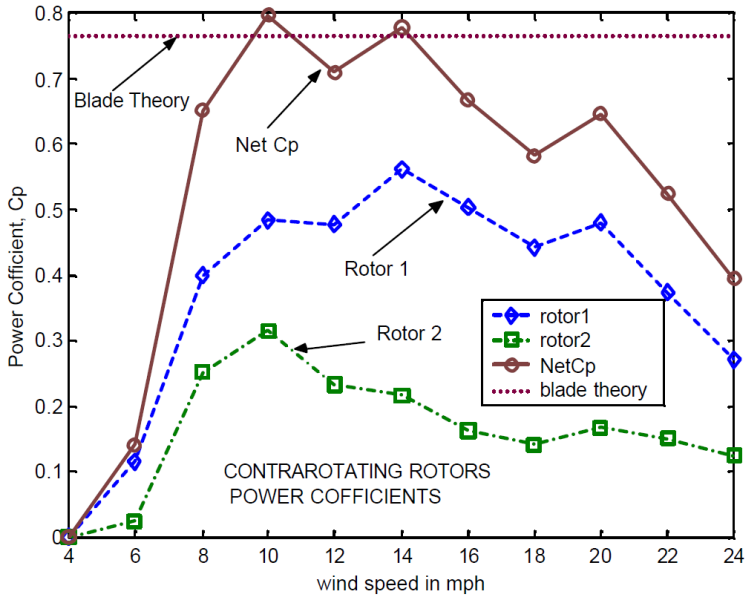

Fig. 11 Experimental power coefficient Cp for each rotor and overall system [69]

Shen et al. proposed [70] a 3D unsteady simulation employing Actuator Line Model (ALM). Two three-blade Nordtank 500 kW wind turbines (D = 41 m, rated $\lambda = 5.81$ at $U_\infty = 10$ m/s) were considered under pure counter-rotation (i.e. rotational velocity of each rotor has the same magnitude and opposite sign). Firstly the separation distance was varied from 0.05D to 0.4D at rated operational conditions. The authors observed that a decreased separation distance had a significant influence on the stability of the system (high fluctuations of torque and thrust force were observed for low separation distance). Next, the influence of changing TSR was examined (Fig. 12a, $\lambda = 1$ to 5.81). Increasing the rotational velocity at constant $U_\infty = 10$ m/s and separation 0.25D leads to increase in Cp. Finally, the influence of U_∞ is examined (Fig. 12b), with conclusion that there is a significant superiority of twin rotor Counter-Rotating WT (CRWT) over a Single-Rotor WT (SRWT) visible for high wind speeds. To improve the system performance for low wind speeds, the authors proposed to reduce the rotational velocity.

Environmental test results for the 30 kW CRWT were presented by Jung et al. [71]. The authors investigated the results of placing a smaller, auxiliary rotor upstream the main rotor. Following the momentum theory they predicted that, while the velocity inside the stream tube generated by the upstream rotor is lower than the ambient values, it is higher outside the tube in close proximity. Profiting from this fact, the authors proposed to replace the inner part of the main rotor (up to half blade length) with supporting mast, and leave the extraction of wind energy in this region to smaller auxiliary rotor. They presented results for a prototype in which upstream rotor diameter was equal to $D_u = 11$ m and downstream rotor diameter - $D_d = 5.5$ m, while the separation distance was set at 2.25 m. Efficiency increase (as compared to the main rotor working alone) was estimated to be 21%, with maximum Cp value of 50%.

Several studies proposed a CRWT, in which the upstream rotor diameter was higher than that of a downstream one. Thus the downstream rotor remains entirely hidden in the upstream rotor wake. Kanemoto and Galal performed [72] a wind tunnel experimental study of a twin-rotor wind turbine

with upstream (D_u = 550 mm) and downstream (D_d = 390 mm) rotor blades of rectangular cross-section and constant chord. Both rotors were operated so as to generate torque of the same magnitude (with opposite signs). The study was aimed to optimise the number of blades (3 in upstream, 5 in downstream rotor) and checking the influence of pitch angle (13° for the upstream and 22° for the downstream blade). Further on, the modified blades are presented, with the same cross-section but chord varying along the radius.

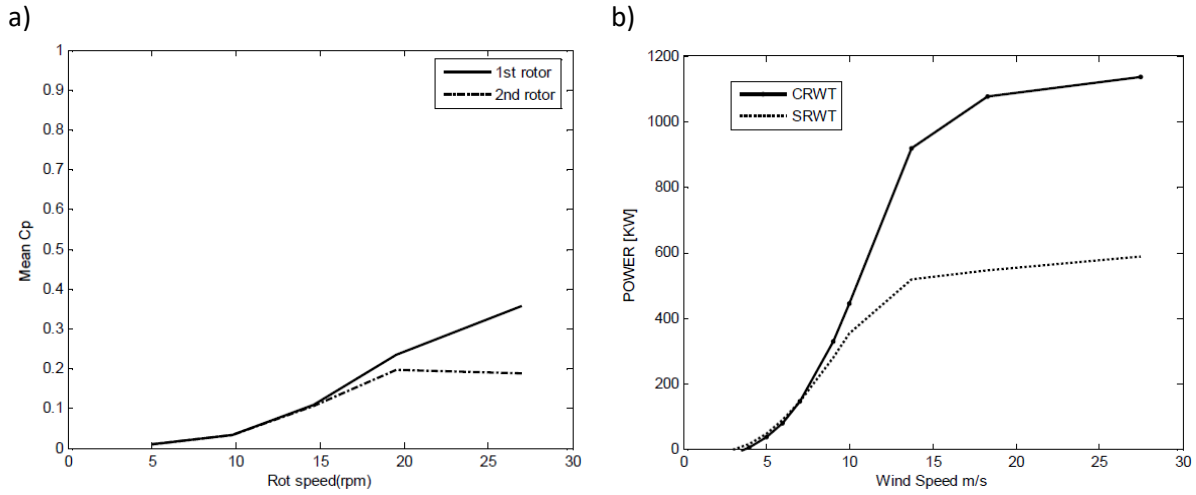

Fig. 12 Performance of Nordtank 500 kW-based counter-rotating WT (separation distance 0.25D) at various rotational speeds (a, U_∞ = 10 m/s) and inflow velocity (b, λ =5.81) (ALM simulation, [70])

The aforementioned experiment was extended by Kubo and Kanemoto in [73], with an employment of blades made of MEL002 aerofoil, not-twisted and twisted for angle of attack of 7° (at λ = 7). The authors checked the influence of rotor size ratio (with maximum Cp at D_d/D_u = 1). The increasing power outcome was mainly influenced by rising D_d, which is not surprising, as it leads to a bigger area swept by the blades. The distance between rotors was also studied, with conclusion that decreasing its value increases the power outcome at price of increasing possibility of collision. Authors presented also velocity measurement results in selected locations.

The same research team also performed [74] an experimental study, unveiling the "*Intelligent Wind Turbine Unit*". The authors presented a generator with two rotating armatures. Their turbine is to be optimised to permit counter-balancing the torque between upstream and downstream rotor, for control purpose above the rated point. This is ensured by the operational behaviour of the downstream rotor, which reaches the maximum ω at rated wind velocity. With further increase in U, the downstream rotor decelerates gradually, stops and then begins to rotate in the opposite direction (i.e. the same one as the upstream rotor). Authors presented the field measurements results, with a CRWT (D_u = 2 m, D_d = 1.33 m) placed on a pickup truck. The blades were based on MEL0012 profile and optimised for angle of attack of 7° (at λ = 7). The authors claimed that by using only the proper setting of downstream blade pitch angle and applied electric load, they were able to set the downstream rotor into operation mode above rated point as explained above, thus avoiding the need for additional external command.

Numerical simulation of a CRWT using FRM was presented further by the same research team in [75]. The same blade geometries as in [73] were tested (D_d/D_u = 0.84). The model was validated versus an experiment performed for one and two rotors. Then the study proceeded (yet again) to optimisation

of blade pitch angles for both rotors. Further on the authors pointed out that the torque contribution of the inner part of the upstream blade (up to 46% of its length) is minimal. Thus it is proposed to design it as provoking no rotational component, i.e. the resultant reaction force should only be acting in the axial direction. Also, the resulting thrust should be minimised to maximise the wind resources for the downstream rotor. For this purpose NACA0015 aerofoil is set with high twist angles (40° at blade base, 20° at 46% of its length) so as to provoke local angle of attack of 8°, which results in this blade portion having only axial force contribution. This operation increases the overall system maximum efficiency by about 5%, whilst shifting the optimal operating conditions for downstream rotor towards higher TSR values.

3. Theoretical introduction

This chapter provides the basic mathematical formulations employed in the thesis.

3.1. Flow analysis

This section discusses the basic theories used for analysis of flows through wind turbine systems.

3.1.1. 1-D momentum theory

The most basic model for wind turbine rotor studies is based on the momentum theory, named also Froude-Rankine theory after its original developers. It states that the (ideal) rotor can be represented as a region of static pressure drop Δp, a frictionless actuator disk with no rotational velocity component imposed [27]. It is assumed that the static pressure at infinity upstream and downstream the disk is equal. The pressure drop Δp results in diminution of the flow velocity. Thus the fluid's kinetic energy changes as well. The axial distribution of the pressure p and streamwise velocity U is presented in Fig 13.

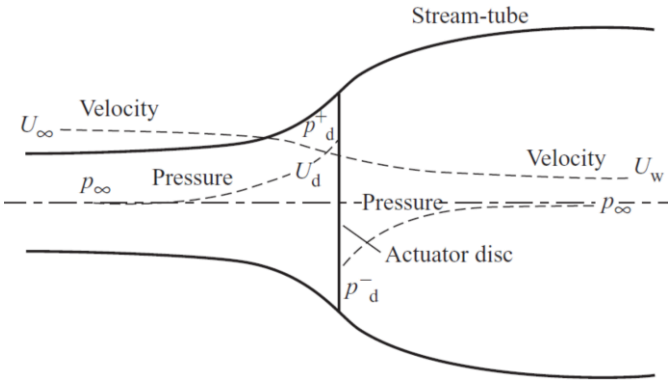

Fig. 13 Illustration of the 1D rotor theory [27]

For this type of flow (incompressible, low-speed, isothermal), the Bernoulli equations for the region in the actuator disk plane, upstream (∞) and downstream (w) yield [67]:

$$\begin{aligned} p_\infty + \frac{\rho U_\infty^2}{2} &= p_d^+ + \frac{\rho U_d^2}{2} \\ p_d^- + \frac{\rho U_d^2}{2} &= p_\infty + \frac{\rho U_w^2}{2} \end{aligned} \tag{1}$$

Summing both equations in (1) by sides yields the following:

$$\Delta p = p_d^+ - p_d^- = \frac{\rho(U_\infty^2 - U_w^2)}{2} \tag{2}$$

Δp in (2) may be interpreted as the aerodynamic pressure, exerting axial force F_t (thrust) onto the disk:

$$F_t = \Delta p \cdot A = \Delta p \cdot \frac{D^2}{4} = \frac{\rho A(U_\infty^2 - U_w^2)}{2} \tag{3}$$

In (3) A and D denote the actuator disk (hence the rotor swept) area and diameter, respectively. F_t is concentrated at the disk and the rate of work (power) done by the force may be related to the local velocity at the disk location, U_d, as:

$$P = F_t \cdot U_d \tag{4}$$

Substituting (2) and (3) into (4) yields the following formula for determination of power:

$$P = \frac{\rho U_d A (U_\infty^2 - U_w^2)}{2} \tag{5}$$

With the change in flow velocity, the fluid is experiencing the change in momentum. Since the fluid is comprised entirely in the prescribed streamtube, the change of momentum comes exclusively from the force F_t, equal consequently to the rate of change of momentum, which for uniaxial flow is [27]:

$$momentum = m \cdot \frac{\Delta U}{\Delta t} = \dot{m} \cdot \Delta U = \rho U_d A \cdot (U_\infty - U_w) = F_t \tag{6}$$

By equating (3) and (6), the following relationship is obtained:

$$\frac{\rho A (U_\infty^2 - U_w^2)}{2} = \rho U_d A \cdot (U_\infty - U_w) \tag{7}$$

Which yields directly to:

$$U_d = \frac{U_\infty + U_w}{2} \tag{8}$$

Equation (8) shows that half of the velocity drop occurs upstream the actuator disk and half – downstream. The velocity deficit is typically described by the axial inductor factor a, that is:

$$\begin{gathered} a \stackrel{\text{def}}{=} 1 - \frac{U_d}{U_\infty} \qquad ,thus \\ U_d = U_\infty \cdot (1 - a) \qquad and \qquad U_w = U_\infty \cdot (1 - 2a) \end{gathered} \tag{9}$$

Placing (9) into (5) yields, after rearrangements, the following formula for actuator disc power:

$$P = \frac{\rho A U_\infty^3}{2} \cdot 4a(1-a)^2 \quad or \quad P = P_{wind} \cdot C_p \tag{10}$$

In (10) P_{wind} denotes the power of undisturbed wind stream of the same cross-section as the actuator disk. Cp is the so-called power coefficient, one of the basic concepts in the wind turbine analysis. It is defined as the ratio the power of actuator disk to the power of wind stream. Its maximal theoretical value can be determined via differentiation with respect to a, giving:

$$\begin{gathered} \frac{dC_p}{da} = 4(1-a)(1-3a) \\ C_{pmax} = C_p\left(a = \frac{1}{3}\right) = \frac{16}{27} \approx 0.593 \end{gathered} \tag{11}$$

An important conclusion drawn from (11) is that the maximum power drawn from an actuator disc cannot exceed 59.3% of the power comprised in a wind stream of the same area. This value is known as the Betz limit. By analogy, putting (9) into (3) gives:

$$F_t = \frac{\rho A U_\infty^2}{2} \cdot 4a(1-a) \quad ,or \quad F_t = F_{twind} \cdot C_t \tag{12}$$

In (12) F_{twind} is the thrust of undisturbed wind stream of the same cross-section as the actuator disk, while Ct denotes the thrust coefficient.

As follows from (9), for a > 0.5 the velocity in the wake would become negative. The experiments prove that the momentum theory assumptions of flow character (notably the laminar wake contained in a streamtube) become invalid for a values higher than approximately 0.4. Above that value corrections are usually used to account for the unstable, turbulent wake phenomena (see ex. [76]).

3.1.2. Rotation effects

HAWT is essentially a device designed to convert the kinetic energy from the axial translational movement of air onto the torque of the rotor and shaft. The power transmitted by the shaft can be expressed as the product of its rotational torque Q and velocity ω:

$$P = Q \cdot \omega \tag{13}$$

Q is the torque with which the passing fluid acts upon the wind turbine rotor. According to the Newton's 3rd law, the reaction torque, equal in magnitude but with opposite direction, is exerted by the rotor upon the flow. Consequently, the flow acquires a tangential velocity component Vt. A priori the tangential flow velocity upstream the turbine is equal to 0. The magnitude of Vt is proportional to the rotational velocity and distance from the rotation axis r, and similar relationships as in (9) may be proposed, with a' – the tangential induction factor, and Vw – the tangential velocity in the wake:

$$\begin{gathered} a' \stackrel{\text{def}}{=} \frac{V_t}{\omega r} \qquad ,thus \\ V_t = \omega r \cdot a' \qquad and \qquad V_w = 2 \cdot \omega r \cdot a' \end{gathered} \tag{14}$$

A relationship between wind turbine rotational and flow axial velocity is given in the form of tip-speed ratio (TSR) λ:

$$\begin{gathered} \lambda_{local} = \frac{V_t}{U_\infty} = \frac{\omega r}{U_\infty} \\ \lambda_{global} = \lambda_{local}(r = R) = \frac{\omega R}{U_\infty} = \lambda \end{gathered} \tag{15}$$

Let one consider now an annular ring of the rotor, placed at a distance r from the rotation axis, of thickness dr and area dA_d. Similarly as for equation (6) it can be assumed that the torque on the ring dQ will be equal to the rate of change of angular momentum of the fluid [27]:

$$\begin{gathered} \dot{angular\ momentum} = \dot{m}\frac{\Delta V}{\Delta t} \cdot r = \dot{m} \cdot \Delta V \cdot r = \\ = [\rho \cdot U_\infty (1 - a) \cdot dA_d] \cdot [2\omega r a'] \cdot r = dQ \end{gathered} \tag{16}$$

Putting (16) into (13) and integrating from 0 to R gives consequently [67]:

$$P = 4\pi\rho\omega^2 U_\infty \int_0^R (1 - a)a' \cdot r^3 dr \tag{17}$$

It is easily noticeable in eq. (17) that it is necessary to optimise the expression to increase the power. It is possible to show (see e.g. [67]) that this optimum relationship for pre-stall conditions is in the form:

$$a' = \frac{1 - 3a}{4a - 1} \tag{18}$$

3.1.3. Blade-Element Theory (BET)

The relatively high length of the wind turbine blades makes the spanwise velocity component much lower than the streamwise and rotational ones. Treating the flow as 2D, with the spanwise velocity component neglected, one may assume that every blade section is independent from any other one. This assumption is the foundation of the Blade-Element Theory, involving discretization of the blade into infinitesimally small sections at different radial positions (stations). At each station the local aerodynamic forces are then computed, assuming that the sections may be treated as 2D aerofoils (Fig. 14). Then, the forces are integrated along the blade span, giving the total thrust and torque [27].

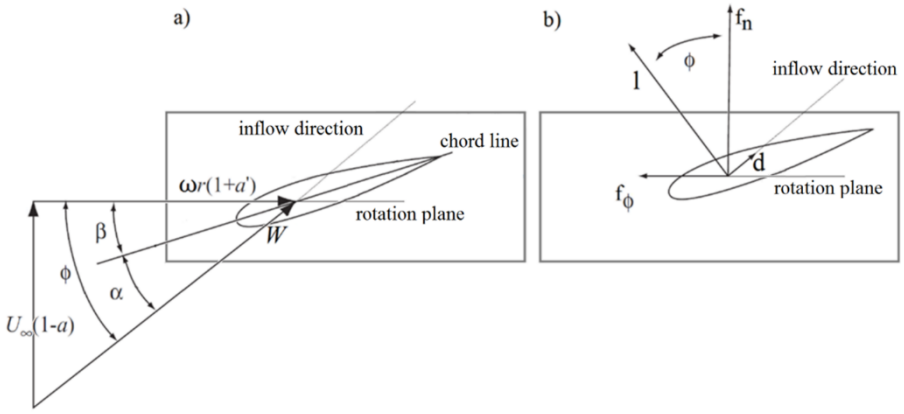

Fig. 14 Illustration of the BET, basing on [67]

The original formulation of BET was proposed by Drzewiecki (see ex. [77]). The employment of this original formulation was limited, since it did not take into account the induced velocity effects. Vortex theory studies by Prandtl at the beginning of the 20th century enabled to address this issue by Joukowski and Betz [78]. Further development of the model, up to the formulation used commonly nowadays, was proposed by Glauert [79].

One is to consider a blade station chosen at a radial position r, with cross-section being an aerofoil. The associated velocity triangle is seen in Fig. 14a. The inflow velocity W is the vector sum of the axial and tangential flow velocities at the studied blade station (neglecting the blade spanwise velocity). Its magnitude W may be calculated using the formula [27]:

$$W = \sqrt{[U_\infty(1-a)]^2 + [\omega r(1+a')]^2} \tag{19}$$

Three angles may be associated with the velocity triangle at the blade station:

- Inflow angle ϕ – the angle formed by the velocity vectors:

$$\phi = \operatorname{atan}\left(\frac{U_\infty(1-a)}{\omega r(1+a')}\right) \tag{20}$$

- Pitch angle β – blade section twist, determined by the rotor design - the angle between the chord line and the plane of rotation;
- Angle of attack (AoA) α – the difference between the abovementioned:

$$\alpha = \phi - \beta \tag{21}$$

From the 2D aerofoil aerodynamics it is possible to compute the aerodynamic forces per unit blade length, lift l and drag d, as:

$$l = \frac{\rho W^2}{2} \cdot c \cdot C_l \qquad and \qquad d = \frac{\rho W^2}{2} \cdot c \cdot C_d \tag{22}$$

In eq. (22) c denotes the chord (distance between aerofoil's leading and trailing edges). Cl and Cd are lift and drag coefficients, respectively. The lift force is parallel to vector W, while the drag force is perpendicular to vector W, thus both are defined in a local coordinate system associated with the inflow velocity. They may be converted to a global coordinate system associated with the plane of rotation and flow direction, knowing the inflow angle, as [67]:

$$f_n = l \cdot cos\phi + d \cdot sin\phi \qquad and \qquad f_t = l \cdot sin\phi - d \cdot cos\phi \tag{23}$$

A proper choice of the aerodynamic force coefficients Cl and Cd is one of the most challenging aspects of the BET. A discussion concerning this problem is presented in Section 6.2.

In eq. (23) fn and ft are normal and tangential forces determined for unit blade length, respectively. fn, directed axially, contributes to the thrust force, while ft, directed tangentially, contributes to the production of rotational torque:

$$F_t = \sum_{i=1}^{B} \int_0^R f_n dr \qquad and \qquad Q = \sum_{i=1}^{B} \int_0^R r \cdot f_t dr \tag{24}$$

In eq. (24) B denotes the number of blades and R is the rotor radius. The classic BET assumes that the force from the blades on the flow is constant in each annular element. This means that on each blade the force is of the same value, and the summation operation in (24) may be replaced by multiplication by B [67]. The original formulation of BET also assumes that the 2D character of the flow is preserved at all blade stations. Although this holds true for majority of blade span, near the end of the blade the phenomenon of tip leakage occurs, where the spanwise flow tends to appear. Thus the aerodynamic forces generated in that region do not correspond to those derived from the 2D aerofoil properties and correction is needed. Such a correction was indeed proposed by Prandtl (and reported by Betz in [80]), and further developed by Glauert [79]. It involves multiplication of the force components (23) by the tip loss factor F, defined as:

$$F = \frac{2}{\pi} \cdot acos\left(e^{-f}\right) \quad , where \quad f = \frac{B}{2} \cdot \frac{R - r}{r \cdot sin\phi} \tag{25}$$

Numerous attempts were made over the years to develop alternative versions of the tip loss correction (see ex. [81]). For DAWT the proper formulation of the tip loss factor is potentially more complicated, as shown by Takahashi et al. [65], due to the damping effects of the diffuser. A discussion concerning this subject can be found in Subsection 5.4.4.

The formulae (24) can be coupled with those derived previously in Sections 3.1.1 and 3.1.2. This is indeed done, in an approach known as the Blade-Element Momentum (BEM) theory. It is an iterative method of computing of the rotor performance based on an approximation of a and a', permitting consequently to compute the wind turbine performance. The detailed calculation procedure may be found for example in [67]. This thesis, however, concentrates on the so-called hybrid model. The

influence of the rotor is computed basing on the local velocity fields directly, so there is no need to estimate a and a' analytically. The principles of the model are discussed in Section 6.1.

3.1.4. Flow through diffuser in open flow conditions

The so-called Venturi effect states that the flow velocity magnitude is inversely proportional to the conduit section area for confined flows. Blocken et al. [82] and Li et al. [83] in their studies of flow around buildings proved, however, that for the open flows this phenomenon is not universally observed. The investigators have observed a velocity increase at the inlet (i.e. the narrowest) section. In turn, the velocity at the widest cross section attains values of order of free stream conditions (Fig. 15). It is claimed that the velocity increase comes from the so-called upstream corner streams. The origin of velocity increase at a divergent building configuration is identified as a superposition of two such corner streams, as well as wind-blocking effect, where large amount of the oncoming air flows over and around the buildings, not through the passage opening.

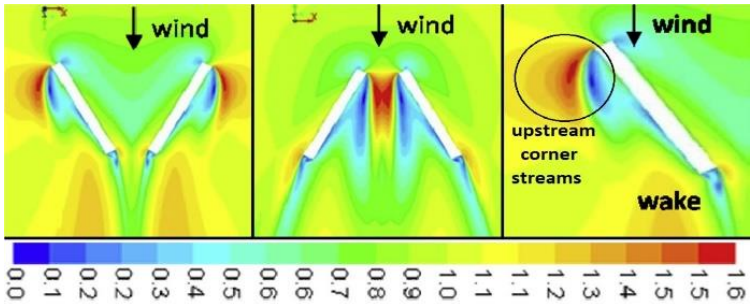

Fig. 15 Dimensionless streamwise velocity U/U_∞ values for convergent and divergent building configuration (numerical results) [83]

Ohya et al. [84] show experimental results that prove that the same phenomena occur in flows through channels of square cross-section (Fig. 16), and claim that they were also observed for axisymmetric (i.e. of circular cross-section) ducts. In the same paper the authors underline that high L/D_d ratios are of little interest from the practical point of view. They suggest that L/D_d ratio should not surpass 2 and apply different modifications to the duct geometry that would follow that constraint, while still providing a significant flow velocity augmentation. Authors propose a proper profiling of the diffuser inlet, and encompassing the external outlet edge by a ring structure, referred to as flange or brim. Smoke visualization technique allowed the authors to observe the vortex structure behind the brim. Low-pressure region thus created is claimed to be the source of an additional flow velocity increase. The magnitude of this augmentation is no less than 50%.

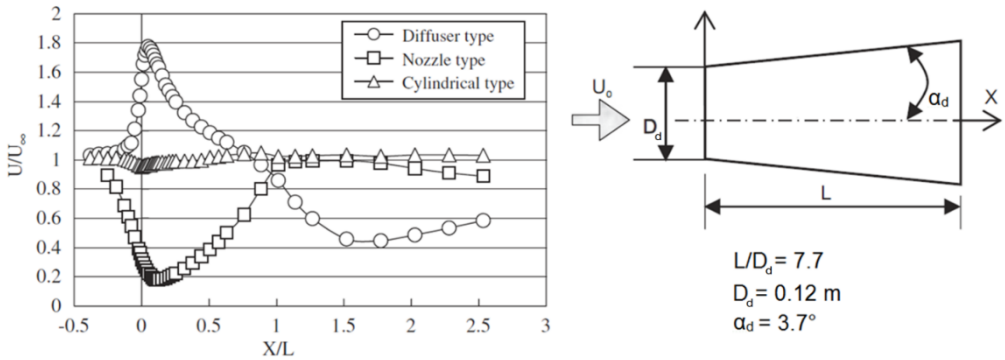

Fig. 16 Axial distribution of dimensionless streamwise velocity U/U_∞ along divergent (circles), constant-section (triangles) and convergent (squares) duct of square cross-section (experimental results after [84])

3.1.5. Diffuser-Augmented Wind Turbine (DAWT)

The analysis presented in Subsection 3.1.4 considers an empty diffuser, with no wind turbine installed. The rotor exerts an additional axial (drag) force, influencing the pressure distribution and the flow structure.

As shown by de Vries [85], the (axisymmetric) shrouding of a wind turbine may be substituted by an annular vortex ring. The vorticity associated with this vortex ring induces additional axial velocity through the diffuser, increasing the mass flow rate through it and, eventually, a wind turbine placed inside. It may easily be proved (see ex. [67]), that at the same reference velocity and identical rotor area, the bare (OR) and shrouded (DAWT) wind turbine power coefficient will share the following relationship:

$$\frac{C_{pDAWT}}{C_{pOR}} = \frac{\dot{m}_{DAWT}}{\dot{m}_{OR}} \tag{26}$$

One is to consider a one-dimensional flow through a DAWT, as seen in Fig. 17. Writing Bernoulli equation for reference and upstream the rotor locations gives [86]:

$$p_\infty + q_\infty = p_+ + q_+ + \varepsilon_i q_\infty \ , \tag{27}$$

with ε_i – air flow momentum loss factor.
Moreover, one is to define η - diffuser pressure recovery efficiency, as:

$$p_e - p_- = \eta(q_- - q_e) \quad , recalling \quad \begin{matrix} A_- \cdot U_- = A_e \cdot U_e \\ A_- = A_d = A \end{matrix}$$
$$p_e - p_- = \eta q_- \left(1 - \left(\frac{A}{A_e}\right)^2\right) \tag{28}$$

Recalling equations (2), (3) and (12) (note thrust coefficient C_{td} is computed with respect to q_d, not q_∞):

$$\Delta p = p_+ - q_- = C_{td} q_d \tag{29}$$

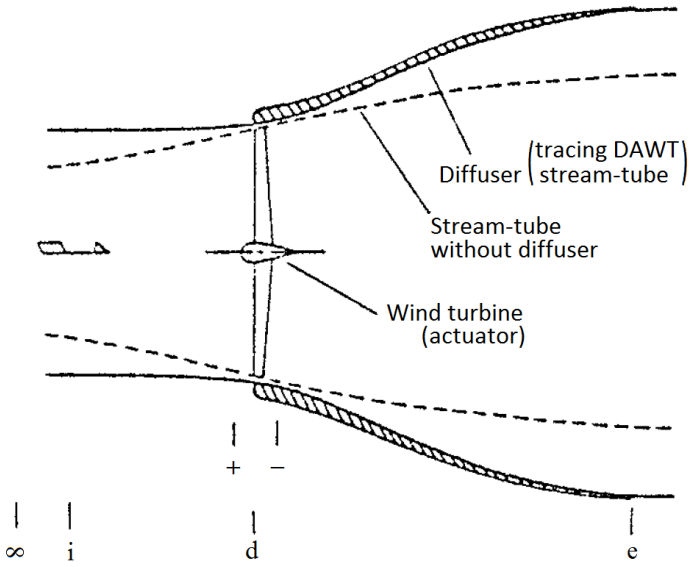

Fig. 17 Illustration of the 1D rotor theory (DAWT), prepared on the basis of [86]

One is to define the following pressure coefficients cp as:

$$cp_d = \frac{p_e - p_-}{q_-} \quad ,from\ (28) \qquad cp_d = \eta\left(1 - \left(\frac{A}{A_e}\right)^2\right) \tag{30}$$

$$cp_- = \frac{p_- - p_\infty}{q_\infty} \quad ,from\ (27)\ and\ (29) \qquad cp_- = (1 - \varepsilon_i) - (1 + C_{td})\frac{q_d}{q_0} \tag{31}$$

$$cp_e = \frac{p_e - p_\infty}{q_\infty} \quad ,from\ (41)\ and\ (42) \qquad cp_e = cp_d\frac{q_d}{q_0} + cp_- \ , \tag{32}$$

with cp_d – diffuser pressure recovery coefficient; cp_- , cp_e – pressure recovery coefficients at location downstream rotor and diffuser exit, respectively. Putting further on (31) into (32) and rearranging yields:

$$\frac{q_d}{q_\infty} = \frac{1 - (\varepsilon_i + cp_e)}{1 + C_{td} - cp_d} \tag{33}$$

Formula (33) enables one to quantify the increase of velocity through the rotor due to diffuser presence.

One is now to consider power coefficients, C_p defined classically (see formula (10)), and γ defined with respect to the diffuser exit area:

$$C_p = \frac{P}{P_{wind}} = \frac{\Delta p \cdot A \cdot U_d}{\frac{\rho A U_\infty^3}{2}} \quad ,from\ (29)\ and\ (33) \qquad C_p = C_{td} \cdot \left(\frac{1 - (\varepsilon_i + cp_e)}{1 + C_{td} - cp_d}\right)^{\frac{3}{2}} \tag{34}$$

$$\gamma = C_p \cdot \frac{A}{A_e} \qquad ,from\ (30), with\ \frac{A}{A_e} = n \quad \gamma = nC_{td} \cdot \left(\frac{1 - (\varepsilon_i + cp_e)}{1 + C_{td} - \eta(1 - n^2)}\right)^{\frac{3}{2}} \tag{35}$$

Nagai [86] puts $\varepsilon_i + cp_e = 0$, thus stating that the pressure drop at the diffuser exit region is relatively small. This is a fair assumption for a simple, cone-shaped diffuser. Under this condition (34) and (35) become:

$$C_p = \frac{C_{td}}{(1 + C_{td} - cp_d)^{\frac{3}{2}}} \quad and \quad \gamma = \frac{n \cdot C_{td}}{\left(1 + C_{td} - \eta(1 - n^2)\right)^{\frac{3}{2}}} \tag{36}$$

One is to initially set η = 1, (corresponding to a frictionless diffuser, [85]). Computing the maximum power coefficients under this assumption, by differentiating (36) with respect to n , gives that:

$$\gamma_{maxDAWT} = \gamma\left(n = \sqrt{\frac{C_{td}}{2}}\right) = \frac{2}{\sqrt{27}} \quad and \quad C_{pmaxDAWT} = \frac{2}{n \cdot \sqrt{27}} \tag{37}$$

It is first of all noticeable that the maximum power coefficient γ is constant, regardless of the load C_{td}. One is now to consider a case for which n = 0.5:

- if $C_{td} = 2$ the flow conditions become identical to those of an open rotor operating in its optimum (axial induction factor a = 1/3); $C_p = C_{pmaxOR} = 16/27$, the Betz limit for unshrouded rotor,
- for DAWT, as it follows from (37) , $C_{pmaxDAWT} = 4/\sqrt{27} \approx 0.770 = \sqrt{C_{pmaxOR}}$.

From the above mentioned it follows that in the flow conditions corresponding to the open rotor optimum point of operation the diffuser may increase the maximum rotor efficiency at the assumed operating conditions by approximately 30%.

In reality, the efficiency η is lower than 1. Figure 18a shows how γ is influenced by η. The power coefficient increase due to diffuser presence manifests itself notably at n in the range of 0.3 to 0.5. The increase becomes less significant as η drops. For $\eta < 0.7$ the gain from diffuser presence is hardly visible. Nagai [86] postulates that $\eta = 0.8$ is a common-sense choice, as based on his own experimental works. Figure 18b analyses $\gamma(A/A_e)$ relationship at varying C_{td}. It follows that it is advisable to increase C_{td}, although it must be remembered that the model does not account for flow separations in rotor wake and/or at diffuser walls. It is also noticeable that the value of $n = A/A_e$ should not be increased too far, as this eventually leads to a decrease in power coefficient.

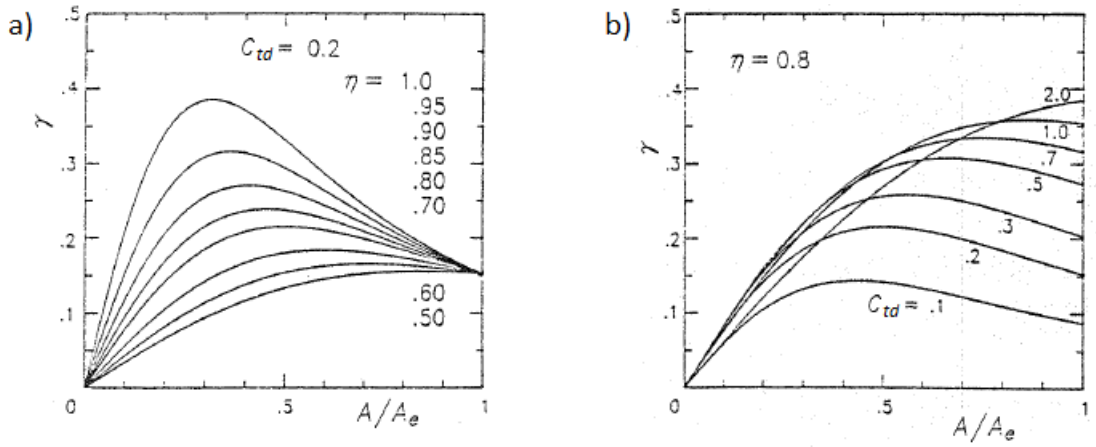

Fig. 18 DAWT power coefficient $\gamma(A/A_e)$ for: a) different values of η at $C_{td} = 0.2$ and b) for different values of C_{td} at $\eta = 0.8$ [86]

The above considerations become more complex as flow separations are taken into account. Therefore, a majority of the contemporary studies relies directly on dedicated empirical data (experimental and/or numerical), rather than own analytical models. A profound, yet hardly exhaustive, summary of different low-order models of flow around DAWT may be found for example in [87].

3.1.6. Counter-Rotating Open Rotor (CROR)

One is now to consider that the second rotor of the same diameter is placed in the wake of the existing one, and 1D momentum theory is applied to the system thus created. At a sufficiently high distance between the two rotors it may be assumed that the flow can be superposed from two independent actuator disks presented in Fig. 13. Newman [88] estimates that this assumption is valid for separation distances of at least one rotor radius (for wind turbines of equal diameter). However, more recent experimental studies by Kanemoto and Galal [72] and Kubo and Kanemoto [73] show that the above assumptions may be still correct even for distance as small as 10% of the upstream rotor diameter. Under the above mentioned hypothesis, the upstream rotor's wake conditions become the freestream flow conditions for the downstream rotor. Recalling (9) and putting it into (10) for the downstream rotor one obtains:

$$P_d = \frac{\rho A U_w^3}{2} \cdot 4a_d(1-a_d)^2 = \frac{\rho A\left(U_\infty \cdot (1-2a_u)\right)^3}{2} \cdot 4a_d(1-a_d)^2 = \\ = \frac{\rho A U_\infty^3}{2} \cdot 4a_d(1-a_d)^2(1-2a_u)^3 \ , \tag{38}$$

where index "u" refers to the upstream rotor and "d" to the downstream rotor. Hence:

$$C_{pu} = 4a_u(1-a_u)^2 \\ C_{pd} = 4a_d(1-a_d)^2(1-2a_u)^3 \\ C_{ptot} = C_{pu} + C_{pd} \ , \tag{39}$$

where index "tot" refers to the total Cp of the system. To compute the maximum C_{ptot} derivations with respect to a_u and a_d are performed:

$$\begin{cases} \dfrac{dC_{ptot}}{da_u} = -8(1-a_u)a_u + 4(1-a_u)^2 - 24(1-a_d)^2 a_d(1-2a_u)^2 \\ \dfrac{dC_{ptot}}{da_d} = 4(1-2a_u)^3(1-a_d)(1-3a_d) \end{cases} \tag{40}$$

Finally, the maximal Cp_{tot} is found at the following conditions:

$$a_{umax} = \frac{2}{5} \qquad a_{dmax} = \frac{1}{3} \qquad ,thus \\ C_{ptotmax}(a_{umax}, a_{dmax}) = \frac{16}{25} = 0.64 \tag{41}$$

The above formula may be interpreted as the Betz limit for a twin-rotor system. This proves that the addition of the second rotor increases the theoretical maximum Cp_{tot} by 8% with respect to a single rotor system. In reality, as noted in [88], the above considerations depend strongly on the separation distance between the rotors.

One is now to consider the effects of rotation of the counter-rotating twin-rotor system. Figure 19 presents the velocity triangles for upstream (bottom) and downstream (top) rotor, formulated on the basis of 2D Blade Element Theory, at different axial positions. The fluid (A), after passing through the first rotor plane (B), diminishes its axial velocity (eq. (9)) and gains a tangential (rotational in 3D) component (eq. (14)). The wake of the upstream rotor (C) becomes consequently the inflow (free stream) conditions for the downstream rotor. The inflow velocity is thus a vector sum of the axial and tangential components. To account for this fact the downstream rotor is required to turn in the opposite direction than the upstream one. Hence the system is referred to as the "counter-rotating rotors". In the plane of rotation of the downstream rotor (D) a tangential velocity component pertinent to ω_d is acquired by the flow, as stated by eq. (14). In the wake of the entire system the flow has had acquired tangential velocity components from both rotors. To minimise the wind energy lost normally in the rotating wake it is advantageous to minimise the total tangential velocity component, that is (assuming the values of ω_d and ω_u are both taken positive):

$$\omega_d r 2a'_d - \omega_u r 2a'_u = min \\ or \\ \omega_d a'_d - \omega_u a'_u = min \tag{42}$$

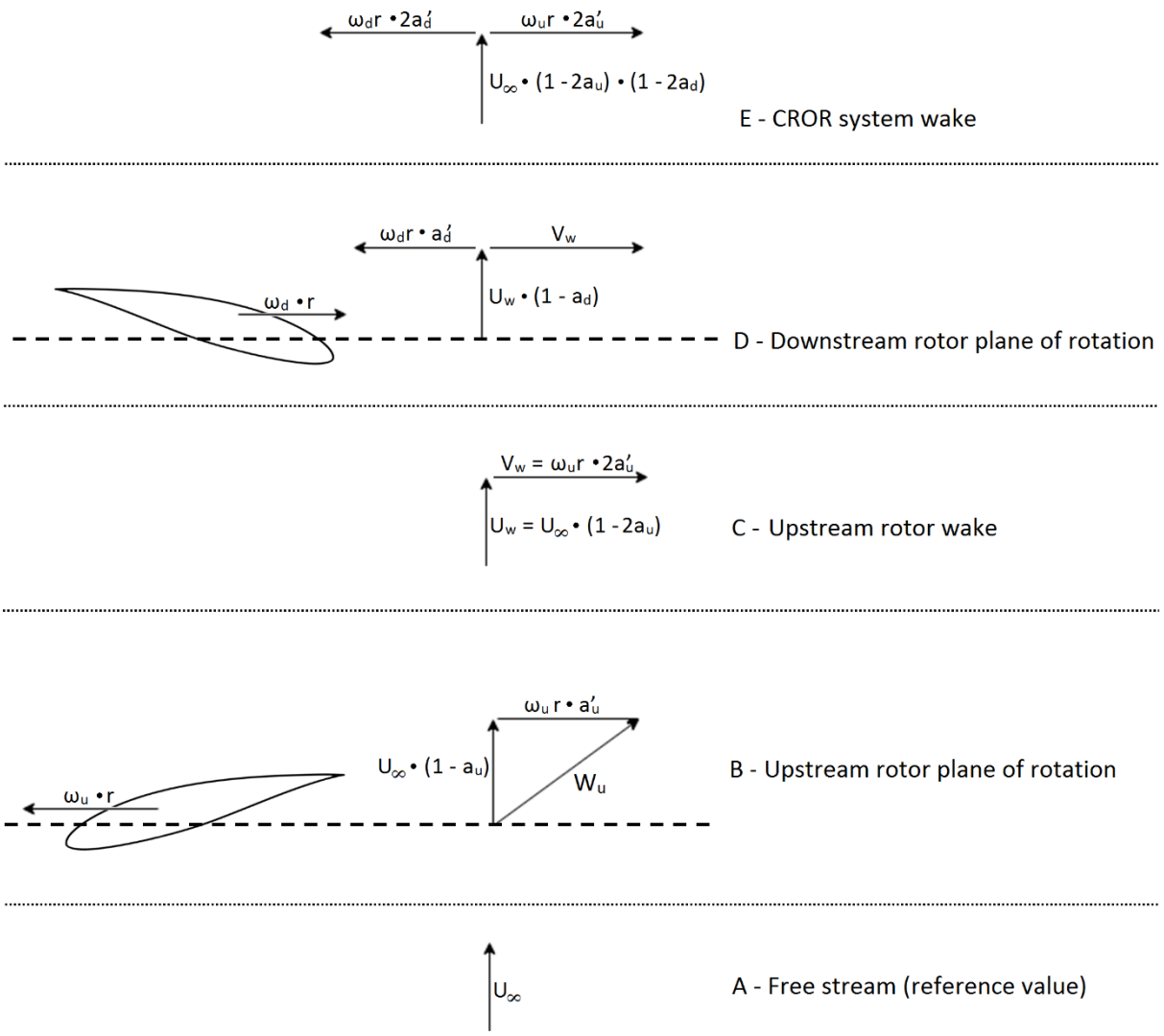

Fig. 19 Flow velocity vectors for upstream (bottom) and downstream (top) rotor

The above mentioned analysis of a twin-rotor system does not take into account the turbulent effects of upstream rotor operation on downstream rotor. The increased turbulence intensity may change significantly the properties of a flow approaching the downstream rotor. In case of SWT this effect may be additionally influenced by the low-Reynolds number flow around the aerofoil. Analytical approximation of these phenomena constitutes a serious problem, and therefore experimental or simulation approach has to be employed, as will be the case of this thesis.

3.2. Similarity criteria in flow analysis

One is to consider the general form of the Navier-Stokes equation for viscous, incompressible flow in vectoral, convective form (ex. [89]):

$$\underset{(a)}{\frac{\partial \mathbf{v}}{\partial t}} + \underset{(b)}{(\mathbf{v}\cdot\nabla)\mathbf{v}} = \underset{(c)}{G} - \underset{(d)}{\frac{1}{\rho}\cdot\nabla p} + \underset{(e)}{\nu\cdot\nabla^2\mathbf{v}} + \underset{(f)}{F} \tag{43}$$

In (43) (a) corresponds to the rate of change of velocity in transient flow, (b) describes fluid's inertia, (c) is related to the mass forces, (d) - to the pressure forces, (e) - to the viscosity effects, (f) - to source terms.

One is to consider now the same set of Navier-Stokes equations, written for a model in a different scale. All variables will be scaled: linear dimensions by L, time by T, velocity by V, mass forces by G', pressure by P, density by R, kinematic viscosity by N, source terms by F'. The equation for the model in scale may be written as follows:

$$\underset{(a)}{\frac{V}{T}\frac{\partial \mathbf{v}}{\partial t}} + \underset{(b)}{\frac{V^2}{L}(\mathbf{v}\cdot\nabla)\mathbf{v}} = \underset{(c)}{G'G} - \underset{(d)}{\frac{P}{RL}\frac{1}{\rho}\cdot\nabla p} + \underset{(e)}{\frac{NV}{L^2}\nu\cdot\nabla^2\mathbf{v}} + \underset{(f)}{F'F} \qquad (44)$$

If both equations are to describe similar flows in different scales, then the coefficients related to all components should have equal magnitude, i.e.:

$$\underset{(a)}{\frac{V}{T}} = \underset{(b)}{\frac{V^2}{L}} = \underset{(c)}{G'} = \underset{(d)}{\frac{P}{RL}} = \underset{(e)}{\frac{NV}{L^2}} = \underset{(f)}{F'} \qquad (45)$$

In reality a simultaneous fulfillment of the above criteria is not possible. Thus usually only selected equalities in (32) are preserved. One is firstly to consider the influence of the viscous component (e) on the fluid movement (represented by the inertia component (b)):

$$\frac{V^2}{L} = \frac{NV}{L^2} \quad ,or \quad \frac{VL}{N} = 1 \quad and \quad Re = \frac{vl}{\nu} \qquad (46)$$

The Reynolds number Re describes the ratio of inertia and viscous forces in a flow. The lower the value of Re number, the higher the influence of viscous forces on the flow. If the fluid viscosity remains constant, $Re(\nu = const) = vl$, the scaling of velocity should be inversely proportional to scaling of linear dimensions. Re number similarity criterion is among the most essential ones in the aerodynamic studies. Its influence is particularly important for the drag force estimation.

One is now to evaluate the influence of alternating transient effects (a) on the fluid movement (b):

$$\frac{V^2}{L} = \frac{V}{T} \quad ,or \quad \frac{VT}{L} = 1 \quad and \quad St = \frac{l}{vt} = \frac{fl}{v} \qquad (47)$$

In eq. (47) f denotes a characteristic frequency. The Strouhal number St describes the flow periodicity. St number similarity criterion is of primary interest in the case of oscillating and/or periodic flows, vortex separation, etc. In the case of wind turbine studies this criterion corresponds to the tip-speed ratio (see eq. (15)), with f = ω.

One is to finally examine the influence of compressibility effects (d) on the fluid movement (b):

$$\frac{V^2}{L} = \frac{P}{RL} \quad , or \quad \frac{P}{RV^2} = 1$$
$$and \quad Ma = \sqrt{\frac{\rho v^2}{p}} = \sqrt{\frac{v^2}{v_s^2}} = \frac{v}{v_s} \tag{48}$$

In eq. (48) v_s describes the velocity of sound in the flow. The Mach number Ma describes the compressibility effects. Their influence is important in flows with relatively high velocities, for Ma > 0.7. Such elevated velocity values may be achieved at the tip of blades of big-scale wind turbines, but are not of primary concern in the case of low-speed flows observed for small wind turbines.

It is important to underline, that for certain flows the similarity numbers do not have to be strictly identical, but may be comprised within certain range of values [90]. However, in the case of this thesis the influence of low Reynolds number at which the rotor operates is relatively strong (see the analysis in Section 6.2) and even small changes may be critical to flow character.

The above criteria are referred to as the dynamic flow similarity criteria [89] and are the extension of the kinematic flow similarity criteria, referring to the similarity of velocity fields. A third similarity criterion deals with geometry. It states that to consider two flows as similar it is necessary that all corresponding size ratios (scales) of a real object and the model should be constant.

In all, in the thesis the chosen dynamic flow similarity criteria will be that of Re and St numbers. Due to subsonic flow character (Ma < 0.3) the compressibility criterion was not deemed crucial, and the flow is treated as incompressible. The geometrical similarity criterion between the real-life wind turbine and the used model is fulfilled as well, with the scale being equal to 1:6.

3.3. Solver description, turbulence modelling

ANSYS CFX and ANSYS Fluent are commercial flow solvers based on Finite Element Method. In case of Fluent (cell-centred code) the finite elements are volumes, while for CFX - mesh vertices (cell-vertex code). ANSYS CFX is essentially a pressure-based solver, while Fluent offers more elasticity in that various pressure- or density-based solvers may be employed [91].

To describe the flow both solvers use a set of conservation laws, i.e.:

- Conservation of momentum: Navier-Stokes equations - from Ma < 0.3 (subsonic flow) it follows that the current case(s) may be treated as incompressible, thus defined by eq. (43),
- Conservation of mass: continuity equation, since air is assumed to be a heterogeneous, continuous medium. The equation for incompressible flow is in the form:

$$\nabla \cdot \mathbf{v} = 0 \tag{49}$$

- Conservation of energy (first law of thermodynamics): rate of change of energy of a fluid particle is equal to the rate of heat addition plus the rate of work done. Since the flow is assumed to be isothermal (no heat exchange between fluid inside and surroundings, constant temperature) and incompressible, the conservation of energy equation does not need to be considered (see ex. [91]).

The investigated viscous flow problem is considered as fully turbulent in both solvers. In numerical research performed previously at IMP TUL wind tunnel flow studies numerous modelling approaches were used, including Large-Eddy Simulations (LES, not discussed in the current problem), Reynolds-Averaged Navier-Stokes (RANS, see ex. [92], [93]) and Unsteady-RANS (URANS).

In the classic RANS approach it is assumed that in a considered flow problem every variable f can be computed as a sum of its (temporal) mean f_{ave} and instantaneous variation Δf (see ex. [91]):

$$f = \Delta f + \bar{f} = \Delta f + \frac{1}{\Delta t}\int_{t}^{t+\Delta t} f(t)dt \tag{50}$$

The term Δf vanishes when the solution is time-averaged, and thus a steady-state solution is reached[1]. From the practical point of view, pressure and velocity are the time-averaged variables in the considered problem. When time averaging is applied to equations (43) and (49), the following forms of RANS for incompressible flow are reached (given here in tensor notation, see ex. [89]):

$$\frac{\partial \overline{v_i}}{\partial x_i} = 0 \tag{51}$$

$$\frac{\partial \overline{v_i}}{\partial t} + \frac{\partial \overline{v_i}\partial \overline{v_j}}{\partial x_j} = -\frac{1}{\rho}\frac{\partial \bar{p}}{\partial x_i} + \frac{\partial}{\partial x_j}\left(\nu\left(\frac{\partial \overline{v_i}}{\partial x_j} + \frac{\partial \overline{v_j}}{\partial x_i}\right) - \overline{\Delta v_i \Delta v_j}\right) \tag{52}$$

In case of a steady-state flow the time derivative $\partial\overline{v_i}/\partial t$ is omitted (flow is invariant in time). However, in some problems (as will be in the case of FRM model in ANSYS CFX), the Unsteady-RANS (URANS) approach is employed, whence the time derivative is preserved in order to account for changes in flow physics (in this case rotation of the rotor, see [91]).

Compared to the classic Navier-Stokes equations, the RANS equations possess an additional term, $\overline{\Delta v_i \Delta v_j}$,referred to as the Reynolds stress. This additional term is responsible for turbulent stresses and normally it is approximated by the so-called turbulence models. The current study deals with only one turbulence closure, the k-ω SST (Shear-Stress Transport) model by Menter [94]. This choice comes from the previous experiences of wind turbine studies conducted at IMP TUL (see ex. [92], [93], [95]) and will therefore be presented more thoroughly.

k-ω SST turbulence closure is developed from an earlier k-ω BSL (Baseline) model (itself basing on k-ω and k-ε models). It is a two-equation turbulence model, basing on the transport of the turbulent quantities [91] presented in Tab. 1.

The classic k-ε model was developed mainly for free-shear flow, due to improper prediction of separations and problems with depicting the adverse pressure gradients. k-ω, in turn, was originally used for flows near walls (and in general low-Reynolds number flows). The advantages of both models were firstly connected in the k-ω BSL closure, where k-ω is used in the near-wall treatment, and k-ε in the free-shear flows. In the transitory region the so-called blending functions are applied, ensuring a

[1] In some textbooks (see ex. [64]) a more general definition, in which the mean value of considered parameter changes in an orderly manner, meaning for example regular oscillations

smooth transition between the two closures. Finally, k-ω SST develops the model one step further, in that it accounts for the changes in eddy viscosity term [91].

An important aspect in the turbulence closures is the near-wall treatment. Boundary layer is the region of high velocity gradients. To correctly predict the velocity profile, it is necessary to properly capture the flow character, especially in the region immediately near the wall. In boundary layer analysis the so-called dimensionless velocity $u+=u/u_\tau$ is defined, with u – velocity parallel to wall, u_τ - friction velocity (a form of shear stress expressed in units of velocity). Determination of u+ distribution perpendicular to the wall is crucial from the point of view of prediction of the boundary layer phenomena, such as separation [91].

Tab. 1 Definitions of turbulent quantities: k, ω, ε [91]

Quantity	Equation	Interpretation
k – Turbulent Kinetic Energy (TKE)	$k = \frac{1}{2}\overline{\Delta v_i \Delta v_i}$	Kinetic energy per unit mass of the turbulent fluctuations
ε – Turbulence dissipation rate	$\varepsilon = \overline{\frac{\partial \Delta v_i}{\partial x_k}\frac{\partial \Delta v_i}{\partial x_k}}$	Rate at which TKE is converted into thermal internal energy
ω – Specific turbulence dissipation rate	$\omega = \frac{\varepsilon}{k\beta^*}$ with β^* - model constant	Rate at which TKE is converted into thermal internal energy per unit volume and time; mean frequency of the turbulence

u+ is related to another dimensionless quantity, y+. By definition it is the dimensionless distance, calculated as the product of the height of first layer of the elements from the boundary y and u_τ, divided by the kinematic viscosity ν:

$$y+= \frac{y \cdot u_\tau}{\nu} \tag{53}$$

Following the general recommendations for the k-ω SST turbulence model and the law of the wall, the y+ value should be:

- y+ < 5, whence the dimensionless velocity in the wall vicinity u+ = y+, or
- 30 < y+ < 200÷600, whence the log-law law is used:

$$u+= \frac{1}{\kappa}\ln(y+) + (C+), \text{ with } \kappa, C+ \text{ - constants} \tag{54}$$

For 5 < y+ < 30 the so-called buffer layer occurs, in which neither of the above approximations may be applied and u+ must be determined using empirical data. For 200 < y+ the first element layer is considered to lay in the outer boundary layer [91].

Figure 20 presents the aforementioned relationships and corresponding u+ and y+ regions.

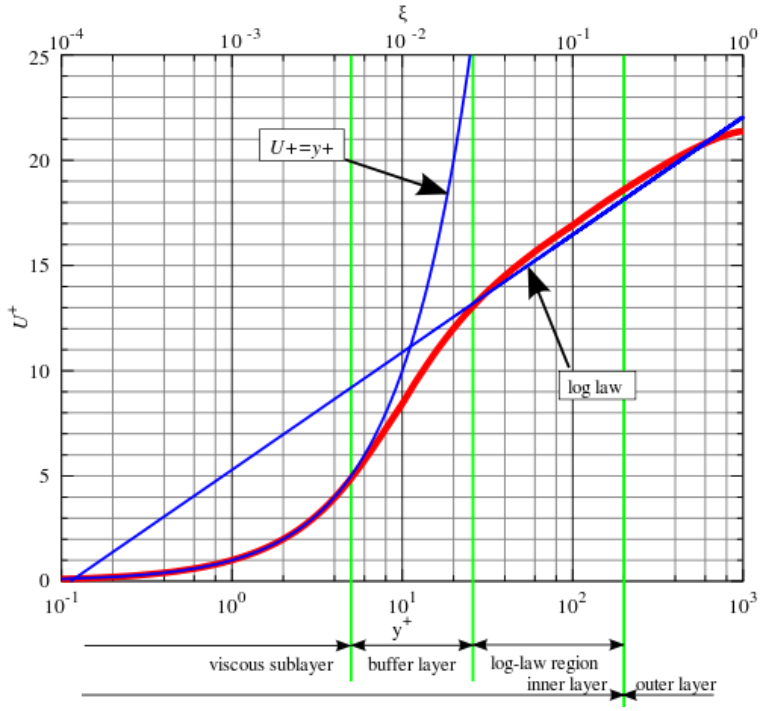

Fig. 20 Dimensionless velocity u+ as a function of y+ in the boundary layer flow [96]

4. Experiment

The following chapter presents the overview of the experimental campaign undertaken in frames of this thesis: its methodology and results. Bare- and shrouded rotors were examined, in both single- and twin rotor configurations.

4.1. Methodology

The composition of the measurement apparatus is visible in Fig. 21. It involves different equipment that may be divided into the following three groups, depending on measurement field of interest:

- **Flow properties**: temperature, relative humidity, absolute pressure, dynamic pressure - these quantities are used to estimate the flow velocity and perform temperature compensation of other selected measurement devices, if needed,
- **Aerodynamic forces**: force plate - this device is used to estimate the value of rotor thrust (axial force F_z),
- **Rotor performance**: rotational torque and velocity.

Information from captors, in a form of analogue signals, is collected and converted into digital form by a DAC converter DAQbook 2020. The data is then recorded and stored on a computer.

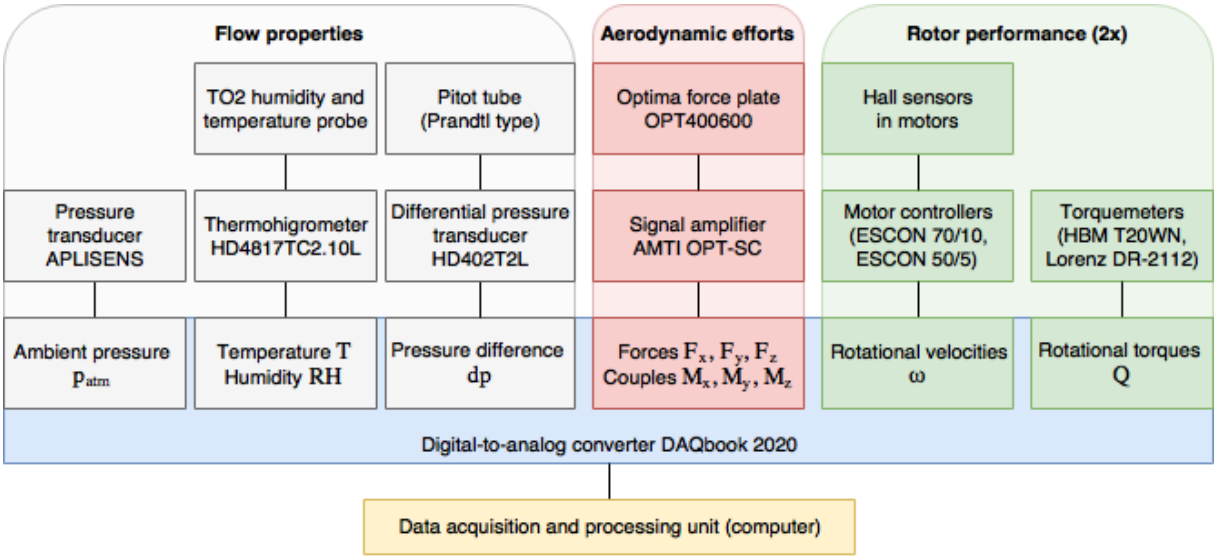

Fig. 21 Wind tunnel measurement apparatus schema

The first group of measurements was realised for estimation of flow velocity. For that purpose pneumatic measurements with Pitot tube (Prandtl type) were employed. The difference (dp) between total pressure p_{tot} and static pressure p_{st} is dynamic pressure p_{dyn}, which may be recomputed into the wind velocity V as [97]:

$$V = \sqrt{\frac{2 \cdot dp}{\rho}} \tag{55}$$

To account for changes of flow condition in the wind tunnel, the flow density ρ is calculated separately for every test point. Humid air is treated as a mixture of two ideal gases: dry air and water vapour. Then it is possible to determine the flow medium density ρ as the sum of densities of both constituting ideal gases:

$$\rho = \rho_{dry} + \rho_{vap} = \frac{p_{atm}}{r_{dry} \cdot T} + \frac{p_{vap}}{r_{vap} \cdot T} \quad (56)$$

In formula (56) r_{dry} = 287.05 J/kg·K and r_{vap} = 461.50 J/kg·K are individual gas constants for, respectively, dry air and water vapour. p_{vap} is the partial pressure of water vapour, which may be computed using empirical formulas. In this case the so-called Buck equation [98] was used:

$$p_p = 6.1121 \cdot \exp\left(\left(18.678 - \frac{T}{234.5}\right) \cdot \left(\frac{T}{257.14 + T}\right)\right) \quad , [hPa] \quad (57)$$

In formula (57) the temperature T is expressed in °C, while relative humidity RH in %.

To estimate the value of rotor thrust F_t a force plate is used. Wind turbine test stand was mounted on the measurement platform. One has to note that the aerodynamic efforts on the diffuser were not captured, as it was not attached to the platform. At each fixed wind velocity the platform was first tared without rotor (test stand only) to account for the influence of test bench drag. Due to the fact that the measured force values are relatively low and the equipment is sensible to temperature changes, the measurement results may be laden with additional errors and will be approached with caution.

Wind turbine performance was determined by measuring shaft rotational velocity ω and torque Q. The product of both quantities is the rotor power, as seen in eq. (13). Before the measurement campaign the idle test stand torque was determined (coming from friction, bearings, etc.). For this purpose the rotor was detached and torque was measured at different rotational velocities.

Within each test point the above mentioned variables were captured. If not stated otherwise, the measurement acquisition rate was equal to 1 000 Hz, with 65 536 samples collected. Their values were then averaged over time. The typical measurement would consist of capturing a complete wind turbine characteristic by varying its rotational speed at a fixed wind velocity V. The rotation velocity was set and maintained by motor controllers working in a closed-loop control system. Their employment enabled capturing turbine characteristic for ω both lower and higher than rated.

4.2. Wind turbine test stands

Appendix 1 presents a detailed description and study of the IMP TUL wind tunnel.

Appendix 2 shows the diagnostic process of measurement equipment and tested installations of the IMP TUL wind tunnel.

Whenever referring to wind turbines, the notation of “configuration” is used to describe the placement of the rotor with respect to the test stand. Otherwise “upwind” and “downwind” are used to describe the location of one turbine with respect to the other in twin-rotor operation.

The test stand consists of three principal elements (Fig. 22):

- T1 upwind wind turbine – the default wind turbine used for the tests, placed nearer to the test section inlet, at the default distance of 1 m from it,
- T2 downwind wind turbine – the second wind turbine, whose streamwise position with respect to T1 may be adjusted,
- Diffuser – a divergent duct, with turbine(s) placed at its inlet and inside.

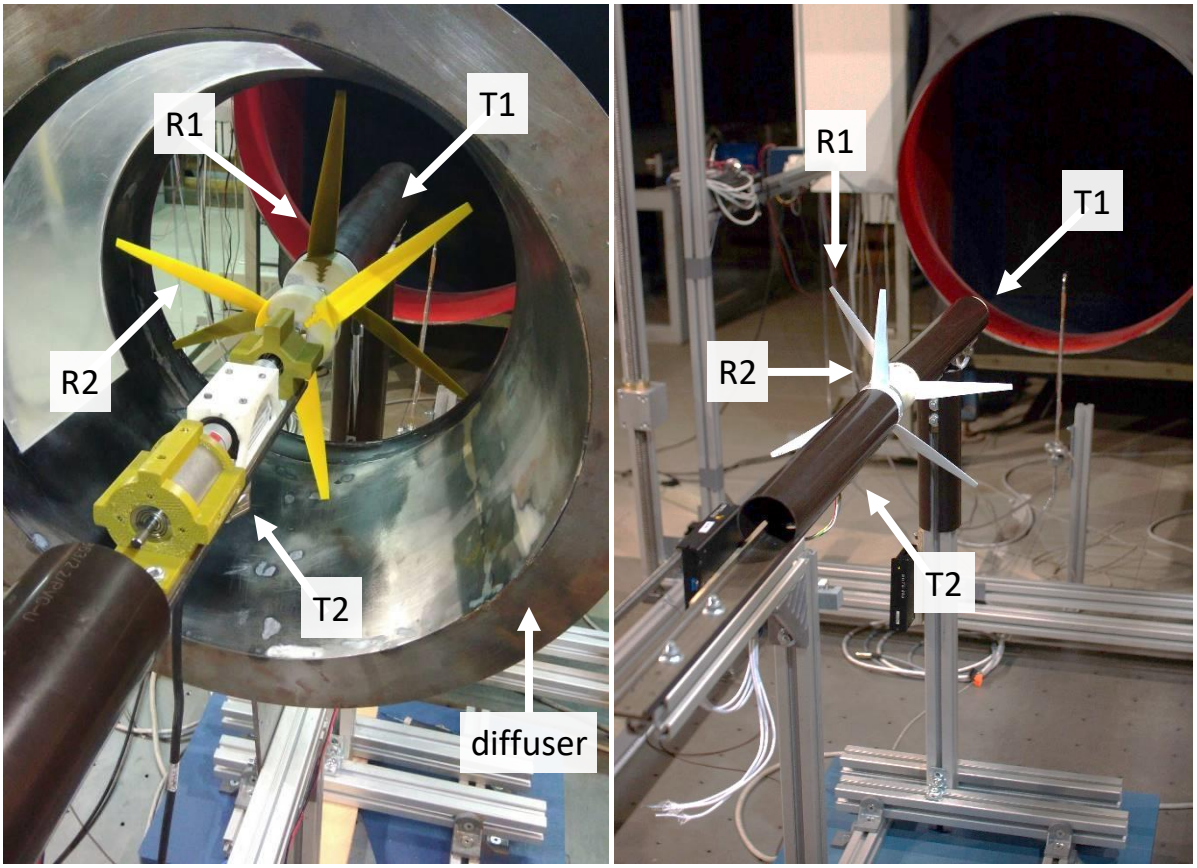

Fig. 22 Various components of the ducted twin-rotor test stand: rotors (R1,R2), test stands (T1, T2), diffuser

Both considered three-bladed rotors share the same geometry, based on aerofoils SG6040 and SG6041. Blade geometry of spanwise-variable chord and twist angle (Fig. 23) was originally designed for a research project *Small Wind Turbine Optimized for Wind Low Speed Conditions (STOW)*; its description may be found in [99]. The rotor diameter D is equal to 0.32 m. This value was chosen in previous analysis works performed at IMP TUL [93] as a compromise between small scale and wind tunnel blockage. At wind velocity 15.95 m/s and optimum TSR the local Reynolds number calculated on the basis of chord length is of order of magnitude 10^5.

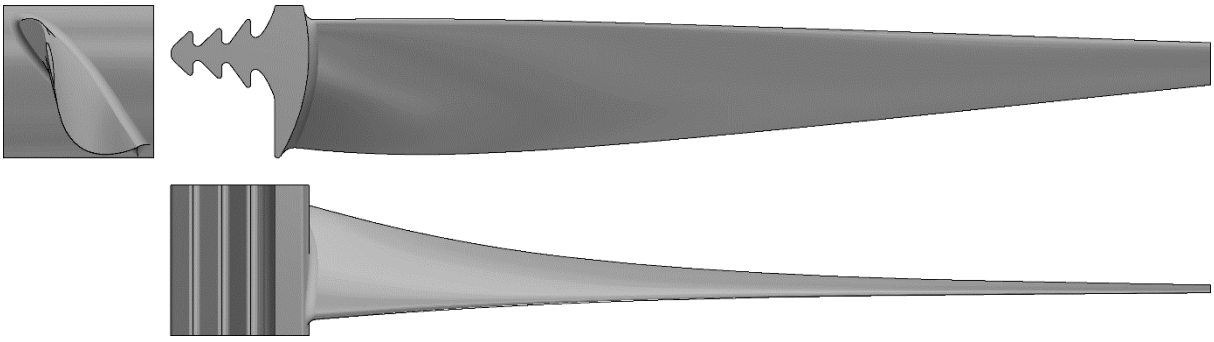

Fig. 23 Views of the blade geometry: top, pressure side, leading edge side

The diffuser is a divergent duct of cut-cone shape of total length approx. 0.85D and cone angle 22°. Diffuser inlet is equipped with a convergent section (“throat”). Its role is to attract more mass flow through the diffuser inside, and tranquilize the flow to prevent additional separations at rotor location

and downstream. The diffuser outlet is equipped with a brim, installed to increase low-pressure zone downstream diffuser and additionally increase the mass flow rate through the rotor.

Each wind turbine is controlled and measured separately, on a test stand as seen in Fig. 24. Each measuring track is composed of four principal components:

- Rotor – composed of three blades, fixed to hub. The blades and hub are manufactured in 3D printing rapid prototyping technology (FDM – Fused Deposition Modelling). This ensures high fidelity of depiction of the computer-designed geometry. Two rotor specimens will be used in the considered study, named R1 and R2, the latter being a mirrored geometry of the former one.
- Bearing unit – the shaft, on which the rotor is mounted, is supported by a set of three straight ball bearings. An over rigid arrangement is used to minimize the vibrations coming from the rotor and ensure maximum robustness of the system.
- Torquemeter – captor-transducer used to measure the torque produced by the wind turbine rotor and transported via the shaft.
- Permanent magnet motor/generator – used to actively impose the system's rotational velocity. The device itself is regulated by a dedicated controller. The latter governs if the energy transformer works in motor mode (propelling the rotor) or generator mode (converting mechanical energy into electricity). Connection of the electric circuit to battery accumulator enables electric energy supply and storage in the same source.

All aforementioned components are housed in tailor-made holders, manufactured in 3D printing technology. This process ensures rapidity and gives virtually unlimited possibilities of adapting the holders' shapes. All elements are mounted on a C-profile, which itself is mounted on a pillar. The test stand and the pillar are enclosed in covers made of plastic pipe.

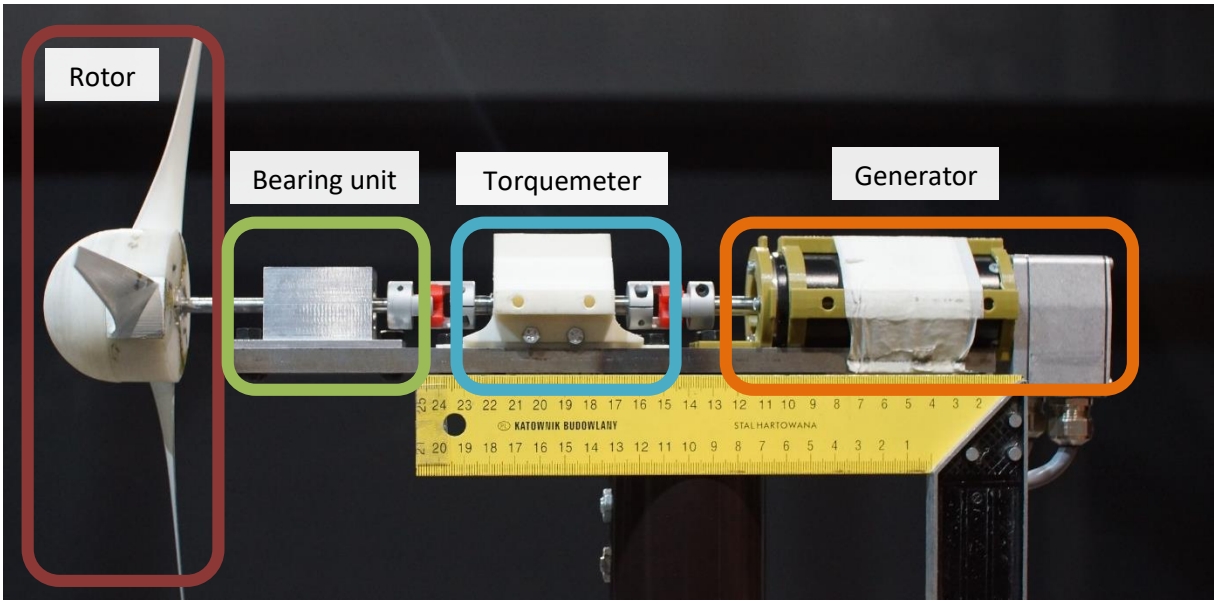

Fig. 24 T1 test stand overview (without covering)

4.3. Experimental campaign composition

Table 2 lists all the experimental tests performed and described in the thesis.

Preliminary tests constitute the first group of measurements (Appendices A2.1 - A2.3). Since both test stands were purpose-made for the current studies, their separate examination was needed. This included calibration of the measuring equipment and measured signal analysis/filtration.

Further works, evaluated in Appendices A2.4 - A2.6, concentrate on the comparison of different rotor specimens and test stand configuration.

The actual experimental campaign is presented in Sections 4.4 - 4.7.

Tab. 2 Performed tests - overview

Section	T1			T2			Comments
	Position	Config	Rotor	Position	Config	Rotor	
A2.1 A2.2 A2.3	upwind	upwind	R1/ R2	upwind	upwind	R1	Measurement apparatus calibration, signal analysis, hysteresis determination
A2.4	upwind	upwind	R1	no	no	no	Different blade sets (material, manufacturing)
A2.5	upwind	upwind/ downwind	R1	no	no	no	Upwind/downwind configuration tests
A2.6	upwind	downwind	R1/ R2	no	no	no	Comparison of two used rotor specimens
4.4	upwind	upwind	R1	no	no	no	Open rotor tested at different wind velocities
4.5	upwind	downwind	R2	no	no	no	Shrouded rotor tested at different wind velocities
4.6	upwind	downwind	R2	downwind	upwind	R1	CROR system tested at U_∞ = 15.95 m/s
4.7	upwind	downwind	R2	downwind	upwind	R1	CRSR system tested at U_∞ = 15.95 m/s

4.4. Open rotor operation

Changing the wind velocity, one also changes the inflow velocity magnitude W at each blade station (see Fig. 14). Thus, at different wind speeds the aerodynamic profiles will operate at different local Reynolds numbers. For SWTs this remark is significant, meaning that their blades will usually operate in transitory region between laminar and turbulent regimes. The Reynolds number influence should be the most significant at low wind speeds, and become less evident with increasing wind speed (see Section 6.2 for a further discussion).

Wind speed in IMP TUL wind tunnel may be regulated continuously in the range from about 6 – 8 m/s, up to about 18 m/s. Lower wind velocities are not advisable due to the observed flow behaviour (stream instability, interaction with recirculating flows). Figure 25 presents wind turbine measurement results for wind speeds in the range 8 – 18 m/s, with step of approximately 2 m/s. $Cp = f_1(TSR)$ characteristic is shown in the upper part of Fig. 25, $Ct = f_2(TSR)$ in the lower one.

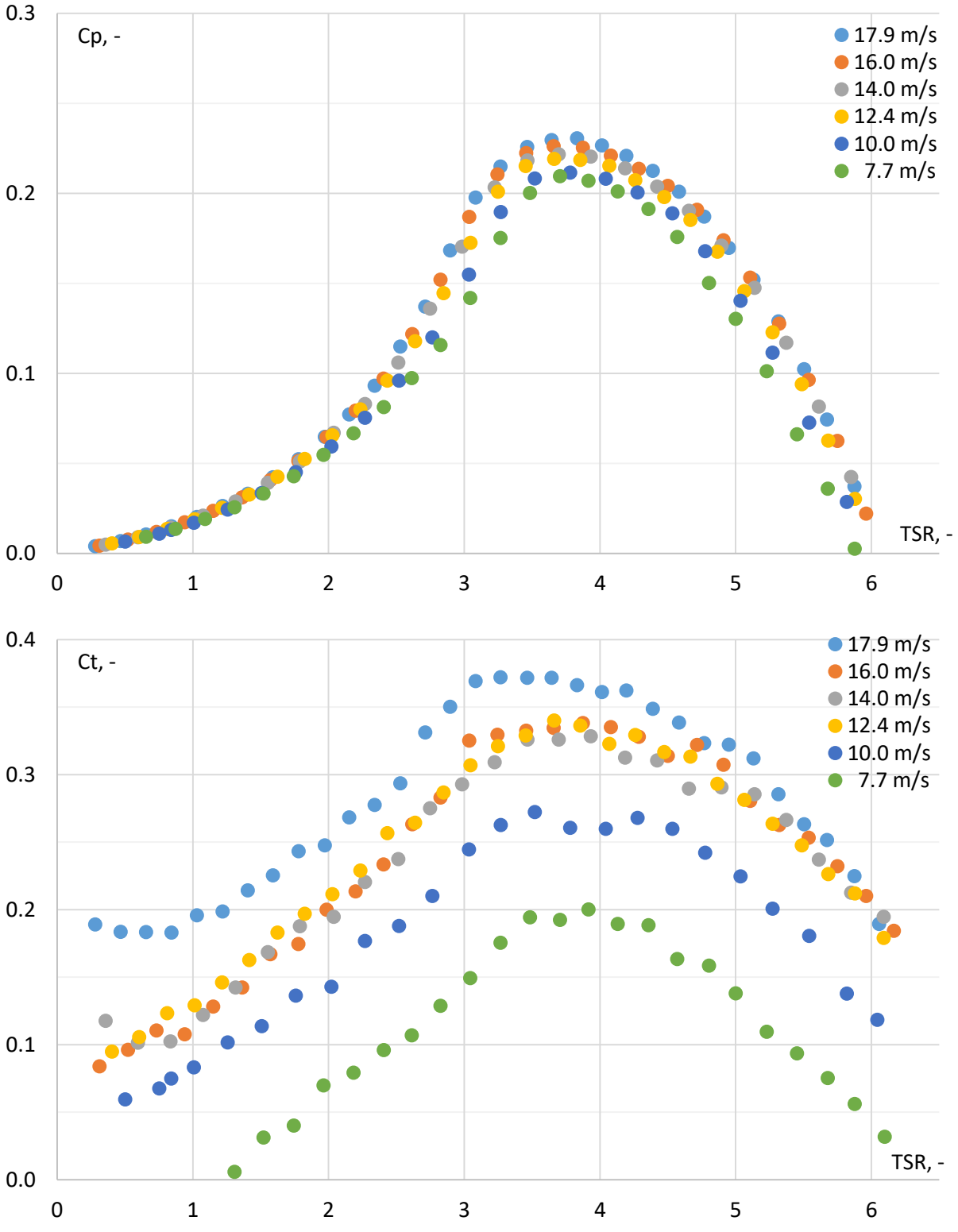

Fig. 25 Cp(TSR) (top) and Ct(TSR) for different relative wind speeds; R1 open rotor in upwind configuration

Characteristics for all wind speeds share a common region for maximum Cp and Ct at approximately TSR = 3.5 - 4. All Cp curves remain very close at low TSR (up to approximately TSR = 2). With increasing TSR the curve traces start differing, yet this variation is modest. The difference in Cpmax between reference velocities of 7.7 m/s and 17.9 m/s is equal to approximately 9%. As expected, the differences become less significant with increasing wind velocity. The characteristics captured for reference wind

speeds of 14.0 m/s, 16.0 m/s and 17.9 m/s share almost the same traces. The Cp values for 16.0 m/s and 17.9 m/s vary by no more than 2% along the entire considered TSR range. This observation has permitted to pick the reference velocity of 16.0 m/s for further tests. On the one hand, it will contain the Reynolds number influence within acceptable limits and at the same time the torque generated in DAWT configuration will not surpass the generator-controller limits.

For all wind speeds the predicted idle rotational velocity is at about TSR = 6.

Concerning the values of Ct, the differences are significantly more visible. The traces of curves for two lowest wind speeds (7.7 m/s and 10.0 m/s) are located significantly lower than the rest of the curves. Since such big differences are not reproduced in the Cp graph, this behaviour is more likely due to the limits of the measuring equipment: at the lowest wind speeds the rotor thrust force does not surpass 1 N. The characteristics for reference wind speeds of 12.4 m/s, 14.0 m/s and 16.0 m/s share, once again, very similar traces, with differences up to approximately 5%. In contrast, the curve corresponding to 17.9 m/s differs noticeably from the previously discussed ones, with its trace laying significantly higher than those for lower wind speeds. The characteristic also seems to be corrupted at the region of low TSR. Having in mind that the measurement campaign starts at low rotational velocities and that this was the first characteristic collected in the considered measurement session, it is fair to assume that the thermodynamic conditions might not have been established yet at the time of dataset collection, influencing the measurement system. Thus, the Ct characteristic for reference wind speed 17.9 m/s is considered to be not entirely trustworthy and is excluded from further considerations.

Summing up, the Reynolds number analysis permitted to choose the reference wind velocity of approximately 16 m/s for further measurements. This will ensure reliable rotor operation from the aerodynamic point of view and permit a safe operation of the generator, especially in DAWT configuration. The analysis also enabled one to quantify the results distortion by the Reynolds number influence at the level of approximately 2% for Cp and 5% for Ct.

4.5. Diffuser-Augmented Wind Turbine (DAWT) operation

The shrouded wind turbine operates at the local wind velocity higher than the open rotor. This enables it to attain relatively higher power values at the same reference wind speed, compared to open rotor.

Figure 26 shows datasets collected for R1 rotor operating in DAWT mode (downwind configuration) and its comparison with R1 operating in open rotor mode (upwind configuration). It is readily visible how the shrouding permitted to increase the Cp at the same wind velocity (16 m/s) by a factor of 2 to 3. This translates to increase in flow speed through the wind turbine rotor by as much as 40%. Such a significant amelioration is possible, as the rotor-diffuser assembly has been optimised to operate together. As a result, the ensemble is able to surpass the Betz limit for open rotor. This is due to the fact that the local modification of pressure and velocity fields effectively violate the assumptions of the one-dimensional flow theory. Due to higher flow velocity through the wind turbine, the rotor rotational velocity range is also higher. For high wind speeds this translates into values of order of magnitude 10 000 rpm and more. It was observed that the test stand operation at such high rotation velocity becomes unstable and blade fixation rupture is possible. Thus the characteristics a majority of wind speeds considered in this measurement campaign end before reaching the idle operating conditions (at approximately TSR = 10).

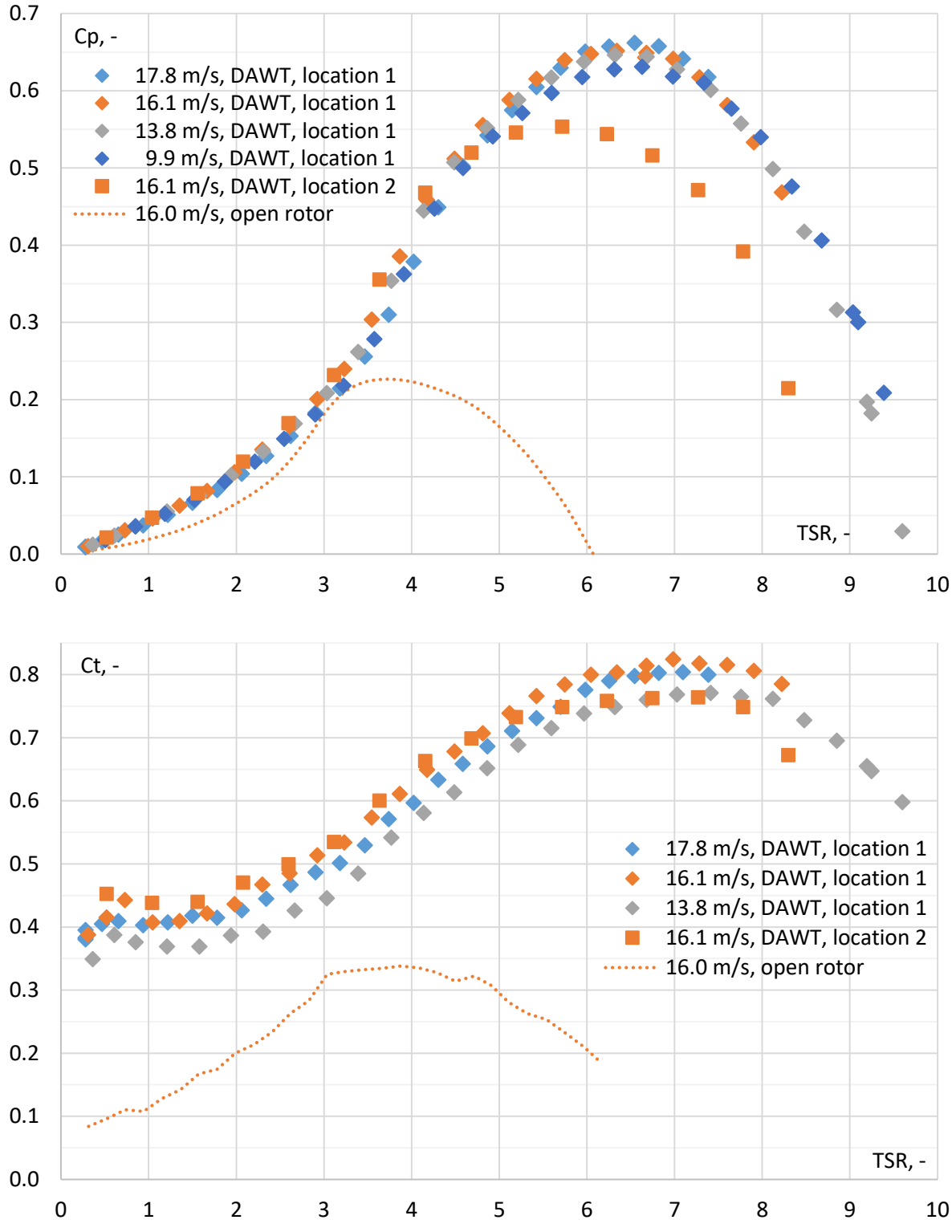

Fig. 26 Cp(TSR) (top) and Ct(TSR) for different relative wind speeds;
R1 DAWT (squares, diamonds) in downwind, and open rotor (dotted line) in upwind configuration

The wind turbine performance depends strongly on its position relative to the diffuser inlet. This translates into differences between square and diamond marks in Fig. 26. Location 1 denoted rotor placement directly at the diffuser narrowest cross-section. In location 2 the rotor was shifted upstream (by distance of about 0.05 D), to permit accommodation of the downstream wind turbine in the further tests. Consequently, in the latter case it operates at a lower local wind velocity (approximately 5%, as

computed from power difference), which in turn results in its lower power production (by about 15%). In the further twin-rotor tests R1 was maintained at location 2.

As in the case of the open rotor, Cp characteristics' traces tend to increase with increasing wind velocity and, as previously, these differences become less significant as the wind speed increases. Overall, the differences between the 4 collected datasets are less significant than in case of the open rotor configuration.

The above mentioned remarks can also be considered for the Ct graphs. The influence of increasing wind velocity is most visible at low Reynolds number (open rotor, lower wind velocity). Between 16.1 m/s and 17.8 m/s the differences are of order of magnitude of 3%. It is also very much noticeable how the results obtained for an open rotor are much lower than those for ducted wind turbine. This mimics the situation observed previously for open rotor examined at different wind speeds. It also shows that for DAWT the price for increasing Cp is a drastic increase in axial loads (maximum Ct higher by more than 130%) at the same wind velocity.

An additional commentary is needed to address the behaviour of Ct curves at TSR < 3, which is similar to that of Ct curve for open rotor at 17.9 m/s. Following the literature (ex. [67], [27]) and own experience, the experimental curves should descend towards 0 as TSR is reduced. The source of a different behaviour in this case is not clear. It may be connected with problems with the measuring device or improper estimation of the test stand's drag. This observation is important from the point of view of future validation process, when assessing the numerical results for DAWT cases.

4.6. Counter – Rotating Open Rotor (CROR) operation

Twin-rotor wind turbine systems were examined at U_∞ = 15.95 m/s.

The twin-rotor test stand is composed of test stand T1 operating in downwind configuration and T2 operating in upwind configuration. The rotors face one another. The spherical cups topping the shaft were dismounted for the smallest separation distance. The upwind rotor (R2) remains at location 2, while the downwind rotor (R1) rotation plane is placed at distance 32 mm = 0.1D (diffuser inlet, case a), 96 mm = 0.3D (diffuser middle, case b), 200 mm = 0.625D (diffuser outlet, case c). Figure 27 compares the Cp characteristics for each wind turbine, separately. Cptot (the arithmetic sum of both power coefficients) and Ct for T1 are consultable in Fig. 28.

The Cp1 and Cp2 coefficient distributions take form of a saddle-shaped surfaces (Fig. 27). The Cp1 surface shape follows roughly the trace of Cp1 curve without T2. The optimal TSR1 remains at the vicinity of the same value (approximately 3.7). Their values are significantly smaller than in the case of standalone characteristic, by up to about 20% – 30% in the region of optimal TSR. This observation is easily explained having in mind that the rotors operate at separation distances lower that T1 diameter. Thus the interference of T2 on T1 cannot be neglected. This influence is best visible in the case a, for which the saddle shape deepens as T2 approaches its optimal operating conditions. Contrarily, in case c the surface trace is almost constant along the entire TSR2 range. In all, as the distance between rotors increases, the attainable Cp1 values increase as well. Once again it may be attributed to the lowering influence of T2 on T1.

As for the Cp2, the distribution surface shapes remain very similar in all three locations, with a form of a relatively deep saddle. It is noticeable that, surprisingly, the Cp2 values at CROR operation get lower

with increasing separation distance. As seen in the case of Cp1, low separation distance promotes strong interaction between the two rotors. Thus the loads are more evenly distributed between the two rotors. The standalone T2 characteristic was measured in each case with T1 test stand in place, hence the reduced performance. This characteristic attains higher maximum values with an increasing separation distance, since the influence of T1 test stand diminishes with increasing distance.

In all, the total power characteristics (Cptot in Fig. 28) show global maxima at T1 wind turbine operating near the optimal point and T2 at lower rotational speed. The exact numerical values are seen in Tab. 3. In all three configurations the CROR system achieves maximum total Cp higher than that for a single wind turbine, by approximately 11% - 13%. This observation proves that there is a potential in using the CROR wind turbine systems, even at small separation distances between rotor rotation planes (less than the rotor diameter). It must, however, be underlined that this particular blade geometry was designed to collaborate with a custom-designed diffuser. This observation might become less evident if a rotor designed to operate in open-rotor mode was studied (compare with Section 4.7 to see the less significant performance increase when T1 operates in diffuser).

The operating region in which CROR system presents better performance than the single open-rotor spans at approximately TSR1 ∈ (2.6, 4.2) and TSR2 ∈ (2.8, 4.1). This means a relatively wide plateau of wind turbine preferable operating conditions. It is also shifted towards lower TSR values than in the case of standalone rotor operation. This may be translated into further advantages: easier rotational velocity control (the system may be less robust than in case of single open-rotor), and lower mechanical efforts (lower rotational speeds and centrifugal forces). An interesting remark concerning the relative velocity of the rotors may also be made. Changing (increasing or decreasing) the rotational velocities of both rotors at the same time leads to a quick and abrupt drop in the overall system performance. To change the relative rotational velocity it is actually more efficiency-reasonable to maintain either rotor's TSR at near-optimal value and change the rotational velocity of the other one.

Tab. 3 Maximal total Cp for CROR

Separation distance	Maximal Cptot	Optimal TSR1 (CROR)	Optimal TSR2 (CROR)
a	0.251	3.66	3.16
b	0.251	3.66	3.08
c	0.256	3.64	2.94

In what concerns the Ct1 parameter, similar observations may be forwarded as in the case of Cp1. The influence of T2 on T1 is the strongest as the rotors approach one another (i.e. case a). As the separation distance increases the saddle gets flatter in case b, to become almost completely uniform along the entire TSR2 span in case c. In all, the values of Ct attain the highest values for case c. This observation is consistent with the Cp1 results, which in turn is consistent with the one-dimensional flow theory. Compared with the standalone performance, Ct1 in CROR mode attains its maximum at almost identical TSR1. The values for CROR are, however, lower than for single rotor operation – similarly to those observed in the case of Cp1.

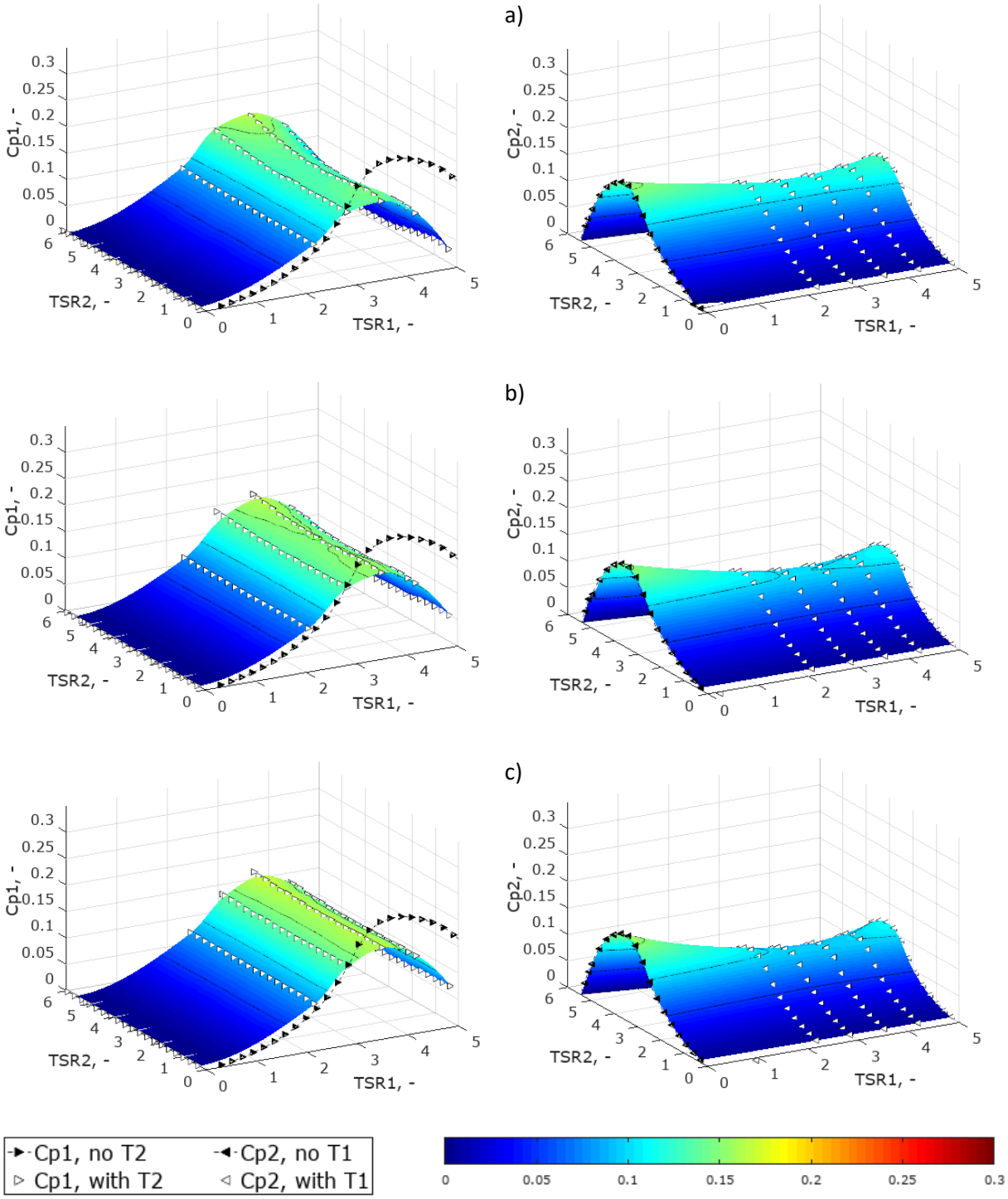

Fig. 27 Cp(TSR1,TSR2) for upstream (R2, left) and downstream (R1, right) rotor operating in CROR mode; rotor separation distance: 0.1D (a, top), 0.3D (b, middle), 0.625D (c, bottom); black points denote performance when only the considered rotor (either 1 or 2) is examined

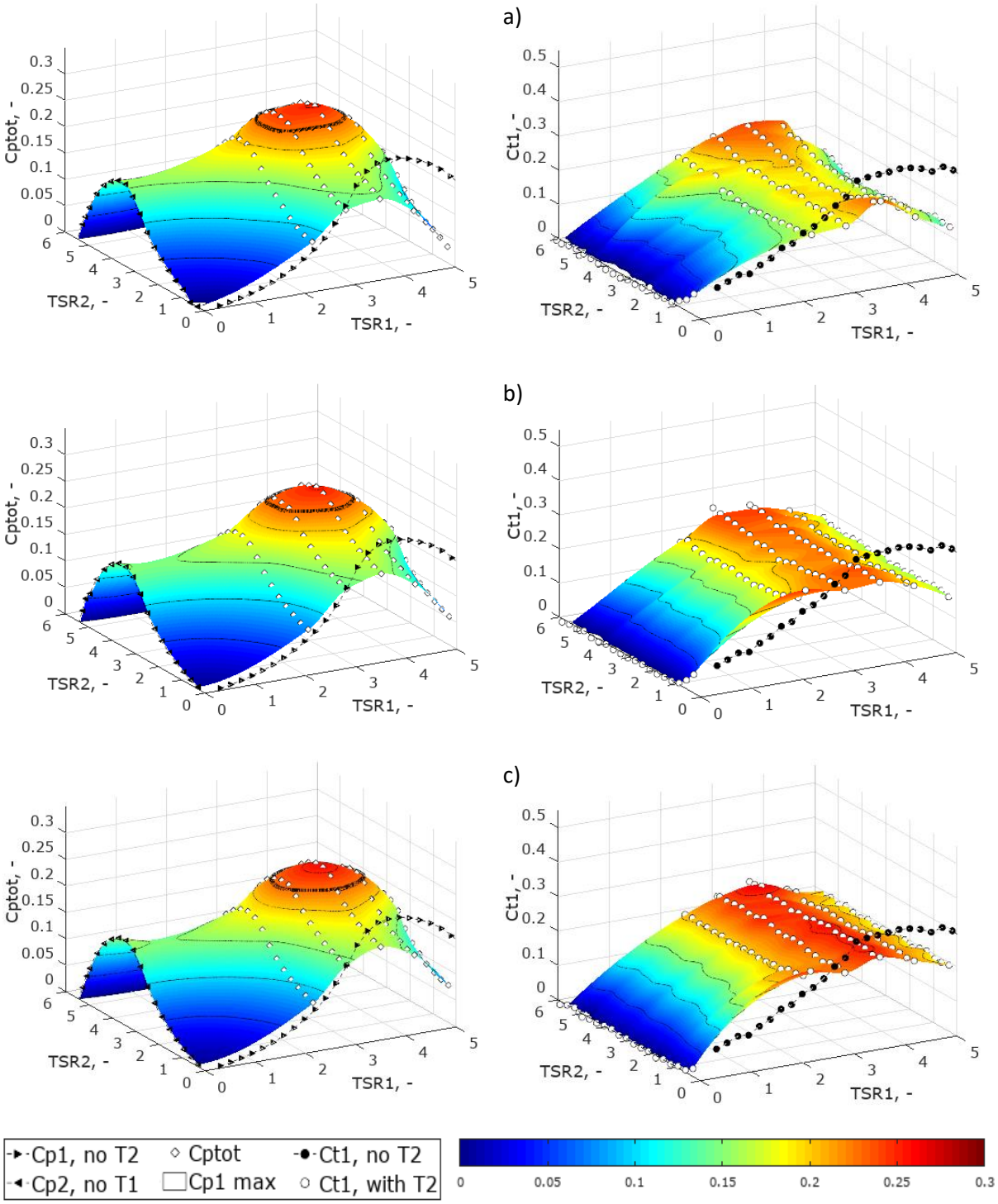

Fig. 28 Cptot(TSR1,TSR2) (left) and Ct1(TSR1,TSR2) (right) for rotors operating in CROR mode; rotor separation distance: 0.1D (a, top), 0.3D (b, middle), 0.625D (c, bottom); black points denote performance when only the considered rotor (either 1 or 2) is examined; thick black line on the Cptot graphs denotes Cp = 0.226, the maximum recorded Cp of bare rotor

4.7. Counter – Rotating Shrouded Rotor (CRSR) operation

The shrouded twin rotor wind turbine (CRSR) is examined in exactly the same configurations and manner as CROR. The results are visible in Fig. 29 and Fig. 30.

The Cp characteristics for both wind turbines (Fig. 29) are of saddle shape once again, as in the case of CROR. The interaction of both wind turbines is, however, both stronger and steeper than in the latter case. Additionally, the influence of T2 on T1 becomes stronger as the separation distance rises, especially at T1 rotational velocity that corresponds to optimal TSR1. The possible explanation of this phenomenon may be derived by analysing the T2 rotor performance. The range of T2 rotational velocities in which the downstream rotor operates as a turbine is getting smaller as the separation distance rises. For example in case c Cp2 becomes negative when TSR2 is bigger than approximately 4 – 5. At higher T2 rotational velocities the power becomes negative. Under these conditions the energy is transmitted from the rotor to the fluid, which means that it effectively operates as a ventilator. Low pressure zone thus generated inside the diffuser promotes additional augmentation of flow rate through T1 rotor. Hence ne observes the dramatic increase in Cp1 values at high TSR2 in cases b and c. However, this comes at a cost of high power demand of T2, which results in low net power (and thus Cptot, see Fig. 30) under these conditions.

The study and development of such a “turbofan” system might be of interest for future works. However, at this moment the possibility of positive energy balance of such system is unlikely. Also, the diffuser outlet is a region of high pressure gradients and strong separations. Placement of a rotor in this region promotes its unstable operation, increasing stresses and fatigue wear, as well as augmenting the vibrations of the diffuser and T1.

In all, the Cp1 values tend to increase along with separation distance between the two rotors. This is an adverse information, in that the highest velocity augmentation in the diffuser occurs at its inlet, thus the interest in placing both rotors in that region. In the meantime, the Cp2 values attain the highest values at low separation distance. As the distance increases, the operation range of T2 gets narrower and the power outcome becomes abysmal. In case a the maximal value of Cp2 (at TSR1 = 0) is about 0.476, while in case c it is equal to 0.302. In case a the Cp2 values are higher than those for case c by as much as 5 times or more. Consequently Cptot (Fig. 30) attains its high values in cases a (due to high Cp2) and c (thanks to high Cp1). These values surpass the maximum Cp1 for a single-rotor DAWT, that is 0.554.

It is also seen that in case c, when TSR2 is very low, Cp2 attains almost the same values as for a single rotor DAWT. This means that with the highest separation distance between the two rotors and at low TSR2 the influence of T2 on T1 is marginal.

Similarly as in the case of CROR, high overall performance of CRSR is ensured at a plateau around the optimal functioning conditions (see Tab. 4). This plateau is of comparable size for both open- and shrouded rotors (notice different scales in both cases). It is, however, very clear that in order to maximise the Cptot it is particularly important to maintain TSR1 near the optimal value. This is especially visible in case c, for which even a small decrease of TSR1 below the value of 4 results in a dramatic loss of power outcome.

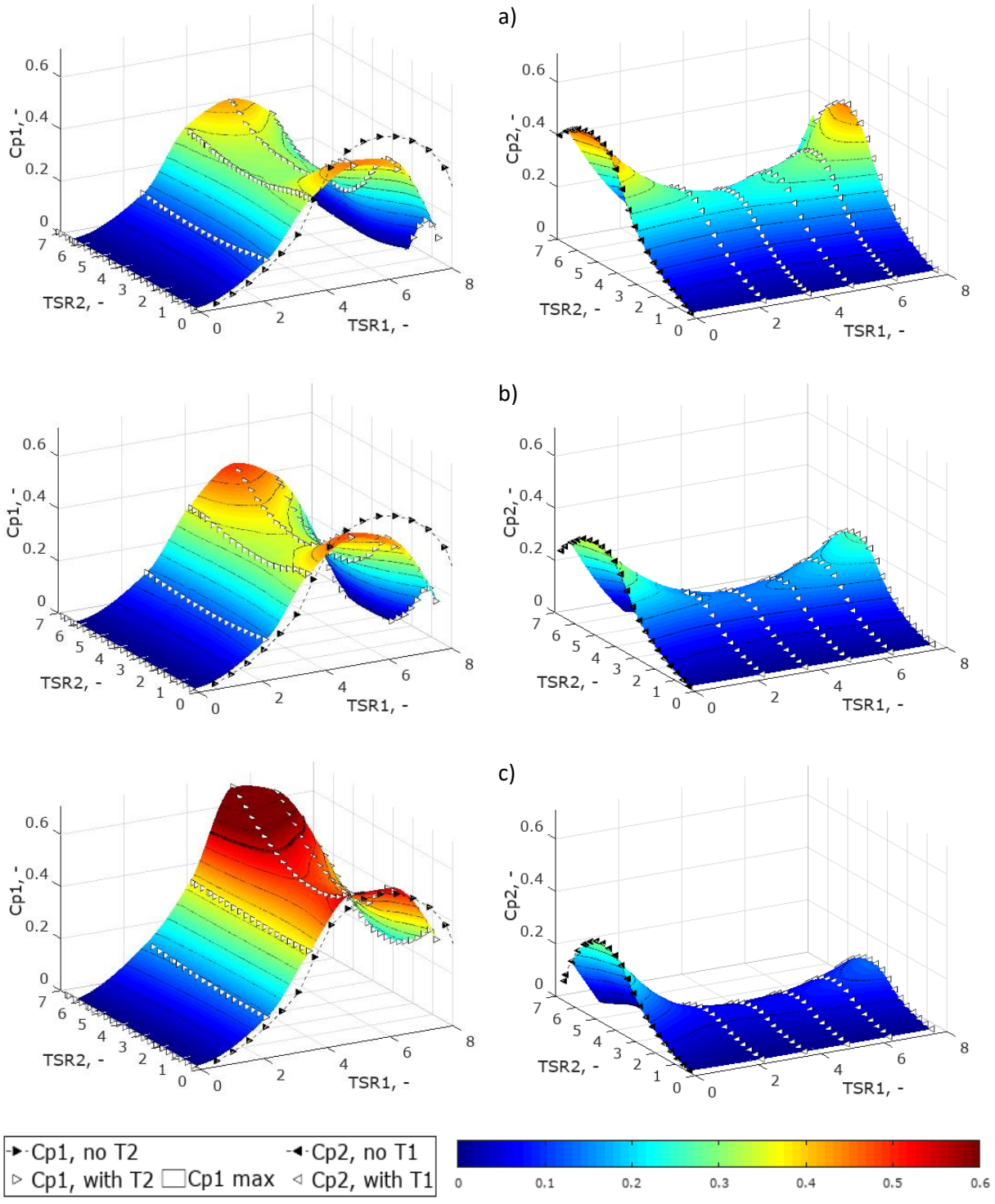

Fig. 29 Cp(TSR1,TSR2) for upstream (R2, left) and downstream (R1, right) rotor operating in CRSR mode; rotor separation distance: 0.1D (a, top), 0.3D (b, middle), 0.625D (c, bottom); black points denote performance when only the considered rotor (either 1 or 2) is examined; thick black line (Cp1 max) on the Cp1 graph denotes Cp = 0.554, the maximum recorded Cp for DAWT

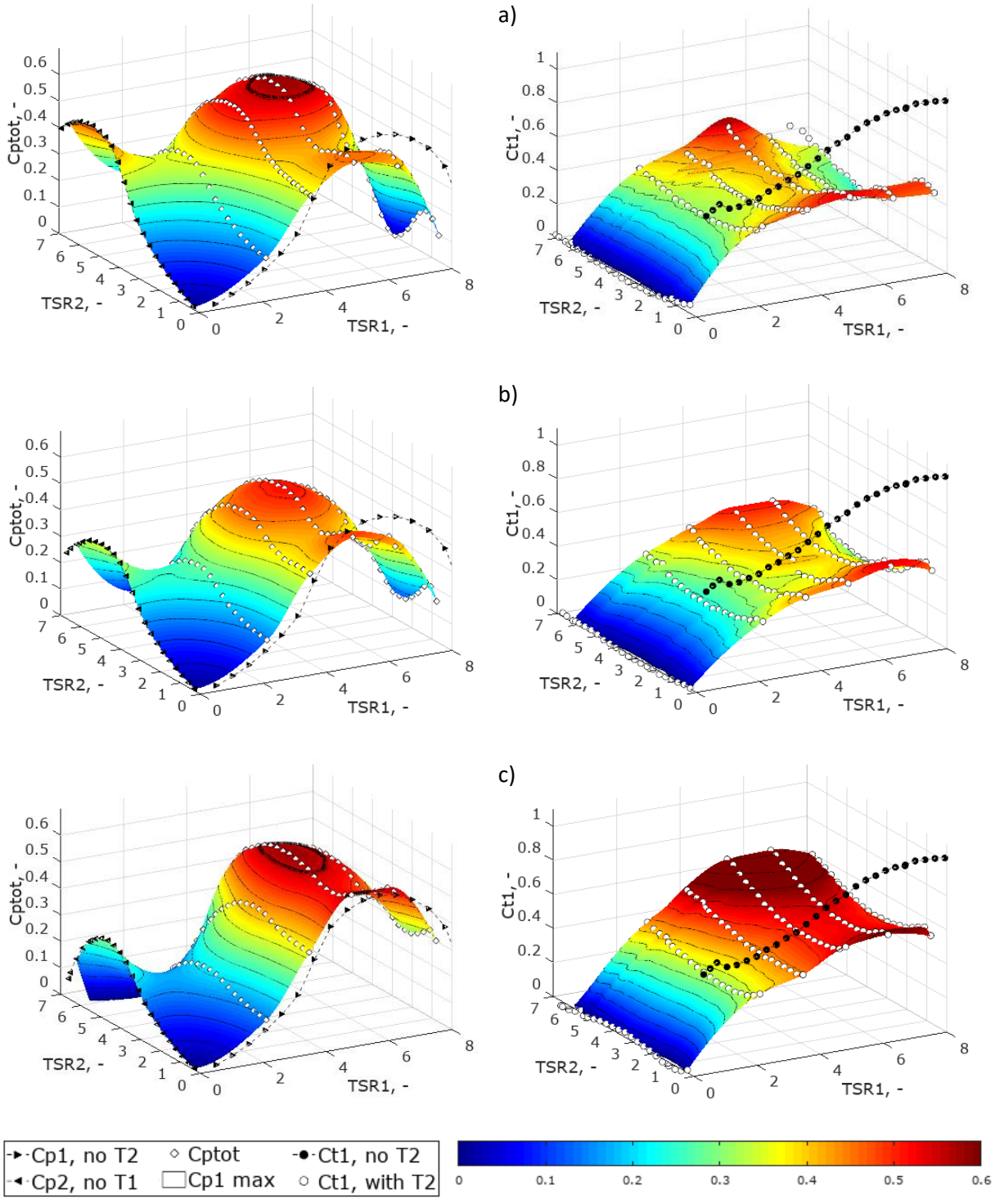

Fig. 30 Cptot(TSR1,TSR2) (left) and Ct1(TSR1,TSR2) (right) for rotors operating in CRSR mode; rotor separation distance: 0.1D (a, top), 0.3D (b, middle), 0.625D (c, bottom); black points denote performance when only the considered rotor (either 1 or 2) is examined; thick black line (Cp1 max) on the Cp1 graph denotes Cp = 0.554, the maximum recorded Cp for DAWT

Considering the distribution of Ct1 values, the saddle shape mimics that observed for Cp1. The surfaces get steeper as the separation distance increases. The latter also results in attaining globally higher Ct1 values, although they are still significantly lower than the ones for single-rotor DAWT. Local maxima of the characteristics fall at approximately the same TSR values as the Cp1 maxima.

Tab. 4 Maximal total Cp for CRSR

Separation distance	Maximal Cptot	Optimal TSR1 (CRSR)	Optimal TSR2 (CRSR)
a	0.582	5.32	4.52
b	0.515	5.16	3.82
c	0.579	5.12	3.44

4.8. Summary and conclusion

This chapter presented the new, custom-tailored test stand for examination of CRSR at IMP TUL wind tunnel. Thus the first scientific objective of the thesis - creation of experimental apparatus for the studied system - is fulfilled.

The obtained and presented results show a potential for increasing the wind turbine performance for shrouded rotors, counter rotating rotors and CRSR systems. Further analysis of these systems will be provided using the numerical results in following chapters.

5. Fully-resolved Rotor Model (FRM)

This chapter concentrates on the first of developed CFD models - the Fully-resolved Rotor Model (FRM). The model principles and assumptions are presented. The model is verified and validated. The chapter then continues towards presenting the most significant flow features, such as velocity and angle of attack distribution evaluation and determination of the aerodynamic force coefficients.

5.1. General information

The Fully-resolved Rotor Model (FRM) is rotor modelling approach in which the entire rotor geometry is discretised and modelled in the simulation domain. A high-resolution mesh must be generated around the blades to permit proper solution of the Navier-Stokes equations, especially in the high-gradient regions. To increase the model fidelity even more, a LES (or even DNS) approach is sometimes used (see ex. [65]). Nevertheless, RANS method is reported to give satisfying results in most applications [75].

FRM is generally used to extend the knowledge gained in the experiment, also delivering data for definition and validation of simplified models (see ex. [65]). However, increasing the resolution and precision of the model elongates the simulations' time, while requiring substantial computational resources. It is also important to remember that every assumption and simplification with respect to the actual flow conditions decrease the results' fidelity.

In the proposed model the simulation domain is composed of a stationary part, comprising the flow in the wind tunnel and rotating part(s), comprising wind turbine blade(s) and (parts of) hub assembly. The employed commercial solver ANSYS CFX 18.1 offers the possibility to model the relative motion of stationary and rotating coordinate systems in both steady-state (previously studied in [92]) and transient simulations (sliding mesh approach, employed in this study). In the latter model the interface position between the domains is updated in each timestep, as the relative position of the grids on each side of the interface changes [91]. Thus the sliding mesh approach may account for all interaction effects between components being in relative motion to each other. In FRM approach this proposes a more realistic depiction of the near-wake phenomena, crucial from the point of view of rotor power estimation.

The FRM simulations in this study are envisaged as a complement for the experimental results. The results of these simulations will be employed especially to check the flow performance in the vicinity of rotor blades, such as local angles of attack and force coefficients along the blade span.

In all, 18 simulations were performed (listed in Tab. 5), to provide basis for different rotor configurations and modes, as studied in experiments. For both CROR and CRSR the rotor separation distance of 0.1D (case a) was considered.

Tab. 5 FRM simulations considered in the study; T1 always in downwind configuration, U_∞ = 15.95 m/s

Mode	TSR1	TSR2	Rotor mesh size	Stationary domain mesh size
Open rotor	2.30	-	$14.8 \cdot 10^6$ nodes $18.6 \cdot 10^6$ elements	$2.1 \cdot 10^6$ nodes $10.3 \cdot 10^6$ elements
	3.67	-		
	5.03	-		
	6.39	-		
DAWT	2.30	-	$14.9 \cdot 10^6$ nodes $18.6 \cdot 10^6$ elements	$2.8 \cdot 10^6$ nodes $10.6 \cdot 10^6$ elements
	3.67	-		
	5.03	-		
	6.39	-		
	7.75	-		
CROR	2.30	2.30	$14.8 \cdot 10^6$ nodes $18.6 \cdot 10^6$ elements (2 times)	$2.7 \cdot 10^6$ nodes $14.6 \cdot 10^6$ elements
	3.67	2.30		
	3.67	3.45		
	5.03	3.45		
CRSR	2.30	2.30	$14.9 \cdot 10^6$ nodes $18.6 \cdot 10^6$ elements (2 times)	$4.7 \cdot 10^6$ nodes $27.9 \cdot 10^6$ elements
	3.67	2.30		
	3.67	3.45		
	5.03	3.45		
	5.03	5.03		

5.2. Preprocessing schemes

This Section presents the FRM domain geometry and simulation definition.

5.2.1. Stationary domain

The stationary domain has been designed to mimic the geometry of the test section of IMP TUL's subsonic wind tunnel, in which the wind turbine experimental tests were performed. It is comprised of a parallelepiped of size 4.2 m x 2 m x 2.15 m (13.125D x 6.25D x 6.7D, length x width x height). This sizing was chosen basing on the actual test section chamber geometry and the tests performed previously during the wind tunnel test section study (Appendix 1). The domain overview is visible in Fig. 31.

While the external size and shape of the domain remains constant for all simulations, the interior changes to accommodate the diffuser and/or T2 test stand. T1 test stand is in every case modelled in downwind configuration, along with the hub and the test stand mounting pole. T2 test stand is in each case considered in upwind configuration, but only hub and no pole is modelled. In the shrouded rotor(s) studies the wind turbine(s) are encompassed by the diffuser. No supports are modelled for it. To accommodate the rotor, a hollow space in shape of a flat cylinder is cut off of inside of the domain. For the single-rotor configuration only one hollow cylinder space is created, to accommodate the upwind rotor. In the case of twin-rotor system two separate hollow spaces are present.

The front part of each test stand ("the dome") is attached to the shaft and rotates. It was therefore given a rotational velocity component, along the wind turbine axis of rotation, corresponding to the rotational velocity of the wind turbine.

The mesh sizing parameters were chosen basing on the previous studies performed for the entire wind tunnel test section. The mesh is of unstructured, tetra-dominant type. It was generated using the Octree/Advancing Front Tetra Method in ICEM CFD software. The mesh was concentrated in the

boundary layer regions, notably near the hub(s) (to ensure an accurate modelling of the boundary layer phenomena). At the interfaces between stationary and rotational domains (to allow for a high resolution of data transmission between the domains) and in the wake region (to properly resolve the rotating wake phenomena). The mesh size is presented in Tab. 5, while its overviews are visible in Fig. 32 (DAWT) and Fig. 33 (CROR).

All simulations are performed for the same inlet velocity. It is defined using the profile presented in Fig. A1.3 (0), with reference velocity U_∞ = 15.95 m/s, which was used previously for the experimental investigation.

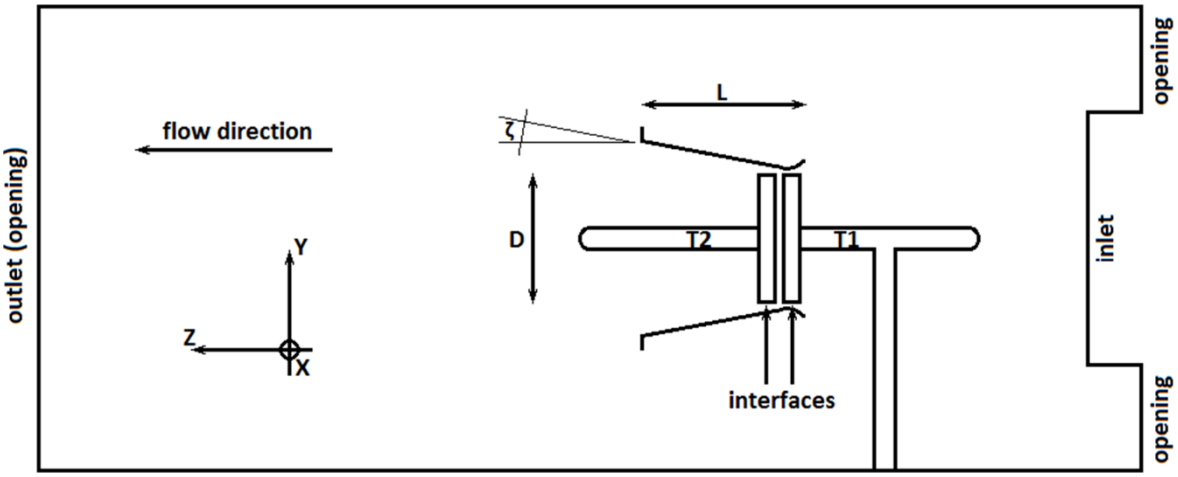

Fig. 31 Section view of the stationary domain geometry and boundary conditions in FRM CRSR case; all unmarked faces are no-slip walls

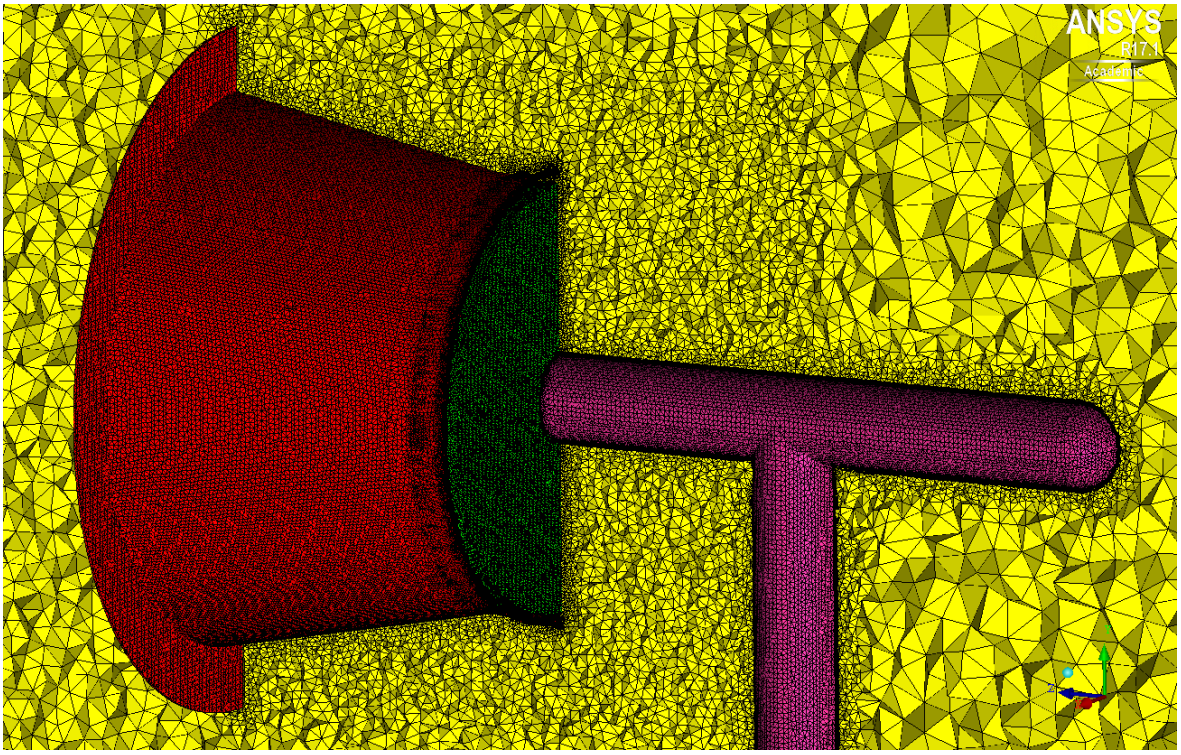

Fig. 32 Vertical section (yellow, x = 0 m) view of the stationary domain mesh in rotor vicinity in DAWT simulations; rotor interface marked green, diffuser marked red, T1 test stand marked pink

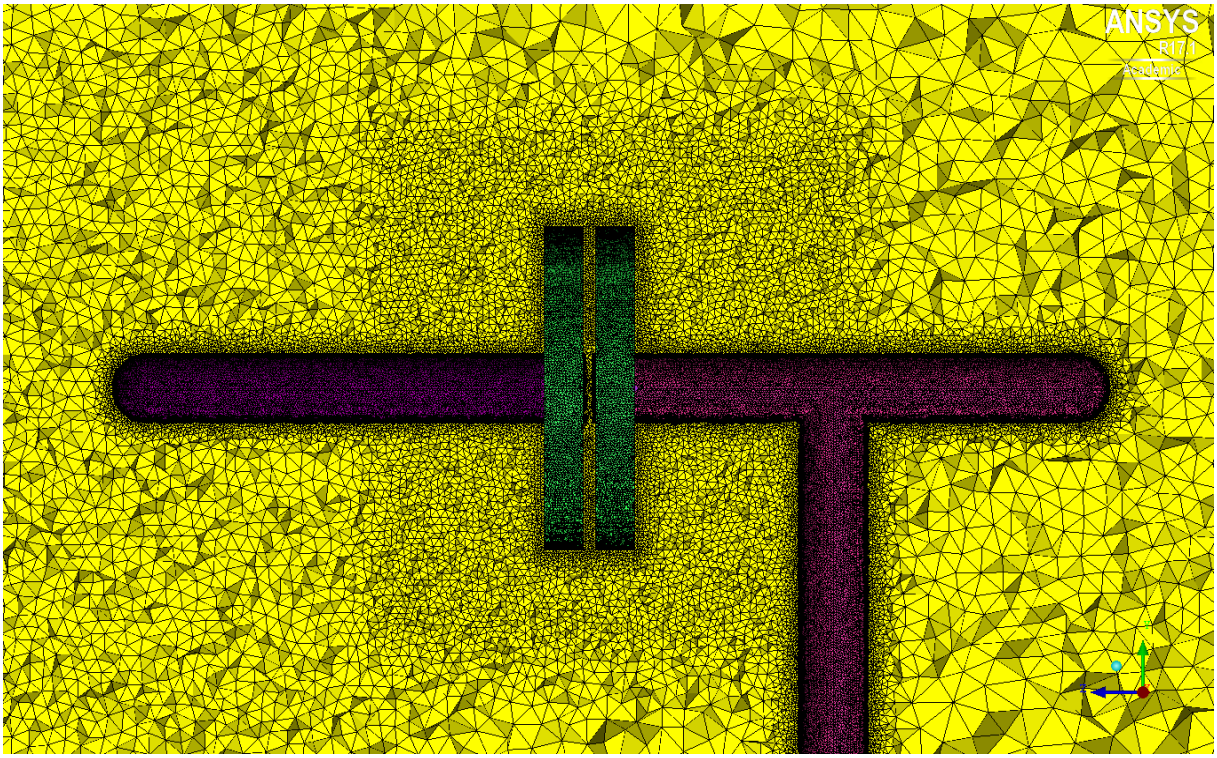

Fig. 33 Vertical section (yellow, x = 0 m) view of the stationary domain mesh in rotor vicinity in CROR simulations; rotor interfaces marked green, T1 test stand marked pink, T2 test stand marked violet

5.2.2. Rotating domain

The rotating domain contains three blades and the rotating section of the hub. The domain was sectioned and only 1/3 of the domain will be meshed independently. The whole rotor domain will then be reconstructed by triplicating the section.

It was observed in previous works that the sizing of the rotating domain has a considerable influence on the obtained results. This is caused by the relatively high gradients of pressure, velocity and turbulent quantities, observed in the blade vicinity. The rotating zone must be sufficiently long in the streamwise direction, in order to allow for proper development of flow fields (especially velocity upstream and turbulent quantities downstream the blades). In turn, in the radial direction the domain must contain the high-gradient pressure fields that cause the tip leakage. No dedicated size test was performed in the thesis, instead the sizing was based on the up-to-now experience gained in the previous simulations for BT4 (Blind Test 4, see [100]). Following those studies the domain spans 0.05D upstream and 0.075D downstream blade extrusion line. Its diameter is equal to 1.03D.

The hybrid mesh approach was employed for this domain. The blade's nearest vicinity was discretised using the structured mesh approach. This technique was also employed in the "flaps" – regions in between the consecutive blades. As a connector between these two, an unstructured mesh was generated using the Octree Method in ICEM CFD software. The mesh was inflated near the blade and hub surfaces to allow for proper solution of boundary layer phenomena.

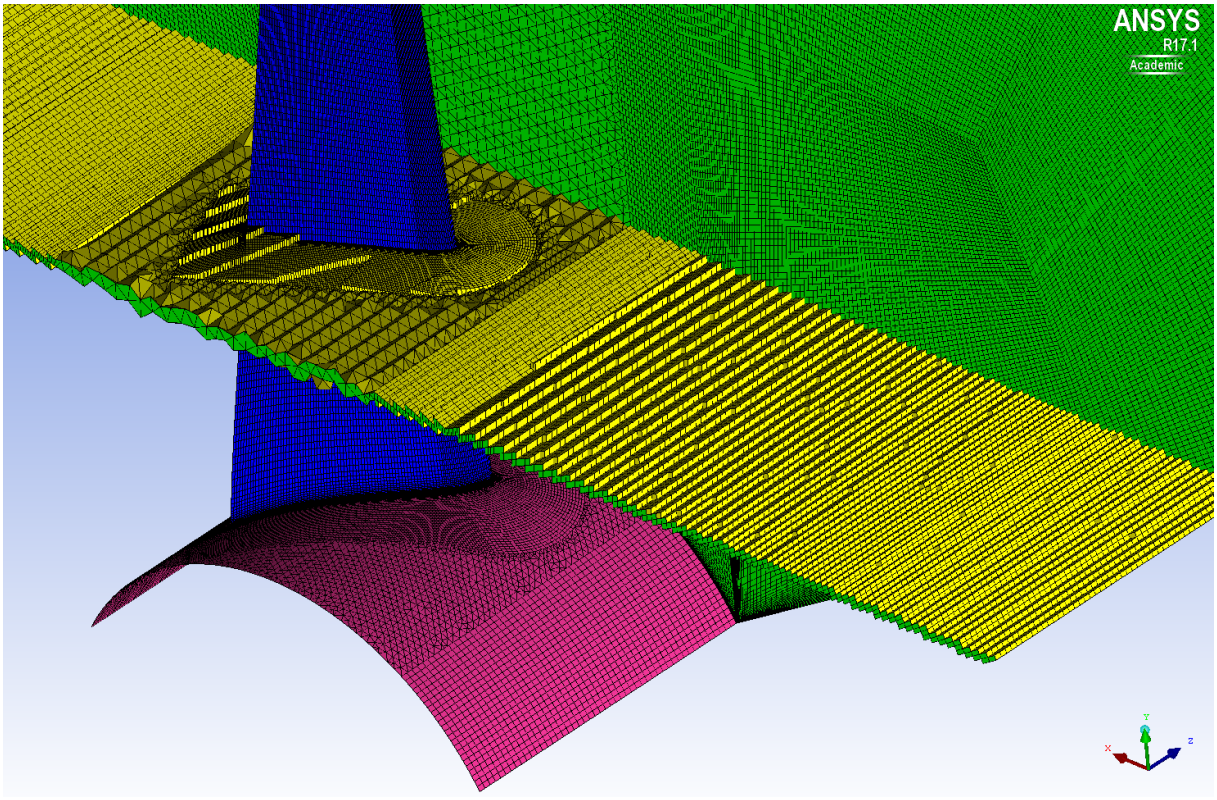

Fig. 34 Horizontal section (yellow) view of the rotating domain mesh, as viewed from blade suction side; 1/3 of domain is seen; rotor interface marked green, blade marked blue, hub marked pink

5.2.3. Simulation setup

All FRM simulations were of transient type. The reason for this choice is the unsteady character of the flow, coming from its physical definition. In the steady state analysis the wake was not properly modelled in the stationary domain, which in turn influenced the rotor performance. Thus the decision to use an approach that gives a priori more trustworthy results.

The time step for the simulations dt was associated with the T1 rotor rotational velocity. Every simulation was started with dt corresponding to T1 angular displacement of 15° (eq. (19)). During the calculations dt would be decreased gradually to correspond to the displacement of 5° and 3°, so as to increase the simulations' convergence level. These values were chosen after a case study for an open-rotor wind turbine. 1° was also tested, but no amelioration over 3° was observed (concerning simulation stability or convergence), while increasing the time needed to obtain a solution.

$$dt = \omega_1 \cdot \left(\frac{2\pi}{360} \cdot 15\right)/n, \quad \text{where n = 1, 3, 5} \tag{58}$$

"*Air at 25°C*" of properties from standard ANSYS Material Library is the considered fluid. It defines dry air at reference temperature 298 K (25°C) and pressure 101 325 Pa (1 atm). The data for this material are based on the CRC Handbook of Chemistry and Physics [101]. Selected information is grouped in Tab. 6. The fluid is considered to be an ideal gas and the simulation is isothermal (T = 298 K).

Tab. 6 Selected air properties defined in the simulation

Property	Value	Property	Value
Dynamic viscosity	$1.831 \cdot 10^{-5}$ kg·m^{-1}·s^{-1}	Coefficient of thermal expansion	$3.356 \cdot 10^{-3}$ K^{-1}
Density	1.185 kg·m^{-3}	Thermal conductivity	$2.61 \cdot 10^{-2}$ W·m^{-1}·K^{-1}
Molar Mass	28.96 kg·mol^{-1}	Specific heat capacity	$1.004 \cdot 10^{3}$ J·kg^{-1}·K^{-1}

High resolution modelling was used for solution of both flow and turbulent quantities equations, due to expected high pressure gradients.

The double precision of the partitioner, solver, and interpolator executables was tested, but did not give significant differences as compared with the single precision schemes. This observation was made despite the fact that the computational domain involved a significant variation in grid dimension and aspect ratio. Due to the double precision executables requesting prohibitively large numerical resources, a standard single precision scheme was employed.

MeTiS was the employed partitioning scheme. The simulations were ran at different numbers of partitions, ranging from 7 to 20. A comparison revealed no influence of the number of parallel processes on the simulation results or convergence level.

The simulations are performed using the Reynolds-Averaged Navier-Stokes (RANS) approach. This approach requires a turbulence closure. The k-ω SST turbulence model with a standard set of parameters was used in this case.

5.3. Model evaluation

The model was checked for numerical consistency and coherence with experimental results.

5.3.1. Numerical verification

Rudimentary tests of the numerical correctness of the obtained results were performed. The evolution of resolved equation residuals and monitored variables was performed during calculations (Fig. 35). In what concerns the equation residuals, a satisfactory level of RMS values lower than 10^{-4} was obtained in twin-rotor simulations for the continuity and momentum equations under the chosen numeric schemes (excluding turbulent kinetic energy, TKE). In the case of single-rotor simulations the convergence level was even higher, with residuals RMS values being of order 10^{-6}.

As for the temporal evolution of Cp and Ct coefficients, their trace is highly influenced by the dt value. For a time step relatively big with regards to the rotor velocity (to the left of the black dotted line in Fig. 35) the traces of all monitored coefficients change in an abrupt way. Whereas lowering the value of dt results in more smooth characteristics. Thus a pattern appears, in which the Cp and Ct traces fluctuate in a repetitive manner. The dominant frequency of these oscillations is equal to 1/3 the rotational velocity of the upwind rotor and is related to the interaction between test stand mounting pole wake and the wind turbine blade. The values of Cp and Ct were computed once three full cycles were completed, and evaluated as an average out of two last cycles.

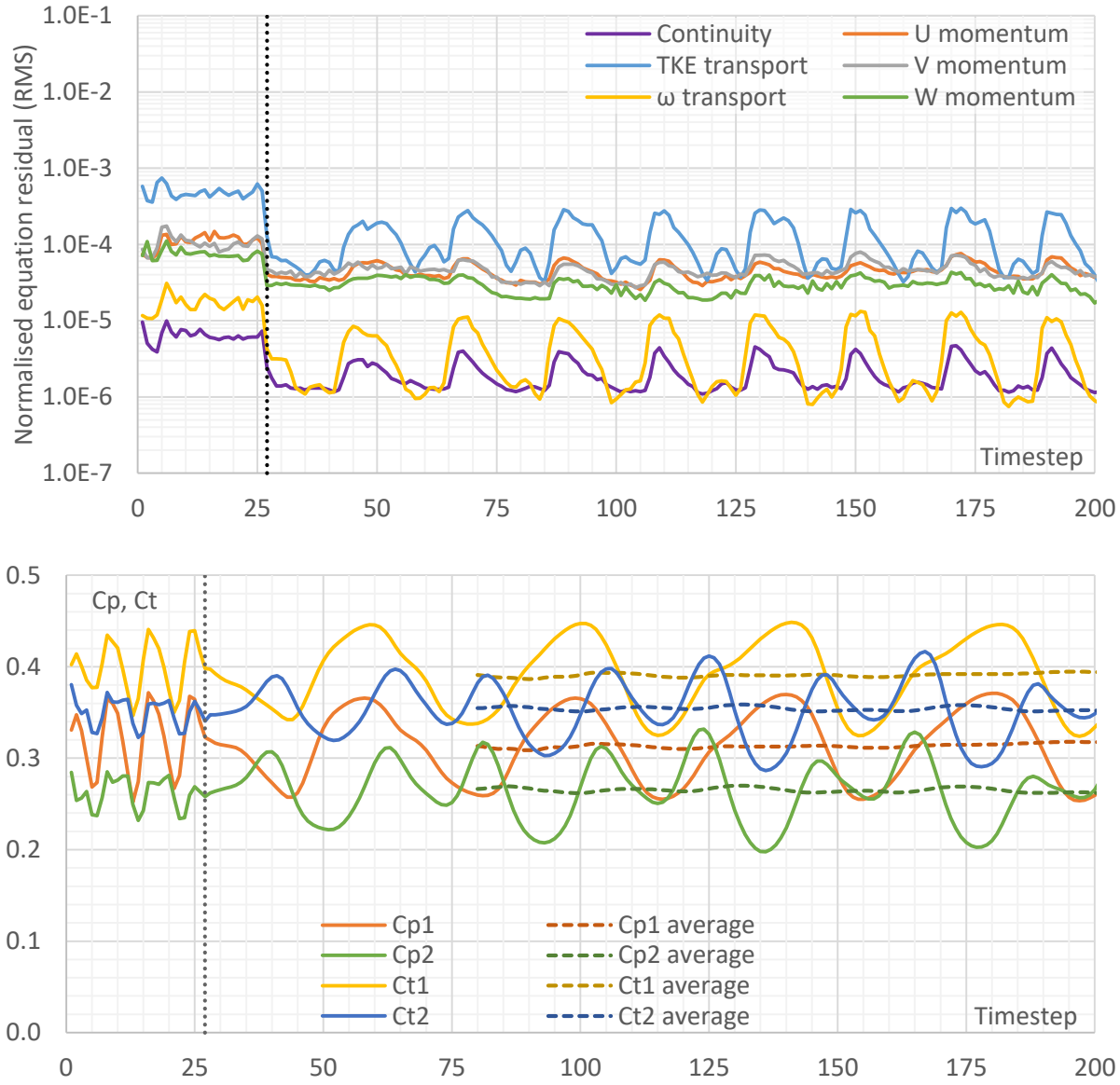

Fig. 35 Exemplary temporal evolution of simulation monitors in a CRSR simulation (TSR1 = 3.67, TSR2 = 3.45); normalised equation residuals (RMS values) for 6 governing equations solved in FRM simulation (top); Cp and Ct for both turbines (dashed line is moving average from last 80 iterations, bottom); the black dotted line denotes the iteration in which dt was changed from n = 1 (15°) to n = 5 (3°)

To evaluate the quality of solution in the boundary layer regions the y+ parameter is analysed on the primary surfaces of interest, notably the blades and the diffuser (Fig. 36), following the comments stated in Section 3.3. To decrease the problem's appetite for numerical resources it was decided that for the either rotor's blades the y+ should not exceed 3 at all the TSR range. The condition was fulfilled with exclusion of the high velocity gradient zones (notably the blade tip and leading edge) at high TSR (above the optimum, i.e. TSR > 6). The same target for boundary layer flow was put forward for the diffuser, and similar observations were made. The y+ values tend to attain higher values in the high velocity gradient regions, namely at the diffuser and brim edges. There are also several spots of increased y+ at the diffuser gorge (narrowest section). This phenomenon can be associated with the mesh structure in that region, deteriorated due to the interface between the stationary and rotating domains.

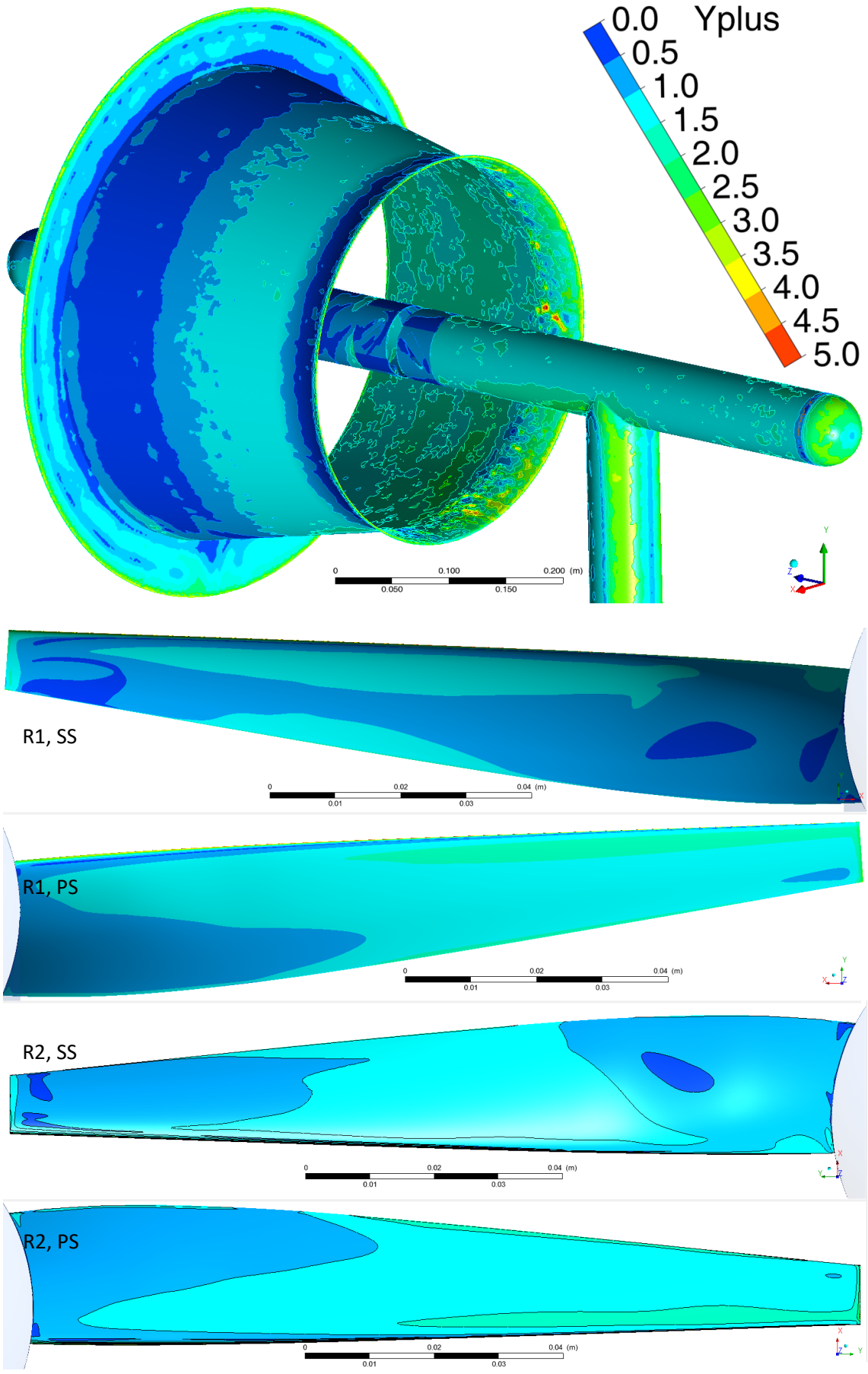

Fig. 36 Y+ distribution on the surfaces of test stands and diffuser (top) and wind turbine blades (bottom); CRSR, TSR1 = 3.67, TSR2 = 3.45; SS – suction side, PS – pressure side; colour code is the same for all images

5.3.2. Experimental validation

In order to evaluate the model's ability to represent the real-life turbine, simulation results were compared to the experimental results described previously. The data is visible in Fig. 37 (single rotors) and Fig. 38 (CRSR).

For open rotor results the correlation between simulation and experiment is very good for both Cp and Ct values. For the latter, the numerical predictions follow the experimental data accurately, the maximum difference is about 6%. Results for Cp are more complex to interpret. The difference between simulation and experiment in the TSR range below nominal point in majority is at the level of 3%. Above it, however, the difference grows and the idle rotational velocity is predicted at TSR ≈ 5.5. These two observations suggest that the model may tend to underestimate the value of drag coefficient Cd. In formula (23) the drag component in the normal force value is much smaller than the lift component. Whereas in the tangential force formula both components have similar order of magnitude. Hence a small change in Cd will influence Cp in much more significant way than Ct. Figure 45 confirms this hypothesis, showing that the numerical Cd values are smaller for low angle of attack, as compared to the experiment.

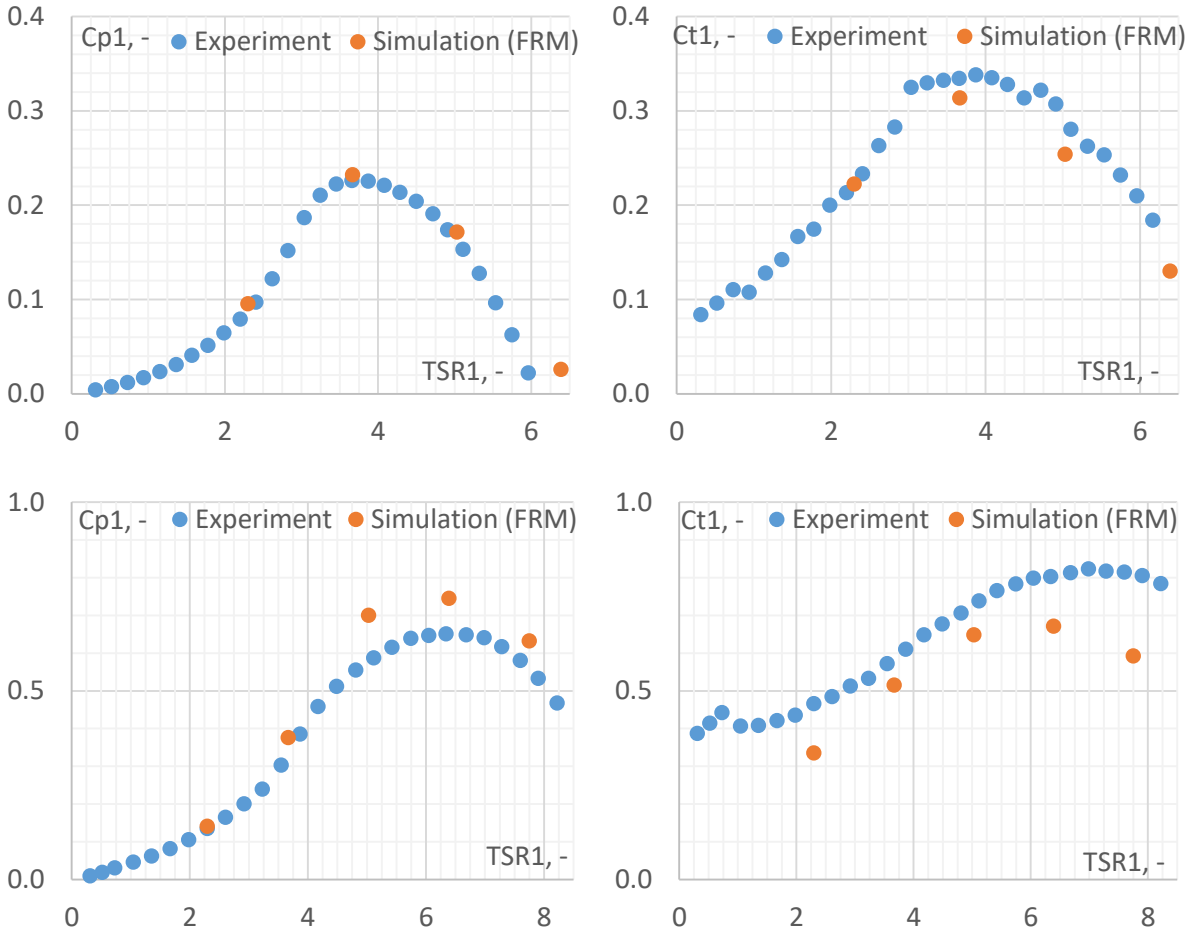

Fig. 37 Experiment (blue) vs. simulation (orange) comparison of Cp (left) and Ct (right) for open rotor (top) and DAWT (middle)

As for the DAWT results, the discrepancies between experiment and simulation are more significant. The model is capable of predicting the optimal TSR (for maximal Cp) correctly. However, the Cp values are overestimated by as much as 15% near the optimum and at higher TSR. The thrust coefficient

results are underestimated more significantly, by even as much as 36%. These two observations lead to the conclusion that the model may overestimate the flow velocity through the rotor plane. As it follows from formula (20), a rise in the axial velocity component will increase the inflow angle. This leads consequently to a rise in the tangential force and a drop in the normal force, as it follows from the trigonometric relationships in formula (23). It is important to underline that the performance of a DAWT is very strongly influenced by rotor's position with respect to the diffuser inlet. Even a relatively small axial shift in rotor position between simulation and experiment may be responsible for a significant discrepancy in the obtained results, as was proven previously, in the experiment.

Figure 38 compares the total Cp output (Cptot, left) and thrust coefficient of the upwind rotor (Ct1, right) for experiment (surface plot) and FRM simulation (scatter plot). In this case the Cp values from simulation are yet again overestimated. An analysis of the results obtained for each rotor separately revealed that this overestimation comes almost exclusively from the downstream wind turbine. For the upstream rotor both Cp and Ct values from simulation and experiment are very similar. The differences do not exceed 10% and are increasing with TSR2. Contrarily, the Cp values for the downstream rotor proved to be more overestimated. The differences grow more significantly as TSR2 rises, hence the rise in the overall system's performance Cptot. Summing up these observations it may be assumed that once again the model may have a tendency to overestimate the mass flow through the diffuser inlet. This leads to the increase in kinetic energy available for the downstream rotor, and thus – to increase in Cp.

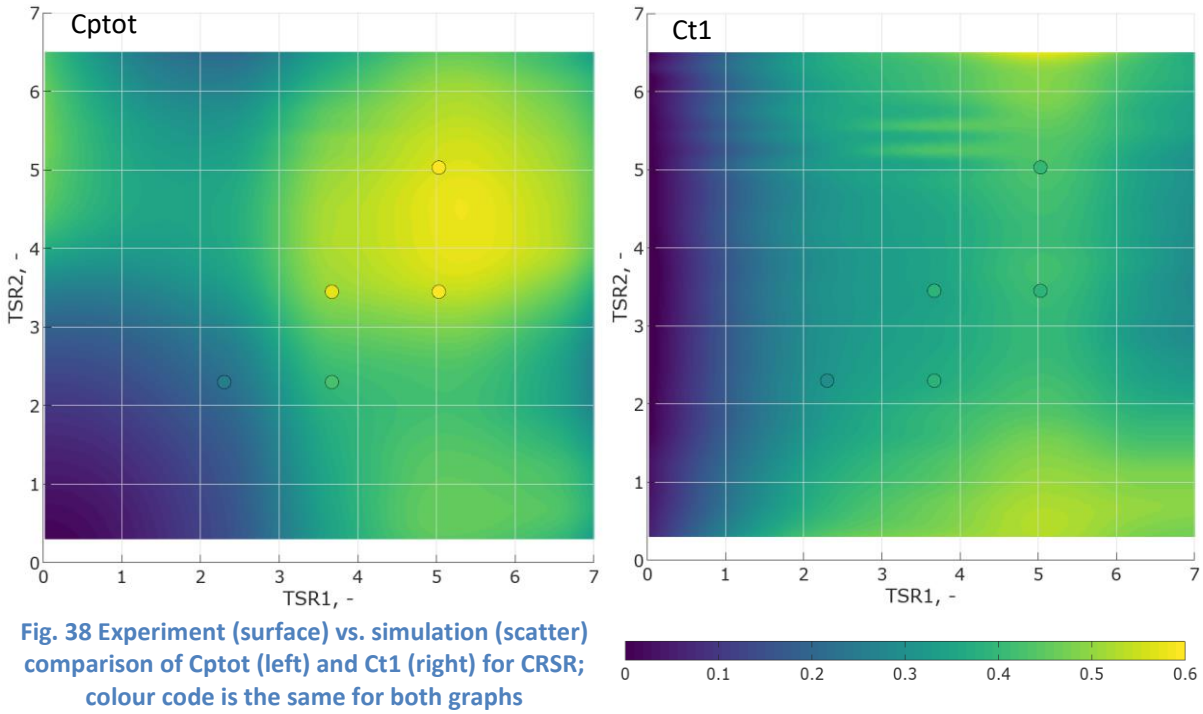

Fig. 38 Experiment (surface) vs. simulation (scatter) comparison of Cptot (left) and Ct1 (right) for CRSR; colour code is the same for both graphs

It is worthy to note that the discrepancies between simulation and experiment are more significant with increasing TSR2 than TSR1, both for downstream and upstream rotor. This proves that the downstream rotor has a very strong influence on the flow through the diffuser. One possible explanation of this phenomenon is that the interaction between the helical wake and the diffuser boundary layer postpones the separations and consequently the kinetic energy losses are lower. Proving this hypothesis would, however, require a more thorough study, which is not the objective of this thesis.

5.4. FRM - results and discussion

The following section will evaluate the distribution of selected flow fields in the wind turbines' Plane of Rotation (PoR). The applied procedure is as follows: at a selected radial position in PoR a circle is traced. Points on the circle are chosen, fixed in the stationary (global) reference frame. Throughout one full rotor revolution the velocity data is recorded and averaged. If there is a blade at an angular distance of 30° or less from the point, the velocity data is omitted, to prevent the influence of the blade singularity. Circular interpolation is then performed. The datasets are collected at different radii and interpolated throughout the entire PoR.

5.4.1. Flow velocity through rotor

The axial flow velocity through rotor is the first analysed parameter. Figures 39 and 40 show distribution of the normalised axial velocity in the PoR in representative DAWT and CRSR cases, respectively. Similarly, Figures Fig. 41 and 42 show distribution of the same parameter in the radial direction.

As for the DAWT, the average wind speed in the upper half of the PoR for both cases is approximately $1.36U_\infty$. In all considered simulations the velocities in PoR were augmented by about 30% - 40% with respect to the ambient wind speed U_∞. Having in mind that for an open rotor the axial velocity component in the PoR is normally lower than the ambient wind speed (equation (9)), it is fair to estimate that the shrouding increases the flow velocity by the value of order of 50%.

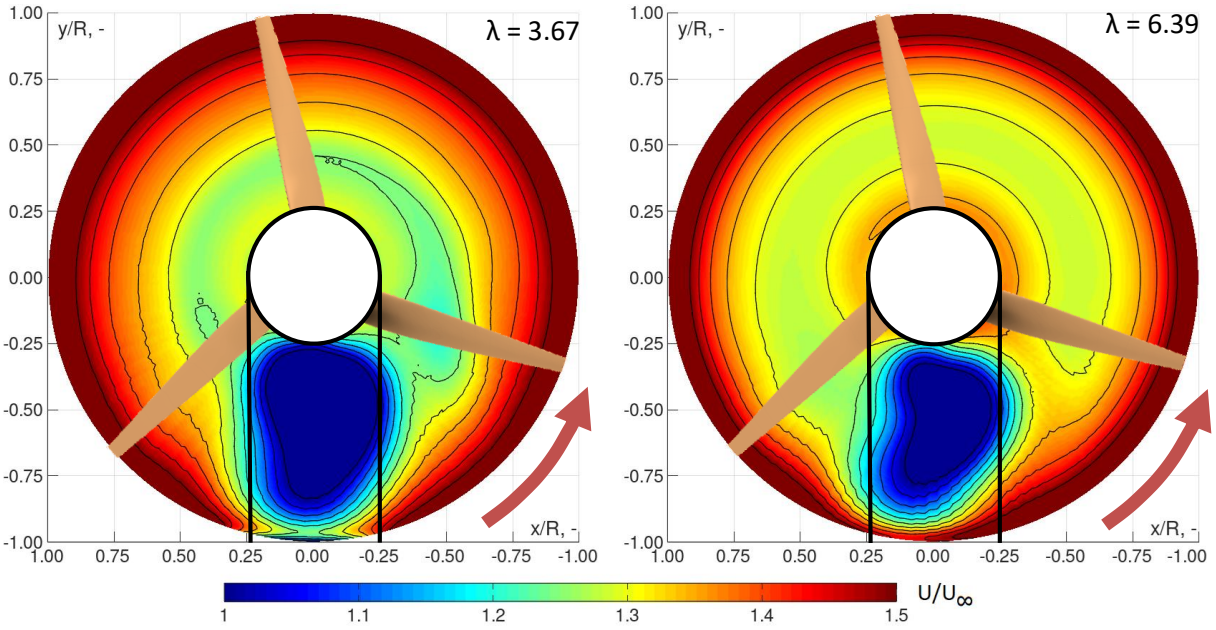

Fig. 39 Normalised axial velocity fields in PoR for TSR = 3.67 (left) and 6.39 (right) for DAWT

The flow fields are significantly affected by the presence of the mounting pole, manifesting itself as the velocity deficit in the lower half of the PoR. A more thorough discussion about the possible influence of this phenomenon on the overall results will be performed in Subsection 5.4.2. The disturbed region may qualitatively be estimated to span in angular positions $\varphi \in (150°, 330°)$. Outside this region, the quantitative flow analysis proved that the flow may be treated as uniform along the circumferential position, with differences not surpassing 5%.

In what concerns the radial distribution of the axial velocity, the data presented in Fig. 41 compares the values at the location φ = 90° (upper half of the y axis). For all cases except TSR = 2.30 the velocity experiences a similar behaviour - near the hub a flow velocity recovery from the boundary layer is visible. As the radius increases, the velocity deficit is observed up to about 75% of the blade length. The decrease in flow kinetic energy may be taken as a proof that the blade aerodynamic design was well done in this region. For the last 25% of the rotor radius a rapid increase in flow velocity is observed. This might be connected with the tip leakage. Abe et al. [63] have also seen this phenomenon and underline that it occurs when no flow separations are present at diffuser walls. The obtained curves and distribution of the axial velocity may be used in further blade optimisation studies, to determine the radius range in which the remaining wind kinetic energy is still exploitable.

Figure 40 shows the velocity fields in PoR for both rotors in the CRSR case for TSR1 = 3.67 and TSR2 = 3.46. It is noticeable that the wind speed magnitude for the upstream rotor is globally lower than that in the DAWT case, by approximately 20 – 25 percentage points. This difference grows further for the downstream rotor, which is a predictable observation, since it is placed farther from the flow contraction zone and velocity augmentation effects are lower. It is also noticeable how the downstream rotor is influenced by the upstream rotor's blades. The flow field in the upper half of the PoR is not circumferentially uniform, but fluctuates periodically.

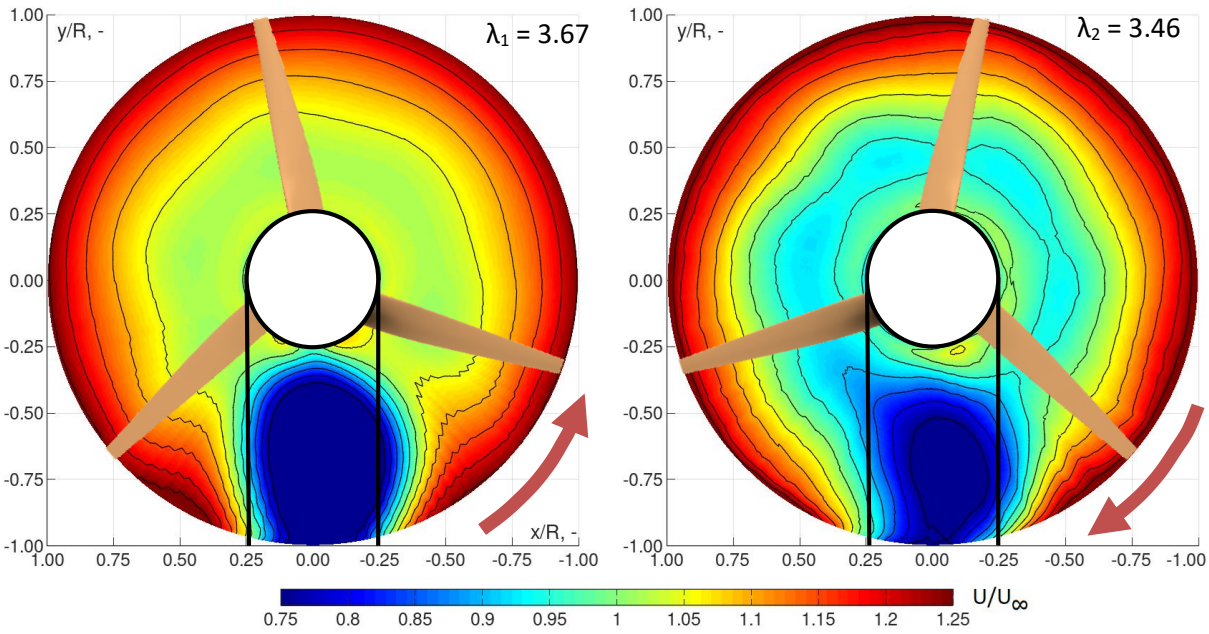

Fig. 40 Normalised axial velocity fields in PoR for TSR1 = 3.67 (left) and TSR2 = 3.46 (right) for CRSR

As for the radial distribution of the axial velocity (Fig. 42, values for line at angular position φ = 90°) the observations made for DAWT remain valid for the upstream rotor. It is noticeable how the velocity values are lower in CRSR simulations for the same TSR values. The downstream rotor operates indeed at lower axial velocity values (by approximately 5 – 10 percentage points in average) than the upstream rotor. For TSR = 2.30 it is also visible how the above mentioned influence of the upstream rotor manifests itself in the abrupt deficit of flow velocity at r/R in the range 0.3 – 0.55.

In all it may be said that the CRSR wind turbines operate at globally lower wind speeds. This explains why their optimal TSR is shifted towards lower values than those for the DAWT and why the attained

Cp values are lower. The obtained flow velocity fields will be an important tool used to verify the actuator model in further steps.

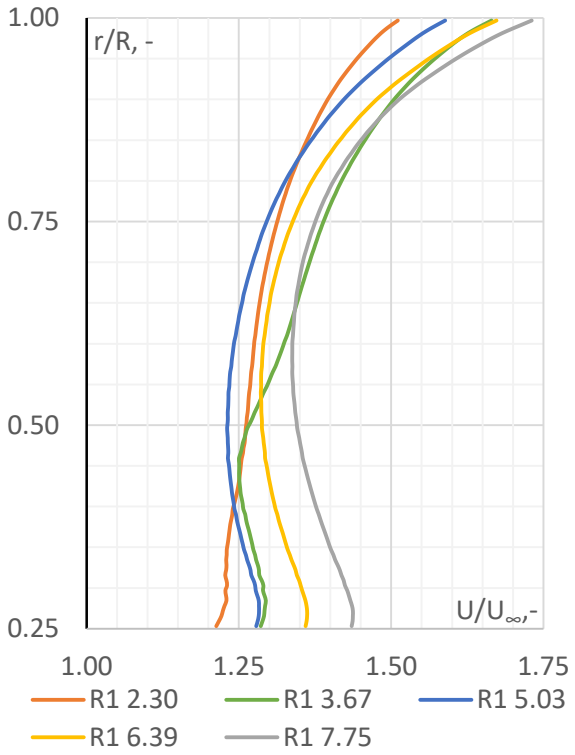

Fig. 41 Radial distribution of normalised axial velocity in PoR for DAWT at different TSR

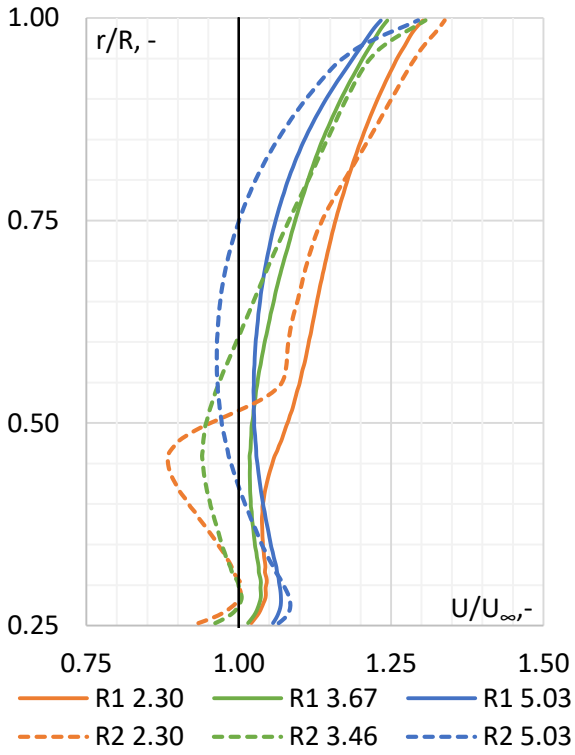

Fig. 42 Radial distribution of normalised axial velocity in PoR for CRSR at different TSR; same colour denotes the same computational case

5.4.2. Angle of attack and aerodynamic force coefficients - single rotor

In the hybrid BET-CFD model the crucial role is played by the proper depiction of the angle of attack (AoA) and lift and drag coefficients (Cl, Cd). The FRM simulations will be used to cross-check the values observed in the hybrid model simulations (AoA), and confront the used characteristics (Cl, Cd).

The angle of attack is, a priori, a 2D concept. For the rotating blades it may be approximated on the isoradial cylindrical surfaces at different blade stations [102]. Numerous techniques were proposed to estimate the angle of attack, based mostly on analytic models. Shen [103] proposed to analyse the local bound circulation, useful especially in the experimental studies. Rahimi et al. [104] proposed the determination of AoA using 6 characteristic points surrounding the aerodynamic profile.

In this thesis a different approach is proposed, which is the determination of AoA using its definition from equation (21). This requires the knowledge on the local flow velocity fields, which are readily available through the CFD simulations. The remaining question concerns the axial location for velocity data extraction. In this study a philosophy derived from studies elaborated in [105] is applied. The plane of rotation (PoR), defined by the extrusion lines of the blades, is the reference location.

Figure 43 shows the distribution of local AoA on upper halves of PoRs at different TSR. As the rotational velocity increases the tangential velocity component dominates the local velocity triangle. Consequently, the local AoA decreases. Maximum Cl/Cd ratio for the used profiles, a parameter having

a direct influence on the obtained Cp values, occurs at $\alpha \approx 5°$ (see Section 6.2). This AoA resonates with the values observed in simulation at $\lambda = 6.39$. Indeed, in the vicinity of this rotational velocity the maximum Cp occurs (the rotor is designed for $\lambda_{opt} = 6.00$). As TSR decreases, the local AoA attains bigger values, corresponding to stall- and post-stall conditions and translating into lower Cp. In turn, as TSR increases, the profiles operate at AoA lower than the optimum, in the linear part of the $Cl(\alpha)$ characteristic.

The AoA distribution in the upper half part of the rotor does not change significantly with varying angular position, meaning that the blades operate in relatively uniform conditions as they turn. Contrarily, the variation of AoA is very much visible in the radial direction, and is similar in all cases. The AoA values attain low values in the closest vicinity of the hub. This is a consequence of the viscosity force effects in the hub boundary layer. It decreases the axial velocity vector, while preserving the rotational velocity component. Thus α is decreasing. Outside the boundary layer, the axial velocity regains its value and AoA grows. However, the tangential velocity component increases with radius, thus the AoA values decrease once again. To overcome the latter, the blade employed in this study is of variable pitch design, optimised for $\lambda = 6$. Indeed, for results collected at $\lambda = 6.39$ the AoA values distribution is more uniform than for other rotational velocities. The above mentioned tendency is also observed in Fig. 44, presenting distribution of normalised AoA (i.e. divided by the average AoA in the upper half of the PoR, α_{ave}) in the entire PoR at two different rotational velocities, $\lambda = 3.67$ (top) and $\lambda = 6.39$ (bottom).

Figure 44 also shows how the mounting pole (marked by thick black lines) influences the AoA values. The wake region is characterised by axial velocity deficit, which diminishes the numerator of equation (20), decreasing the inflow angle ϕ. Consequently, the AoA value decreases as well (equation (21)). Dynamic phenomena around the profile in the pole's wake region may significantly influence the aerofoil's performance, for example due to hysteresis effects or by provoking premature stall [106]. The flow in the wake of mounting pole is non-stationary, as proved by the qualitative analysis of the instantaneous velocity fields. To account for this behaviour, a more elaborate time averaging would be necessary, possibly covering several turns (see for example [107] – in the case of Darrieus WT). However, the detailed study of flow in that region was not the principal aspect of the thesis. Due to a prohibitively large size of the demanded computational resources, a single-turn averaging was chosen as a necessary compromise. Hence the results in that region must be taken with caution and were used only for qualitative analysis. The wake behind the mounting pole is not symmetric, but moved correspondingly to the rotor direction of rotation. Rotor operating in downstream configuration is exposed to varying velocity conditions for as much as a half of the spun range, in angular position range approximately $\varphi \in (150°, 330°)$.

An analysis of aerofoil properties was performed for data collected for rotor angular position range $\varphi \in (-30°, 150°)$, judged previously as relatively unaffected by the mounting pole's wake. Using an inverted BET theory, basing on the local velocity and force values, it is possible to estimate lift and drag coefficients' values. Figure 45 shows plots of Cl and Cd vs AoA for SG6041 aerofoil, used in the blade for approximately 60% of blade outer part. Each colour group of points represents data at a given rotational velocity collected at locations marked blue in rotor miniature. The data is compared with experiment and XFoil predictions (lines). It is immediately visible that the FRM dataset covers almost exclusively the positive AoA range. There is a good global correlation between the three datasets. Although FRM simulations do not show precisely at which AoA the stall occurs, the simulation results

in both pre- and post-stall conditions follow the trends of both experimental values and XFoil prediction. For more data considering aerofoil performance refer to Section 6.2.

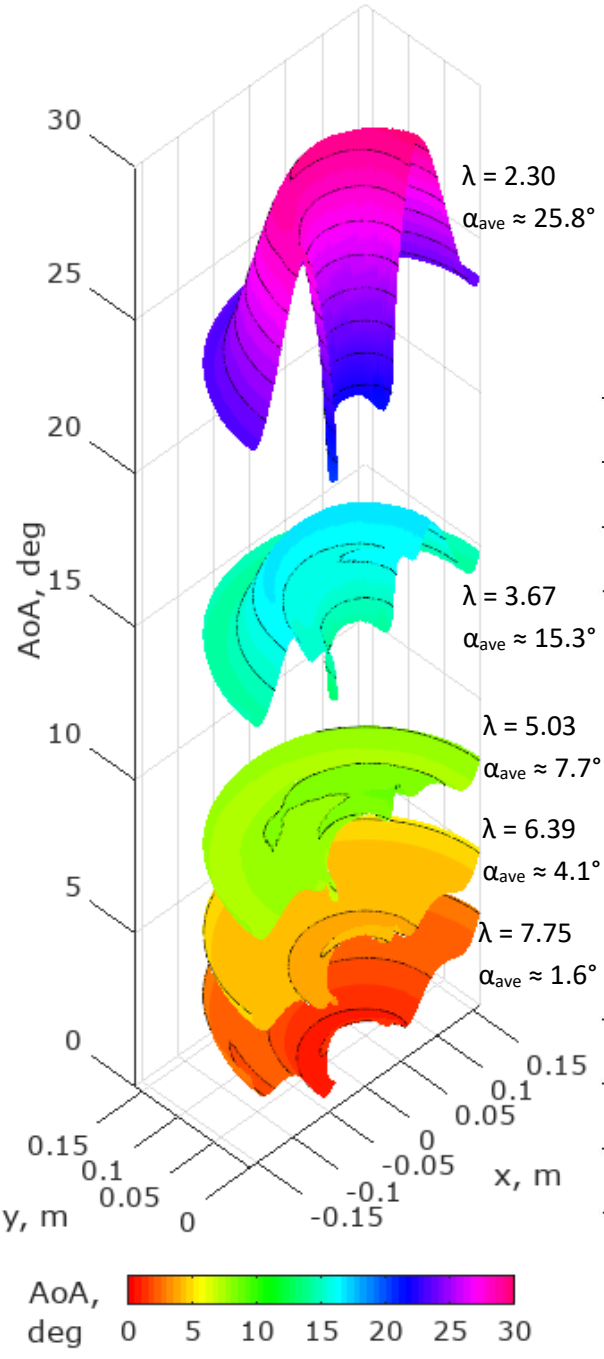

Fig. 43 AoA distribution in the upper half of PoR for various TSR values and corresponding average values (DAWT)

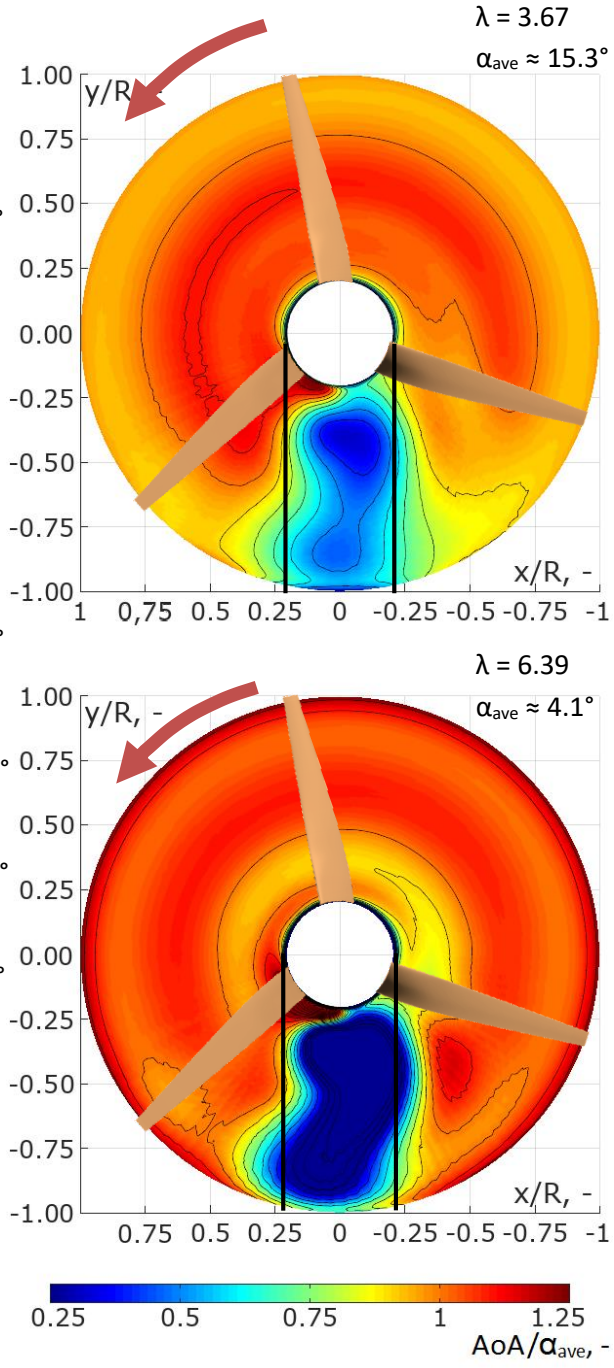

Fig. 44 Normalised AoA distribution in PoR at TSR = 3.67 (top) and 6.39 (bottom) as seen from inflow direction (DAWT); red arrows denote direction of rotation, black lines denote pole location

In the AoA region close to zero FRM tends to underestimate the Cd results, as compared with the experiment. A reason for this behaviour could be connected with the boundary layer behaviour in these two cases. In FRM the boundary layer is assumed to be fully turbulent (due to the nature of the k-ω SST turbulence model). This may be justified by the fact that the 3d-printed blades are

characterised by a relatively rough surface, which promotes transition of the boundary layer into the turbulent regime. In the external experimental study this assumption might be too optimistic, and the aerofoil could still be operating in the transitory region. Hence the associated drag would also be higher, as observed in Fig. 45.

In the immediately pre-stall flow conditions the Cl values from FRM are underestimated with respect to the experimental data. This may be due to the influence of Reynolds number changes. It is also important to note, that for XFoil prediction and experimental study the reference velocity (ambient) is defined differently than for FRM (local). This may introduce additional discrepancies at normalisation process.

It is also worthy of note that the employed inverted BET uses the local total inflow velocity, influenced by the rotor's operation. This is opposed to the free-stream conditions used for a classic aerofoil study, but is a typical approach in the BEM studies.

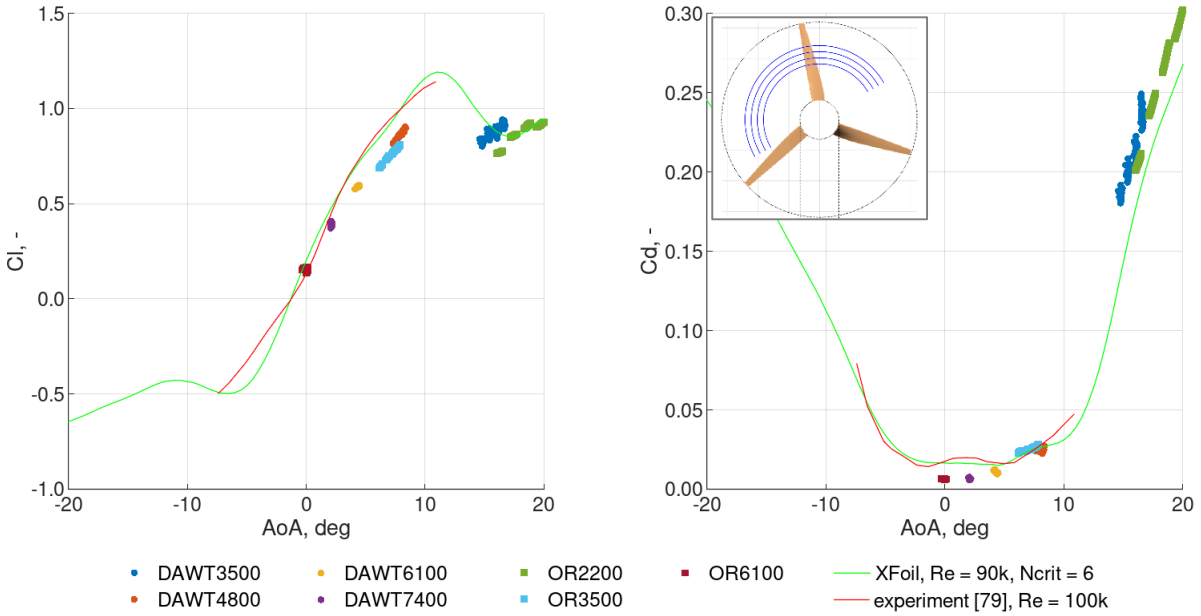

Fig. 45 Cl (left) and Cd (right) vs AoA for SG6041 aerofoil;
DAWT and open rotor FRM simulations (points) compared to XFoil prediction and experiment ([108]);
FRM data extracted from locations marked blue in rotor image in box (180° arcs at 4 different radii)

5.4.3. Angle of attack and aerodynamic force coefficients – twin rotor

Evaluation of the AoA distribution was also performed for the CRSR system, with results visible in Fig. 46. AoA distributions in the PoR of rotors - upstream (left) and downstream (right) with both turbines rotating at TSR = 2.3 (top) and approximately 3.5 (bottom) are presented.

Comparing to the single-rotor system, both CRSR rotors operate at lower AoAs. For the upstream rotor this difference may be as high as 30%. The average value of AoA in the upper half of the PoR is higher for the downstream rotor. However, as it is clearly visible in Fig. 46, this rotor tends to actually operate at lower AoA than the upstream one. The reason for this discrepancy is that the AoA distribution in the PoR is very heterogeneous. The primary reason for that is the upstream rotor's wake. In the analysed images its presence manifests itself in the form of local AoA deficit regions at an angular distance about 60° from each other. This is because the angular velocity of both rotors in this case is identical or very similar. Consequently, per one full turn of the downstream rotor, each of its blades will pass in the

wake of the upstream rotor 6 times. Due to the assumed averaging scheme these passages are visible in AoA fields as deficit regions. The regions of local AoA augmentation between blade passages are also noticeable.

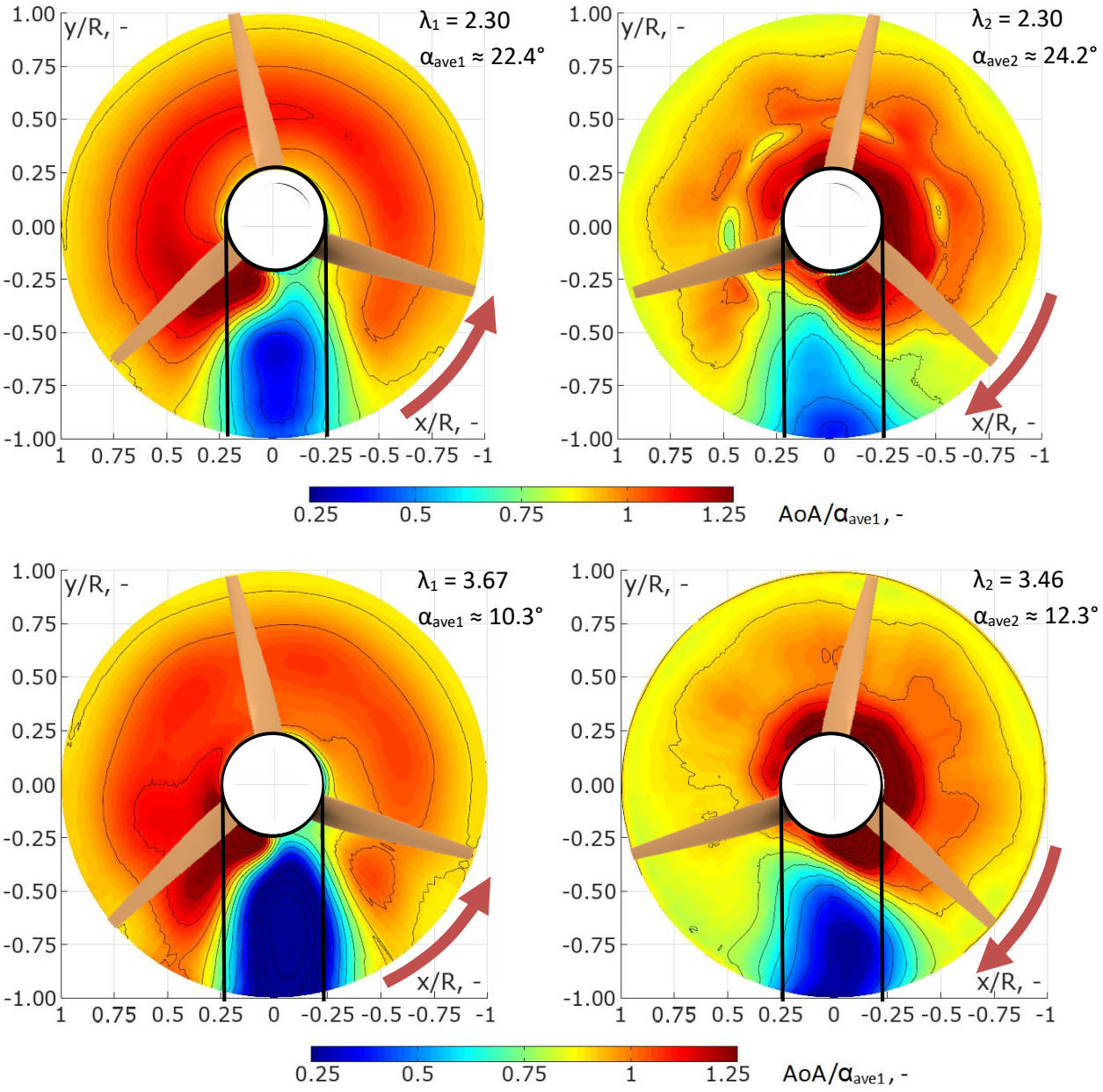

Fig. 46 Normalised AoA distribution in the plane of rotation (PoR) of upstream (left) and downstream (right) rotor in CRSR cases at TSR 2.3 (top) and approximately 3.5 (bottom) as seen from inflow direction (DAWT); red arrows denote the direction of rotation, black lines denote pole location

5.4.4. Tip loss correction modelling - DAWT

In its essence, the tip loss correction for Blade Element models is introduced to account for the fact that the real rotor has a finite number of blades B [79]. The latter has a direct influence on the flow behaviour near the tip of the blade, where the leakage occurs, decreasing the performance of this blade sector. The traditional formulation (eq. (25)) assumes a free development of the rotor's helical wake (see ex. [109]). This is clearly not the case for a shrouded wind turbine, for which the wake

interacts strongly with the diffuser's walls. To take this into account Takahashi proposed a tip loss coefficient based exclusively on the radial location (original notion as seen in [65]):

$$F = \begin{cases} 1 & r \leq r_i \\ \dfrac{1-0.7}{r_i - R}(r - r_i) + 1 & r_i < r \end{cases}, with\ r_i = 0.93 \cdot R \tag{59}$$

The above formula relies uniquely on the radial location along the blade and does not take into account either the local velocity fields or the number of blades.

To check the performance of both aforementioned formulae a simple BET analysis was performed, on the basis of the FRM results - AoA and velocity fields, Cl and Cd values (determined from FRM simulation). The point was to compute the force coefficients: tangential ft and normal fn (see equation (23)) and apply a tip loss correction (multiply by F) if needed. The results are presented in Fig. 47, with reference data (FRM) presented as scatter plot. It is easily seen that the "raw" BET (R, i.e. with no tip loss correction) overestimates both ft and fn values in the vicinity of diffuser wall, at r/R higher than 0.88. This is a typical phenomenon for uncorrected BET, in which radial flow is neglected and tip losses are not present. However, application of the classic Prandtl tip loss correction leads to a much more destructive loss in performance for the entire analysed r value range. Both normal and tangential force coefficients are underestimated. This is a reasonable observation, since the correction accounts for a fully-developed wake. In the case of DAWT this development is, however, influenced by the shrouding geometry. In other words the diffuser may be represented as an additional source of circulation, modifying the flow properties in PoR and the (helical) wake.

The force damping effects are much lower when the Takahashi correction (T) is applied, since the model is only effective at the last 7% of the blade length. However, in the current study the discrepancies between FRM and "raw" BET are observed for the last 12% of the blade length, which means the correction is "activated" too late. Moreover, the corrected fn(r) and ft(r) relationships are almost perfectly linear, whereas in the case of FRM this relationship is of more complex form. Nevertheless, the Takahashi correction might perform better if the value of r_i was a function of flow character and DAWT geometry.

The proposed in-house correction is based on the original Prandtl formulation. The modification lays in value of B (number of blades in the classical model). As B rises, the correction becomes effective in a smaller range of the blade tip. This property was employed to overcome the aforementioned observed limitations of the original correction. From the physical point of view, the number of blades modifies the solidity of the rotor and the circulation distribution in its wake (see [109] for an exhaustive derivation and analysis). FRM results were used to determine the value of B for different tested rotor velocities (Tab. 7). The preferable value of B was found out to be of range approximately 9 – 12, depending on λ. These empirical values are employed in the "own", modified tip loss correction, in which B = B(λ). The results are marked as "O" in Fig. 47.

The developed B(TSR) relationship was verified in the CRSR case, at TSR1 = TSR2 = 5.03 (Fig. 48). The BET and FRM curves for the upstream rotor are almost identical up to r/R equal to approximately 0.8. Closer to the tip, the BET prediction overestimates both ft and fn (by up to 10%), as compared to FRM. This suggests a possible increased tip leakage effects for the upstream rotor in CRSR, coming from e.g. different load distribution than for a DAWT configuration. In contrast, for the downstream rotor the ft

and fn radial distributions near the blade tip obtained from FRM and BET are very similar and differences are of order of 5%. Farther from the tip this value rises to approximately 10%. All obtained curves follow the same trend.

Tab. 7 Proposed values of B for different TSR for the analysed rotor

TSR	2.30	3.67	5.03	6.39	7.75
B	9	11	14	11	9

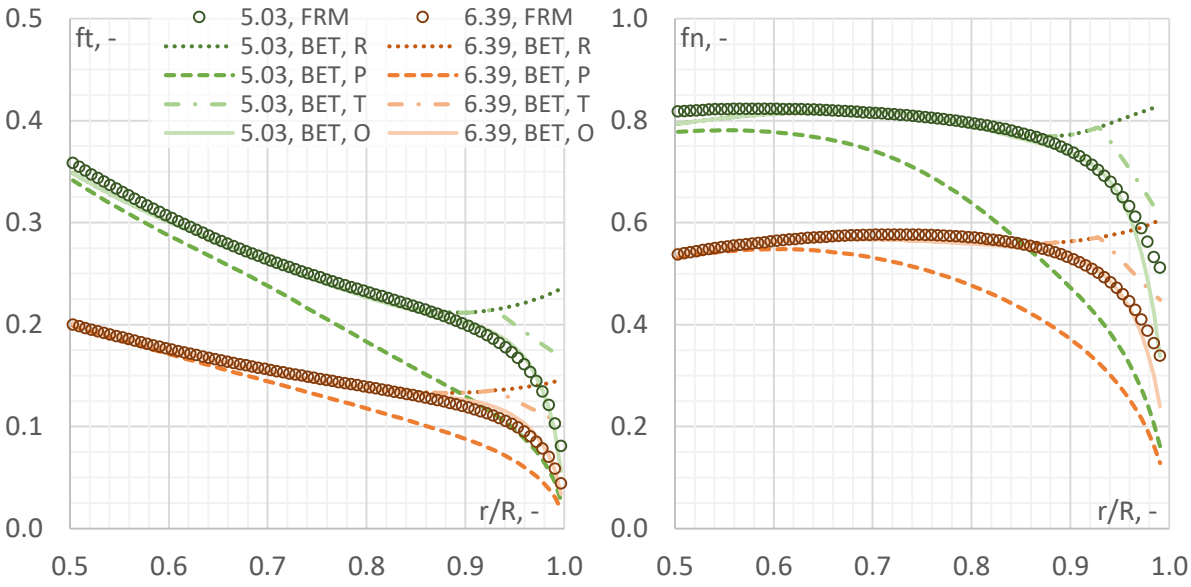

Fig. 47 Torque (left) and thrust force (right) coefficient distribution at TSR 5.03 (green) and 6.39 (red) in DAWT simulations: FRM (scatter), BET with no tip loss correction (R, raw) and models by Prandtl (P, (25)), Takahashi (T, (59)) and own (O); blade angular position is 60°

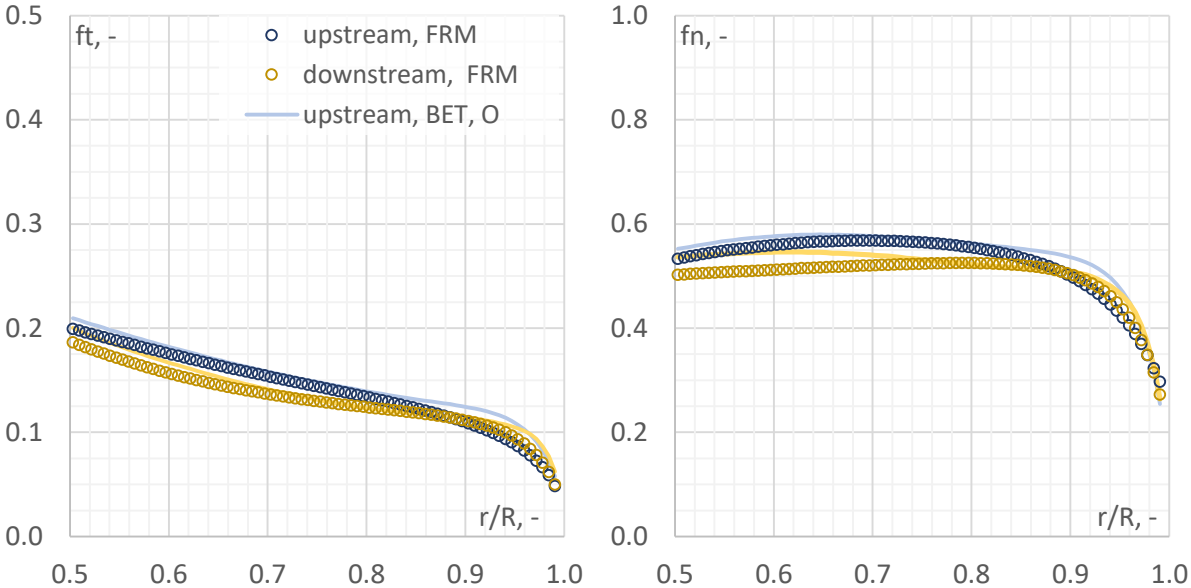

Fig. 48 Torque (left) and thrust force (right) coefficient distribution at TSR1 = TSR2 = 5.03 in CRSR simulations for upstream (blue) and downstream (yellow) rotor: FRM (scatter) and BET with own (O) tip loss correction; blade angular position is 60°

The above mentioned observations and analysis are assumed to be satisfactory to prove the validity of the proposed Prandtl tip loss correction modification. This in-house formulation will be embedded in the developed numerical hybrid model presented in Section 6.1.

To conclude, it is important to underline that the estimated B(TSR) values are sensitive to rotor geometry and operating conditions changes. The performed analysis shows that, although the classic formulation of the tip loss correction may be adapted to serve the DAWT analysis, it requires caution when doing so. Development of additional, analytical model similar to that of Prandtl might permit to study the problem more profoundly and precisely. This, however, surpasses the frames of the current study and may be suggested as further development of the studied models.

5.5. Summary and conclusion

This chapter presented first of the numerical models evaluated for the thesis - the Fully-resolved Rotor Model. Presentation of simulation principles, domain discretisation and preprocessing schemes are given, followed by model verification and validation.

The obtained and presented results constitute a basis for a more elaborate flow analysis, such as distribution of AoA in selected locations or evaluation of aerodynamic forces and their coefficients. These results will have an important role for further assessment of the hybrid model, as shown in Chapter 6.

6. The hybrid CFD-BET model

This chapter presents the principles, formulation, verification and validation of the developed hybrid CFD-BET simulation model.

6.1. General information

The hybrid CFD-BET model is composed of two coupled elements:

- Flow solver – provides the information about flow velocity, pressure and turbulent quantities fields, by solving the corresponding equations.
- BET code – computes the aerodynamic forces exerted by the fluid on the rotor using the 2D-aerodynamics. Flow solver provides the velocity fields, while user introduces the blade and profile characteristics. The forces are then recomputed onto source terms, inserted (with opposite sign) into flow equations.

The syntax of calculation procedure using the hybrid model, employed in the current study, is presented in Fig. 49. The operations performed by the solver are comprised in the red box to the left. Those realised by the BET code are grouped in the green box on the right. In every calculation iteration the solver would commence by identifying the cells that belong to the disk and extract the information about velocity fields. This data, along with the corresponding mesh cell coordinates, is transferred to the BET code, implemented as ANSYS Fluent User-Defined Function (UDF). The code estimates the local pitch angle and chord on the basis of cell coordinates and local Cl and Cd values on the basis of velocity triangles and Re value. Basing on this data, as well as the local velocity triangles, the code computes the aerodynamic forces (in the local coordinate system, related to the considered blade station). These forces are then translated onto the global coordinate system, in the form of source terms.

The practical implementation of the procedure described above was done using an UDF routine, in the form of a standalone code in C language. The corresponding block diagram of a solution process for a wind turbine characteristic is visible in Fig. 50.

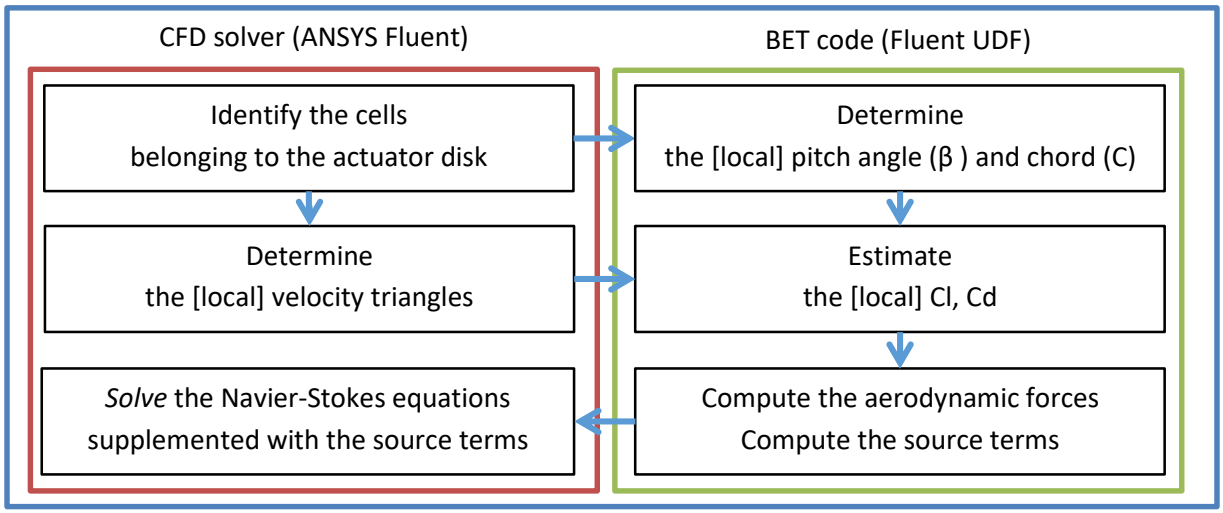

Fig. 49 Syntax of the flow calculation using a hybrid CFD-BET model, realised in every iteration for every cell

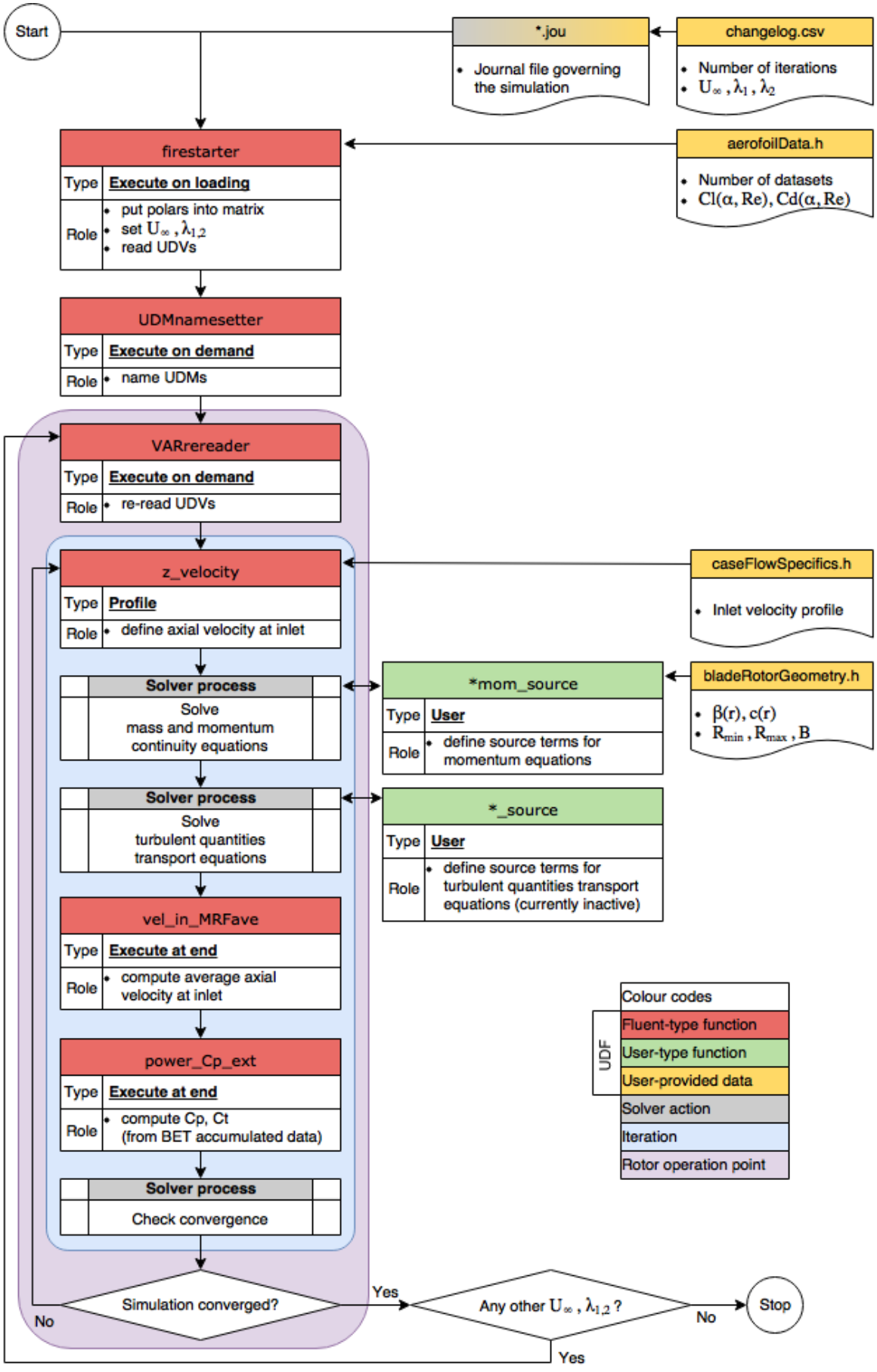

Fig. 50 Hybrid CFD-BEM model realization - overview of the solution process for a wind turbine characteristic

The developed script is divided into several parts, which enables one to separate the user-customizable sections (blocks marked yellow in Fig. 50) from the coded functions (marked red and green). The computation procedure starts with the preparation of the journal file, governing the entire simulation. The file is prepared automatically for each wind turbine characteristic, on the basis of user-provided U_∞, $\lambda_{1,2}$. A routine executed at the case loading is responsible for setting the above mentioned variables, as well as read the aerofoil polar data and store it in the code matrices. User-Defined Memory (UDM) slots are then allocated and named for storage of chosen computation variables (i.a. α, Re). User-Defined Variables (UDVs) are then read again, defining the rotor operating conditions. The solver (in this case steady state) then proceeds to iterative calculations of the solution. In each passage the following sequence is conducted:

- Definition of the inlet velocity profile – based on the U_∞ and the distribution presented in Fig. A1.3 (0);
- Solution process I – in this case the coupled solver was used, thus the mass and momentum equations are solved together. At this stage the solver communicates with the actual BET script. It sends cell coordinates and velocity values and receives the source term magnitudes;
- Solution process II – the turbulent quantities transport equations are solved after the above mentioned conservation equations. A separate procedure was developed to implement the source terms into these equations, to account for additional production of TKE. However, this functionality is not currently used, due to the problems in calculation of TKE values;
- Computation of the average axial wind velocity at inlet – the average axial velocity serves as a reference for further estimations of the flow conditions;
- Computation of the Cp and Ct values for R1 and R2 – during execution, BET accumulates information concerning the computed aerodynamic loads. This information is then used to evaluate the rotor power and thrust;
- Solution process III – the solver checks whether the specified convergence level was achieved. If not, then the simulation continues iterating.

Once a rotor operation point solution end criteria are fulfilled, the solver proceeds to a next set of parameters U_∞, $\lambda_{1,2}$. Once the entire characteristic(s) is collected the simulation terminates.

6.2. Aerofoil properties

The studied blade geometry is based on the Selig/Giguere SG6040 and SG6041 aerofoils (Fig. 51). These were originally developed by Giguère and Selig for the use in the small HAWTs [110]. SG6041 aerofoil is referred to as the primary aerofoil, providing a fine performance in a wide range of operating conditions. The thickness is 10% chord. Since this value might be too low for the high bending moments at the blade base, a 16% thick SG6040 profile was also designed as root profile. The authors recommend to use the root aerofoil up to approximately 30% of the inboard blade length, and the primary aerofoil at the outer 25% of the blade length. The inner part of the blade is to have a blended profile [110]. In the case of the studied blade geometry the SG6041 aerofoil occupies more than 60% of the outer part of the blade, while SG6040 – less than 15% of the inner part. In the following part of this section only the SG6041 aerofoil will be analysed in detail, as the observations for SG6040 are similar.

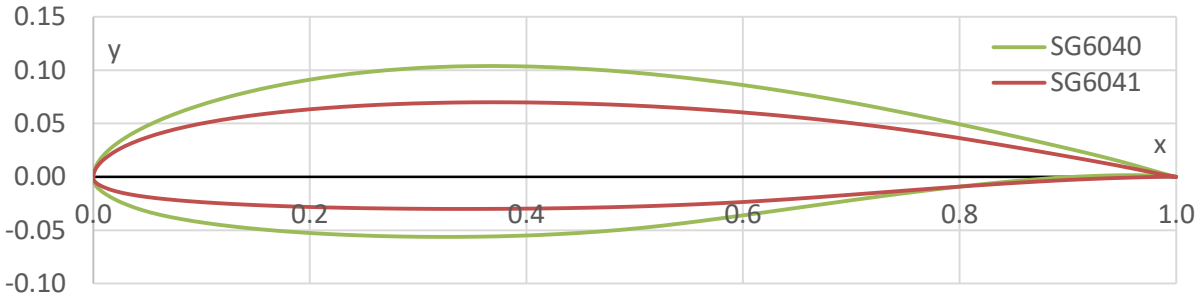

Fig. 51 SG6040 (green) and SG6041 (red) aerofoils used in the presented current study

Having in mind relatively low Reynolds number observed for small HAWTs, the profiles were originally designed for Re = 200 000 (SG6040) and 500 000 (SG6041). Nevertheless, it may be observed in Fig. 52 that their range of operation expands to lower Re values, although at the cost of increased drag values. This is seen in the Re = 100 000 Cd dataset in Fig. 52, characterised by relatively high Cd for AoA close to 0°. It is, however, important to underline that the presented results concern a smooth aerofoil surface. In the studied case it is assumed that the 3D-printed blades' structure provokes turbulent transition of the boundary layer flow. Thus the laminar separation effects are shifted towards lower Re values (compare e.g. with results seen in Fig. 45).

For Re = 100 000 the experimental maximum Cl/Cd ≈ 54 (at AoA ≈ 5°) suggests a relatively fine performance for these flow conditions. For example NREL S833 aerofoil, recommended by NREL as a principal aerofoil for SWTs of diameter size up to 3 m, has a lower maximum Cl/Cd ≈ 40 (at AoA ≈ 8.5°). The price for this is, however, a very quick loss of performance in the negative AoA range.

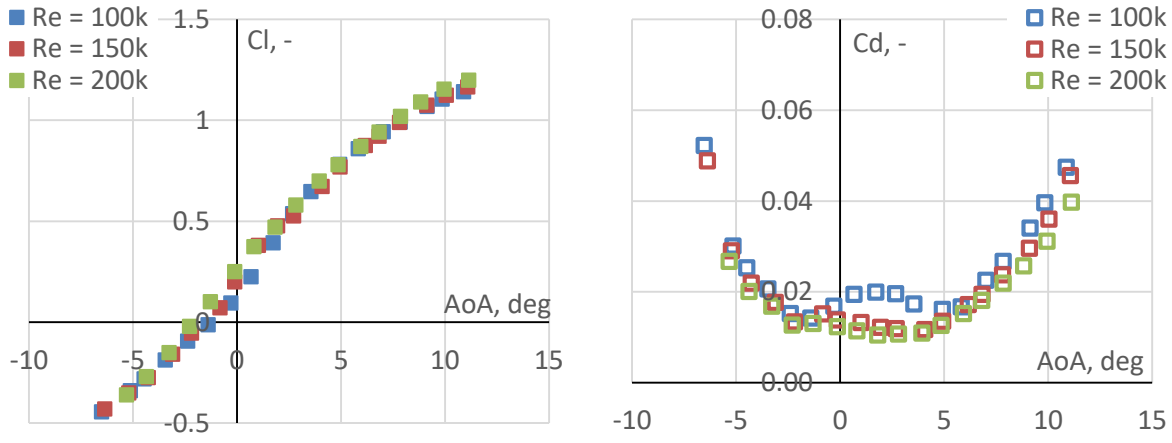

Fig. 52 Experimental data for SG6041 aerofoil: lift (left, filled marks) and drag (right, hollow marks) coefficients at different Reynolds numbers [108]

To extend the available lift and drag data over a higher AoA range, numerical analysis was performed using the XFoil software. Although the aerofoils are expected to operate in the linear part of the characteristic, it is possible that certain working conditions will force post-stall operation, hence the importance of data availability. Using XFoil it is also possible to emulate the aerofoil behaviour for different surface roughness. This is done via the Ncrit factor, which controls and triggers the laminar-turbulent transition [111]. The standard value of Ncrit is 9. Higher values are advised for "clean wind tunnel" flow conditions, and lower Ncrit is advised for "dirty wind tunnel" flow conditions. Figure 53 compares results of XFoil simulations (blue) with experimental (green, [108]) and FRM (red) results. It is important to remember that the FRM results are collected for different Reynolds number, while

other data is for constant Re ≈ 100 000. Ncrit is the parameter responsible for triggering the laminar-turbulent transition. The presented curves are representative cases from a wider, tested range. Ncrit lower than 9 corresponds to “dirty wind tunnel” flow conditions. Ncrit equal to 9 is a standard value. Ncrit higher than 9 corresponds to “clean wind tunnel”.

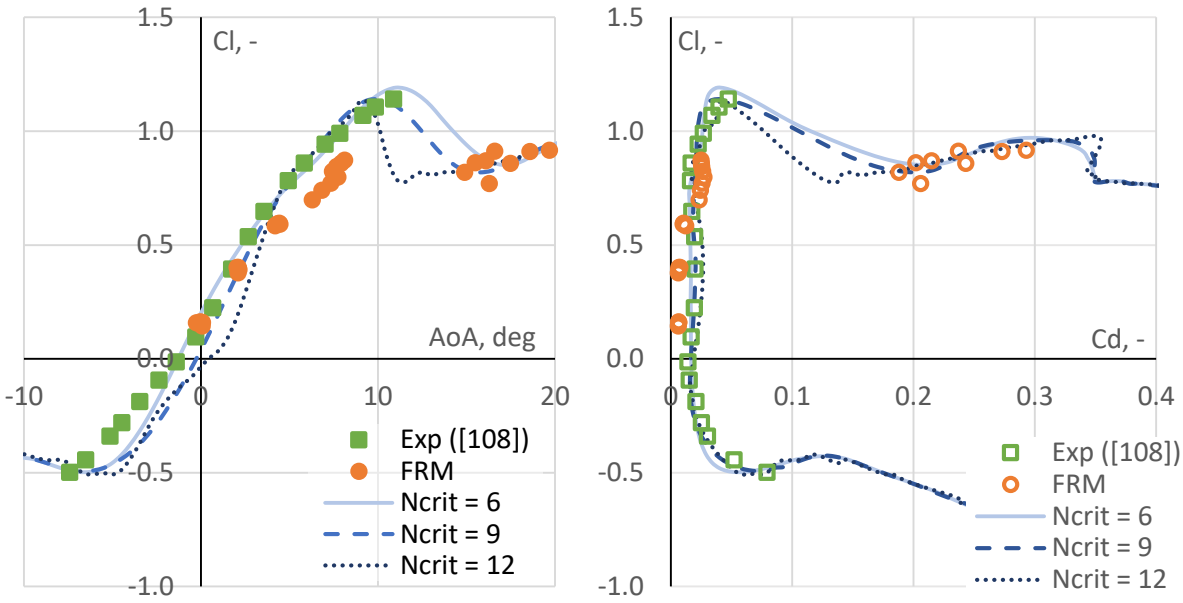

Fig. 53 SG6041 Cl as a function of AoA (left) and Cd (right) for Re ≈ 100 000 from experiment (green, [108]), FRM (red) and XFoil at different Ncrit (blue lines)

None of the numerically-obtained characteristics follows the experimental data exactly. As seen in the Cl(AoA) graph, when Ncrit increases, the values of Cl are globally higher, while Cd – lower. Also, for higher Ncrit the stall is shifted towards lower AoA. These are sensible observations, as with higher Ncrit the aerofoil operates in unstable, laminar-turbulent transitional regime, as opposed to the more stable, fully-turbulent regime for lower Ncrit values.

For Ncrit equal to 12 the obtained data is characterised by relatively rapid (at 9°) and deep stall. This also influences the Cl(Cd) curve, as visible for positive Cl and Cd in the range (0.04, 0.18). Aerofoil performance is globally significantly lower than for other XFoil or experimental data, as suggested earlier. Moreover, the performed XFoil simulations showed relatively high instability. These observations generally hold true for other examined values of Ncrit higher than 9, which were hence declared an unfavourable choice.

The aerofoil performance datasets obtained for Ncrit equal to 6 and 9 are very similar to one another, particularly in the linear part of the Cl(AoA) characteristic. Ncrit equal to 9 is relatively closer to experimental results in the positive AoA range of Cl characteristic linear part. However, when approaching the stall conditions, the model loses the superiority and underpredicts both the stall AoA and maximum Cl. The post-stall aerofoil for Ncrit = 9 is also lower than for 6. Both of the discussed Ncrit values were deemed a favourable choice in further simulations, with a particular interest in Ncrit = 6.

Cl and Cd curves for both examined aerofoils used in the ADM simulations at Ncrit = 6 are seen in Fig. 54. Presented data includes curves for various Reynolds numbers. With increasing Re, the global values of Cl increase, while Cd – decrease. At this range of values of Reynolds number and aerofoil thickness-

to-chord ratios this behaviour is reasonable, as the boundary layer flow passes into the fully turbulent regime [112].

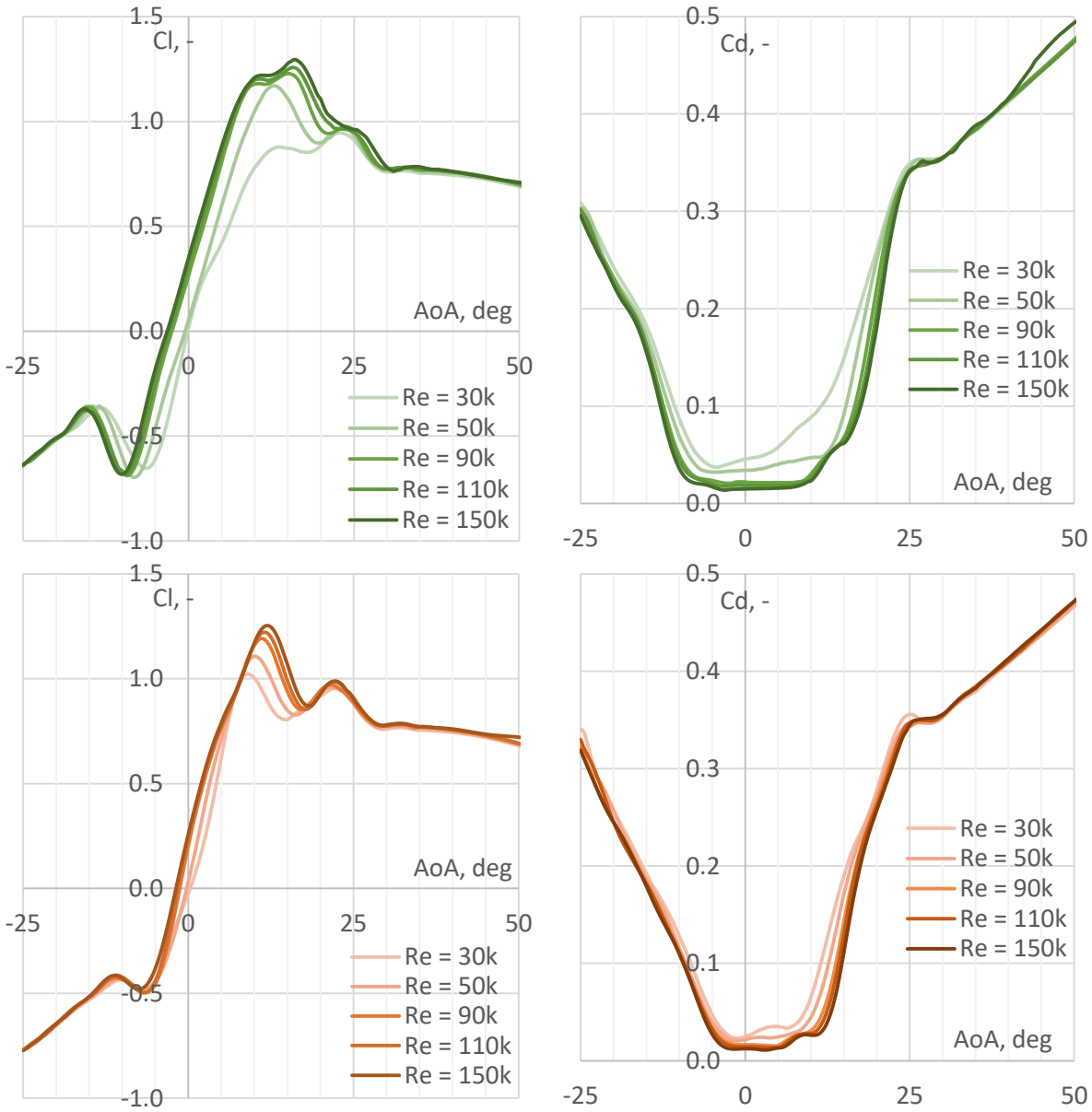

Fig. 54 Cl (left) and Cd (right) vs AoA for SG6040 (top, green) and SG6032 (bottom, red); XFoil data for Ncrit = 6, different Reynolds numbers as used in ADM simulations

In total, the aerofoil performance data used in the analysis was collected at 8 different Re values: 10 000 to 150 000, with interval of 20 000. This corresponds roughly to the Re range observed for all the simulations. However, since at very low Reynolds number the ability of XFoil to predict accurate aerofoil performance data is limited, it was necessary to evaluate the influence of the used Re range on the final results. The power curves for a DAWT case with various Ncrit values and different minimal Reynolds number value are presented in Fig. 55. As the minimal value of Reynolds number increases, an increase in maximum Cp and Ct is visible. The discrepancies between dataset obtained with minimum Reynolds number of 90 000 (Re90k+) and experimental results are relatively high (up to 14%). For Re10k+ and Re50k+ these differences are less significant and amount to about 7%. All models overestimate Cp at TSR higher than optimal. They also tend to underestimate Ct at low rotational velocities, for approximately TSR < 4. This resonates with observations made with FRM simulations. An

additional comment must be given for results obtained with Re10k+ calculations. Even though the simulation tends to give satisfactory results, the model's behaviour is highly instable. This may be attributed to the fact that the differences between polar plots for Re = 10 000 up to 50 000 are much higher than between polars for higher Re. Thus a small change in flow velocity may trigger significant changes in Cl and Cd, and consequently the source terms. This is why Re10k+ model was deemed an unfavourable choice.

In all the chosen polar data will be that for Ncrit = 6 and minimal Reynolds number 50 000. As seen in Fig. 55 this combination proves to give results coherent with experimental data in the widest range of all other configurations. The aforementioned considerations should a priori be correct for the twin-rotor system. The downstream rotor will operate at increased turbulence intensity conditions, for which low Ncrit should give more reasonable results than default values.

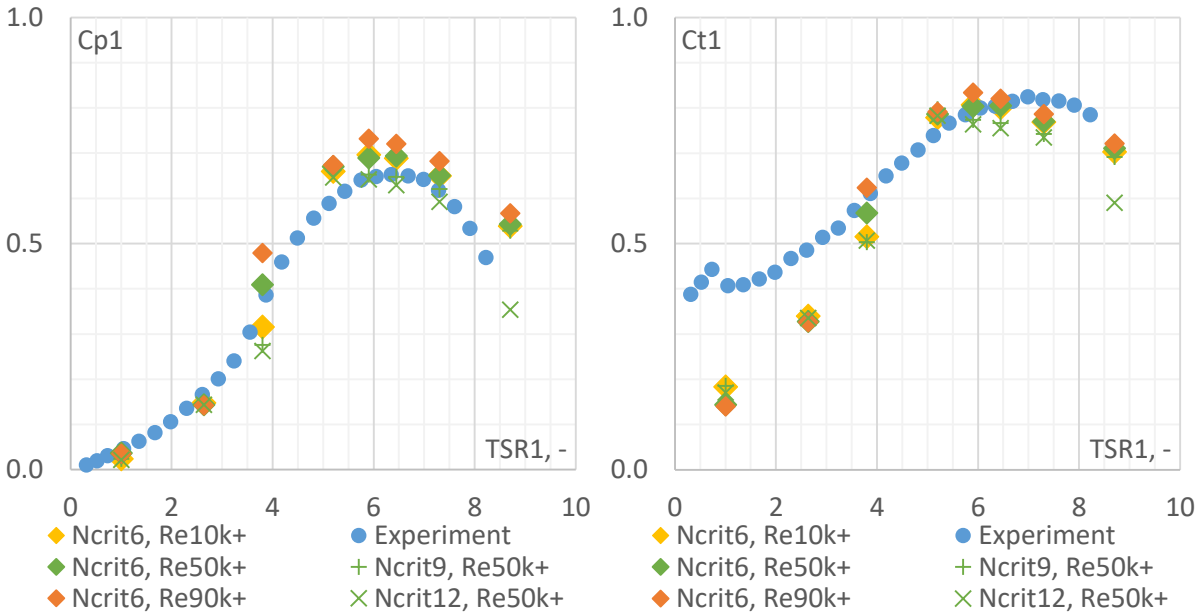

Fig. 55 Experiment (blue) vs. ADM simulation at different Ncrit and minimum value of Reynolds number, comparison of Cp (left) and Ct (right) for DAWT

6.3. Preprocessing schemes

This Section presents the hybrid simulation domain geometry and simulation definition.

6.3.1. Simulation domain

Geometry and boundary conditions of the ADM simulation domain are the same as those of the FRM model. The domain is composed exclusively of the stationary part (see Subsection 5.2.1). The CFX opening boundary conditions were set to pressure-outlet type, which also enables backflow.

The rotors are represented as disk-shaped surfaces directly embedded in the domain, in the rotor PoR. Hence no hollow cylinder spaces are present in this case. The disks mimic the rotor swept area, hence their radius R is equal to 0.16 m. The domain overview is visible in Fig. 56.

The mesh was created using the same paths as the FRM mesh, but with higher element sizing (the mesh is relatively coarser). This choice was made to make the computation problem less time- and resource demanding, which resonates with the main features of the hybrid model. Number of mesh nodes is equal to $4.3 \cdot 10^6$, while elements: $17.0 \cdot 10^6$.

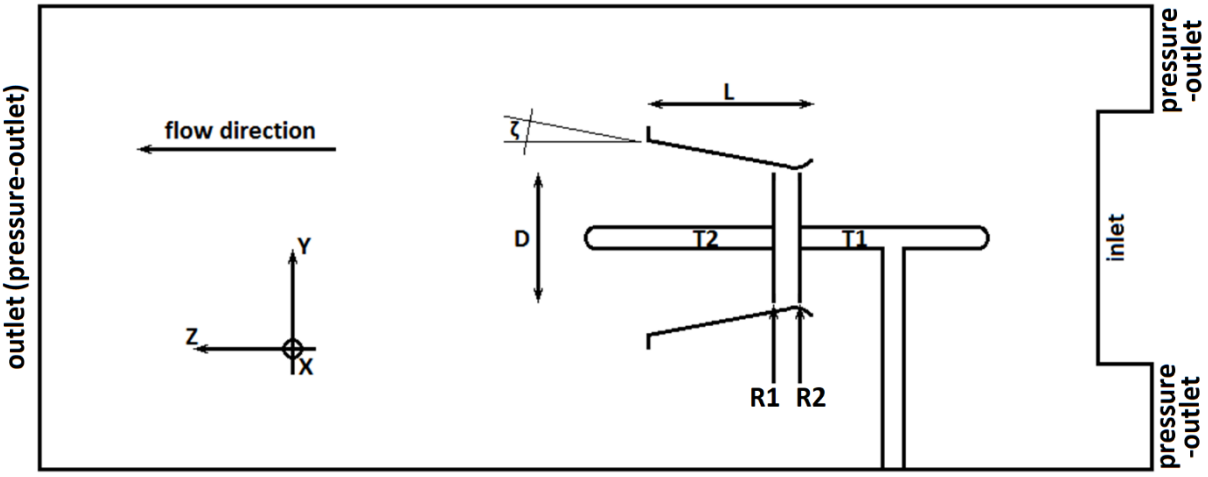

Fig. 56 Section view of the stationary domain geometry and boundary conditions in ADM CRSR case; all unmarked faces are no-slip walls

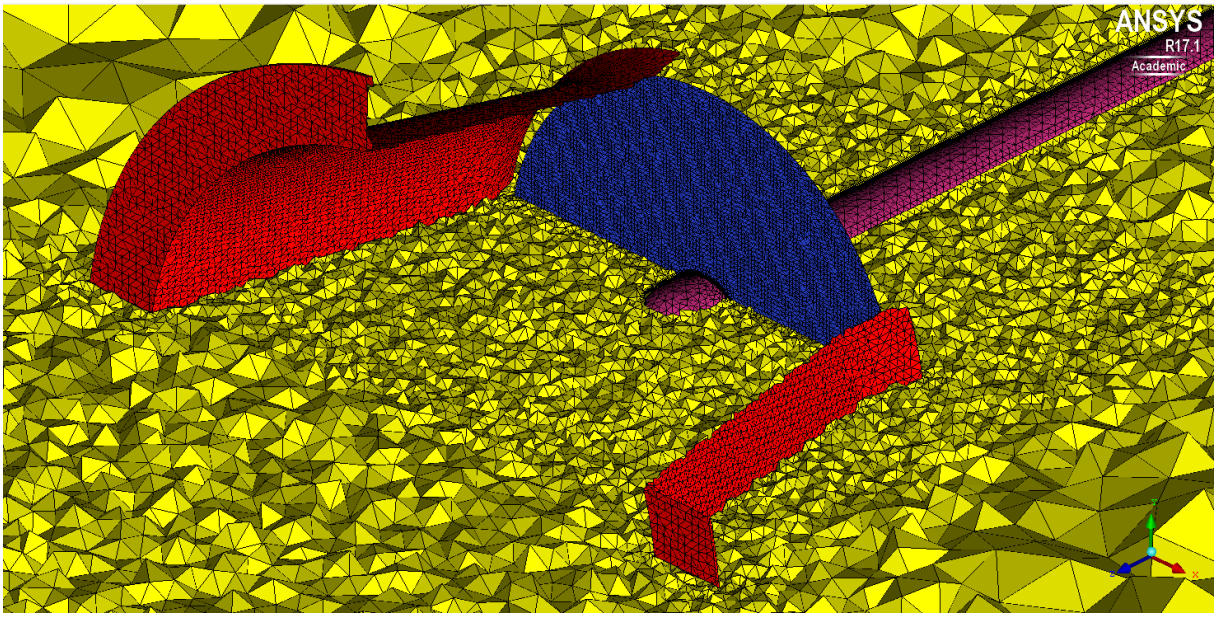

Fig. 57 Horizontal section (yellow, y = 0 m) view of the stationary domain mesh in rotor vicinity in DAWT simulations; actuator disk marked blue, diffuser marked red, T1 test stand marked pink

6.3.2. Simulation setup

The simulation is conducted as steady-state RANS. The solver is of pressure-based type. A separate study was performed to choose the pressure-velocity coupling algorithm. Time-to-results and overall simulation stability were identified as the most significant factors.

The first tested coupling scheme was pseudo-transient, directly coupled one. For the basic scheme it was observed that the simulation convergence level and rate were relatively poor, even despite decreasing the under-relaxation factors (down to 0.3 for both momentum and pressure equations). A pseudo-transient approach with different timescale factors was tested. This would result in higher level of convergence, but the monitored parameters (Cp, Ct) would not stabilise in course of the iterating calculations. To decrease time-to-results, the segregated schemes (SIMPLE, PISO) were tested, with standard under-relaxation factors. The differences between these approaches were not significant, with convergence level and rate remaining almost the same in all cases. It was observed that PISO and SIMPLE-Consistent schemes with standard coefficients would occasionally increase the monitored

parameters' instability. Hence SIMPLE scheme was chosen as the most conservative one. In order to decrease the calculation time the under-relaxation factors were modified, but this proved to be unusable due to resulting simulation divergence.

Having in mind the above mentioned, SIMPLE pressure-velocity coupling scheme with standard set of under-relaxation factors was employed. Second order spatial discretization was used for solution of both flow and turbulent quantities' equations. The fluid definition is the same as in the FRM simulations (Tab. 6). The simulation is isothermal.

6.4. Model evaluation

Whenever CRSR is considered the evaluated model is for rotor separation distance a (0.1D).

6.4.1. Numerical verification

Rudimentary tests of the numerical correctness of the obtained results were performed.

The developed hybrid model is primarily meant for a fast, robust calculation of wind turbine characteristic. Thus the accurate resolution of flow phenomena, such as far-wake development, are of secondary interest as long as the model is capable of predicting reliable rotor performance data. Hence a relatively high level of simulation residuals may be acceptable as long as the model ensures repeatable results coherent with experiment. As can be seen in Fig. 58 the residuals of momentum and turbulent quantities transport equations level-off at order of magnitude of 10^{-4} – 10^{-3}. The residuals of the continuity equation, however, remain at the level of 10^{-2}. The reason for this behaviour may be connected with the singularity effect, associated with the model. The source terms for the Navier-Stokes equations in every iteration are computed based on the local velocity value, computed previously. However, these source terms will modify the local velocity field for the next iteration, hence introducing an additional instability.

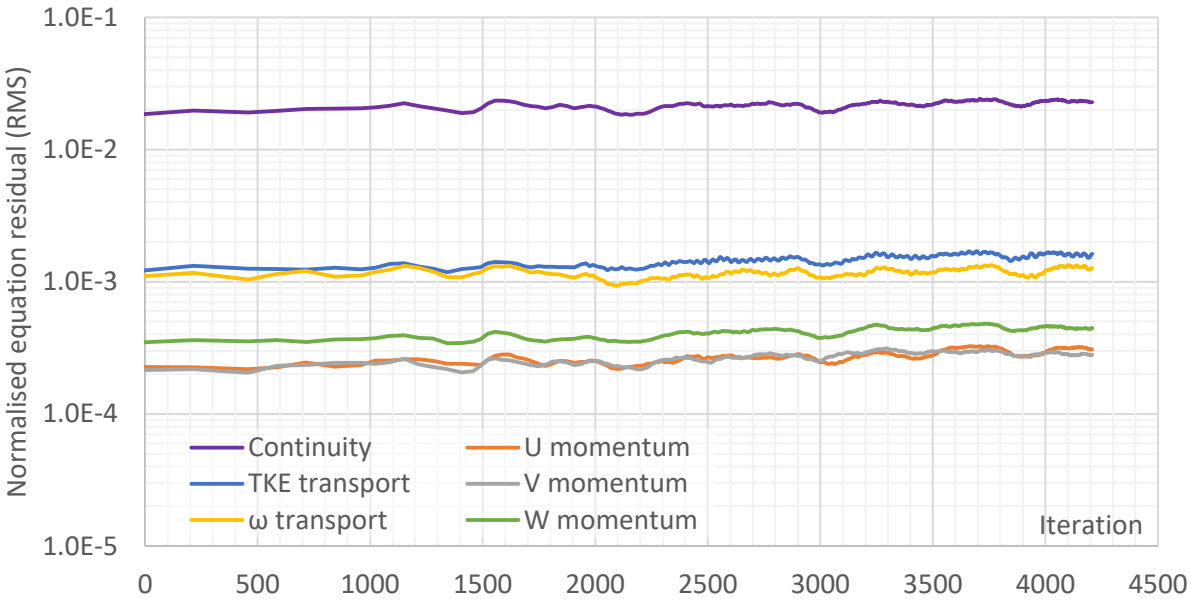

Fig. 58 Evolution of normalised equation residuals during CRSR simulation (TSR1 = 6.39)

The aforementioned phenomenon is well visible while monitoring the evolution of Cp and Ct during the calculation process (see Fig. 59). The model operates in automatic manner - TSR1 remains constant, while TSR2 is increased when Cp and Ct are stabilised or until 750 iterations are computed. The model

then uses the previously computed results as initial conditions for the next TSR2 simulation. It is visible that the R1 results fluctuate modestly, as compared to the R2. The limit of 750 iterations has been chosen basing on the rudimentary tests performed on the model and proves to be an appropriate amount to ensure the proper estimation for Cp, Ct for both rotors.

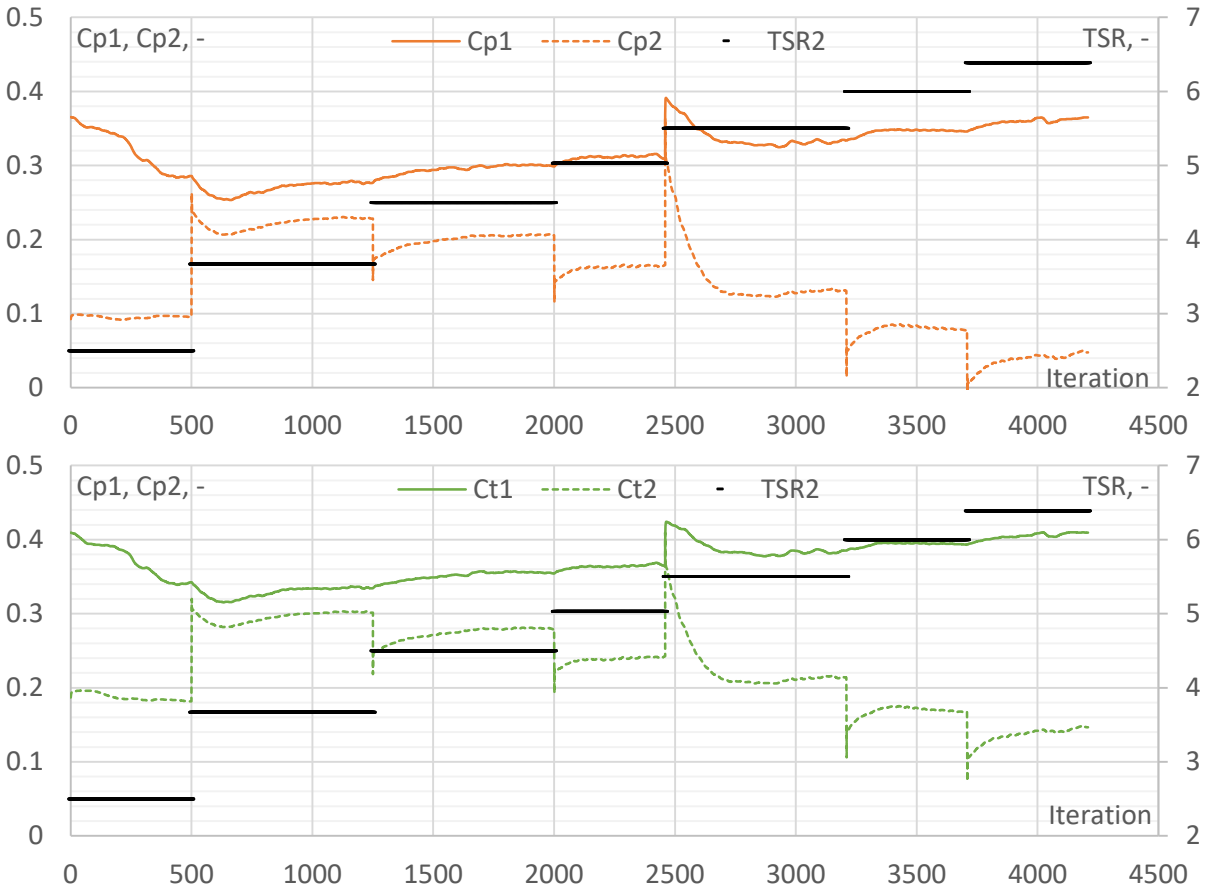

Fig. 59 Cp (top) and Ct (bottom) evolution during calculation for R1 (continuous) and R2 (dashed); black dots denote a TSR2 value at the current iteration; CRSR, TSR1 = 3.67

To check the solution quality in boundary layer y+ on selected surfaces (Fig. 60) and flow character in diffuser boundary layer (Fig. 61) have been analysed. Y+ is smaller than 2 at the integrity of analysed surfaces, which ensured a proper resolution of the boundary layer flow. This is reflected in vector field, with vector length diminishing towards diffuser surface. It could be argued that the vectors inside diffuser do not fully reach the ambient conditions outside boundary layer. However, prolonging the mesh inflation zone in this region would result in high computational effort increase and deterioration of element quality at curvatures and edges (notably diffuser inlet), thus actually decreasing the solution quality.

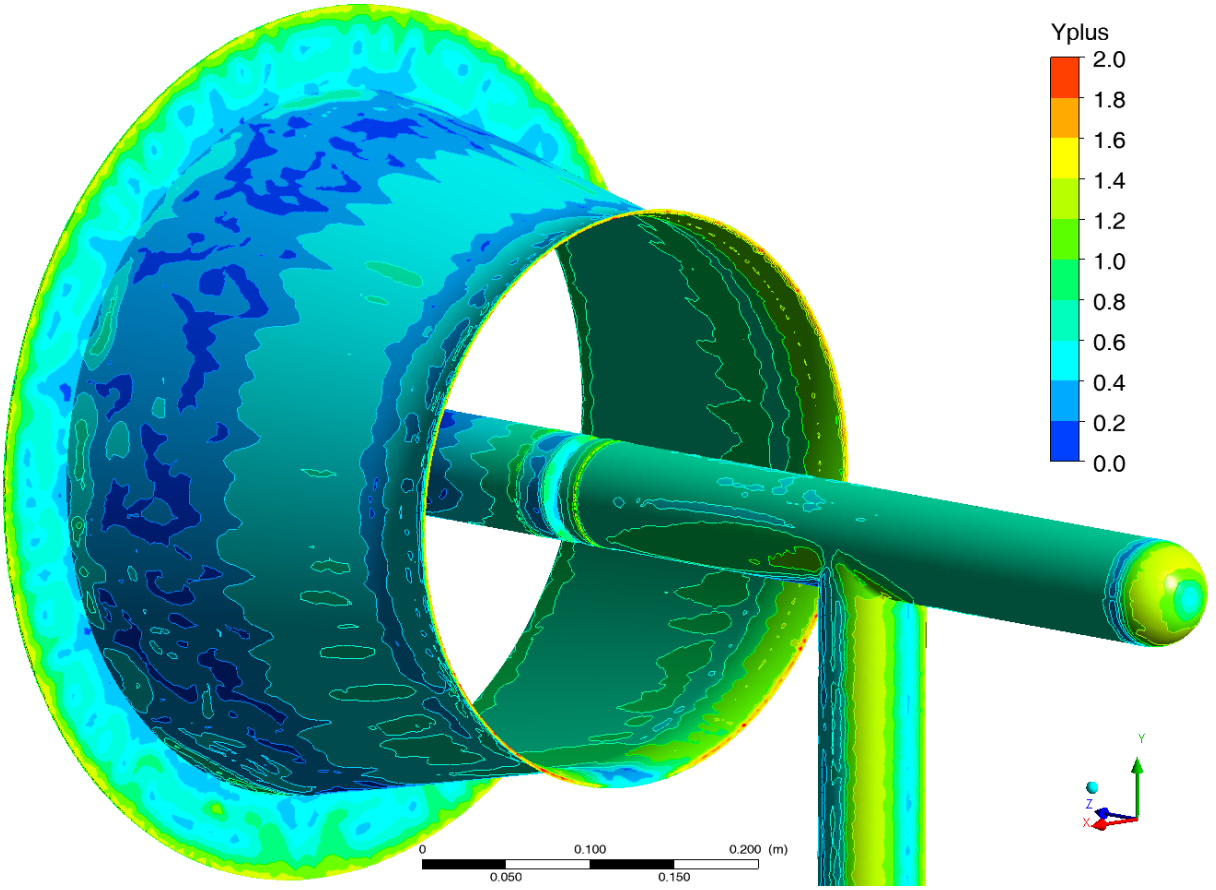

Fig. 60 Y+ distribution on the surfaces of test stands and diffuser; CRSR, TSR1 = 3.67, TSR2 = 3.45

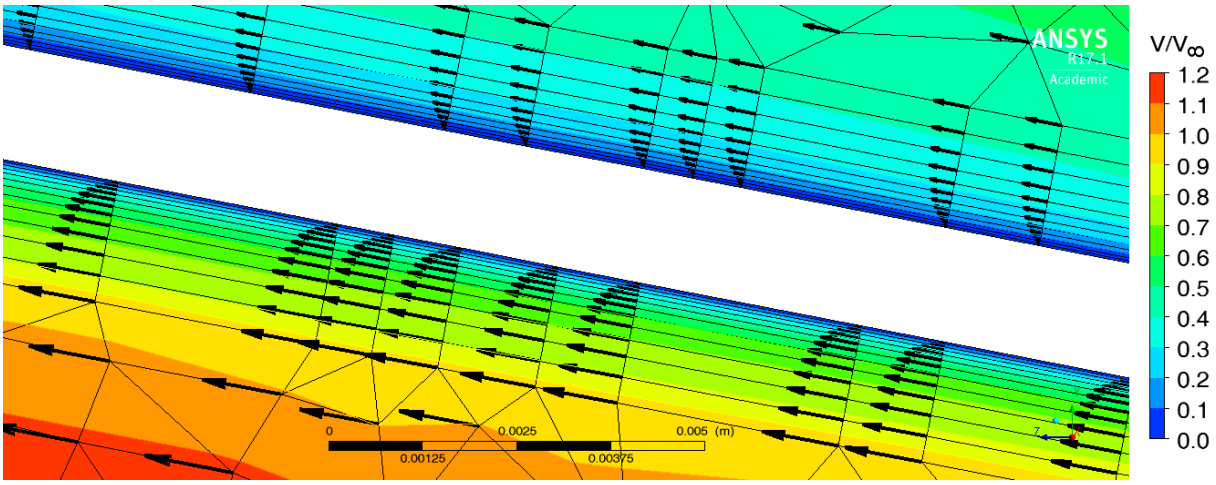

Fig. 61 Flow in boundary layer at diffuser surface: normalised velocity contour and velocity vectors fields; thin black lines denote mesh cell boundaries; CRSR, TSR1 = 3.67, TSR2 = 3.45

6.4.2. Experimental validation, comparison with FRM

The first stage of comparison between experiment and simulation was already performed in Section 6.2 (Fig. 55), where wind tunnel results were compared with numerical analyses for different Reynolds numbers and XFoil Ncrit parameter in DAWT analysis. The model has shown an overall good qualitative and quantitative performance in assessing Cp. For Ct the model's overall behaviour can be deemed satisfactory. The results for TSR < 4 differ significantly from the experimental data, yet

comparing with literature (see e.g. [27]) the behaviour of experimental data may be described as unconventional, while the numerical results tend to be much more conservative.

Figure 62 compares Cp1 (top), Cp2 (middle) and Ct1 (bottom) interpolated results from experiment (left) and ADM simulation (right) for CRSR case. First of all it is visible that the ADM simulations preserve the saddle-like shape of characteristics for both rotors. The structure is well represented for Cp and Ct datasets, with inflection zones located at approximately the same TSR1 and TSR2. Cp1 and Ct1 attain local maxima along TSR1 = 5 for experiment, and about 4.5 for ADM simulation. For Cp2 values the same is seen at approximately TSR2 = 4 – 5 for both experiment and simulation. The above observations permit to state already that the actuator model gives qualitatively good results and is able to depict the twin-rotor system operation properties. This is more important, as the considered case (shrouding, low separation distance) is possibly the most difficult one due to the strong interference between rotors and simulation convergence issues.

It is noticeable that the simulation results for the upstream rotor attain globally lower values than those from experiment. This holds true for both Cp and Ct, and in the entire range of TSR1 and TSR2. One of the reasons for this behaviour could be the underestimation of the flow velocity through diffuser (and consequently the rotor) by the numerical model. This is the more probable since, as stated above, the optimal TSR1 is shifted towards lower values than the experimental ones. The reason for this is most probably the underestimation of the axial velocity component (flow velocity through rotor); and more profoundly - the underestimation of the mass flow rate through diffuser. In a classic diffuser this would be associated with flow separation inside diffuser, but investigation of pressure and velocity fields (in DAWT simulation) show no detachment. Instead, the difference seems to come from the diffuser brim. The underpressure zone it creates is bigger and more profound in case of FRM simulation, which can be a reason of increased suction through the inside of diffuser.

For the downstream rotor the ADM simulation is able to depict the quantitative experimental results very accurately and in the entire TSR1 and TSR2 ranges.

Figure 63 compares the radial distribution of axial velocity along a line at angular position $\varphi = 90°$ (vertical in the upper half of the rotor). Once again it is visible that ADM tends to underestimate the axial velocity value with respect to FRM. For the upstream rotor this difference is in average about 1.5% and is distributed relatively uniformly along the blade span. For downstream rotor it is 2% and grows more important towards tip blade. The developed tip loss correction gives a relatively good performance. The axial velocity at the upstream rotor PoR is overestimated in the outermost 10% of blade length by 2 – 4%, which can be judged as a very good performance. In case of the downstream rotor this difference is about 6 – 8%, but it is visible that for both analysed cases the ADM and FRM curves follow almost the same trace, with ADM shifted towards higher velocity values.

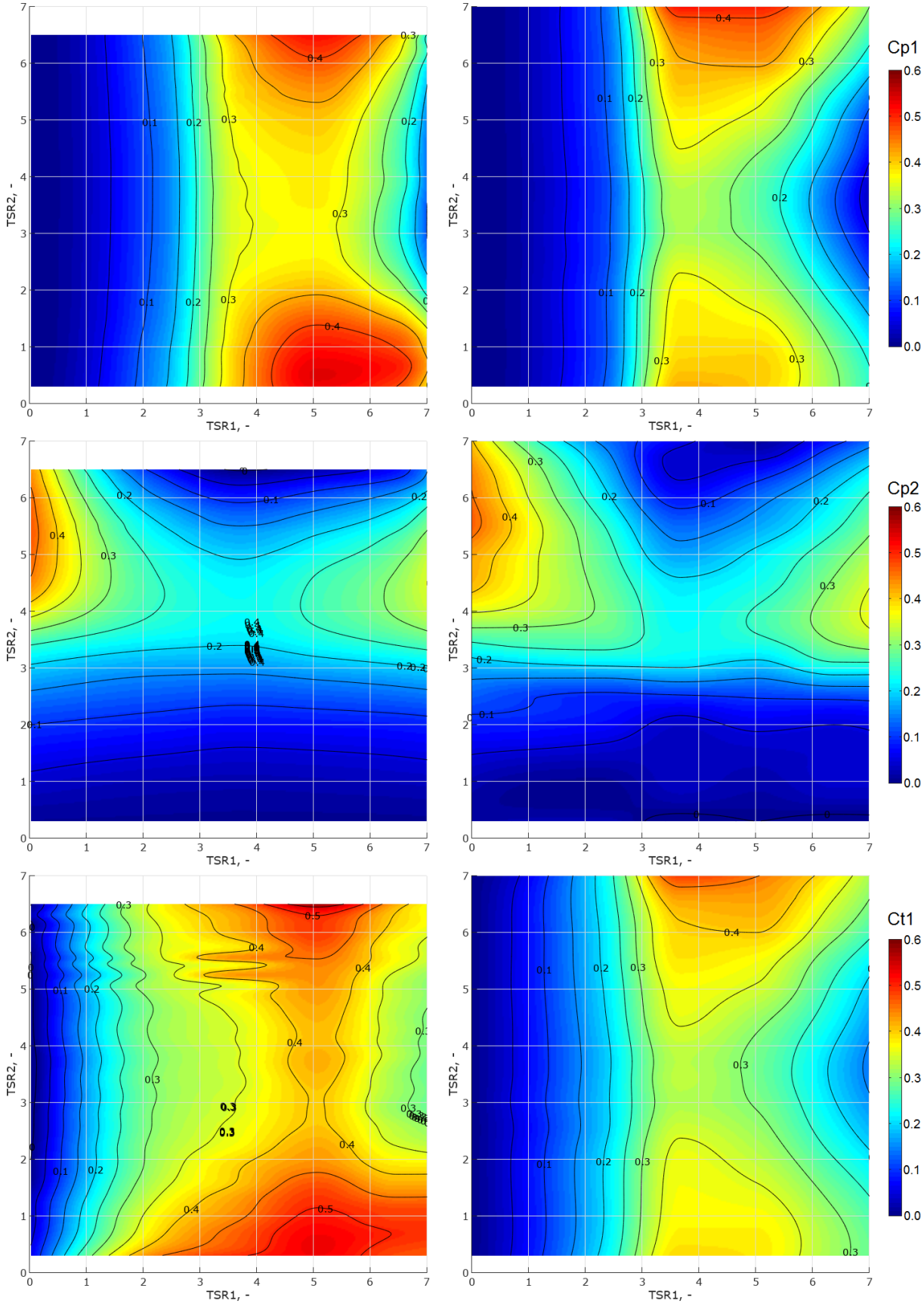

Fig. 62 Cp of R1 (top) and R2 (middle) and Ct of R1 (bottom) as function of TSR1 and TSR2; experiment (left) vs. hybrid simulation (right), CRSR

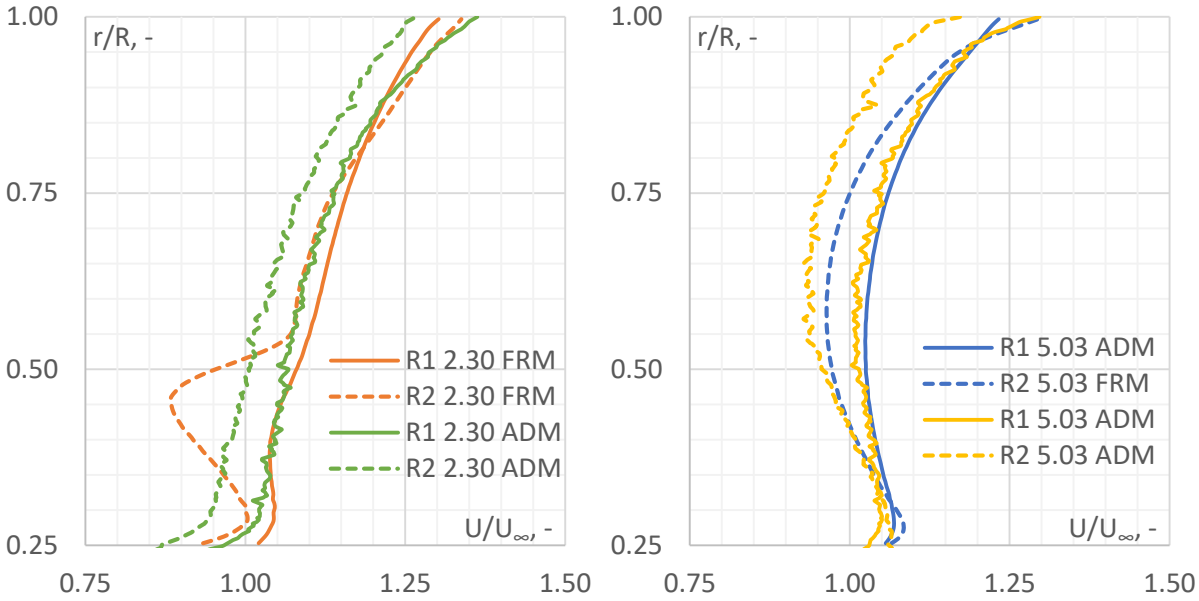

Fig. 63 Bladewise distribution of normalised axial velocity for FRM (time-averaged, continuous line) and ADM (dashed line); CRSR cases: TSR1 = 2.3 and TSR = 2.3 (left) and TSR1 = 5.03 and TSR = 5.03 (right)

Lastly, Fig. 64 compares the normalised axial velocity fields for R1 and R2 from AD and FRM. Once again, a very good coherence between the two modes is visible especially for the upstream rotor, where differences are of order of magnitude 1 – 2% for majority of rotor area. For downstream rotor the difference is more significant, especially in the middle part of the blade, where it can be up to about 5%.

To sum up, the two-stage evaluation of solution results quality proves that the developed hybrid model is capable of reproducing the wind turbine performance results observed in experiment. Although some simulation flow equation residuals attain relatively high values, this is deemed acceptable due to the model's robust ability to assess rotor performance. Comparison of velocity distribution with FRM simulations show that the model is capable to reproduce the physical conditions at which the model operates. In conclusion, the model is deemed fit for quantitative assessment of wind turbine performance and qualitative analysis of selected flow phenomena. Thus the second scientific objective of the thesis is fulfilled, that is a creation of a ameliorated hybrid simulation model for two counter-rotating shrouded wind turbine rotors and its validation.

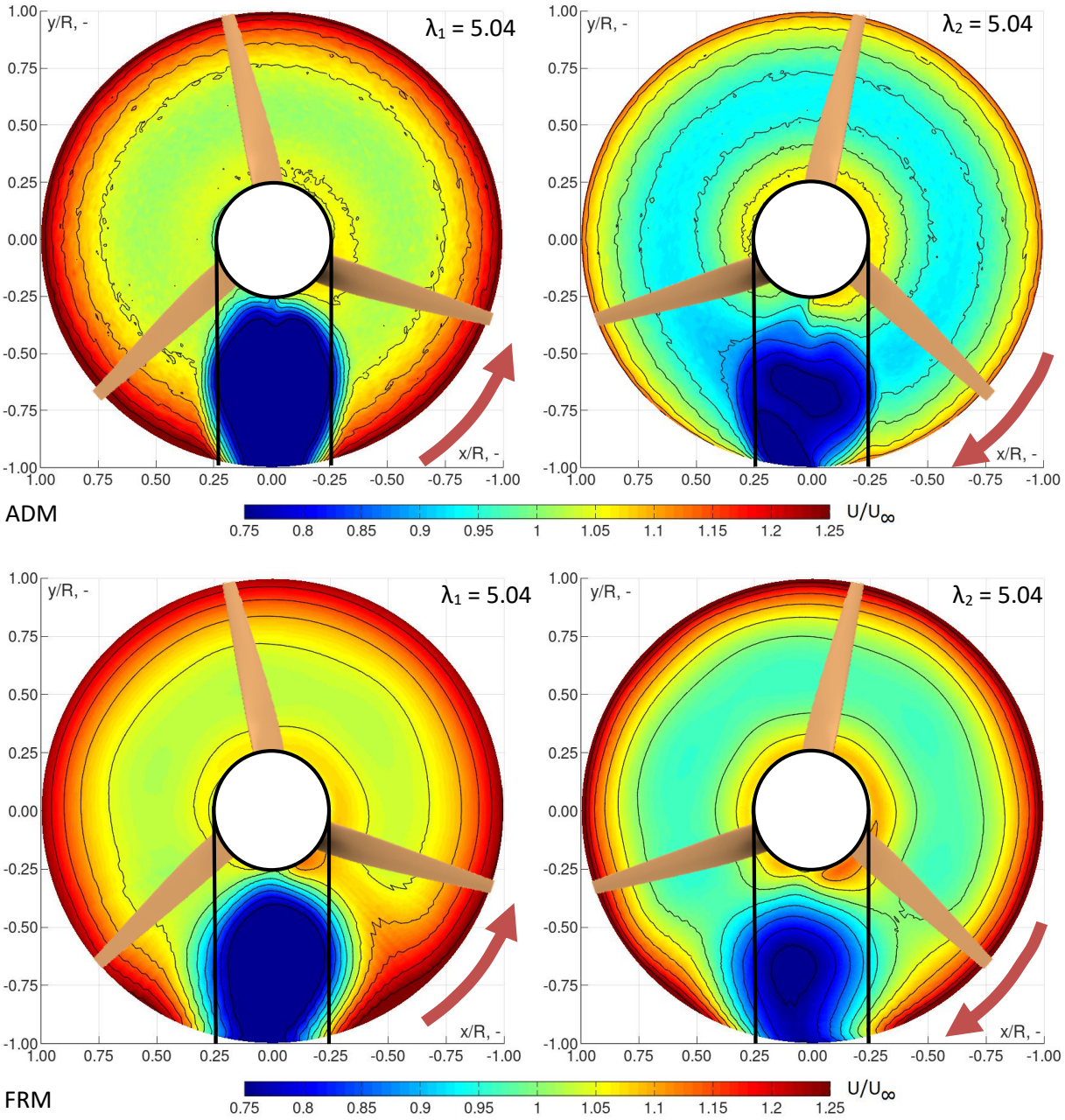

Fig. 64 Normalised axial velocity fields in PoR of R1 (left) and R2 (right) from ADM (top) and FRM (bottom); CRSR, TSR1 = TSR2 = 5.03

7. Discussion - case study: CRSR wind turbine

The Counter-Rotating Shrouded Rotor wind turbine system presents an interesting problem for general flow and performance assessment. Since the model has only been validated from the point of view of rotor performance, the flow investigation has to be limited to qualitative study. Probing locations for this study, referred to as a – d, are marked red in Fig. 65.

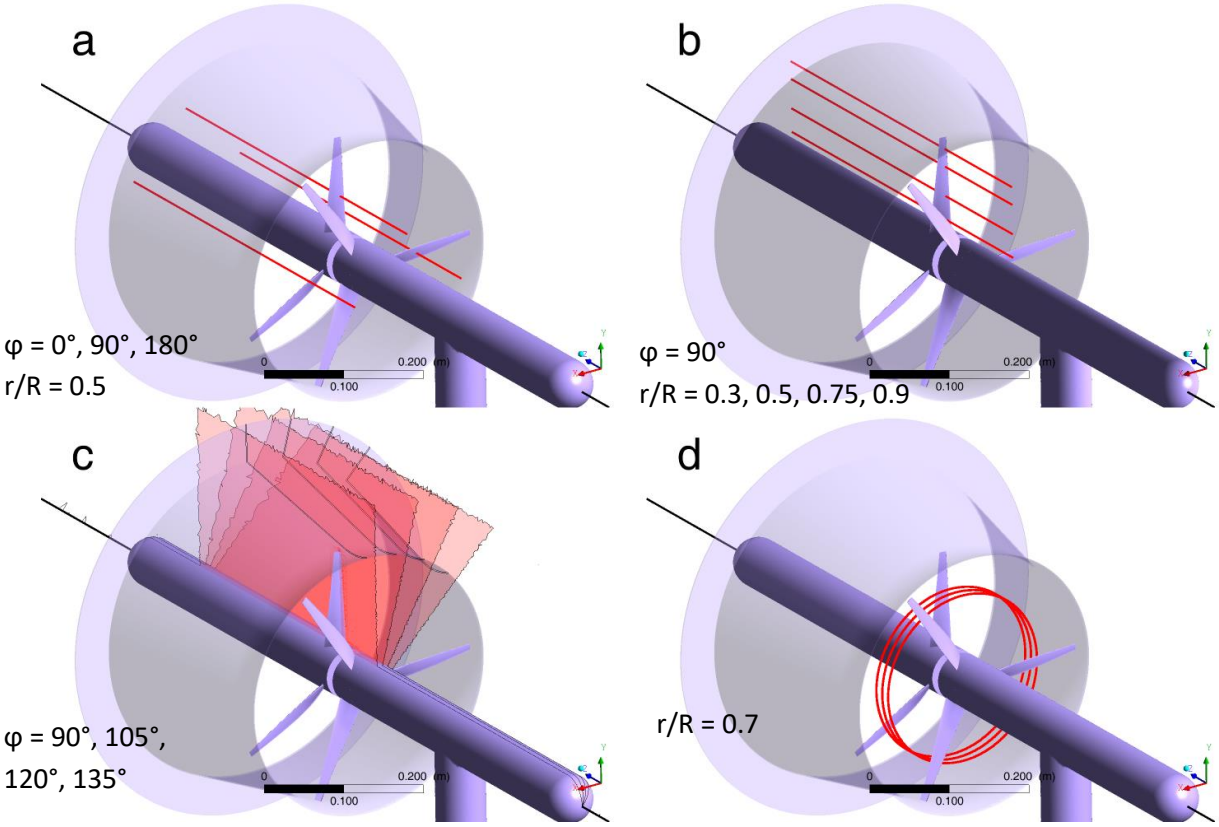

Fig. 65 Probing locations (red)

7.1. CRSR performance assessment (ADM, experiment)

Figure 66 presents the results of CRSR system operating points (i.e. when the sum Cp1 + Cp2 attains its maximum value) for different rotor separation distances. TSR (left) and Cp (right) results of distinct rotors are presented for ADM (green/red) and experiment (blue/yellow). The optimal TSR1 remains mostly at a stable level of 5.1 – 5.3, regardless of the distance between rotors. The only difference is at the lowest separation distance. A closer assessment of the upwind rotor operation in this case revealed that TSR1 range for which total Cp of the system is relatively wide (approximately 3 – 6). The values obtained for TSR1 = 5.1 are lower only by approximately 1%, which is in range of error of the simulation.

In turn, the optimal TSR2 becomes lower as l/D increases. This is a rational observation - as the downstream rotor moves farther from the diffuser inlet, the axial velocity component decreases due to stream expansion. As a consequence, the optimum rotational velocity must also be lower, influencing TSR2.

At low rotor separation distance both wind turbines have a very similar Cp (of order of magnitude of 0.2 – 0.3). The difference grows more important as the downstream rotor is pushed towards the

diffuser outlet. Optimum Cp1 increase rate is very similar to Cp2 decrease rate. As a result, the sum Cp1 + Cp2 remains roughly constant in the considered l/D range. Relatively lower values are spotted as downstream rotor is placed approximately half-way through the diffuser.

Although the ADM results follow the general trends observed in the experiment, significant quantitative differences may be spotted. This is especially noticeable for Cp values. They are relatively well depicted at low separation distance, but the simulation underpredicts the upstream rotor performance and, consequently, overpredicts the downstream rotor performance as the separation distance becomes greater. The increasing complexity of the flow character when approaching the diffuser outlet may be an explanation for this behaviour. Some examples include the influence of the helical wake (see further on) and low-pressure zone downstream the brim. These factors affect the flow stability, but also increase the turbulence intensity, changing the aerofoil characteristics. A remedy for that might be an additional correction of the aerofoil polar data, taking into account the local turbulence intensity, especially at the downstream rotor.

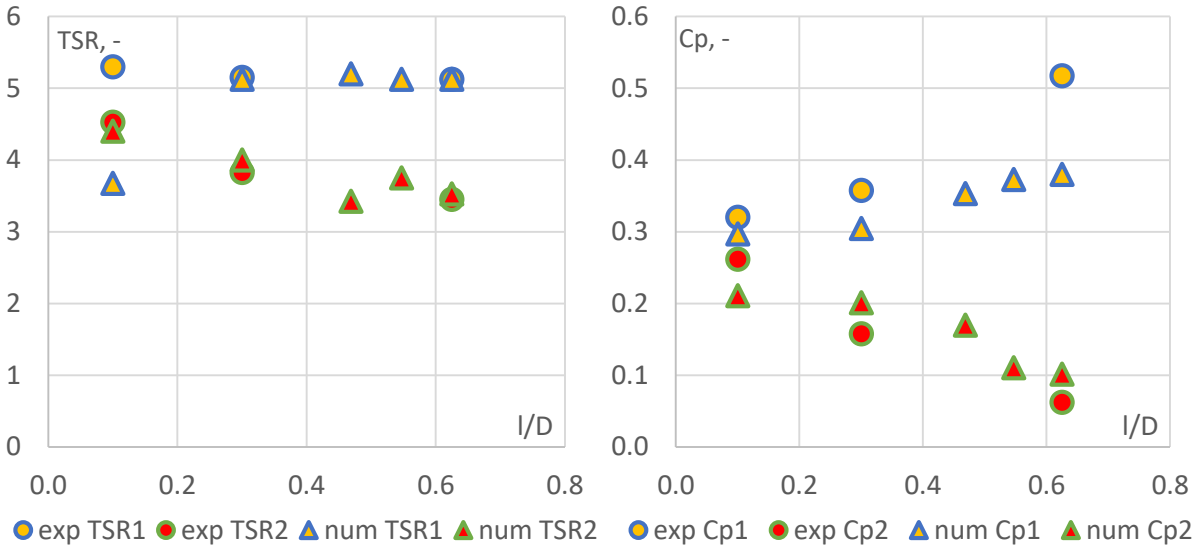

Fig. 66 TSR (left) and Cp (right) of distinct rotors when total Cp of the CRSR system is maximum, as a function of separation distance l/D; experiment (blue/yellow) vs. ADM (green/red)

Figure 67 shows available Ct data and Cp1/Cp2, Ct1/Ct2 ratios of the system when total Cp of the CRSR is maximal. As for the Ct data roughly the same comment may be stated as for the Cp results. It is worthy of note that the maximum total Cp occurs at TSR1 approximately 1% lower and TSR2 1.5% higher than the maximum total Ct, which are marginal differences.

Cp1/Cp2 and Ct1/Ct2 relationships for which the total Cp of the system attains its maximum value permit to evaluate how to distribute the loads between the two rotors of the wind turbine in order to maximise the performance of the system. It is seen that, as the distance between the two rotors increases, most of the aerodynamic effort is taken by the upwind rotor. This is an adverse phenomenon from the mechanical point of view, since the two rotors would experience different deformation in operation.

To conclude, it may be said that the best location for the downwind rotor among all tested alternatives is near the diffuser inlet. This ensures relatively uniform distribution of Cp and Ct and preserves a high total Cp of the system.

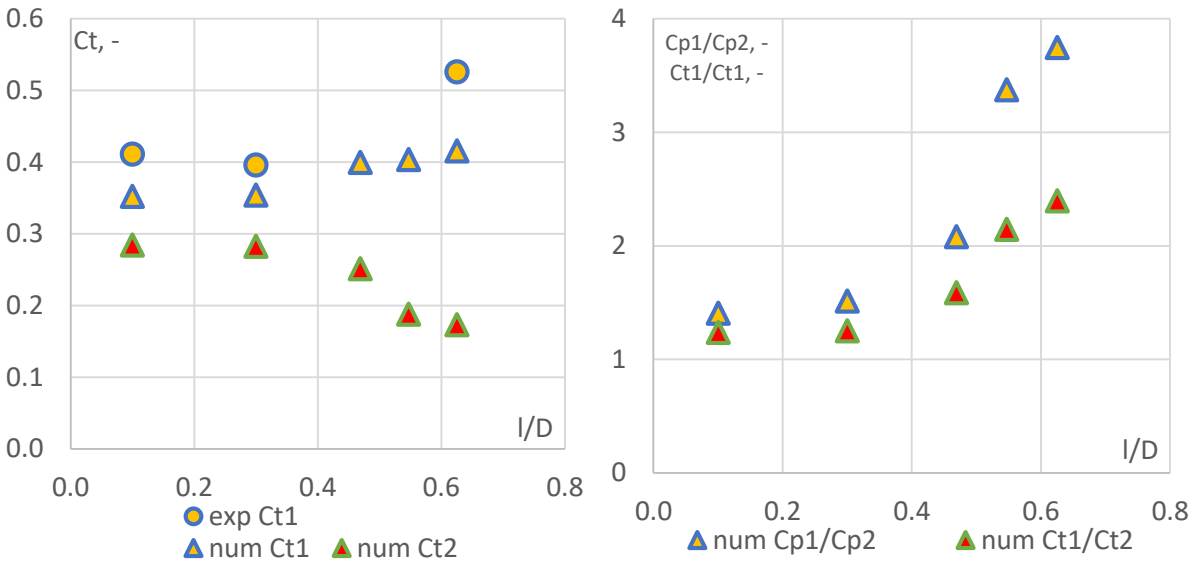

Fig. 67 Ct of the distinct rotors (left) and Cp1/Cp2, Ct1/Ct2 ratios (right) when total Cp of the CRSR system is maximum, as a function of separation distance l/D; experiment (blue/yellow) vs. ADM (green/red)

7.2. Time-averaged flow fields (ADM, FRM)

The FRM results presented in this chapter are time-averaged over one full turn of the upstream rotor.

To study the flow evolution in the streamwise direction, Fig. 68 shows the distribution of normalised axial velocity U/U_∞ (top) and pressure coefficient cp (bottom) at r/R = 0.5 and angular locations - 90°, 0°, 90° (a in Fig. 65). Upstream a bare rotor a wind speed deficit and underpressure zone are observed (see Fig. 13). In the case of a shrouded rotor, placed at the diffuser inlet, this phenomenon is not observed.

It was shown previously that the effect of wind speed increase is globally lower in case of CRSR than for DAWT (see Subsection 5.4.1). In the cp graph the pressure drop is divided into two stages, that is the upstream and downstream rotor. Since the upstream rotor is forced to operate under the rated TSR, the pressure drop is accordingly lower. This causes that the maximum pressure deficit region is shifted downstream and attains lower absolute numbers than in comparable case of DAWT (see ex. [92]). The effect of underpressure zone at diffuser inlet is thus decreased, consequently decreasing its potential to increase the mass flow rate through wind turbine rotors. As the downstream rotor is shifted downstream, the underpressure zone at the inlet is deepened, thus increasing the mass flow rate through the upstream rotor and – consequently – its Cp. This is a very interesting observation, leading to the conclusion that the downstream rotor operation may alter the development of pressure deficit zone at diffuser inlet. Referring to literature [73] it is possible to imagine a solution in which, instead of shifting the two rotors away from each other, the distance between them is actually decreased to a very low value. This would result in concentrating the pressure drop at the vicinity of diffuser inlet and might result in increased mass flow rate through diffuser.

Comparison of ADM and FRM results shows that for the velocity there is a very good correlation up to z/D ≈ 0.5. Further downstream the flow predicted by URANS FRM simulation becomes very much dependent on the angular position of the probing line, suggesting that the unsteady wake phenomena play an increasingly important role. This is not visible in case of ADM simulations, in which the streamwise distributions of the normalised velocity bear much more resemblance, regardless of the

probing line locations. The similar comments may be made for the cp(z/D) relationship. It is also noticeable that the ADM simulation underpredicts the pressure drop at both rotors.

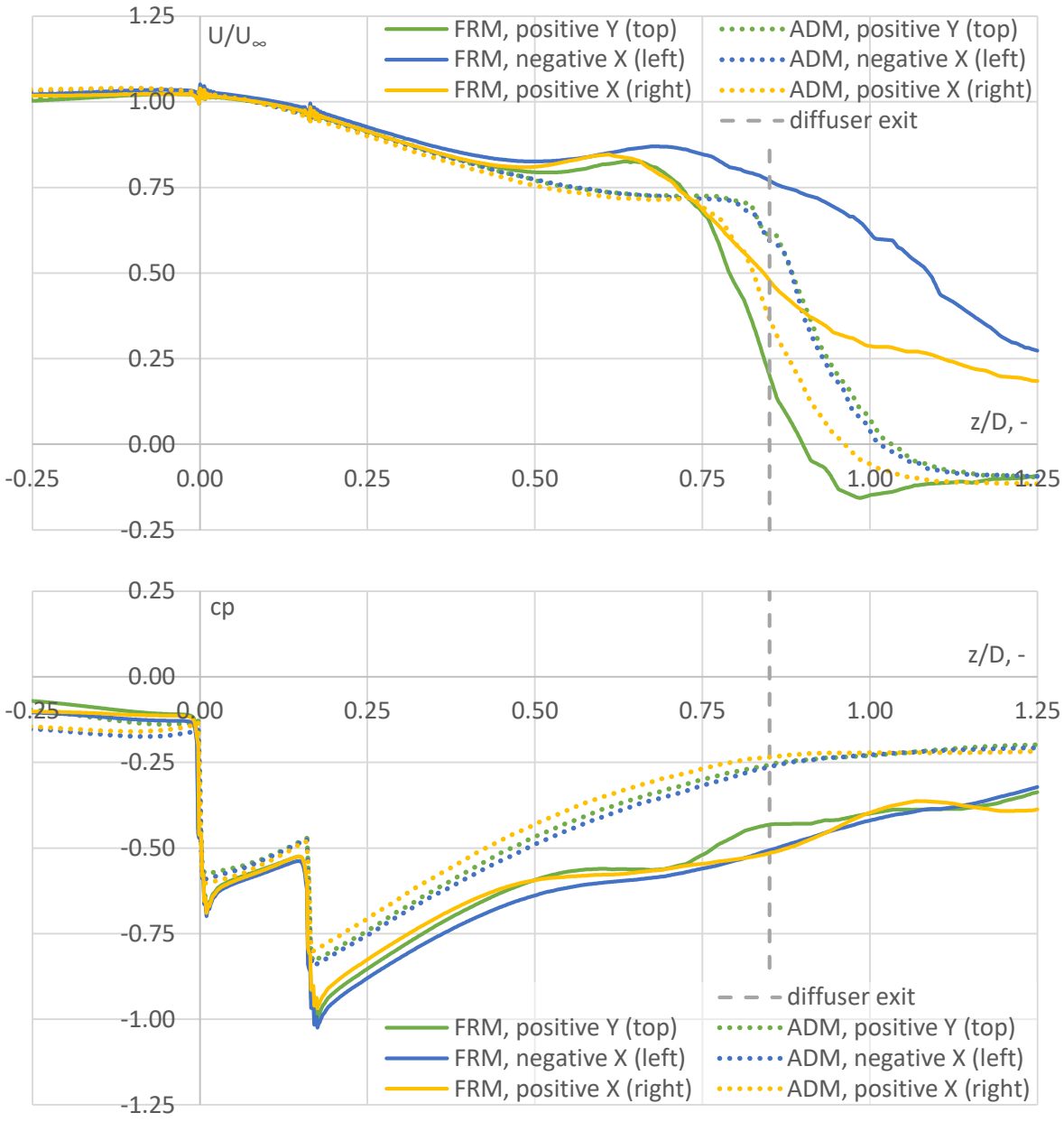

Fig. 68 Streamwise distribution of normalised axial velocity (top) and pressure coefficient (bottom) at 3 locations (a); simulation data: FRM (continuous line) and ADM (dotted line); CRSR, TSR1 = TSR2 = 5.03

Figure 69 presents the streamwise distribution of the normalised axial velocity, at φ= 90° and r/R = 0.3, 0.5, 0.75, 0.9 (b in Fig. 65). The sudden velocity decrease at 0.5 < z/D occurs for all considered locations. The phenomenon takes place farther downstream as the radial position of the probing line increases. This phenomenon is connected with the boundary layer separation near the downstream rotor hub. It is seen for r/R = 0.3 and 0.5 that recirculating flows occur at this z/D range, not observed at higher r/R. Additionally, the ADM simulation tends to overpredict the axial location of this velocity drop, leading to conclusion that the separation is predicted to occur too late.

The velocity decreases gradually in the inner portion of the blade (seen here for up to r/R = 0.75) and increases when approaching the blade tip. This tendency was also observed previously in Fig. 63, from which it is also possible to derive the conclusion that in range r/R = 0.3 – 0.75 the velocity values at the two rotor locations do not differ by more than 5%. The velocity increase in the outer part of the blade can be traced back to the tip loss phenomenon.

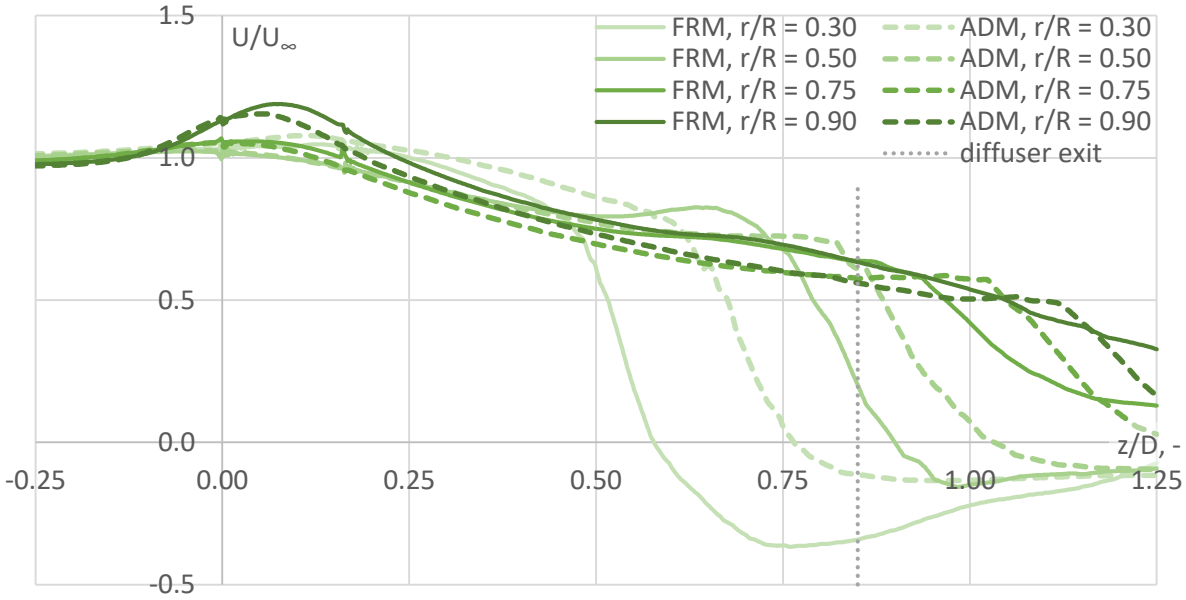

Fig. 69 Streamwise distribution of normalised axial velocity at 4 locations (b); simulation data: FRM (continuous line) and ADM (dotted line); CRSR, TSR1 = TSR2 = 5.03

7.3. Instantaneous flow fields (URANS FRM)

An (qualitative) analysis of the instantaneous flow fields (from URANS FRM) was performed at four angular positions (c in Fig. 65). Figure 70 presents normalised axial velocity and pressure coefficients, with colour schemes chosen so as to represent the deficit (blue) or increase (red) of the parameter with respect to ambient conditions (white). Figure 71 shows the normalised circumferential velocity and circumferential vorticity, with colour scheme representing the negative (blue) or positive (red) value in the cylindrical coordinate system (note that white colour again corresponds to ambient conditions). The considered case is for TSR1 = 3.67 and TSR2 = 3.45 (difference between TSR1 and TSR2 is approximately 6%). At the chosen timestep blades of both rotors are visible at an angular position φ = 120°.

The axial wind velocity increase at the diffuser inlet is followed by a decline deeper inside the diffuser. This phenomenon is not uniform radial-wise: the deepest velocity deficit occurs at the hub vicinity. This is connected with the boundary layer separation and flow recirculation, most likely coming from the interaction of low pressure zones in the boundary layer and downstream the rotor. This effect is additionally amplified by the adverse pressure gradient of swirling flow, as suggested by [113].

The observation of axial velocity values in the close vicinity of the blade shows that their value is increased as the blade approaches the probing plane and decreased as the blade moves away from it. Additional axial velocity component is created by the bound vortex associated with the blade. The direction of this additional velocity is positive (with respect to wind direction) afore the blade and

negative before it, consequently increasing or decreasing the axial velocity. The tip leakage phenomenon is visible in the form of increased axial velocity values near the tip.

The pressure coefficient fields reveal underpressure zones of circular shape grouped in regular manner inside the diffuser, near its boundary. A comparison with the other presented datasets permits to state that these are the cross-sections of the helicoidal tip vortex structure. The circulation associated with these vertices induces additional radial and axial velocity components. Hence the regular, local axial velocity increase zones inside diffuser, near its boundary.

The influence of the helical wake vortex structure manifests itself the most in the form of vorticity, seen in Fig. 71. The comparison of images for different angular positions reveals that the velocity curl due to both rotors shares the same direction (positive in the assumed cylindrical frame of reference). This is deemed correct, following the traditional vortex model of a rotor. However, the overall structure of the wake differs dramatically between the different angular positions of the probe plane. This is because the two helices have different chirality (the one associated with the upstream rotor is right-handed, the other is left-handed). Following the first Helmholtz's theorem the tip-vortex structures from distinct blades cannot cross, and so the visible twin-helix system is preserved along the flow.

The different handedness of the helices will result in alternating changes of distance between the cross-sections of the two helices. Since the two rotors' TSRs are very similar, the blades of the two rotors will shadow every 60° (approximately), and so should the wake structures. This is visible in that at the probe plane $\varphi = 90°$ the distance between the consecutive vortex cores is approximately 2 times bigger than at $\varphi = 120°$. This means that for this particular timestep the two helices come close at the first location, and move away at the latter. Since the TSRs of the two rotors are different, the exact φ for which the two helices come close or move away will vary in time, owing additionally to the flow complexity.

Takahashi et al. [65], in their LES study of DAWT tip vortices observed the presence of an induced vortex, created between blade tip and diffuser surface, of opposite direction than the tip vortex. This phenomenon was not observed in the current study, possibly due to a higher tip clearance. However, the presented vorticity images confirm that the interaction of tip vortex with the diffuser boundary layer leads to the thinning of the latter.

To the tip-vortex corresponds a base-vortex, of opposite direction, situated at the blade bottom. This vortex system is indeed visible, but is weaker than the one corresponding to the tip-vortices and overshadowed by the vortex structure in the hub boundary layer.

To study the velocity components in the rotor wake, Fig. 72 presents circumferential distribution of axial (top) and circumferential (bottom) normalised velocity at seven axial locations between R1 and R2: 3 downstream R1, 1 in the middle, 3 upstream R2 (d in Fig. 65).

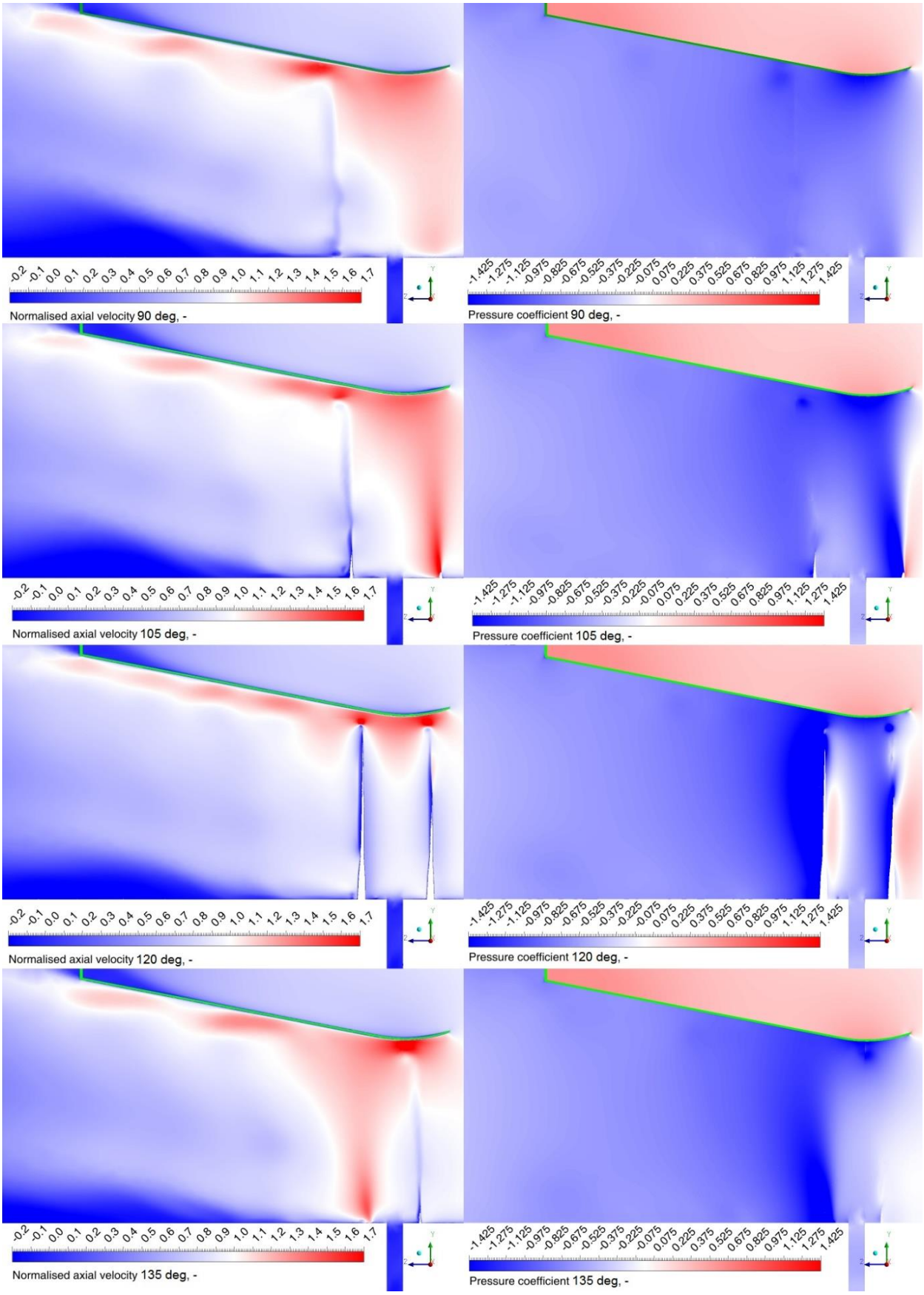

Fig. 70 Instantaneous (FRM) normalised axial velocity fields (left) and pressure coefficient (right) at 4 planes in the diffuser vicinity (c, φ = 90°, 105°, 120°, 135°); blades visible at φ = 120°; note different colour ranges; CRSR, TSR1 = 3.67, TSR2 = 3.45

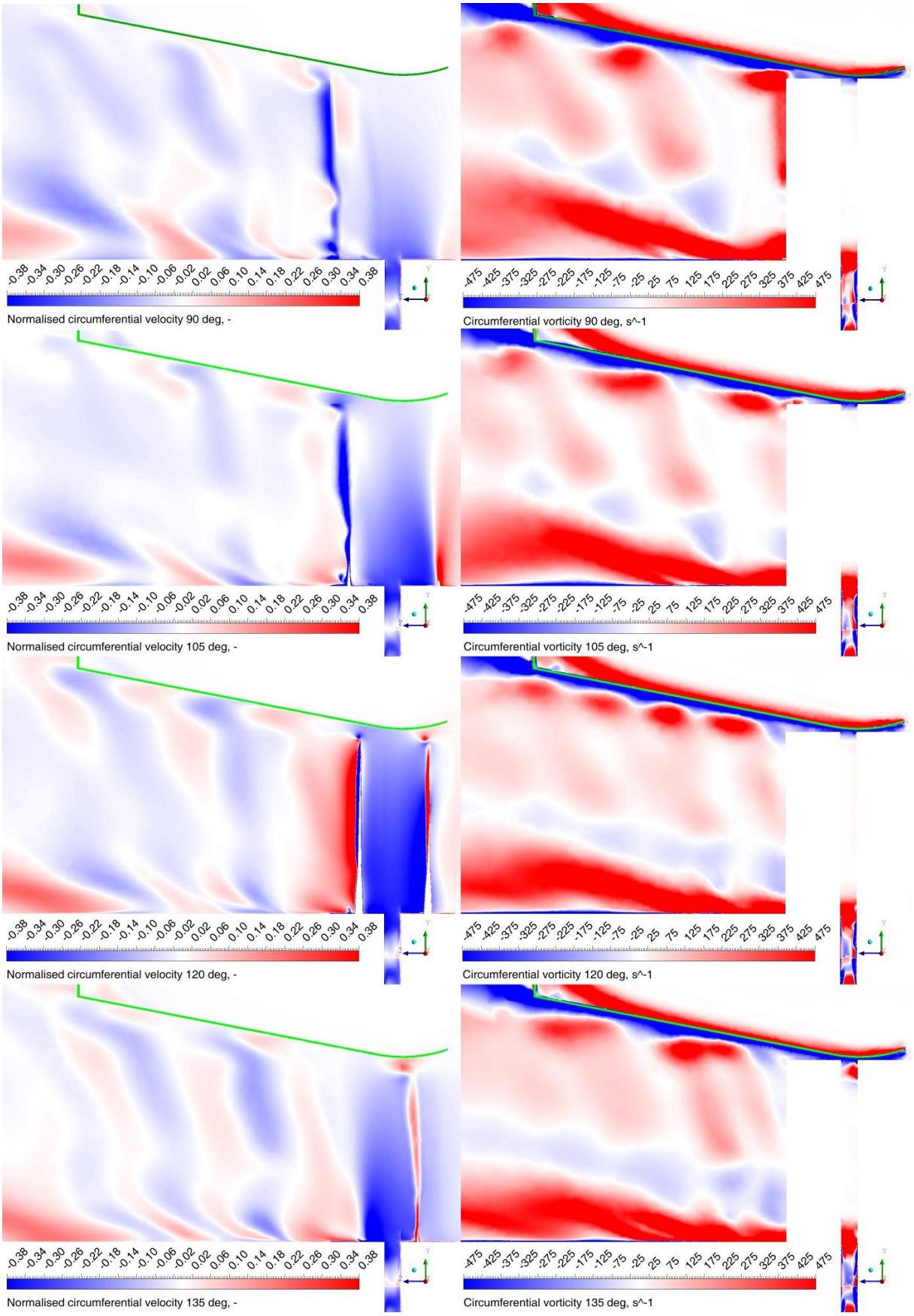

Fig. 71 Instantaneous (FRM) normalised circumferential velocity fields (left) and circumferential vorticity (right) at 4 planes in the diffuser vicinity (c, φ = 90°, 105°, 120°, 135°); blades visible at φ = 120°; note different colour ranges; CRSR, TSR1 = 3.67, TSR2 = 3.45

The considered velocity distributions are, in general shaped by several sources:

- Velocity induced by the helical wake: axial velocity component, opposed to the wind direction. In case of an open-rotor configuration this manifests itself in the form of an axial velocity deficit at the PoR level. In case of shrouded rotor this is opposed by the effect of diffuser augmentation of the axial velocity.
- Velocity induced by the bound vortex associated with the blades (Fig. 72 a): at the point under consideration the circulation of the bounded vortex generates an additional velocity component. By definition it is tangential to an imaginary circle centered at the blade extrusion line, and inversely proportional to the distance between this line and the point in question. The axial component of the induced velocity vector will be positive (i.e. of the same direction as wind velocity) at the angular locations upstream the blade and negative downstream. The circumferential component of the induced velocity is positive (i.e. of the same direction as rotation velocity of the turbine) upstream rotor, and negative in the wake. In CRSR the two rotors turn in opposite directions, thus the induced circumferential velocities in region between R1 and R2 will be in the same directions as well. In Fig. 72 it is seen how the circumferential velocity component induced by the R1 blades is the highest close to the blades, then decreases gradually, and then increases again when approaching R2. Due to the fact that the considered velocity is induced by the bound vortex, the circumferential location of the discussed phenomena is always the same with respect to the blades.
- Velocity interruption resulting from the blade surface boundary layer (Fig. 72 b): the viscous boundary layer around the blade leaves its trace behind the rotor. It manifests itself in the form of an axial velocity drop and circumferential velocity decrease (with respect to direction of rotation). The angular location of the viscous wake effects is a function of distance from the PoR, as seen in Fig. 72.
- In the considered case the wake is also massively influenced by the mounting pole, situated at approximately $\varphi = 90°$.

A brief analysis of the inflow conditions for R2 shows that the R1 wake associated with bounded vortex is of minor influence, and is mostly damped by the time the fluid reaches R2 PoR. This cannot be, however, said of the viscous wake, whose influence is clearly visible in both components of velocity near R2. Due to this phenomenon the R2 blades experience circumferentially non-uniform loads.

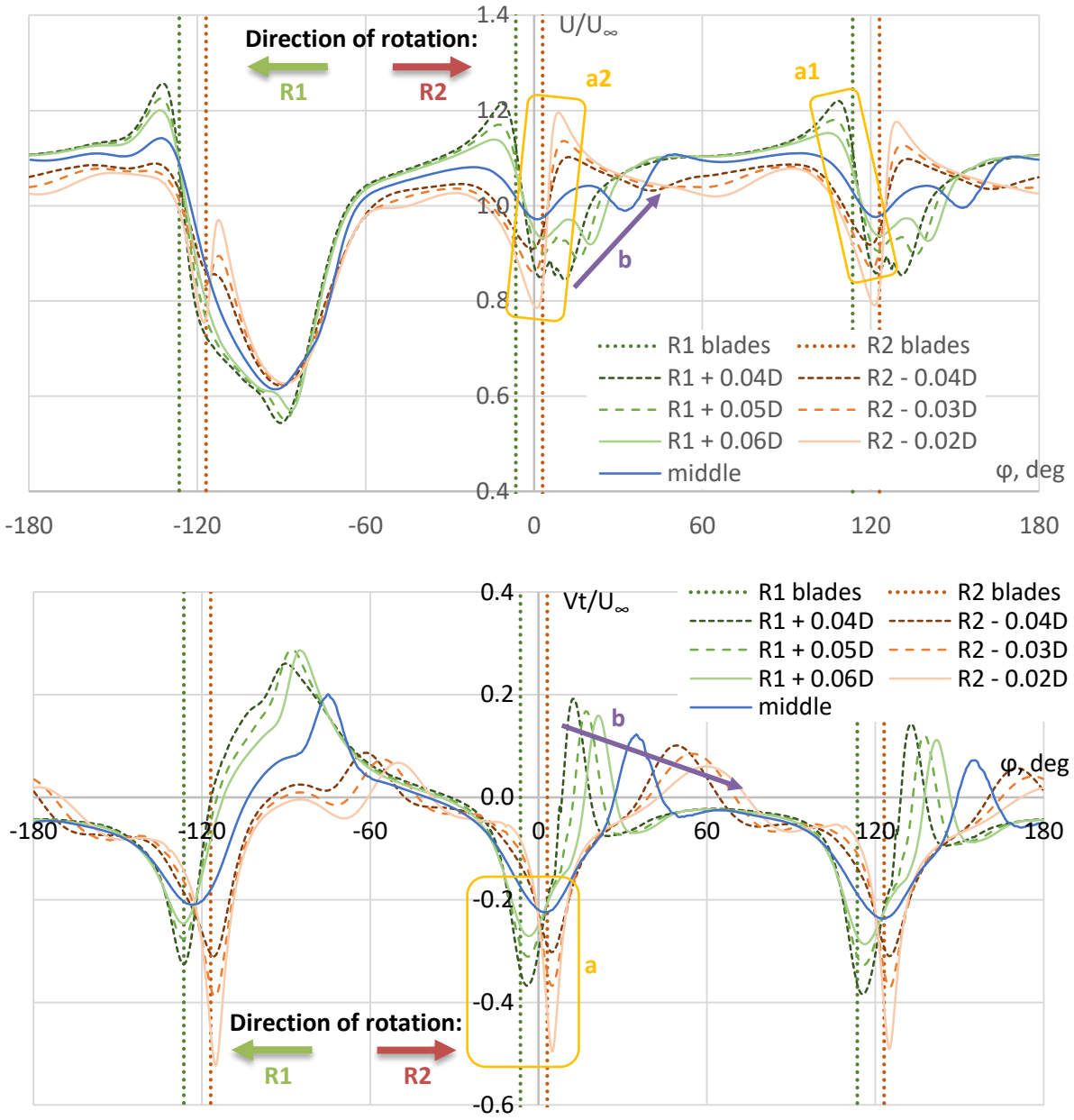

Fig. 72 Instantaneous (FRM) normalised velocity fields: axial (top) and circumferential (bottom): circumferential distribution at r/R = 0.7 and various positions downstream R1 (green) and R2 (red); a – velocity component induced by the bound vertices associated with the blades, b – viscous wake due to blade boundary layer; data taken at location d in Fig. 65

8. Summary and concluding remarks

The thesis *The hybrid simulation model for a twin-rotor diffuser-augmented wind turbine and its experimental validation* was supposed to answer the question of possibility of increasing the energy yield of a wind turbine by combining two solutions: a shrouded turbine (DAWT) and a counter-rotating turbine (CROR). Formalising the above description, the forwarded hypothesis was in the form: *Creation of a hybrid simulation model of a twin-rotor diffuser-augmented wind turbine will enable a sterling analysis of this system's functioning.* The following scientific objectives were assumed:

- creation of a hybrid simulation model for two counter-rotating shrouded wind turbine rotors,
- creation of experimental apparatus of the above mentioned system in the wind tunnel for functional analysis of the system and validation of the hybrid simulation model basing on the experiment-simulation integration approach.

In the first stage of the investigation, an experiment was conducted in the subsonic wind tunnel of IMP TUL. The tests were preceded by evaluation of flow character and measuring equipment diagnostics. The experimental campaign was mainly based on pneumatic and mechanical power/forces measurements. To carry out the tests, a new set of wind turbine measurements benches was developed. The rotor specimens were prepared using the "fast track" approach, based on rapid prototyping, developed at IMP TUL.

The experimental results allow one to formulate the following observations and conclusions:

- The maximum power coefficient of a wind turbine decreases significantly along with the wind reference speed. This is due to the relatively low values of the Reynolds number (in the order of 100,000 determined on the basis of the rotor diameter) and is a significant obstacle in the study of small wind turbines;
- After the application of the shrouding, an approximately twofold increase in the upwind wind turbine power coefficient was observed at the same wind speed. This is due to the fact that the tested rotor-diffuser system has been aerodynamically optimized. However, an increase in the tip-speed ratio corresponding to the maximum Cp value (from 4.5 to 6) and an increase in the axial force coefficient were also observed. The stresses in the blades have also increased, which must be taken into account during their design process;
- The use of the second rotor allowed one to increase the total power coefficient by about 11 - 13% in the case of an unshrouded turbine and about 4 - 5% for the shrouded turbine. This is due to the aerodynamic optimization of the diffuser-turbine arrangement mentioned above, favouring the single-rotor solution;
- The use of the two-rotor system allowed one to reduce the thrust coefficient of the upwind turbine and decrease the optimal TSR (by about 20% for upstream and 33% for downstream rotor). This lowers the stress in the blades of both rotors;
- Due to the presence of the second rotor, the TSR range in which the system works with Cp close to the maximum has also widened;
- The maximum cumulative Cp is strongly dependent on the mutual position of the rotors. Notably, as the downstream rotor approaches the diffuser outlet, the range of TSR for which it operates as a turbine (i.e. receives energy from the flow) decreases significantly.

In the second stage of the investigation a numerical research was performed in ANSYS package software. It began with a further evaluation of the flow in wind tunnel, helping to determine the

simulation domain size and conditions. The study then proceeded towards development of the actual wind turbine simulation models:

- Fully-resolved Rotor Model (FRM) – URANS model prepared in the ANSYS CFX environment. The model allowed the quantification of such quantities as local speed triangles and angles of attack. The results also allowed proposing a proprietary tip loss correction, which in the case of boiled turbines cannot be identical as for the open rotor simulation;
- Hybrid CFD-BET model (Blade-Element Theory) – RANS model prepared in the ANSYS Fluent environment. A more appropriate choice for evaluating the performance of a wind turbine due to lower necessary resources. The application of such an approach allowed for a significant reduction of the calculation time. The comparison of results with experimental data confirmed that the hybrid model gives qualitatively and quantitatively acceptable results. This allows one to claim that it can be used, for example, for optimization tests of considered turbine systems.

The numerical results allow one to formulate the following observations and conclusions:

- Both models have been validated experimentally and verified numerically. FRM showed a relatively higher convergence of calculations than the hybrid model, which resulted from the used calculation schemes and denser grids. At the same time, the calculation time and resources necessary for FRM calculations are significantly larger (approximately several days for one operation point, compared to 36 hours for the full characterization of two turbines);
- In the case of both numerical models, the negative impact of the upstream wind turbine assembly post on the flow stabilization and convergence of calculations is very important;
- The existing methods of modelling the tip leakage phenomenon do not work well in the considered problem. On the basis of FRM results, a proprietary tip loss correction was formulated and further employed in the hybrid model. Its correct operation was confirmed by the confrontation of results (radial speed distributions) obtained with the hybrid model with the results of FRM simulations;
- Proper selection of the aerofoil lift and drag coefficients for the hybrid model is very difficult due to the low Reynolds numbers and the unknown turbulence intensity in the upstream rotor wake. Experimental data are usually insufficient in this respect. Thus, the estimations obtained with the XFoil panel code were used;
- The RANS CFD-BET hybrid model has been used to investigate the influence of the distance between rotors on the operating parameters of the shrouded twin-rotor wind turbine system. According to the obtained results, the optimal TSR value remains approximately unchanged for the upstream rotor, and decreases as the distance between the rotors increases for the downstream rotor. Decreasing the distance between the rotors results in an increase of downstream and decrease of upstream rotor power coefficient;
- Analysis of the time-averaged FRM flow fields showed that the presence of the second rotor may reduce the mass flow rate through the upstream wind turbine, in particular when the downstream rotor is located close to the diffuser inlet;
- The use of the URANS FRM model allowed one to collect a wide set of instantaneous flow data, such as velocity and pressure fields. This allowed one to observe elements such as the interaction of helical vortex structures coming out of the rotor blades, a relatively quick detachment of the boundary layer near the hub or the impact of the tip leakage phenomenon.

Basing on the above presented summary it is justified to state that the objectives of the thesis have been achieved and the hypothesis was confirmed.

The work done in frames of this thesis may be used as a basis for further studies. The following advices and perspectives may be stated:

- The general principle of using the hybrid model for the considered case was proved. It may further be developed towards more sophisticated solutions. These might include the addition of turbulent quantities source terms to account for production of turbulent kinetic energy of both rotors and observe its influence on the wind turbine performance (especially the downstream rotor). Another possible development would be the use of URANS hybrid model based on the actuator line approach and/or vortex theories;
- The FRM model simulation could be repeated using higher-order modelling approaches, notably the LES/DES approach. This would allow one to see more profoundly the phenomena such as interaction between diffuser boundary layer and rotors' helical wake;
- The thesis concentrated on the assessment of rotor performance, hence the experimental campaign was focused on measurements of wind turbine power and thrust. A more flow-assessment-oriented campaign way could be performed in future, including for example PIV and/or CTA determination of flow fields.
- The validated numerical hybrid model may be use in the wind turbine optimization studies. Among the possible optimization targets the maximization of system performance and/or best decomposition of aerodynamic loads may be mentioned. This task is especially challenging due to a multitude of optimization variables, such as rotors' diameters, blade and diffuser geometry, rotor placement etc.

Literature and sources

[1] European Comission, *Communication from the Commission to the European Parliament, the Council, the European Economic and Social Committee and the Committee of the Regions - 20 20 by 2020 - Europe's climate change opportunity /* COM/2008/0030 final */,* Brussels, 2008.

[2] EWEA, "Wind in power - 2015 European statistics," 2016.

[3] Energy Regulatory Office (URE), "Potencjał krajowy OZE w liczbach - moc zainstalowana," 2018.

[4] Kancelaria Sejmu RP, "Ustawa z dnia 20 lutego 2015 r. o odnawialnych źródłach energii," *Dziennik ustaw Rzeczpospolitej Polskiej,* no. 1148, pp. 1 - 115, 06 2017.

[5] H. Lorenc, Atlas klimatu Polski, Warszawa: Instytut Meteorologii i gospodarki Wodnej, 2005.

[6] RTE (Réseau de Transport d'Electricité), "Bilan électrique 2017," 2018.

[7] ADEME (L'Agence de l'Environnement et de la Maîtrise de l'Energie), "Le petit éolien," 2015.

[8] W. Tong, Fundamentals of wind energy, Southampton, UK: WIT Press, 2010, p. 769.

[9] B. E. G. Clark, Symington and the Steamboat, Lulu.com, 2010.

[10] A. Flettner, The story of the rotor, London: Crosby, Lockwood and Son, 1926.

[11] A. Clarke, More Windmill Land, London: J.M.Dent & Sons Ltd., 1917.

[12] P. D. Fleming and S. D. Probert, "The evolution of wind-turbines: An historical review," *Applied Energy,* vol. 18, no. 3, pp. 163-177, 1984.

[13] M. Pasqualetti, R. Righter and P. Gipe, "Wind Energy, History of," in *Encyclopedia of Energy*, Elsevier Inc., 2004, pp. 419-433.

[14] "Nashtifan windmills | tishineh tourism," [Online]. Available: http://www.tishineh.com/touritem/1529/Nashtifan--windmills. [Accessed 17 September 2018].

[15] "Outwood Windmill (Explored)," [Online]. Available: https://www.flickr.com/photos/adam_swaine/14421090805/. [Accessed 17 September 2018].

[16] "De Noord - Wikipedia," [Online]. Available: https://en.wikipedia.org/wiki/De_Noord. [Accessed 17 September 2018].

[17] T. L. Baker, A Field Guide to American Windmills, Oklahoma: University of Oklahoma Press, 1985.

[18] “Metro News - cleveland.com,” [Online]. Available: http://media.cleveland.com/metro/photo/brush-wind-dynamo-f07e3438dc210438.jpg. [Accessed 17 September 2018].

[19] “1905 - Danmark - Postkort - Brugt m. mærke,” [Online]. Available: http://roskildeonline.com/da-DK/lot/18247/danmark-askov-parti-med-moeller-prof-poul-la-cour. [Accessed 17 September 2018].

[20] “Wind Energy Pictures - Gedser Wind Turbine,” [Online]. Available: http://drømstørre.dk/wp-content/wind/miller/windpower%20web/en/pictures/juul.htm. [Accessed 17 September 2018].

[21] “Scientific inquiry should be an American value, too,” 20 April 2017. [Online]. Available: https://religionnews.com/2017/04/20/scientific-inquiry-should-be-an-american-value-too/. [Accessed 18 September 2018].

[22] “WIND-WORKS: Éole,” [Online]. Available: http://www.wind-works.org/cms/index.php?id=506. [Accessed 18 September 2018].

[23] NASA wind turbines - Wikipedia, [Online]. Available: https://en.wikipedia.org/wiki/NASA_wind_turbines. [Accessed 18 September 2018].

[24] “Giant Offshore Wind Turbines Tempt European Market - Softpedia News,” [Online]. Available: https://news.softpedia.com/news/Giant-Offshore-Wind-Turbines-Tempt-European-Market-238260.shtml. [Accessed 18 September 2018].

[25] P. Gipe, Wind Energy for the Rest of Us: A Comprehensive Guide to Wind Power and How to Use It, Bakersfield, CA: wind-works.org, 2016.

[26] G. J. M. Darrieus, “Turbine having its rotating shaft transverse to the flow of the current”. USA Patent US1835018A, 1 October 1926.

[27] T. Burton, N. Jenkins, D. Sharpe and E. Bossanyi, Wind Energy Handbook, 2nd ed., West Sussex: John Wiley & Sons, 2011.

[28] P. Musgrove, “The economics of existing wind-turbines in the size range 10 to 100 metres diameter,” in *Wind Energy Conversion 1983: Proceedings of the Fifth BWEA Wind Energy Conference*, 1984.

[29] International Renewable Energy Agency (IRENA), “Renewable Power Generation Costs in 2017,” IRENA, Abu Dhabi, 2018.

[30] WindEurope, “Wind in power 2017 - Annual combined onshore and offshore wind energy statistics,” windeurope.org, Brussels, Belgium, 2018.

[31] BP plc, *BP Statistical Review of World Energy 2018,* 2018.

[32] RTE (Réseau de Transport d'Electricité), *Panorama de l'électricité renouvelable,* 2018.

[33] gramwzielone.pl, "Mikroinstalacje zdominowały polski rynek OZE. W 2017 r. codziennie przybywało ich średnio 35," GRAMWZIELONE.PL Sp. z o.o., 15 May 2018. [Online]. Available: http://gramwzielone.pl/trendy/31084/mikroinstalacje-zdominowaly-polski-rynek-oze-w-2017-r-codziennie-przybywalo-ich-srednio-35. [Accessed 20 July 2018].

[34] MHI Vestas Offshore Wind A/S, *The V164-9.5 MW™ Turbine.*

[35] GE Renewable Energy, *Haliade-X offshore wind turbine platform.*

[36] American Wind Energy Association (AWEA), "U.S. Wind Industry Annual Market Report; Year Ending 2017," 2018.

[37] WindEurope, "Wind energy in Europe: Scenarios for 2030," windeurope.org, Brussels, Belgium, 2018.

[38] K. S. R. Murthy and O. P. Rahi, "A comprehensive review of wind resource assessment," *Renewable and Sustainable Energy Reviews,* vol. 72, pp. 1320-1342, 2017.

[39] U. S. Paulsen, T. F. Pedersen and L. Vita, "Existing VAWT Technologies," Risø National Laboratory, Roskilde, 2008.

[40] "Vertical Axis Wind Generator 500w-20kw For Home Use For Sale VAWT," [Online]. Available: https://www.alibaba.com/. [Accessed 18 September 2018].

[41] "Wind generator VAWT 300W 12/24V Light and Portable wind turbine / 300W enough power Vertical Axis Wind Turbine Generator," [Online]. Available: https://www.aliexpress.com/. [Accessed 18 September 2018].

[42] "Renugen solar panels wind turbines," [Online]. Available: http://renugen.co.uk/. [Accessed 18 September 2018].

[43] "Elektrownia wiatrowa pionowa VAWT - SAVONIUS 280W," [Online]. Available: http://sklep74017.shoparena.pl/. [Accessed 18 September 2018].

[44] "Wonderful Online Wind Turbine Generator 24V 400w Vertical Windmill Power Supply for Home,Business,rv, Marine, Island, House, Farm," [Online]. Available: https://www.amazon.com/. [Accessed 18 September 2018].

[45] "ALEKO WGV2Q300 Three Phase Permanent Magnet AC Synchronous Vertical Wind Generator 300W 24V Wind Generator Turbine," [Online]. Available: https://www.amazon.com/. [Accessed 18 September 2018].

[46] "Rutland Windchargers - Wind Power from Marlec," [Online]. Available: https://www.marlec.co.uk/wind-power/?v=461b1990fe86. [Accessed 18 September 2018].

[47] “Home - Bergey Wind PowerBergey Wind Power | Small Wind Turbines,” [Online]. Available: http://bergey.com/. [Accessed 18 September 2018].

[48] “Aerogeneratore monopala ad asse orizzontale,” [Online]. Available: http://www.lombardiabeniculturali.it/scienza-tecnologia/schede/ST170-00347/?img=8893. [Accessed 18 September 2018].

[49] “Les eoliennes horizontales 1kw skywind - Enerlice,” [Online]. Available: https://enerlice.fr/eoliennes-horizontales-1-kw-skywind/. [Accessed 18 September 2018].

[50] “S-700 Wind Turbine Motor Generator Marine Type Windmill 3 CFRP Blades with External Type WindSolar Hybrid Controller,” [Online]. Available: https://www.alibaba.com/. [Accessed 18 September 2018].

[51] “Horizontal Wind Turbine 24V/48V 800W 6 Blades Residential Garden Wind Power Generator,” [Online]. Available: https://www.alibaba.com/. [Accessed 18 September 2018].

[52] “400W DC12V or 24V 3 blades built-in rectifier module wind turbine generator with 600W waterproof wind controller,” [Online]. Available: https://www.alibaba.com/. [Accessed 18 September 2018].

[53] “EOLFORCE 5 : éolienne horizontale | Etude, installation et maintenance,” [Online]. Available: https://enerlice.fr/en/eolienne-horizontale-eolforce-5/. [Accessed 18 September 2018].

[54] O. Igra, “Research and development for shrouded wind turbines,” *Energy Conversion and Management,* vol. 21, no. 1, pp. 13-48, 1981.

[55] B. M. Gilbert and K. L. Foreman, “Experiments with a diffuser-augmented model wind turbine,” *Journal Energy Resources Technology,* no. 105, pp. 46-53, 1983.

[56] K.-I. Abe and Y. Ohya, “An investigation of flow fiels around flanged diffusers using CFD,” *J. Wind Fengineering and Industrial Aerodynamics,* no. 92, pp. 315-330, 2004.

[57] R. A. Oman, K. M. Foreman and B. L. Gilbert, “Investigation of Diffuser-Augmented Wind turbines, part I,” Grumman Aerospace Co., Bethpage, NY, 1977.

[58] Windlens Co., Ltd., *Windlens WL5000 promo material,* 103 3-2-6, Kamikoga, Chikushino City, Fukuoka Prefecture.

[59] Y. Ohya, T. Karasudani and C. T. Matsuura, “A highly efficient wind turbine with wind-lens shroud,” in *13th International Conference on Wind Engineering*, Amsterdam, 2011.

[60] R. A. Oman, K. M. Foreman and B. L. Gilbert, “Investigation of Diffuser-Augmented Wind turbines, part II,” Grumman Aerospace Co., Bethpage, NY, 1977.

[61] G. M. Lilley and W. J. Rainbird, “A preliminary report on the design and performance of ducted windmills,” The college of aeronautics, Cranfield, 1956.

[62] K. M. Foreman, B. Gilbert and R. A. Oman, “Diffuser Augmentation,” *Solar Energy,* no. 20, pp. 305-311, 1978.

[63] K.-I. Abe, M. Nishida, A. Sakurai, Y. Ohya, H. Kihara, E. Wada and K. Sato, “Experimental and numerical investigations of flow fields behind a small wind turbine with a flanged diffuser,” *J. Wind Engineering and Industrial Aerodynamics,* no. 93, p. 951–970, 2005.

[64] Y. Ohya, T. Uchida, T. Karasudani, M. Hasegawa and H. Kume, “Numerical Studies of Flow around a Wind Turbine Equipped with a Flanged-Diffuser Shroud using an Actuator-Disk Model,” *J. Wind Engineering,* vol. 36, no. 4, pp. 455-472, 2012.

[65] S. Takahashi, Y. Hata, Y. Ohya, T. Karasudani and T. Uchida, “Behavior of the Blade Tip Vortices of a Wind Turbine Equipped with a Brimmed-Diffuser Shroud,” *J. Energies,* no. 5, pp. 5229-5242, 2012.

[66] K. Olasek, M. Karczewski, M. Lipian, P. Wiklak and K. Jóźwik, “Wind tunnel experimental investigations of a diffuser augmented wind turbine model,” *Int. J. Numerical Methods for Heat & Fluid Flow,* vol. 26, no. 7, 2016.

[67] M. O. L. Hansen, Aerodynamics of Wind Turbines, 2nd ed., London: Earthscan, 2008.

[68] C. G. Curtis, “Elastic-fluid turbine”. New york, United States of America Patent 566969, 1 September 1896.

[69] K. Appa, “Counter-rotating wind turbine system,” Appa Technology Initiatives, Lake Forest, 2002.

[70] W. Z. Shen, V. A. K. Zakkam, J. N. Sørensen and K. Appa, “Analysis of Counter-Rotating Wind Turbines,” *Journal of Physics: Conference Series,* no. 75, 2004.

[71] S. N. Jung, T.-S. No and K.-W. Tyu, “Aerodynamic performance prediction of a 30 kW counter-rotating wind turbine system,” *J. Renewable Energy,* no. 30, pp. 631-644, 2005.

[72] T. Kanemoto and A. M. Galal, “Development of intelligent wind turbine generator with tandem wind rotors and double rotational armatures (1st report, superior opertion of tandem wind rotors),” *JSME International Journal Series B Fluids and Thermal Engineering,* no. 49, pp. 450-457, 2006.

[73] K. Kubo and T. Kanemoto, “Development of intelligent wind turbine generator with tandem wind rotors and double rotational armatures (2nd report, Characteristics of tandem WR),” *J. Fluid Science and Technology,* vol. 3, no. 3, pp. 370-378, 2008.

[74] K. Kubo, Y. Hano, H. Mitarai, K. Hirano, T. Kanemoto and A. M. Galal, “Intelligent wind turbine unit with tandem rotors (discussion of prototype performances in field tests),” *Current Applied Physics,* no. 10, p. 326–331, 2010.

[75] Y. Usui, K. Kubo and T. Kanemoto, “Intelligent Wind Power Unit with Tandem Wind Rotors and Armatures (Optimization of Front Blade Profile),” *J. Energy and Power Engineering,* no. 6, pp. 1791-1799, 2012.

[76] D. Eggleston and F. S. Stoddard, Wind Turbine Engineering Design, New York: Van Nostrand Reinhold Company, 1987.

[77] S. Drzewiecki, Théorie générale de l'hélice; hélice aériennes et hélices marines, Paris: Gauthier-Villars et Cie, 1920.

[78] V. L. Okulov, J. N. Sorensen and G. van Kuik, Development of the optimum rotor theories, Moscow-Izhevsk:: R&C Dyn, 2013.

[79] W. F. Durand, Aerodynamic Theory vol. 4, Berlin: Springer Berlin Heidelberg, 1935, p. 453.

[80] A. Betz, Schraubenpropeller mit geringstem Energieverlust, Berlin, Heidelberg: Springer, 1919.

[81] W. Z. Shen, R. Mikkelsen, J. N. Sørensen and C. Bak, “Tip loss corrections for wind turbine computations,” *J. Wind Energy,* no. 8, pp. 457-475, March 2005.

[82] B. Blocken, T. Stathopoulos and J. Carmeliet, “A numerical study on the existence of the Venturi-effect in passages between perpendicular buildings,” *J. Enginnering Mechanics - ASCE,* vol. 12, no. 134, pp. 1021-1028, 2008.

[83] B. Li, Z. Luo, M. Sandberg and J. Liu, “Revisiting the ‘Venturi effect’ in passage ventilation between two non-parallel buildings,” *Building and Environment,* no. 94, pp. 714-722, 2015.

[84] Y. Ohya, T. Karasudani, A. Sakuraib, K.-i. Abe and M. Inoue, “Development of a shrouded wind turbine with a flanged diffuser,” *J. Wind Engineering and Industrial Aerodynamics,* no. 96, p. 524–539, 2008.

[85] O. D. Vries, Fluid Dynamic Aspects of Wind Energy Conversion, Amsterdam, The Netherlands: National Aerospace Laboratory NLR, 1979, p. 148.

[86] M. Nagai and K. Irabu, “Momentum theory of diffuser augmented wind turbine (in Japanese),” *Transactions of the Japan Society of Mechanical Engineers Series B,* vol. 53, no. 489, pp. 1543-1547, 1987.

[87] A. C. Aranake and V. K. Lakshminarayan, “Assessment of low-order theories for analysis and design of shrouded wind turbines using CFD,” *Journal of Physics: Conference Series,* vol. 524, 2014.

[88] B. Newman, “Multiple actuator-disc theory for wind turbines,” *Journal of Wind Engineering and Industrial Aerodynamics,* no. 24, pp. 215-225, 1986.

[89] N. S. Arzanikow and W. M. Malcew, Aerodynamika, Warsaw: PWN, 1959, p. 511.

[90] Z. Kazimierski and Z. Orzechowski, Mechanika Płynów, Łódź: Redakcja Wydawnictw Naukowych Politechniki Łódzkiej, 1979.

[91] ANSYS 18.1 documentation.

[92] M. Lipian, M. Karczewski and K. Jozwik, “Analysis and comparison of numerical methods for design and development of small Diffuser-Augmented Wind Turbine (DAWT),” in *IECON 2016 - 42nd Annual Conference of the IEEE Industrial Electronics Society*, 2016.

[93] M. Kulak, M. Karczewski, K. Olasek and K. Jozwik, *CFD analysis of Diffuser Augmented Wind Turbine model for wind tunnel investigation,* Florence, 2016.

[94] F. R. Menter, “Two-Equation Eddy-Viscosity Turbulence Models for Engineering Applications,” *AIAA Journal,* vol. XXXII, no. 8, pp. 1598-1605, 1994.

[95] M. Lipian, M. Karczewski and K. Olasek, “Sensitivity study of diffuser angle and brim height parameters for the design of 3 kW Diffuser Augmented Wind Turbine,” *Open Engineering,* vol. V, no. 1, pp. 2391-5439, 2014.

[96] “Law of the wall - Wikipedia,” [Online]. Available: https://en.wikipedia.org/wiki/Law_of_the_wall. [Accessed 18 September 2018].

[97] J. B. Barlow, W. H. Rae Jr. and A. Pope, Low-Speed Wind Tunnel Testing, 3rd edition, New York, NY: John Wiley&Sons, Inc., 1999.

[98] A. L. Buck, “New equations for computing vapor pressure and enhancement factor,” *J. Applied Meteorology,* vol. 20, pp. 1527-1532, 1981.

[99] K. Jozwik, M. Karczewski, M. O. K. Lipian, P. Pycio and P. Wiklak, “Experimental stand for wind turbine power measurements (No Arch. 1851) – STOW project report,” IMP TUL, Lodz, Poland, October 2015.

[100] J. Bartl and L. Saetran, “Blind test comparison of the performance and wake flow between two in-line wind turbines exposed to different turbulent inflow conditions,” *Wind Energy Science,* no. 2, pp. 55 - 76, 2017.

[101] D. R. Lide, CRC Handbook of Chemistry and Physics, Copyright CRC Press LLC, 2004.

[102] W. Z. Shen, M. O. L. Hansen and J. N. Sørensen, “Determination of angle of attack (AOA) for rotating blades,” in *Wind Energy: Proceedings of the Euromech Colloquium*, Oldenburg, 2006.

[103] W. Z. Shen, M. O. L. Hansen and J. N. Sørensen, "Determination of the Angle of Attack on Rotor Blades," *J. Wind Energy,* no. 12, pp. 91 - 98, 2009.

[104] H. Rahimi, G. Schepers, W. Z. Shen, N. R. García, M. Schneider, D. Micallef, C. S. Ferreira, E. Jost, L. Klein and I. Herráez, "Evaluation of different methods for determining the angle of attack on wind turbine blades with CFD results under axial inflow conditions," 2017.

[105] S. Guntur and N. N. Sorensen, "An evaluation of several methods of determining the local angle of attack on wind turbine blades," *J. Physics: Conference Series,* no. 555, 2014.

[106] S. Sarmast and R. F. Mikkelsen, "The experimental results of the NREL S826 Airfoil at low Reynolds numbers," DTU, Lyngby, Denmark, 2013.

[107] F. Balduzzi, A. Bianchini, R. Malecia, G. Ferrara and L. Ferrari, "Critical issues in the CFD simulation of Darrieus wind turbines," *J. Renewable Energy,* vol. 85, pp. 419-435, 2016.

[108] C. A. Lyon, A. P. Broeren, P. Giguere, A. Gopalarathnam and M. S. Selig, Summary of Low-Speed Airfoil Data vol. 3, Virginia Beach, VA: SoarTech Publications, 1997, p. 445.

[109] E. Branlard, "Wind turbine tip-loss corrections; Review, implementation and investigation of new models (Master thesis)," Technical University of Denmark (DTU), 2011.

[110] P. Giguere and M. S. Selig, "New Airfoils for Small Horizontal Axis Wind Turbines," *Transactions of the ASME,* no. 120, pp. 108-114, 1998.

[111] M. Drela, "XFOIL: An Analysis and Design System for Low Reynolds Number Airfoils," in *Lecture Notes in Engineering: Low Reynolds Number Aerodynamics*, New York, Springer-Verlag, 1989.

[112] S. F. Hoerner, Fluid-Dynamic Drag, Bakersfield, CA: Hoerner Fluid Dynamics, 1965, p. 455.

[113] F. Massouh and I. Dobrev, "Exploration of the vortex wake behind of wind turbine rotor," *Journal of Physics: Conference Series,* no. 75, 2007.

[114] J. Porochnicki and J. Prywer, "Tunel Aerodynamiczny do Badan Palisad Lopatkowych," *Cieplne Maszyny Przeplywowe - Turbomachinery,* vol. 89, no. 389, pp. 217-226, 1981.

[115] M. Kulak, M. Karczewski, K. Olasek and K. Jankowski, "Numerical Simulations and Experimental Study of Wind Tunnel Turbulence Intensity Reduction," *Cieplne Maszyny Przeplywowe - Turbomachinery,* vol. 132, p. 14, 2007.

[116] K. Olasek and P. Wiklak, "Application of 3D printing technology in aerodynamic study," *J. Physics: Conference Series,* vol. 530, 2014.

[117] "Wiatromierz czaszowy LB-747," [Online]. Available: http://www.label.pl/po/wiatromierz-lb747.html. [Accessed 18 September 2018].

[118] “WindObserver II | Gill Instruments,” [Online]. Available: http://www.gillinstruments.com/products/anemometer/wind_ob2.htm. [Accessed 18 Septeber 2018].

[119] “Met Mast Alternative | ZephIR 300 Onshore Wind Lidar - ZephIR Lidar,” [Online]. Available: https://www.zephirlidar.com/products/zephir-300/. [Accessed 18 September 2018].

[120] ADEME/Meteolien/Météo-France, “Rapport final sur la cartographie éolienne nationale,” ADEME, Paris, 2015.

[121] M. Lipian, M. Karczewski and K. Jozwik, “Koncepcja modernizacji mikrosiłowni wiatrowej dla polskiej energetyki prosumenckiej,” *Przegląd Naukowo-Metodyczny Edukacja dla bezpieczeństwa,* vol. 30, no. 1, pp. 1212-1226, 2016.

Appendix 1. IMP TUL wind tunnel

The aerodynamics laboratory of IMP TUL is equipped with a subsonic wind tunnel (Ma < 0.3, [114]). Built originally for blade cascade studies in 1970s, it has an open test section construction and may operate in blow or suction mode. Fluid (air) is moved by a centrifugal fan of nominal volume flow rate equal to 6.25 m^3/s, powered by the 2-pole asynchronous motor of nominal power of 55 kW. Installation of honeycomb [115] and recent renovation works adapted the wind tunnel structure for current aerodynamic works conducted at IMP TUL (Fig. A1.1). The wind tunnel outlet (henceforth referred to as test section inlet) is of circular shape, with diameter D = 0.8 m and length of approximately 2 m. Maximum achievable air velocity is equal to approximately 18 m/s.

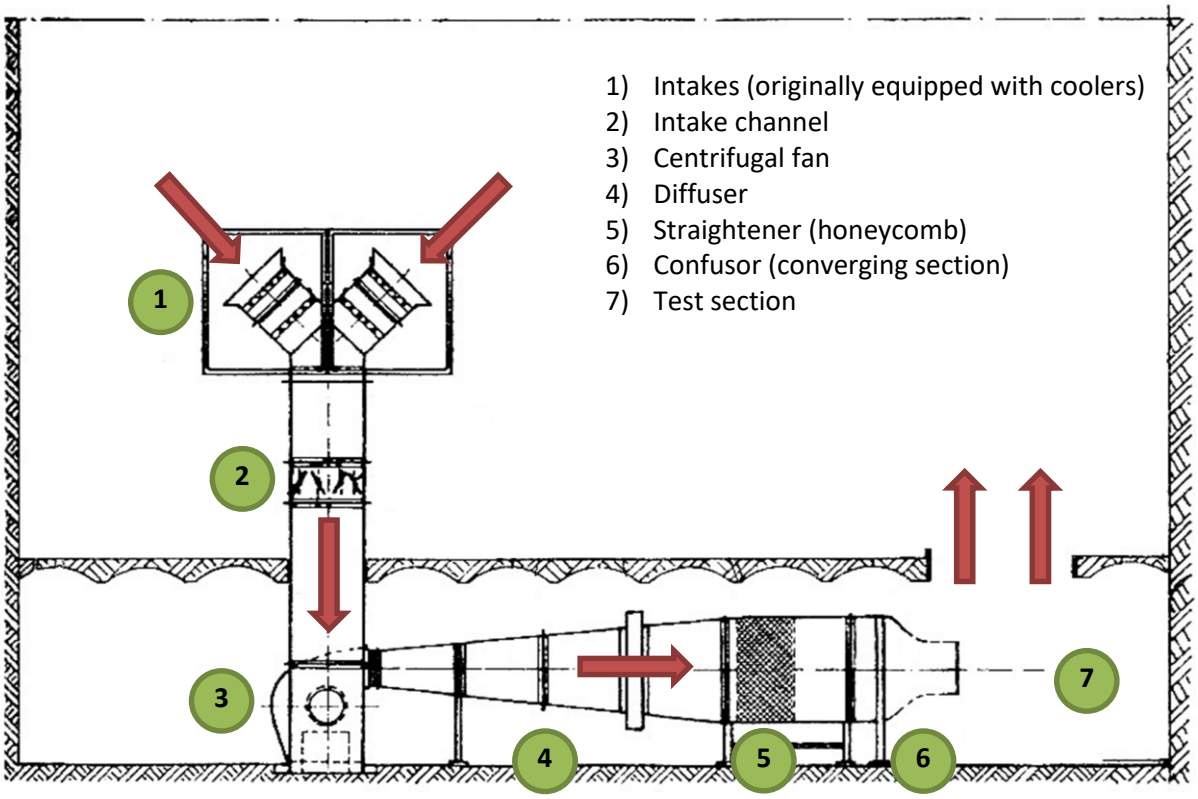

Fig. A1.1 IMP TUL wind tunnel section view; arrows mark flow direction [114]

Pitot tube (Prandtl type) measurements were used to examine the flow nature in selected locations of the wind tunnel lower chamber (housing the test section). These were followed by a numerical study of the room (Fig. A1.2). Together they permitted to identify and analyse the governing flow phenomena in the wind tunnel test section.

In the first phase the test section inlet was analysed at wind tunnel maximum operational conditions. The distribution of axial velocity was measured on two control lines - vertical and horizontal axes (see Fig. A1.2 for locations). This permitted to create an author's model, comprising of two-stage 2D interpolation, and implement it in CFD environment. The obtained velocity field (visible in) was used in numerical simulations performed later one in ANSYS CFX (free flow in wind tunnel) and Fluent (wind turbine simulations). The calculation of velocity in the given point G (see Fig. A1.3), situated at the distance $|\overline{OG}|$ = r from the inlet centre (O) is as follows:

1. linear interpolation of velocity value in points B (based on points A and C, $|\overline{OB}|$ = r) and E (based on points D and F,$|\overline{OE}|$ = r),
2. circumferential interpolation of velocity value in point G, at known α, based on points B and E.

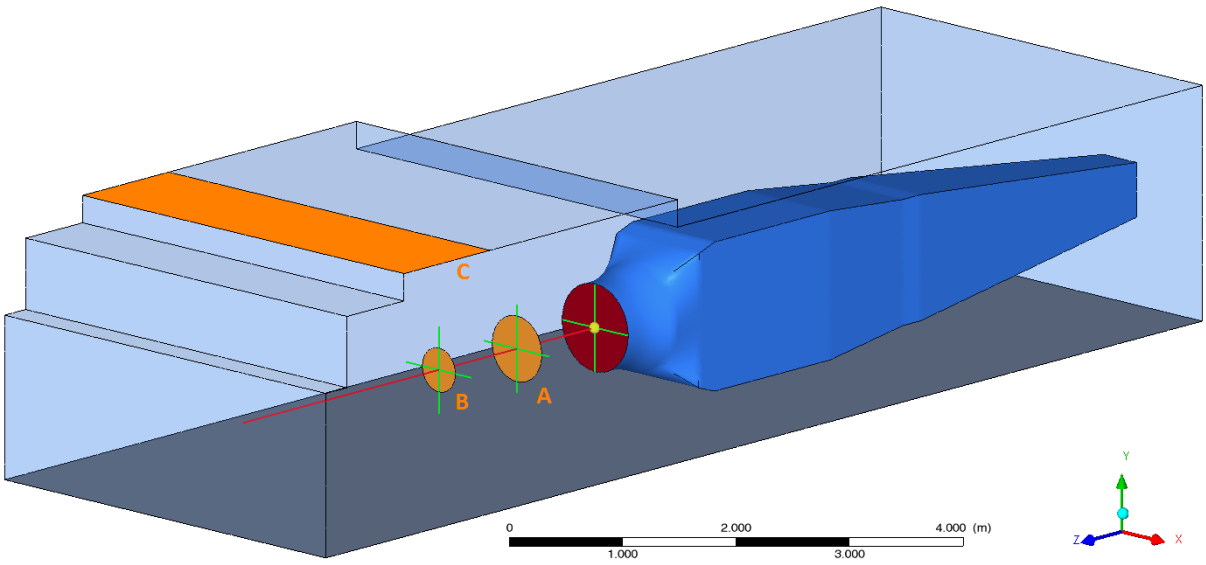

Fig. A1.2 Wind tunnel lower chamber geometry; control lines marked green, control surfaces orange, domain inlet red, outlet orange C; all other surfaces are walls

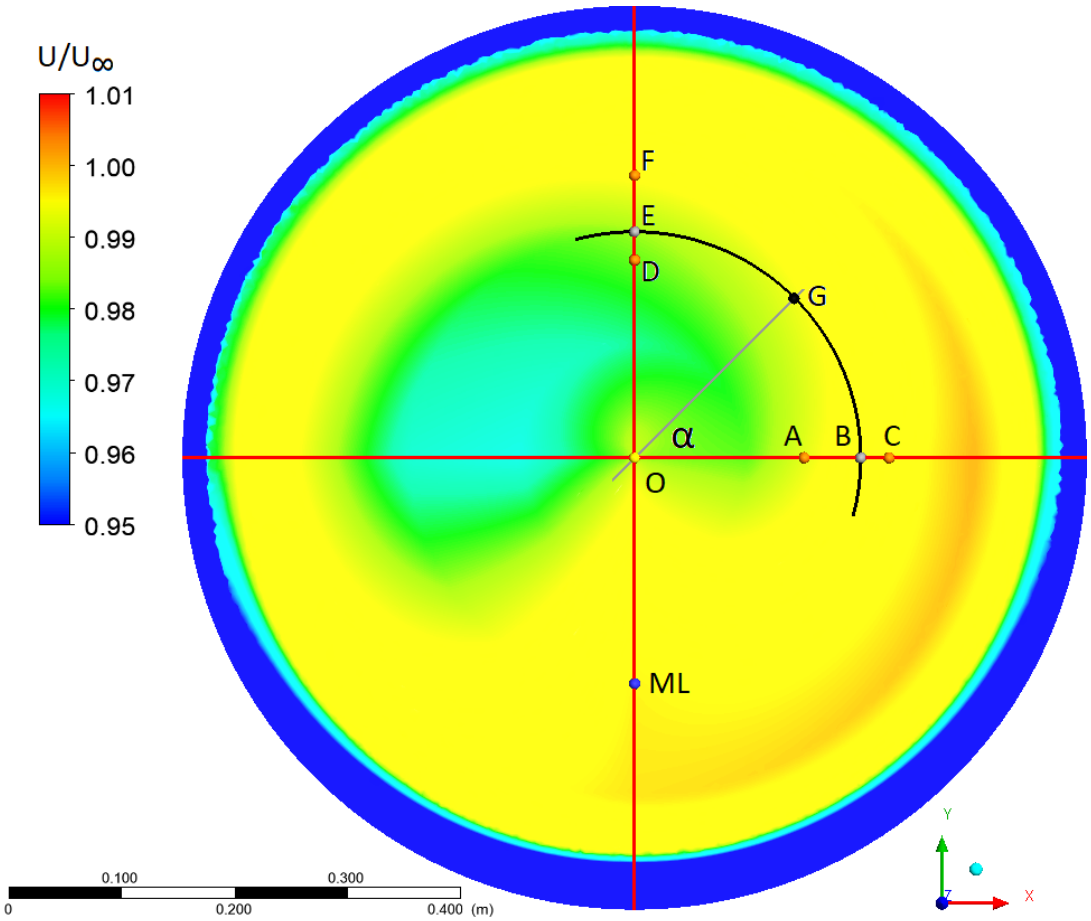

Fig. A1.3 Normalised axial velocity distribution at the test section inlet (interpolation in ANSYS CFX, U∞ = 15.95 m/s)

Since Prandtl tube analysis does not offer possibility of high-frequency measurements of velocity field, it cannot be used for turbulence measurements. Thus the turbulence intensity was taken from earlier experimental analysis using hot-wire anemometry [115] and set to an uniform field of 1%.

On the basis of the wind tunnel lower chamber geometry, a numerical model was created. Inlet is defined by a Dirichlet boundary conditions - velocity field, uniform turbulence intensity 1% and default viscosity ratio $\mu_t/\mu = 1$. Outlet is defined by ANSYS CFX Opening boundary, that permits movement both into and out of the domain. In this case the flow direction was constrained as normal to the boundary. Neumann boundary condition is set for relative pressure (zero gradient at 0 Pa) and Dirichlet condition for turbulent conditions (uniform turbulence intensity 5%, default viscosity ratio $\mu_t/\mu = 1$). All other external surfaces are defined as smooth, no-slip walls. The centre of the global coordinate system is set in the centre of the domain inlet, with flow direction along Z axis.

The mesh (Fig. A1.4) was created in ICEM CFD 17.1 software. It is an unstructured, tetra-dominant mesh, concentrated in the test section region and in boundary layer (with generation of prismatic elements). Dedicated mesh density studies were performed to see the influence of degree of mesh densification - overall and in boundary layer. The final mesh has $15.2 \cdot 10^6$ elements and ensures dimensionless wall distance y+ at all no-slip walls lower than 3.

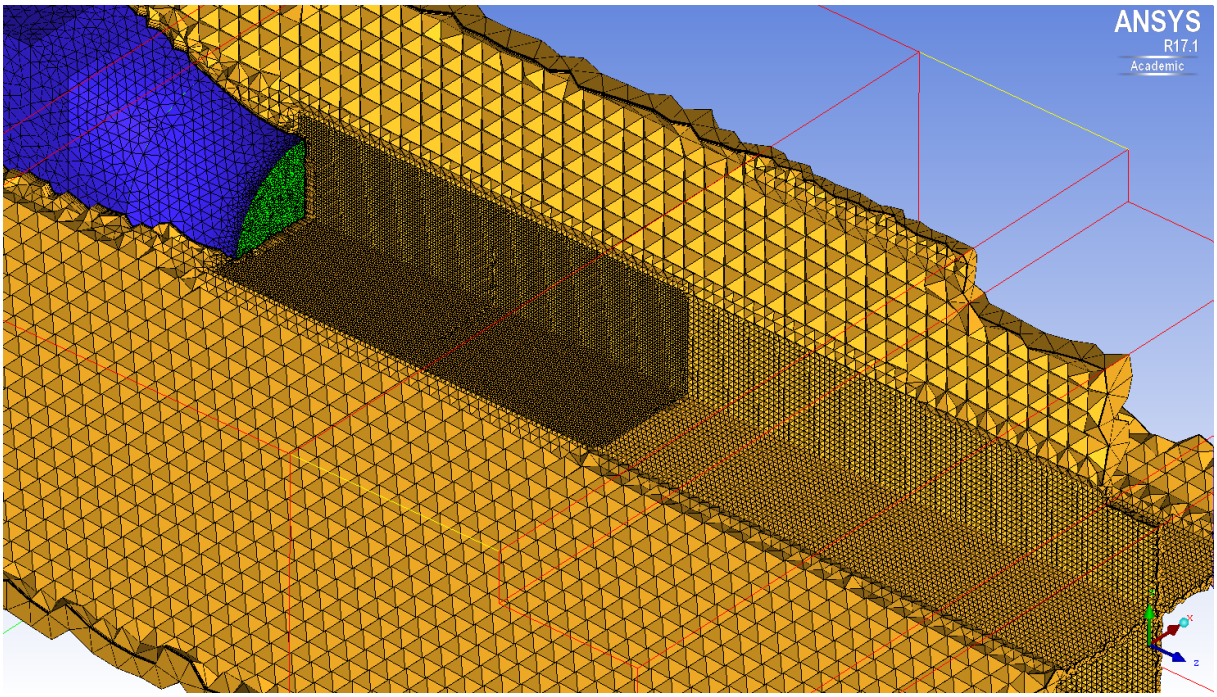

Fig. A1.4 Sectional view of wind tunnel chamber mesh (yellow); wind tunnel marked in blue, inlet in green

"*Air at 25°C*" of properties from standard ANSYS Material Library is the considered fluid (see Tab. 6). It defines dry air at reference temperature 298 K (25°C) and pressure 101 325 Pa (1 atm). The fluid is considered to be an ideal gas and the simulation is isothermal (T = 298 K). The simulations were of steady-state type, with pseudo-timestep $8.25 \cdot 10^{-3}$ s and in transient mode with the same timestep value. k-ω SST with standard set of coefficients was the chosen turbulence model. Both turbulence closure and pseudo-timestep were objects of sensitivity studies. High resolution modelling was used for solution of both flow and turbulent quantities equations, due to expected high pressure gradients. Double precision calculation was applied, due to significant differences in elements' sizing.

To validate the simulation model, numerical results were compared with available experimental data. These are velocity fields at vertical and horizontal lines at 1 m (A in Fig. A1.2) and 2 m (B ibidem) from the domain inlet. Figure A1.5 compares experimental (continuous line), numerical steady state (dashed) and time-averaged transient (dotted) data (averaging time 8.25 s). At distance of 1 m from the domain inlet the compared numerical data shows very little qualitative and quantitative differences. In the steady-state analysis a velocity surplus in the lower, and deficit in the upper part of the fluid stream are observed. Compared to experiment, in horizontal distribution both simulations underestimate the magnitude of free stream axial velocity, while correctly depicting its drop farther from the core. In vertical axis an asymmetry of flow is visible both in experimental and numerical data, with higher flow velocities in the lower part of the core. The transient model is able to predict the velocity magnitude more accurately than the stationary one, but the results obtained with the latter may also be considered as correct. At the distance of 2 m from the domain inlet two main phenomena are visible: overestimation of the degree of asymmetry of the flow stream and underestimation of the velocity magnitude by both simulations. In what concerns the former of the two, it is much more significant in the case of the steady-state analysis. This supports the hypothesis that the flow is actually non-stationary. The steady-state analysis results may therefore only be considered as an approximation of flow picture, dependant on the time instant when the simulation was stopped, and their results should mainly be treated in qualitative, and not quantitative manner. As to the transient analysis results, even though they follow the experimental curve more properly, they still tend to underestimate the velocity magnitudes.

Table A1.1 compares the magnitudes of axial velocity in flow core. This notation is used to describe the area, in which the velocity distribution is roughly uniform, and its magnitude is comparable to that at the domain inlet. The core has circular cross-section of diameter varying in streamwise direction, equal to 0.6 m at the inlet and 1 m from it and 0.4 m at 2 m from the inlet. According to the analysed data, the numerical results are of lower values than the experimental ones by approximately 0.5%. It is therefore reasonable to state that an object tested in this location will operate in similar conditions as in real-life experiment. More significant differences are visible farther downstream, especially in the steady state analysis. This is also visible in the velocity distributions discussed previously, as the steady state curve is significantly bent towards negative x and y coordinates. This once again underlines the fact, that for a more profound flow nature study time-averaged data should be considered.

Due to the complex nature of the analysed flow, it is advisable to first study its overall character. For that purpose the time-averaged velocity fields obtained from the transient simulation were analysed. Figure A1.6 presents the distribution of dimensionless velocity V/u_{ref} (u_{ref} = 17.25 m/s is reference velocity magnitude[2]) contour and vector plots. Red arrows denote main mass flow directions, while purple arrows - the main vortex structures. In the test section (marked TS) the flow direction follows the Z axis. The free stream core is cone-shaped, roughly axisymmetric with respect to the Z axis. This is conformal with the experimental results presented earlier on, where diminution of high-velocity region cross-section was observed. Farther on, downstream the TS, the free stream approaches the chamber wall and splits up. The main part of the mass flow D1 is directed towards the empty part of the chamber, denoted as RZ (recirculation zone). In this region an intensive mixing of the flow is

[2] Velocity measured in point (0.0,-0.2,0.0), location in which the measurements of reference velocity for wind turbine analysis were made; marked ML (measurement location) in Fig. A1.3

observed, manifesting itself in appearing and disappearing local vortex structures that were observed in the instantaneous flow visualizations. Vestigial amounts of fluid from RZ interact with that in TS, although these interactions do not seem to interrupt the flow in the free stream core. This is an important observation, as it suggests that the flow recirculation effects in RZ may be omitted in future numerical studies, and the flow domain may be simplified. In RZ a significant vortex V1 structure is created. It influences the free stream downstream the TS in a much more substantial way. Due to V1 being a zone of relatively low pressure, the stream is significantly bent towards RZ. It is also important to underline, that it is from the RZ region that the majority of mass flow is evacuated from the domain.

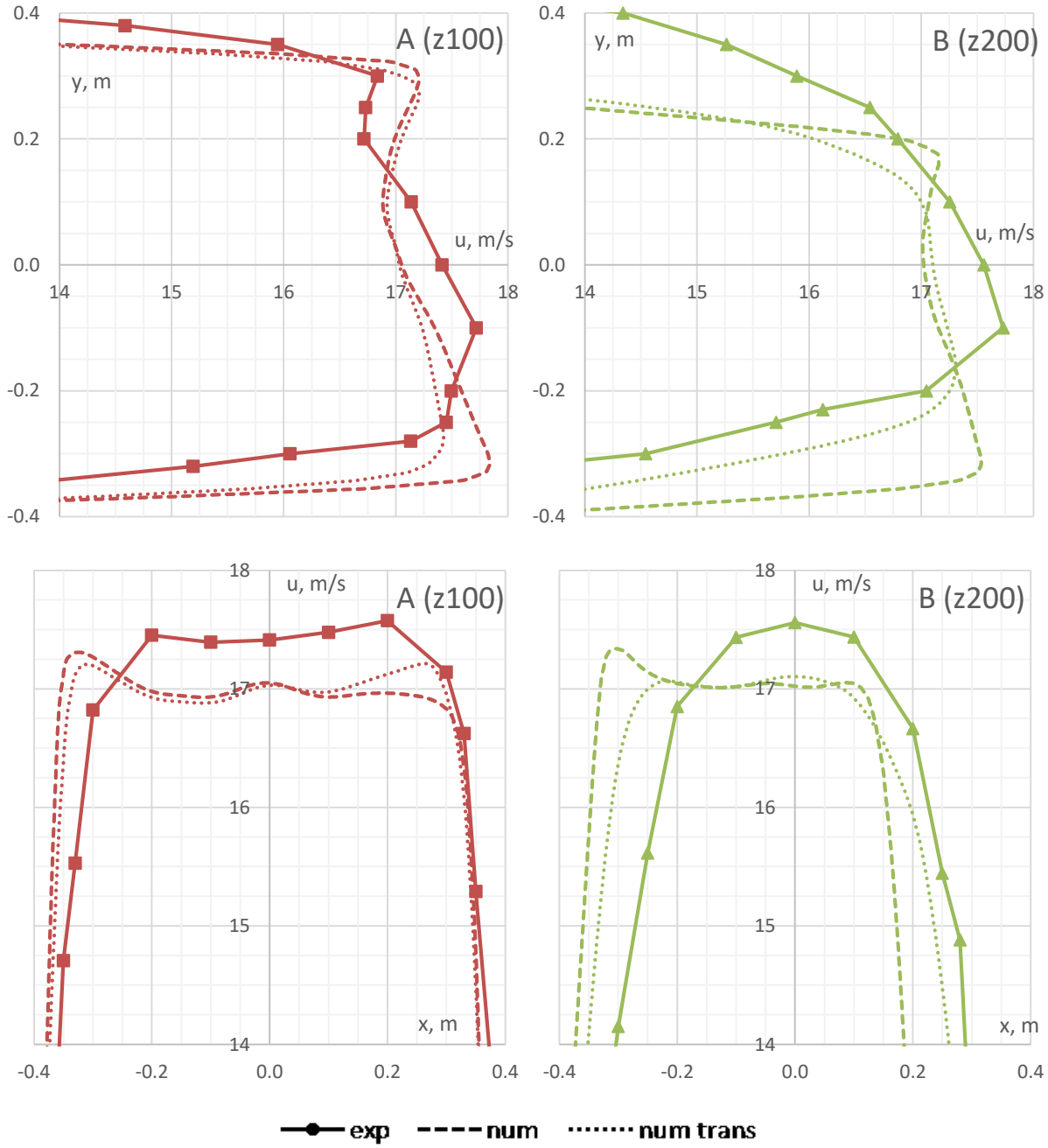

Fig. A1.5 Axial velocity vertical (top) and horizontal (bottom) distribution at locations A (z100) and B (z200); continuous line marks experimental data, dashed – numerical steady state, dotted – numerical transient

A significant amount of mass flow is transported in the direction D1 (towards positive x coordinates). Movement of the fluid provokes a creation of an elongated vortex structure V2. The remaining part of the stream is deflected in the D3 direction, vertically down (towards negative y coordinates). It is important to notice that there is virtually no deflection of the fluid vertically upwards, towards positive y coordinates and the outlet. This fact, seemingly unintuitive, is due to the low parts of the ceiling in this location. Nevertheless, the vortex region V4 is created under the chamber's ceiling. It is also worthy of note, that the structures V1 – V4 are cross-sections of a bigger, global vortex ring, placed approximately in the XY plane. Its presence is due to driving the fluid into movement by the free stream in TS, and flow mixing in RZ.

Tab. A1.1 Mass flow averaged axial velocity in free stream core (i.e. control surface of given diameter)

Z, m	Free stream core diameter, m	Average axial velocity u_{ave}, m/s			Relative error, %	
		Experiment	Steady state simulation	Transient simulation	Steady state simulation	Transient simulation
0	0.6	17.06	17.03	17.03	- 0.18	- 0.18
1	0.6	17.17	17.11	17.08	- 0.38	- 0.50
2	0.4	17.20	16.91	16.97	- 1.68	- 1.30

The domain zones other than the aforementioned, placed in the negative z coordinates, are mainly stagnation regions. Their contribution to the main flow characteristics in TS and RZ is vestigial, and thus they will be neglected.

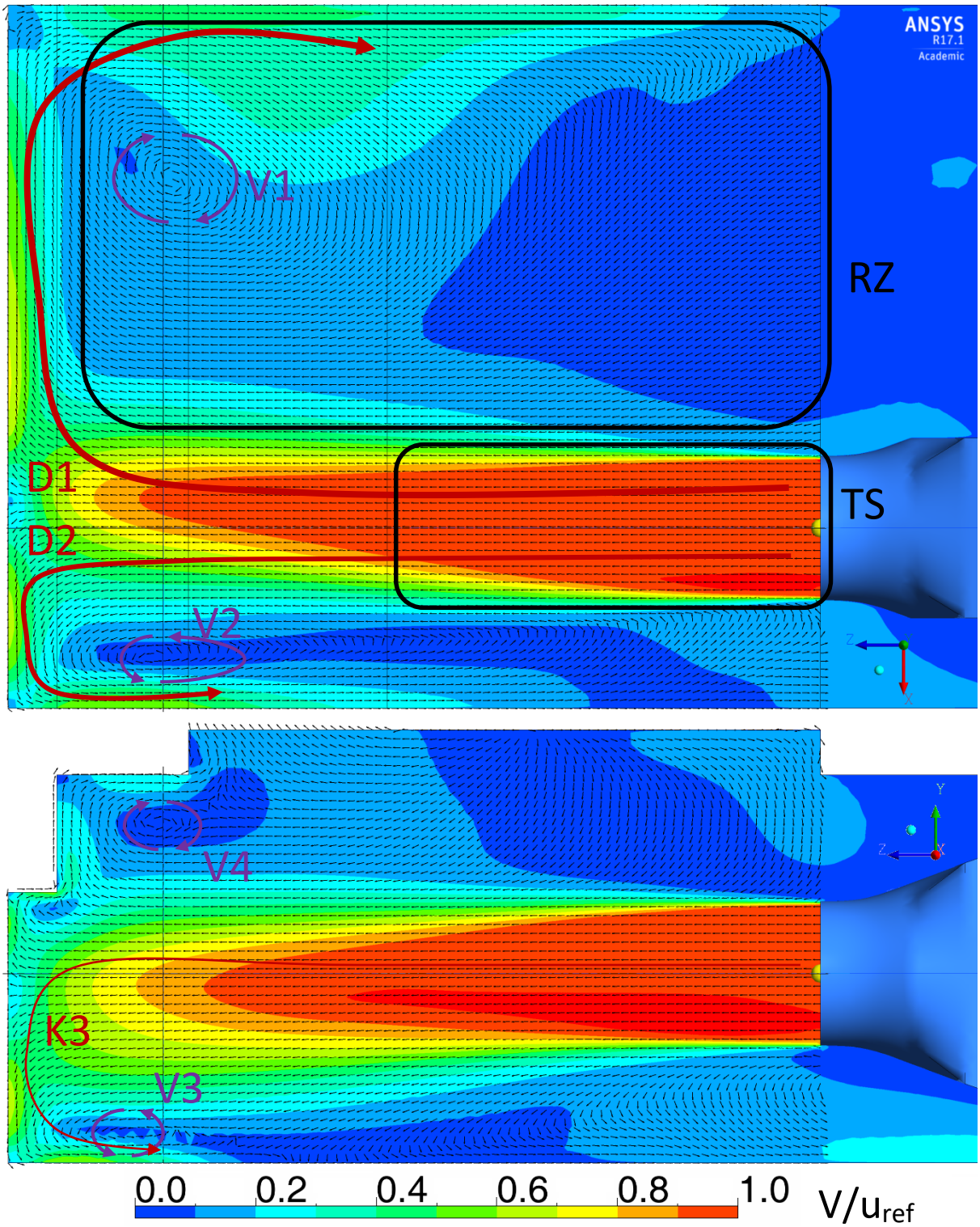

Fig. A1.6 Dimensionless velocity fields contour and vector plots in YZ (x = 0 m, top) and XZ (y = 0 m, bottom) planes; red arrows denote main mass flow directions; purple arrows denote main vortex structures

Appendix 2. Test stand preparation and diagnostics

This chapter presents the test stand examination process prior to the actual experimental campaign. It covers aspects such as calibration of the equipment, analysis of the acquired signal and assessment of distinct rotor specimens performance.

A2.1 Equipment calibration, test stand influence assessment

Prior to proper measurement campaign a rudimentary calibration of torque and pressure difference transducers was performed. The latter was calibrated with the use of a portable pressure calibrator Druck DPI610-IS. For other devices, manufacturers' characteristics were used, since it was impossible to ensure more reliable calibration using the available equipment (notably for the force plate).

The torquemeters were first calibrated statically with a system of masses suspended on a long cord at a known distance from the rotation axis. It followed from the performed experiences, that the system possessed a residual idle torque. Its value was measured by torquemeter to be independent from rotational velocity, but different in static and dynamic operation. Current generated by the system, which is proportional to the shaft torque, was measured as well, and was proved to be independent from rotation direction. To estimate the value of the bias measured by the torquemeter, the dynamic torque was measured and compared for both directions of rotation of the shaft. This was done by turning the torquemeter (switching places between measuring and drive side) and using the same rotor specimen. The resultant characteristics from both devices for test stand T1 at upwind operation are visible in Fig. A2.1. The data from torquemeter is already adjusted for the examined bias. It is noticeable that the magnitudes of torque measured from both devices are different, with the one coming from torquemeter being higher than that from generator. It is a sensible observation, since the mechanical torque on the shaft is converted with a certain efficiency. Using the information obtained with the use of generator it was possible to observe that the generated torque is equal for both direction of rotation. On that basis the correcting constant for torquemeter was determined, to ensure the same behaviour in both measurement directions, as seen in Fig. A2.1.

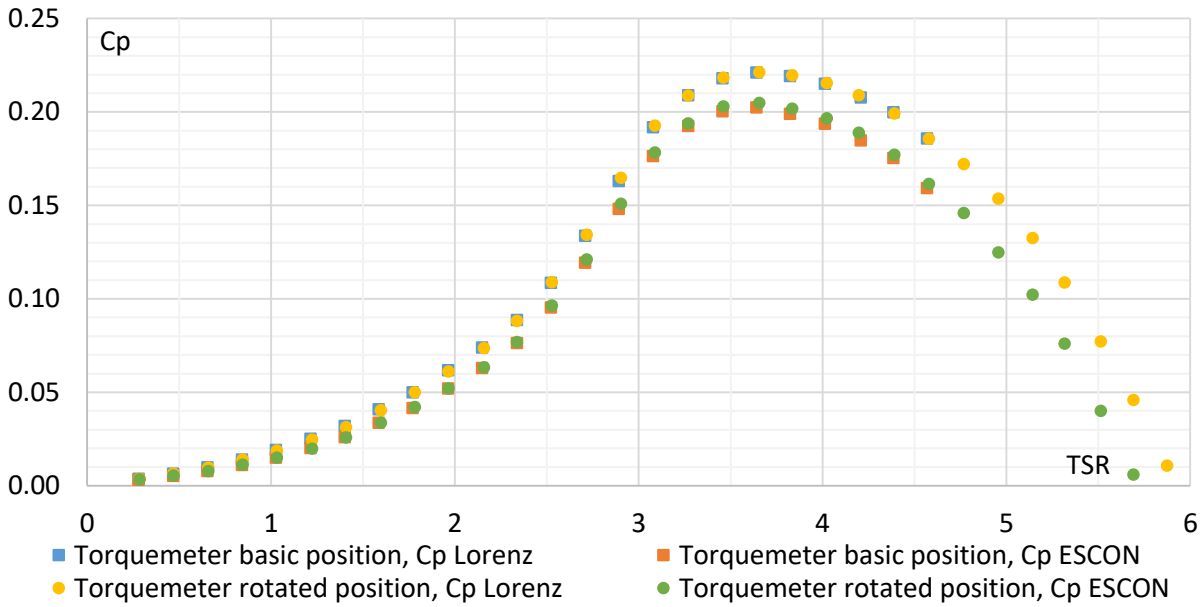

Fig. A2.1 Power coefficient Cp as a function of tip-speed ratio TSR, as measured by torquemeter (*Lorenz*) and motor controller (*ESCON*); wind speed 17.7 m/s, test stand T1 upwind, rotor R1

A study was also performed for both test stands to check their idle (i.e. without rotor) characteristics: test stand drag and bearings' friction. Due to the relatively small scale of the tested models, these factors may influence the obtained results in a non-negligible way. Test stand drag (axial force) was measured at different wind velocities, to supress its contribution to the values measured by the force plate in rotor studies. The bearings' friction was measured at different rotational velocities, to estimate the magnitude of shaft kinetic energy lost due to viscous forces. It was assumed that the rotor axial force does not influence significantly the normal operation of bearings.

A2.2 Fourier analysis of the obtained signals

Before performing the actual measurements, the test stand Fast Fourier Transform (FFT) analysis was performed to determine the natural frequencies of the system and vibration sources. This knowledge may be then used to ensure the safe operation of the test stand, facilitate interpretation of the signals and/or permit eventual filtering. The measurements were made using the force plate and torquemeter, with 65 536 samples taken at acquisition rate of 4 000 Hz .

In the first stage, the static analysis was performed. The test bench was examined for natural frequencies at the state of a rest. The test stand is mounted on the weight, which itself is mounted to the metal base. This metal base is separated from the concrete floor by a layer of rubber, to damp the possible external vibrations. Thus the main sources of vibrations measured in this stage are assumed to be the Prandtl tube and the test stand itself, both connected with the metal base. The vibrations were excited manually, by hitting a hammer near the place, where the test stand is mounted to the force plate. Figure A2.2 presents the results of FFT modal analysis of the signals collected in three configurations: when neither the Prandtl tube nor the test stand are present (red), when only the probe is mounted (green), and when both the probe and the test stand are present. By analysing the presented spectra of force signals (Fig. A2.2 top) it is possible to conclude that the test stand normal frequency is situated at approximately 11.5 Hz. This frequency was also observed in the further analyses, varying slightly with mounting/demounting the rotor blades etc. The natural frequencies associated with the Prandtl probe are situated in the region 30 – 40 Hz, as well as at about 220 Hz. For frequencies in range 220 – 270 Hz the spectra vary significantly with removal of the test stand. The reason for that is most probably due to the construction of the mounting system of test stand to the force plate. After dismounting the test bench, the mounting system may move freely, unlike when the test stand is in place. Thus the additional natural frequencies appear. As to the torque signal (Fig. A2.2 bottom), the dominant frequencies are shifted towards much higher values. The torquemeter is connected rigidly with the motor and bearing unit. Thus it registers mainly the natural vibrations of the measuring and control track, unlike the force plate, which measures primarily the vibrations of the entire structure. To conclude it is important to note, that except for the aforementioned test stand and Prandtl tube natural frequencies, the other frequencies are beyond the range of operation of the wind turbine system, that is 12 000 rpm (200 Hz).

In the second stage a dynamic analysis was performed. The results from weight and torquemeter were analysed for cases when the test bench would be subjected to excitations from the turning wind turbine rotor, operating wind tunnel, or both at the same time. The latter results are consultable in Fig. A2.3. As for the force signal spectrum (top), the dominant frequencies are associated with the odd multiples of wind turbine rotational speed (50 Hz, 150 Hz, 250 Hz). The 50 Hz frequency is associated with rotor imbalance (no balancing was performed). 150 Hz is due to the fact that the rotor has 3 blades, which interfere with the flow. Examples of such an interaction may be the rotating wake

colliding with the mounting pole, or interaction of Prandtl tube wake with the rotor. An important peak in the force signal spectrum is also observed at the natural frequency of the test stand, determined previously as approximately 11.5 Hz. Owing to the overall signal spectrum is also the frequency associated with the operating motor-ventilator system. The ventilator, directly mounted to the asynchronous motor, was in this case turning at approximately 37.6 Hz and this frequency is directly visible in the signal spectrum. As for the torque signal, once again the multiples of the turbine rotational velocity are the dominant frequencies. In this case the explanation is traced back to the bearing system. System's natural frequency is also visible in the spectrum.

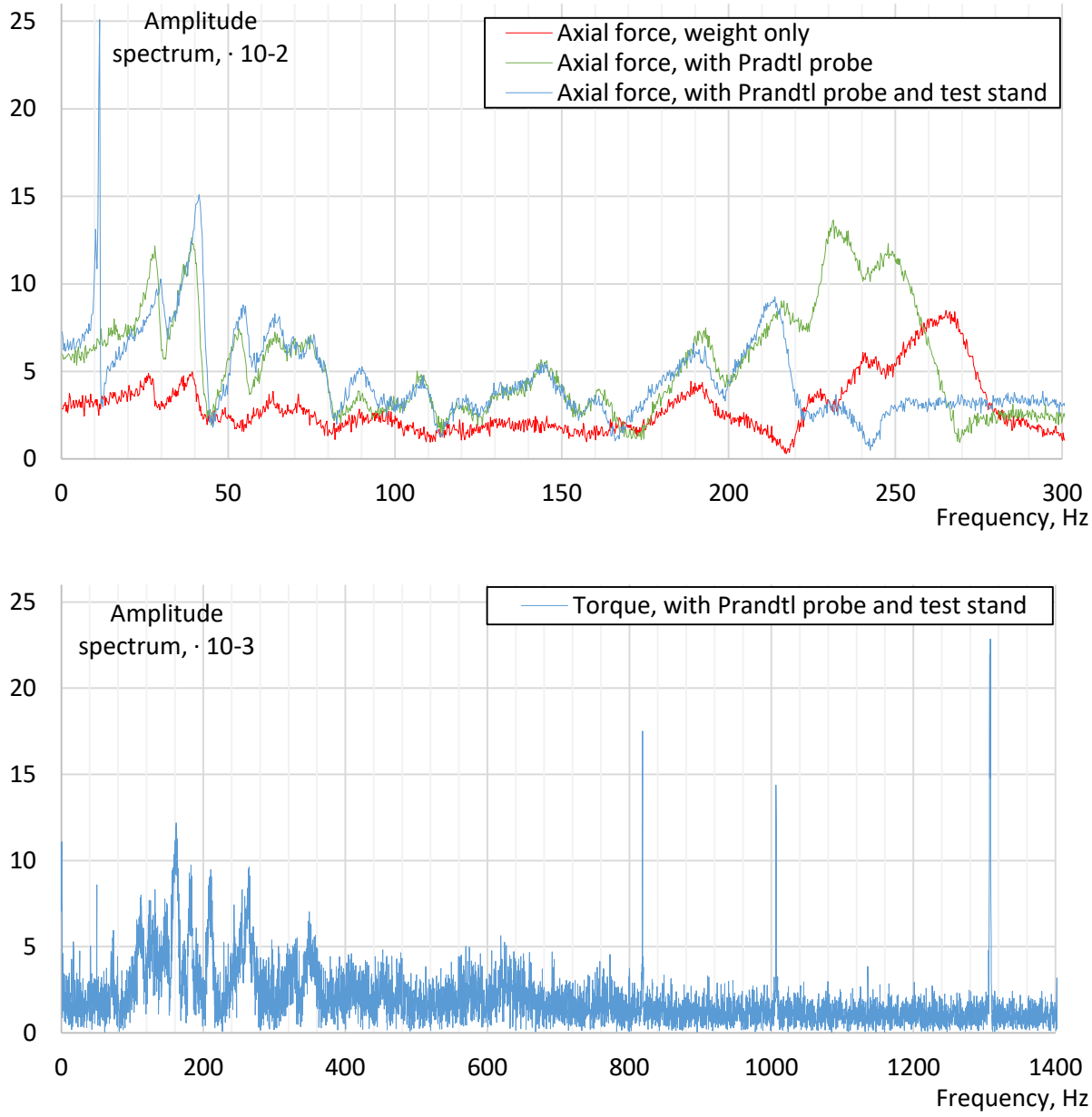

Fig. A2.2 Axial force (top) and torque (bottom) signal amplitude spectra at different test bench configurations; notice different exponents for vertical axes and ranges for horizontal axes

Using the presented analysis, it is possible to determine beforehand certain test stand operating conditions, that may be potentially harmful to the system and may distort the measured signal. The interference between rotational speeds of the tunnel ventilator and the wind turbine (as well as its

multiples), possibly leading to beating, may be identified as one of them. Low rotational speeds should also be exploited with vigilance, due to possible interaction with the system's natural frequency.

The above mentioned considerations permit to identify frequencies deforming the measured signal. Based on this information, a simple 2nd order band reject Butterworth filter was constructed and tested. It damps the signal frequencies being the multiple of wind turbine rotational velocity, as well as the frequency associated with the wind tunnel motor-ventilator. The comparison of raw (blue) and filtered (yellow) signal is visible in Fig. A2.3.

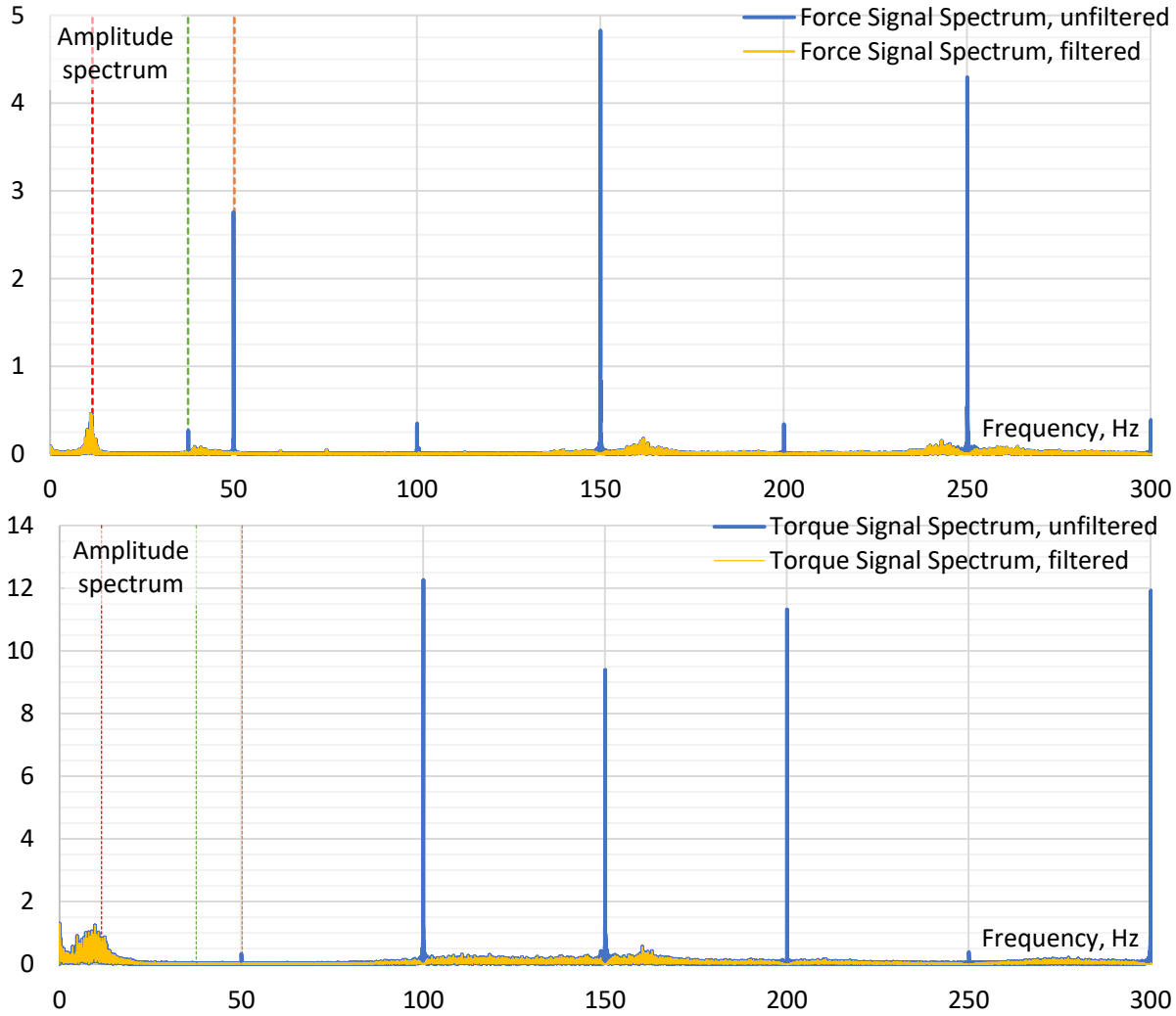

Fig. A2.3 Axial force (top) and torque (bottom) signals in frequency domain: raw (blue) and filtered (yellow); wind speed 13.8 m/s, rotor speed 3015 rpm; dotted lines mark natural frequency of the test stand (11.5 Hz, red), wind tunnel motor-ventilator (37.6 Hz, green), wind turbine rotor (50.2 Hz)

A2.3 Hysteresis

To check the repeatability of the obtained results, a rudimentary test of measurements' hysteresis was performed on both test stands. The R1 rotor was tested at the wind velocity of 17.7 m/s, with first increasing and then decreasing rotational velocity (and thus TSR). The results are visible in Fig. A2.4. In what concerns the power coefficient Cp the differences are relatively small. For TSR values up to 4 the relative difference is lower than 1%. The difference grows bigger at higher TSR, where the values of Cp are lower. These variations may be attributed to the boundary layer behaviour (separation when

increasing and reattachment when decreasing rotor velocity). However, the concerned values are sub-incertitude level, and may be simply to the measurement uncertainties. In the case of thrust coefficient the hysteresis is much more significant. In both cases the maximal value of Ct occurs at TSR ≈ 4. However in the case of decreasing TSR this peak is more apparent, while for decreasing rotor velocity the characteristic is more flat. The relative difference in this region is equal to approximately 5%.

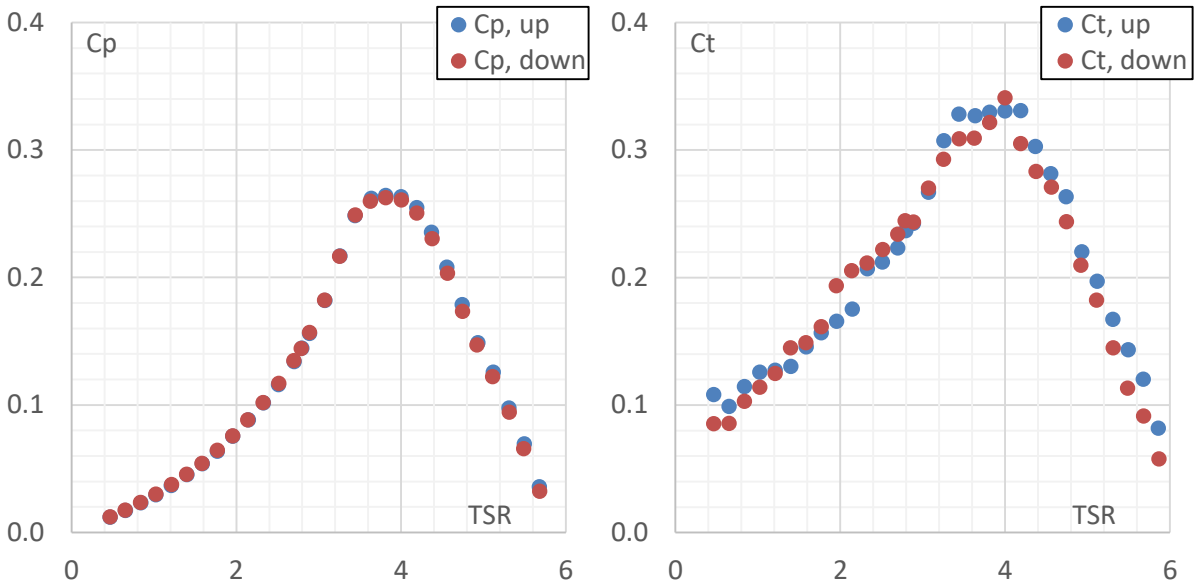

Fig. A2.4 Hysteresis of Cp (left) and Ct (right); T1 test stand, normal rotor, average wind speed 17.7 m/s; "up" corresponds to data acquisition when increasing, "down" when decreasing rotational velocity

A2.4 Various types of blades

The rotor blades (along with numerous elements of test stand) were manufactured in 3D printing technology. Among its most important features the high repeatability and fidelity in model reproduction may be named [116]. However, especially when printing small models, the resolution of the process plays an important role. If it is high relative to the model size, the quality of final product may be deteriorated. In particular, the high relative surface roughness may be problematic when studying flow over objects at low Reynolds number.

Figure A2.5 shows the different compared rotor blade specimens:

- (a) and (b): blades made in FDM (Fused Deposition Modelling) technique. The material is ABS (Acrylonitrile butadiene styrene), plastic characterized by a relatively high strength and machinability,
- (c) and (d): blades made in FDM technique. The material is Ultrat, a derivative of ABS characterized by increased mechanical properties, tailored for 3D printing process,
- (e): blade made in SLS (Selective Laser Sintering) technique of Nylon. This synthetic polymer crates fibers characterized by high tensile strength,
- (f): blade made in MJM (Multi-Jet Modelling) technique out of UV-curable raisin. Liquid plastic is distributed by printer nozzles and hardened by UV light. It is appropriate for printing of small details.

After printing, the blades may undergo an additional, in-house surface treatment process (specimens (b) and (d)). It consists of filling, fine grinding and lacquering. This protects the blades and smoothens

their surface. A 3D object of high surface quality, good coherence with CAD model, and augmented mechanical properties is the result of these processes.

Fig. A2.5 3D-printed blades of various materials: ABS (a, b – before and after surface treatment), Ultrat (c ,d – before and after surface treatment), nylon (e), acrylic raisin (f)

Six rotor specimens were tested in wind tunnel, to check the influence of material and technique of manufacture and surface treatment. The results are visible in Fig. A2.7. All blade sets predict similar optimal TSR, and maximum Cp values are observed at range 0.23 – 0.25 (save it for (b)). Except (b) and (e) all blade sets identify the rotor idle speed at TSR equal to approximately 6.

It is visible that the used finishing technique modifies the rotor performance in a non-negligible manner. For Ultrat blades this resulted in the rotor performance curve being more steep and narrower, but attaining higher maximum Cp. The precise reason behind this phenomenon has not been determined with 100% confidence. Perhaps the blade with polished surface operates in transitory boundary layer regime, which results in more dynamic changes in rotor performance.

Higher Cp for polished blades is also visible in ABS blades. These were manufactured on a different printer, of poorer resolution. This resulted in higher surface roughness and blade geometry deterioration. They were also more prone to deformation during operation. The same problem occurred when the nylon blades were tested – they bended significantly under aerodynamic loads. This significantly deteriorated their main advantage, that is a splendid model representation and very low surface roughness. The same properties were also observed for UV-treated blades, but their

manufacturing technique proved faulty – the blades were easily plastically deformed (bent) in storage, thus losing their original shape.

The final choice was made to use the Ultrat blades with no surface treatment (set (c)). Although this set was observed to give the lowest values, the performance curve shape seems to be the most uniform. It was also noticed that this set of blades operates in the most repeatable manner, almost without hysteresis, and with very little deformation. It is also important to note that this blade set could be quickly reproduced at the IMP TUL 3D printer in case of an accidental blade destruction.

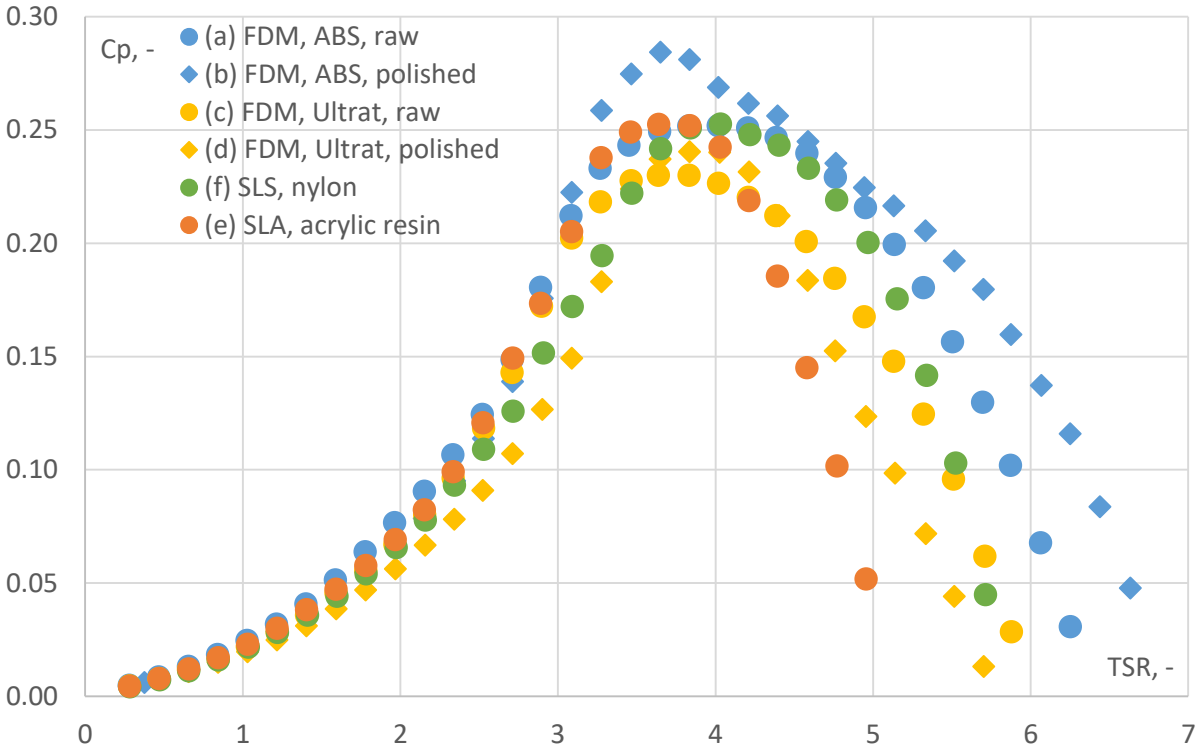

Fig. A2.6 Performance of rotor specimens with blades made of different materials and/or techniques

A2.5 Upwind vs. downwind configuration

Upwind position test stand will be operated in downwind configuration. The influence of fixation pole is assumed to be a non-negligible issue. The flow becomes highly distracted due to high local velocity gradients in the pole's aerodynamic shadow. Heterogeneous loading of the blades may lead to unstable operation of the rotor, and increase the fatigue wear of the blades. The power outcome decrease is also expected, as the rotor operates in unfavourable conditions in certain blades' positions.

To quantify the influence of this phenomenon on the rotor performance, R1 rotor was examined for two test stand configurations, upwind and downwind. The rotor position was always fixed at 1 m from the test section inlet. The results are visible in Fig. A2.7 (points marked in red). For Cp the degree of influence of the test stand configuration varies with TSR. As the latter rises, the difference becomes higher. The reason for such a behaviour is connected with the trigonometric relationships between axial and rotational velocities. At low rotational velocity the inflow angle θ is approaching 90°. In this range the variations of tangential force $L \cdot \sin\theta - D \cdot \cos\theta$ are relatively slow. The dominant factor contributing to θ changes is therefore the magnitude of rotational velocity. As θ increases, the variations become more evident. If the axial velocity component is reduced, θ will attain lower values

and the optimum angle of attack α will not be reached. This is also the reason why the rotor idle velocity is lower. In the meantime the optimal TSR (at which Cp = max) remains the same for both configurations.

A2.6 R1 vs R2 rotor

Two different rotor specimens will be used in the considered study: “basic” (R1) and “mirrored” (R2). 3D printing offers a very good repeatability of manufacturing process, nevertheless both rotors were compared for their performance (in downwind configuration). Squares shown in Fig. A2.7 represent rotors: R1 (positive TSR range) and R2 (negative TSR range). A very high level of Cp and Ct similarity is observed for both specimens, with both characteristics being almost symmetric with respect to the corresponding vertical axes. Hence it may be stated that the results obtained from downwind and upwind test stand configurations may be compared with one another and that the conclusions drawn from the downwind test stand configuration may be extrapolated onto more general cases.

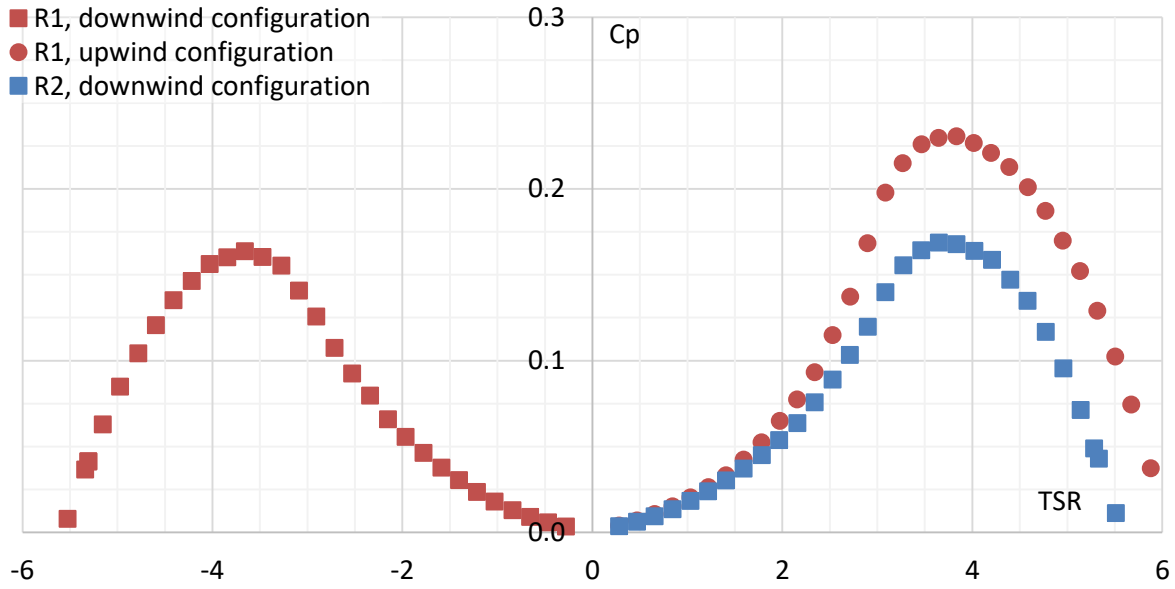

Fig. A2.7 R1 (red) and R2 (blue) in upwind (circle) and downwind (square) T1 configuration, wind speed 17.7 m/s

Appendix 3. Wind as energy source – estimation and evaluation

By the simplest definition, wind energy is a transformed form of solar energy. Heated air, being lighter than the cold air, ascends. Low-pressure zone thus created attracts the movement of (colder) air, along the surface of the Earth. In the high parts of the atmosphere the wind cools down, and descends back towards the surface of the earth. Thus a complete circle is created [27].

Apart from the fact that certain parts of the earth receive more sunshine than the other, the wind is also increased by different altitudes (ex. "downslope" winds) and features of the Earth's surface. The strong winds at coasts are provoked by the difference in specific heat of water and soil, that causes difference in heating above surface of water and soil. It is also important to mention the influence of terrain features. Long, unobscured paths (like that over lake or sea) promote wind development. Natural and artificial obstacles (hills, buildings) diminish the wind velocity. The latter is also curbed as the terrain roughness rises, for example over forests [25]. At even bigger scales, the wind direction is affected by the Coriolis forces, caused by the rotational movement of the Earth [27].

From the point of view of wind energy it is, obviously, the best to place a wind turbine over a terrain with high-speed, preferably steady wind. In order to choose this kind of location, a site assessment is required. This is traditionally done via an experimental campaign, by employing anemometers of various types and construction (see Fig. A3.1). Typical measurement consists of collecting wind speed and direction. This permits to create a so-called wind rose, presenting the distribution of wind intensity as a function of direction.

Fig. A3.1 Popular devices for wind velocity measurements: cup anemometer [117], ultrasonic anemometer [118], LIDAR [119]

In scope of the project *Twin-rotor Diffuser-Augmented Wind Turbine (DAWT) for Polish wind conditions* a test site assessment was performed, using ultrasonic anemometers Gill WindObserver II. It is a 2D anemometer capable of measuring 360° range of wind direction at the maximum frequency of 10 Hz. The test was done to assess the wind resources in a Polish suburban location (Brojce, 16 km South-East of Lodz), where a domestic wind turbine would likely be placed. The data was taken over the period of 33 months at 2 heights: 2.25 m ("Ground") and 10 m ("Roof"). Results are presented in Fig. A3.2, along with indication of dominant wind directions and how they are affected by the local terrain features. Long paths, like fields in the West, facilitate development of wind streams. Obstacles, both artificial (houses) and natural (forests) decrease the wind speed. Surprisingly, the latter was also

observed to serve to direct the wind stream, by forming a passage between two forested regions. This results in an increased occurrence intensity of winds from South-East.

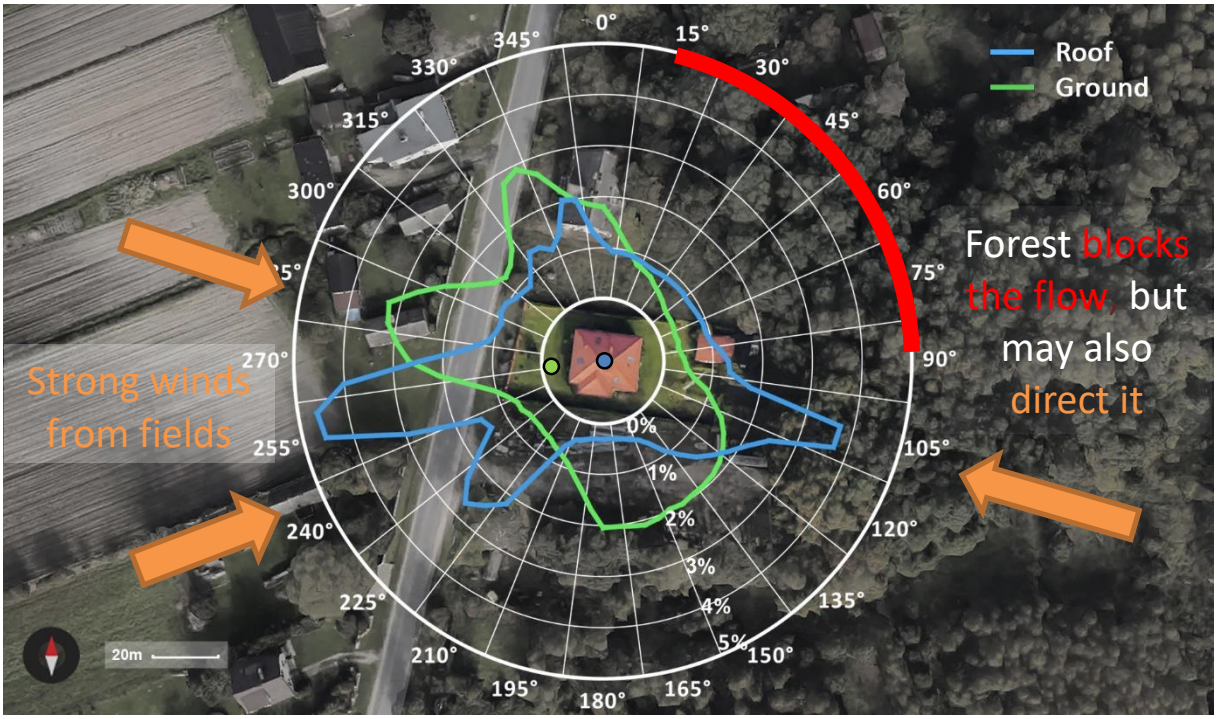

Fig. A3.2 Exemplary wind rose in a Polish suburban area; measurements taken at two elevations, marked with dots: 2.25 m ("Ground", green) and 10 m ("Roof", blue); results are 2-year average

Wind velocity is not constant over time. In micro scale this corresponds to turbulence and gusts. It is usually preferable to decrease the intensity and likelihood of occurrence of both of these phenomena, since they increase the flow non-uniformity and dynamic loads on rotor and the power transmission/conversion chain. Wind velocity also varies depending on the time of the day: it is usually the strongest in the afternoon, since the results of non-uniform heating at different locations are most visible at that time. Finally, the wind velocity changes on an annual pace as well, depending on the intensity of sunlight at different seasons of the year. This comes from different amount of solar energy received at a specific location, depending on its position with respect to sun [25]. This change depends strongly on such features as location' situation, such as distance from equator. The diurnal and annual evolution of wind speed at the considered location is visible in Fig. A3.3. The results are not corrected for the influence of temperature stratification. It is visible that the studied location is far from perfect when it comes to wind turbine installation. Average wind velocities at 10 m AGL are in the range of 1 – 3 m/s. The winds are stronger in the wintertime and in the afternoon, as expected.

As in case of every viscous flow near a surface, the wind is laden with the boundary layer effect, referred to as the atmospheric boundary layer. Big wind turbines tend to operate at relatively high elevations, at which the influence of this phenomenon is reduced. In their case it is an even more important aspect, since the non-uniform vertical wind velocity profile would cause non-uniform loading of the big-scale rotor. In case of small wind turbines the atmospheric boundary layer influence is important in that it decreases the wind velocity and increases the turbulence intensity. Numerous models are used to describe the wind shear profile $\overline{U}(h)$, among which log law (eq. (A3.1)) and more simple power law (eq. (A3.2)) may be cited as the most common:

$$\bar{U}(h) \propto \ln(\frac{h}{h_0}) \quad \text{(A3.1)}$$

$$\bar{U}(h) \propto h^{\alpha} \quad \text{(A3.2)}$$

h_0 (surface roughness length) and α (power law exponent) are empirical constants, that may be found in textbooks and standards to extrapolate the results obtained from one measurement height to an entire profile [27].

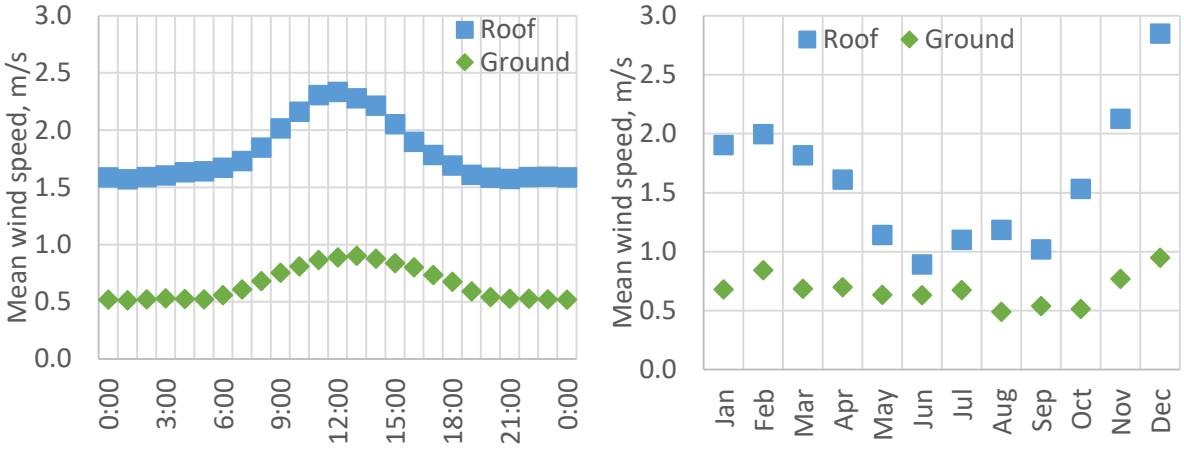

Fig. A3.3 Diurnal (left) and annual (right) evolution of wind speed at the considered location; measurements taken at two elevations: 2.25 m ("ground") and 10 m ("roof"); results are 2-year average

In some cases the time-consuming and relatively costly experimental wind assessment campaign is not achievable. Under such circumstances it is possible to refer to existing databases, for example wind atlases. These documents prove to be useful especially at the early stages of wind project. They may be used e.g. for determination of a potential site for a wind farm. They also serve as a tool for assessment of regional wind energy resources. Figure A3.4 presents the annual average wind velocity distribution in Poland (left, at 10 m AGL) and France (right, at 20 m AGL). It is noticeable that for both countries the vast majority of territory profits from wind speeds of order $3-4$ m/s at the aforementioned heights. This constitutes a starting potential for small wind turbine projects, providing the machines' cut-in speed is sufficiently low. It is also noticeable that the velocity is observed to increase dramatically near the coast (Northern Poland, Northern and Southern France). In both countries these regions are traditionally associated with strong winds coming from the Baltic Sea (Poland), English Channel, Atlantic Ocean and Mediterranean Sea (France). This justifies the location of wind farms in these regions and gives potential for installation of SWTs as well. Increased wind velocities are also observed in mountainous regions of both countries, although these locations are unfit for installation of wind turbines due to complex terrain and generally high fluctuations of the wind velocity [5], [120].

To fully assess the wind potential at a specific location, the average velocity must be accompanied by its distribution. Meteorological data collected at a specific location and over a specific period of time may be presented in the form of a histogram (see Fig. A3.5a). As it follows from experience, the dataset may be approximated by the so-called Weibull distribution, given by the formula:

$$f(U,\overline{U},k) = \frac{k}{\overline{U}} \cdot \left(\frac{U}{\overline{U}}\right)^{k-1} \cdot \exp\left(\left(\frac{U}{\overline{U}}\right)^{k}\right) \qquad \text{(A3.3)}$$

In eq. (A3.3) f is the probability density function, "likeliness" of occurrence of wind velocity U. $\overline{U}$ is the so-called scale parameter and may be approximated by average wind speed. k is the shape parameter, governing the "width" of the curve. In its most common approach, the value of k equals to 2, which results in a so-called Rayleigh distribution [25]. In Fig. A3.5a the experimental data is approximated by the Weibull distribution with $\overline{U}$ = 4 m/s and k = 2, conditions that may be assumed correct for a majority of locations in Poland and France.

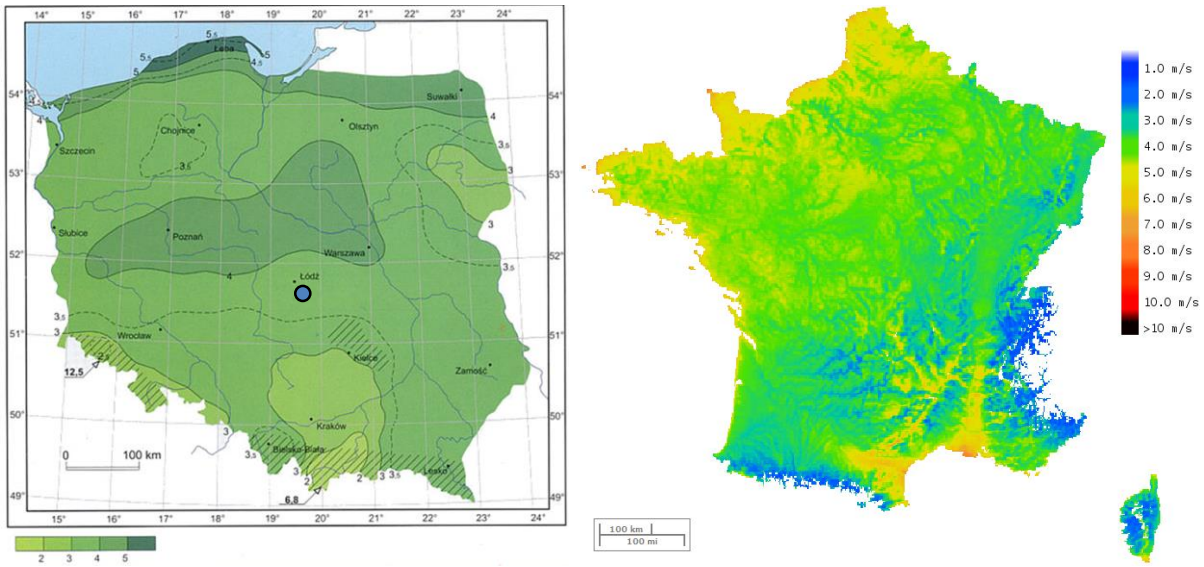

Fig. A3.4 Annual average wind velocity at 10 m AGL in Poland (left, [5]; blue dot denotes location of Brojce) and at 20 m AGL in France (right, [120]); note different colour ranges

The importance behind possession of wind resource distribution becomes evident once it is confronted with the wind turbine characteristic, such as an example given in Fig. A3.5b. It shows a power curve, that is the relationship between wind turbine output and wind velocity for a relatively small machine (rated power of 3 kW). It is visible that the wind turbine starts at wind velocity approximately 3 m/s (cut-in speed) and stops at wind speeds above 25 m/s (cut-off speed). Its rated wind velocity is 13 m/s. Such a characteristic is pertinent to the particular wind turbine and is a result of numerous factors, such as rotor Cp or drivetrain and generator efficiency. It is noticeable how in range between cut-in- and rated wind speed the output power is proportional to the wind velocity cube (as follows from equation (10)).

Finally, the two characteristics: site-specific wind distribution and turbine-specific power curve, can be combined to compute the Annual Energy Output. Multiplication of the theoretical power at the given velocity and the number of days when this velocity is expected, results in annual energy produced at this velocity. The total Annual Energy Output is a sum of these decremental energy values. It is visible that, due to wind turbine's cut-in speed the wind velocities of 3 m/s and less will remain almost completely unexploited. The wind turbine is expected to produce a vast majority of its Annual Energy Output in wind speed ranges 4 – 9 m/s. One has to note that the turbine will most probably not reach its rated wind speed.

In all, the subject of site-specific wind resource assessment is crucial form the point of view of a successful wind energy project [25]. In reality the scientific description of the wind resources at a given location may cover numerous additional aspects, such as turbulence intensity or atmosphere stratification effects. However, these features go beyond the scope of the research project *Twin-rotor Diffuser-Augmented Wind Turbine (DAWT) for Polish wind conditions* and the current thesis. Nevertheless, the analysis presented in this chapter indicates the challenges faced when developing a small wind turbine, such as the interest of decreasing the cut-in wind speed and maximising the performance at low wind velocities.

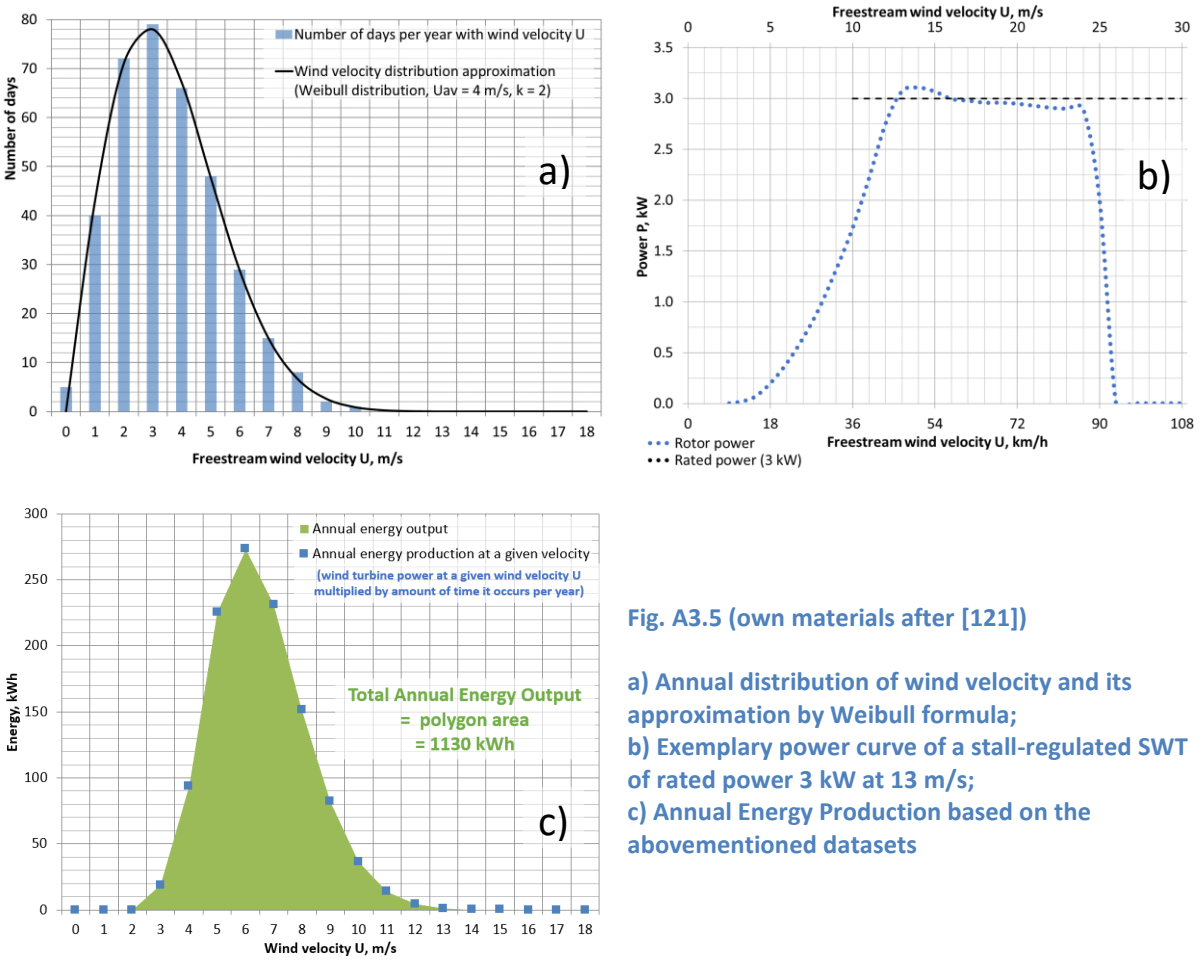

Fig. A3.5 (own materials after [121])

a) Annual distribution of wind velocity and its approximation by Weibull formula;
b) Exemplary power curve of a stall-regulated SWT of rated power 3 kW at 13 m/s;
c) Annual Energy Production based on the abovementioned datasets

Résumé de thèse

The hybrid simulation model for a twin-rotor diffuser-augmented wind turbine and its experimental validation

Modèle hybride pour simuler l'écoulement à travers un birotor éolien caréné et sa validation expérimentale

Hybrydowy model symulacyjny okanałowanej turbiny wiatrowej w układzie tandem i jego weryfikacja eksperymentalna

Michał Lipian, MSc

	Institute of Turbomachinery Lodz University of Technology	DynFluid Laboratory Arts et Métiers ParisTech
Directeurs	Prof. Krzysztof Jóźwik, PhD, DSc	Fawaz Massouh, PhD, MCF
Co-encadrants	Maciej Karczewski, PhD	Ivan Dobrev, PhD

1 L'introduction

Selon la directive de la Commission européenne « 20-20 by 2020 » [1] les pays de l'Union européenne (UE) doivent, d'ici à 2020, limiter leurs émissions de gaz à effet de serre de 20%, accroître leur efficacité énergétique de 20% par rapport aux niveaux de 1990 et augmenter la production d'énergie issue de sources d'énergie renouvelables (SER) à 20% du mix énergétique européen (15% pour la Pologne et 23% pour la France).

Selon l'Association Européenne de l'Energie Eolienne (EWEA), en 2015, une puissance éolienne de 1266 MW a été installée en Pologne. Un nombre dépassé seulement par l'Allemagne, il représentait 9,9% de toute la puissance installée dans les éoliennes de l'UE au cours de cette période [2]. Ainsi, à la fin de 2017, les éoliennes restent les principaux convertisseurs de SER sur le marché polonais: 5858 MW, soit environ 68% de la puissance totale installée de SER [3]. La structure du marché éolien polonais se concentre actuellement sur les machines de grande échelle concentrées dans les parcs éoliens. Malheureusement, la législation en vigueur en Pologne limite considérablement les nouveaux investissements de ce type [4]. Entre-temps, les ressources éoliennes polonaises (voir ex. [5]) semblent traiter de la collecte d'électricité localisée, où chaque consommateur d'énergie peut devenir un prosommateur, en répondant à ses propres besoins en électricité produits par les petites éoliennes (Small Wind Turbines, SWTs). Le haut rendement est un facteur clé dans de telles constructions, pour justifier économiquement leur utilisation.

En France, l'énergie nucléaire est un leader bien établi du marché depuis plusieurs décennies. En 2017 les centrales nucléaires ont représenté 71,6% de la production annuelle totale d'énergie électrique, suivies des centrales hydroélectriques (10,1%) et au gaz naturel (7,7%) [6]. La puissance installée des éoliennes en France a augmenté de 15,3% en 2017 mais, comme en Pologne, elle était principalement concentrée dans les parcs éoliens. L'accès à l'énergie électrique pas chère des centrales nucléaires et la pénurie de données précises sur les ressources éoliennes à de faibles hauteurs rendent les petites éoliennes difficilement rentables en France métropolitaine [7]. Cette situation change toutefois si l'on prend en compte la France d'outre-mer, où les SWTs peuvent répondre aux besoins de sites isolés. Un fonctionnement efficace et fiable est un facteur clé dans ce cas.

Les SWTs fonctionnent généralement dans les conditions de vent faible et dans une plage défavorable de valeurs de nombre de Reynolds. Cela limite considérablement les possibilités d'optimisation aérodynamique des pales et favorise la recherche de solutions plus sophistiquées. Les idées les plus prometteuses incluent l'éolienne carénée (Diffuser-Augmented Wind Turbine, DAWT), précédemment étudiée à l'Institut de la Turbomachine de l'Université de Technologie de Lodz (IMP TUL), et les rotors contrarotatifs (Counter-Rotating Rotors, CRR). Le diffuseur de l'éolienne carénée favorise l'augmentation du débit massique du vent à travers le rotor, ce qui se traduit par une puissance de l'éolienne et une énergie extraite plus élevées. Cette solution présente également l'avantage de protection en cas de la rupture des pales et le potentiel d'amortissement du bruit de l'éolienne. Le CRR explore la possibilité d'extraire l'énergie cinétique du vent dans le sillage. Cela concerne surtout la composante axiale de la vitesse du vent, mais peut également s'appliquer à la composante tangentielle, qui est normalement perdue sous la forme d'un sillage tournant.

Pour répondre aux défis ci-dessus, le projet *Twin-rotor Diffuser-Augmented Wind Turbine for Polish wind speed conditions* a été proposé. Il combine les concepts de l'éolienne carénée et de double rotor. Le DAWT est déjà commercialisé i.a. au Japon et aux États-Unis, ce qui prouve sa détermination. Dans

le même temps, il est tentant (et pas encore exploité) de profiter davantage de l'augmentation de la vitesse du vent due au diffuseur, en plaçant le deuxième rotor dans la ou les régions de vitesse augmentée. On espère que cette idée nouvelle augmentera l'efficacité globale du système, diminuant ainsi le prix effectif de l'énergie électrique par kWh et rendant l'investissement dans les énergies renouvelables raisonnablement motivé.

L'objectif principal de la thèse *The hybrid simulation model for a twin-rotor diffuser-augmented wind turbine and its experimental validation* est d'étudier le fonctionnement d'une éolienne DAWT à double rotor et d'analyser l'écoulement à travers ce type d'appareil. Cette tâche nécessite des outils avancés d'analyse de l'écoulement, à la fois numériques et expérimentaux. Cependant, en raison de la nature complexe de cas considéré, les méthodes expérimentales n'ont qu'une applicabilité limitée. Par exemple, les techniques de mesure du PIV (Particle Image Velocimetry) seraient très difficiles à appliquer pour des raisons techniques. Les tests expérimentaux sont en général limités par les effets d'échelle, qui se produiraient pour tester des modèles relativement petits, et qui ne sont pas présents a priori dans le cas de simulations. Par conséquent, et en raison d'une multitude de paramètres fonctionnels du système concerné, la thèse sera principalement orientée vers les outils de simulation. Cela est dû au fait qu'ils permettent une modification relativement facile de paramètres tels que la géométrie des rotor(s) et/ou leur position relative. Le caractère compliqué du problème rend cependant la modélisation complète des rotors (FRM, modèle de rotor complète) extrêmement consommatrice de ressources (en raison de la taille du maillage, du temps nécessaire aux calculs, etc.). L'idée de recourir à un modèle hybride simplifié semble donc raisonnable. Cette approche représente le rotor par de termes sources dans les équations de Navier-Stokes. Ces termes sources peuvent être appliqués à un disque représentant l'ensemble du rotor (ADM, modèle de disque actif) ou autour de lignes représentant les pales séparément (ALM, modèle de ligne active).

La campagne expérimentale dédiée, réalisée dans la soufflerie de l'IMP TUL, apportera une importante valeur ajoutée. Les résultats seront utilisés pour la validation du modèle et une analyse plus profonde de l'écoulement.

L'hypothèse suivante a été posée:

La création d'un modèle de simulation hybride d'une éolienne carénée à deux rotors contrarotatifs permettra une analyse approfondie du fonctionnement de ce système.

Les objectifs scientifiques suivants ont été supposés:

- création d'un modèle de simulation hybride pour l'éolienne carénée à deux rotors contrarotatifs (CRSR),
- création d'un banc d'essai et appareil expérimental du système susmentionné dans la soufflerie,
- l'analyse fonctionnelle du système et validation du modèle de simulation hybride sur la base de l'approche d'intégration expérimentation-simulation.

La thèse est composée de 8 chapitres et 3 annexes.

Le chapitre 1 présente la motivation du travail proposé et le contenu de la thèse. Il y a aussi la formulation scientifique du problème, et des objectifs scientifiques de la thèse.

Le chapitre 2 donne une introduction au sujet de l'énergie éolienne. L'historique de l'utilisation du vent et les aspects pratiques sont abordés, suivis de l'analyse de l'état de l'art dans le domaine des systèmes d'éoliennes carénées et éoliennes à deux rotors contrarotatifs.

Le chapitre 3 présente les concepts physiques essentiels et les formulations mathématiques utilisés dans la thèse. Cela comprend les principes de base d'un écoulement dans des éoliennes de différentes constructions, les principes d'analyse adimensionnelle, les équations de base.

Le chapitre 4 présente l'étude expérimentale réalisée dans les cadres de la thèse. La méthodologie de mesure est présentée et évaluée. Les résultats obtenus dans le 4 cas: les éoliennes avec et sans carénage à un ou deux rotors sont présentées.

Le chapitre 5 évalue le premier des modèles numériques proposés, le modèle rotor complet (FRM). La validation et la vérification du modèle sont effectuées, suivies de la présentation et de la discussion des résultats pour les configurations d'éoliennes étudiées précédemment. Une évaluation des résultats est effectuée en vue de leur utilisation ultérieure dans un processus de validation de modèle hybride.

Le chapitre 6 présente le modèle hybride développé (ADM). Des informations générales concernant les données aérodynamiques et le code développé sont données afin d'expliquer ses principes. La description du modèle est ensuite présentée, suivie de sa vérification et de sa validation.

Le chapitre 7 compare les résultats de 3 parcours de recherche différents. Les résultats pour une éolienne à deux rotors contrarotatifs sont comparés. Une discussion sur la structure de l'écoulement examiné est effectué, dans laquelle les résultats complémentaires sont utilisés pour évaluer les performances du système et les futurs chemins de développement.

Le chapitre 8 est un résumé des travaux effectués, des conclusions et des recommandations pour les travaux futurs.

L'annexe 1 présente les recherches relatives à l'évaluation de l'écoulement en soufflerie subsonique de l'Institut de turbomachines de l'Université de technologie de Lodz, dans laquelle une étude expérimentale pour la thèse a été réalisée.

L'annexe 2 évalue les aspects pratiques de la campagne de mesures, tels que la préparation et le diagnostic du banc d'essai et du modèle.

L'annexe 3 présente les informations relatives à la nature et à l'évaluation de ressources de vent, sur la base d'une campagne expérimentale dédiée.

2 Les études expérimentales

Les études expérimentales ont été réalisées dans la soufflerie subsonique de l'IMP TUL. C'est une soufflerie avec une section de test circulaire ouverte (diamètre 0,8 m). L'air est entraîné par un ventilateur centrifuge d'un débit nominal égal à 6,25 m^3/s, alimenté par le moteur asynchrone à 2 pôles d'une puissance nominale de 55 kW.

Au début des études expérimentales, une étude de l'écoulement libre dans la soufflerie a été réalisée. Elle a permis de choisir la taille et l'emplacement du modèle de turbine testé. Les paramètres nécessaires aux travaux de simulation ultérieurs ont également été déterminés, tels que les conditions aux limites et la forme (générale) du domaine de calcul.

La première étape des essais d'éoliennes consistait en des mesures pneumatiques et en une visualisation de l'écoulement PIV pour un écoulement à travers un diffuseur. Les résultats obtenus dans le cadre de ces études sont présentés dans l'article [8]. Une géométrie simple, basée sur un diffuseur conique a été utilisée dans ces études. A l'entrée de diffuseur une section convergente (une bouche d'entrée) a été installée pour mieux accumuler l'écoulement à travers le diffuseur. Le diamètre du rotor a également été déterminé comme étant D = 0,32 m.

Pour effectuer les essais, il était nécessaire de créer des bancs d'essais des éoliennes. Les constructions précédemment utilisées ont été modifiées et améliorées. Un rôle important dans la construction des bancs d'essais (Fig. 1) reposait sur une technique de prototypage rapide, utilisée pour produire des éléments d'assemblage (cadres) et des rotors d'éoliennes, solution unique dans ce type de recherche. Les bancs d'essais ont été placées en série (Fig. 2), avec le rotor R1 dans la configuration sous le vent. Cela nécessitait une étude de l'influence de l'obstacle – pôle de fixation de banc d'essais T1 – sur le fonctionnement du système CRSR. L'influence du nombre de Reynolds et du matériau/ la technologie de fabrication de pales du rotor a également été étudiée. Le fonctionnement des rotors R1 et R2 a également été comparé. Les résultats de ce partie des études ont été présentés dans l'annexe 2 de la thèse.

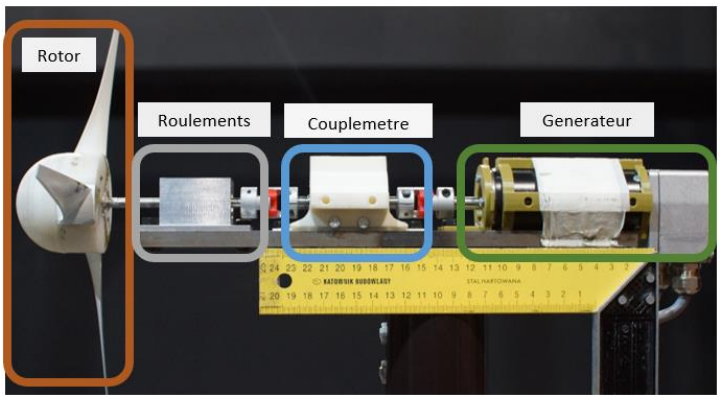

Fig. 1 Banc d'essais T1 (sans boîtier); rotor placée dans la configuration sous le vent (l'écoulement vers la gauche)

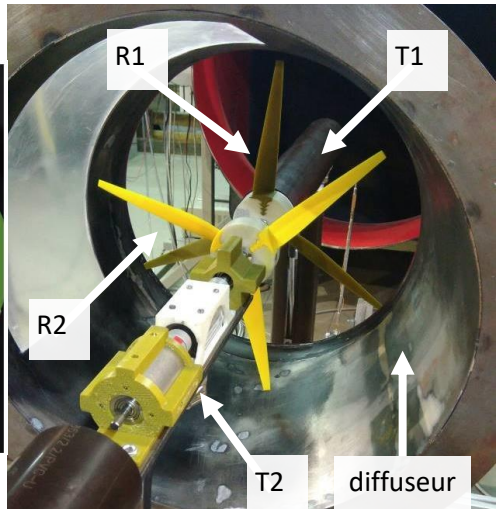

Fig. 2 Bancs d'essais T1/T2, rotors R1/R2 et le diffuseur de CRSR

Les deux rotors ont la même géométrie et ont été testés dans un diffuseur avec une bride et une bouche d'entrée. Les mesures comprenaient l'évaluation de la vitesse de référence (mesures pneumatiques), les coefficients de puissance des deux rotors et la force de traînée aérodynamique de

rotor R1. L'évaluation de diverses configurations d'éoliennes a été mené dans le cadre de la thèse. La vitesse de référence de vent a été établie comme 15,95 m/s. Des essais des éoliennes avec et sans carénage à un ou deux rotors ont été faites. Dans le cas des éoliennes multi rotor on a également modifié le distance entre les rotors. On a vérifié le distance l égal à 0,1 D, 0,3 D et 0,625 D (rotor R2 situé à l'entrée, au centre et à la sortie du diffuseur). Les résultats expérimentaux pour le premier des cas mentionnés ci-dessus (CRR, l = 0,1D) sont illustrés sur Fig. 3.

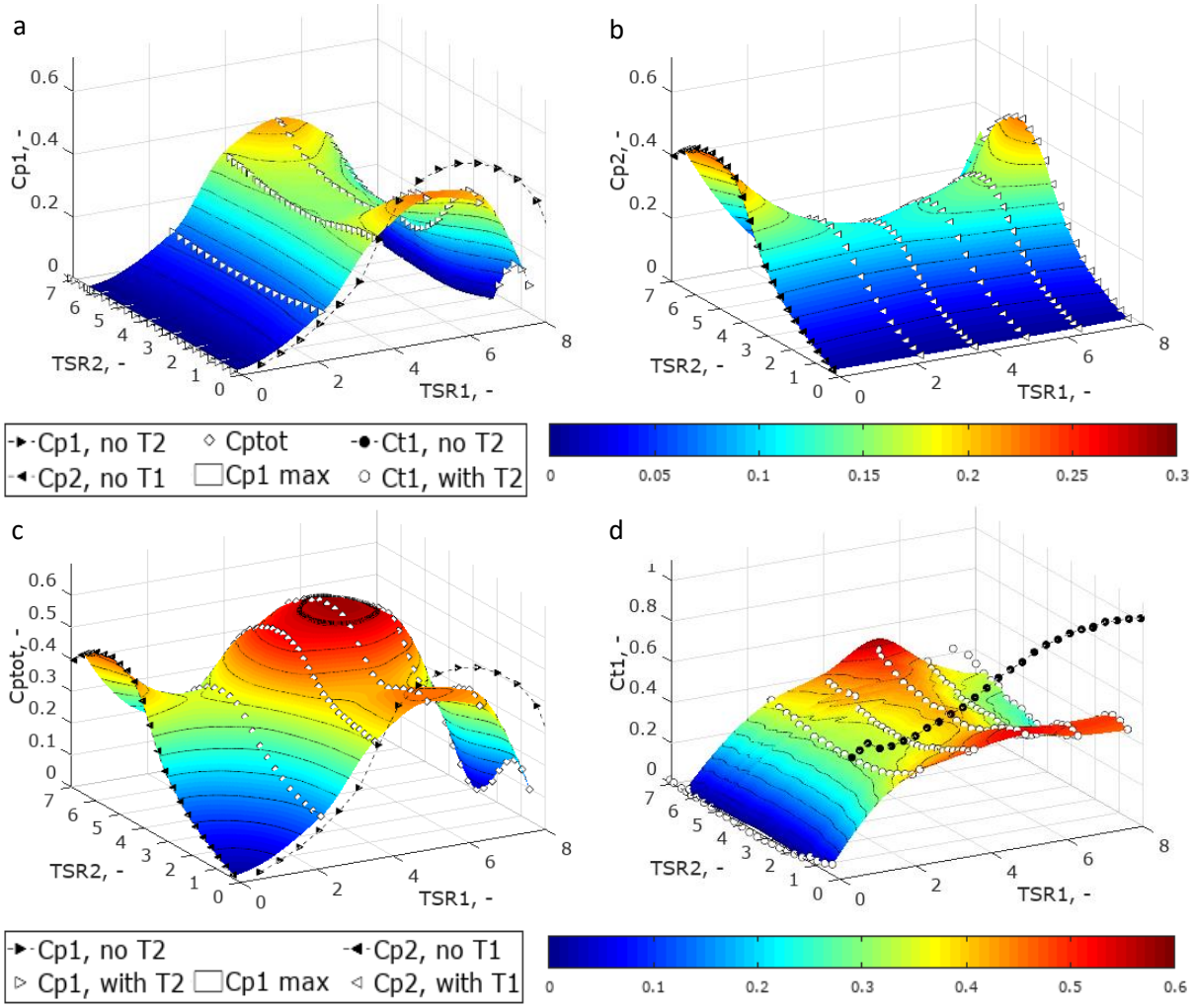

Fig. 3 Les résultats de mesures de puissance et force de trainée en fonction de la vitesse de rotation des éoliennes respectives (TSR1 et TSR2): Cp1 (a), Cp2 (b), Cp1+Cp2 (c), Ct (d) pour CRR ; les points noirs dénotent les valeurs pour DAWT avec un seul rotor ; distance entre les rotors l = 0,1D

Les résultats expérimentaux ont permis de formuler les observations suivantes:

- Le coefficient de puissance (Cp) maximal d'une éolienne diminue de manière significative avec la vitesse de référence du vent. Ceci est dû aux valeurs relativement faibles du nombre de Reynolds (de l'ordre de 100 000, déterminé sur la base du diamètre du rotor) dans le cas considéré, ce qui constitue un obstacle important dans l'étude des petites éoliennes;
- Après l'application du carénage, une augmentation d'environ deux fois du facteur de puissance de l'éolienne R1 a été observée à la même vitesse du vent. Cela est dû au fait que le système rotor-diffuseur testé a été optimisé pour le fonctionnement ensemble. Cependant, ont également été observées une augmentation du coefficient de vitesse TSR correspondant à la valeur maximale

de Cp (de 4,5 à 6) et du coefficient de force axiale. Cela signifie aussi l'augmentation des efforts dans les pales, ce qui doit être pris en compte lors de leur processus de conception;

- L'utilisation d'un deuxième rotor a permis d'augmenter le facteur de puissance totale d'environ 11 à 13% dans le cas d'une turbine non carénée et d'environ 4 à 5% pour la turbine carénée. L'accroissance relativement faible dans le cas de l'éolienne DAWT est dû à l'optimisation aérodynamique susmentionnée du système diffuseur-éolienne, favorisant la solution à un rotor;
- L'utilisation d'un système à deux rotors a permis de réduire le coefficient de force axiale Ct de l'éolienne R1 et de réduire les TSR optimaux (d'environ 20% pour R1 et de 33% pour R2). Cela réduit les contraintes sur les pales des deux rotors;
- En raison de la présence du deuxième rotor, la gamme de TSR optimaux (ou le système fonctionne avec Cp proche du maximum) s'est également élargie;
- Le Cp maximum cumulatif dépend fortement de la position mutuelle des rotors. Fait important, avec l'approche de R2 à la sortie du diffuseur, la plage de TSR2 pour laquelle le rotor fonctionne comme une turbine (recevant de l'énergie du flux) diminue considérablement.

Il faut souligner encore une fois que dans les études menées une méthode unique de fabrication de modèles a été utilisée, la méthode dite « voie rapide » (*fast track*). Elle combine la modélisation 3D et l'impression 3D. L'utilisation de techniques de prototypage rapide a permis une production efficace et reproductible de maquettes pour les essais, tout en garantissant une géométrie de pale de haute qualité et des propriétés mécaniques satisfaisantes. Le résultat de la recherche est une base de données de résultats expérimentaux pour des éoliennes avec et sans carénage à un ou deux rotors. L'expérience acquise, ainsi que les rotors d'éoliennes fabriqués, constitueront la base pour de nouvelles activités de recherche et d'enseignement dans le futur.

3 Les études numériques

La recherche numérique a commencé par l'analyse numérique de l'écoulement libre, basée sur les résultats existants des études expérimentaux. Cela a permis d'identifier le caractère d'écoulement et d'estimer l'influence de la géométrie de la soufflerie sur les résultats obtenus. Grâce à l'analyse numérique, il a également été possible de sélectionner la taille du domaine pour de futures simulations d'éoliennes.

Des outils numériques (logiciels ANSYS, OpenFOAM) et des méthodes de simulation de rotors diverses ont été testées dans le cadre de simulations numériques. Au cours des travaux proposés, entre autres, modèle propre basé sur la philosophie de ligne active (ALM [9]) a été développé. Enfin, les méthodes de simulation 3D suivantes ont été retenues:

- Modèle rotor complet (*Fully-resolved Rotor Model*, FRM) : modèle URANS dans le logiciel ANSYS CFX, basé sur la discrétisation de la géométrie complète du rotor; ce modèle a été utilisé pour l'analyse de l'écoulement,
- Modèle hybride CFD-BET (théorie de l'élément de pale) : modèle RANS dans le logiciel ANSYS Fluent, dans lequel le rotor est représenté par les termes sources dans les équations de Navier-Stokes, déterminés par un code propre; ce modèle a été utilisé pour évaluer les performances de différentes configurations d'éoliennes.

Le premier de ces modèles comprend une discrétisation complète de la géométrie du rotor. Cette approche minimise le niveau de simplifications nécessaires et permet une meilleure représentation de la nature de l'écoulement. Ce modèle a permis de quantifier les variables telles que les triangles locaux de vitesse et l'angle d'attaque (Fig. 4). Les résultats ont également permis de proposer une correction empirique propre de la perte d'extrémité de la pale (*tip loss correction*) qui, dans le cas des turbines carénées, ne peut pas être identique aux solutions utilisées pour les rotors sans carénage.

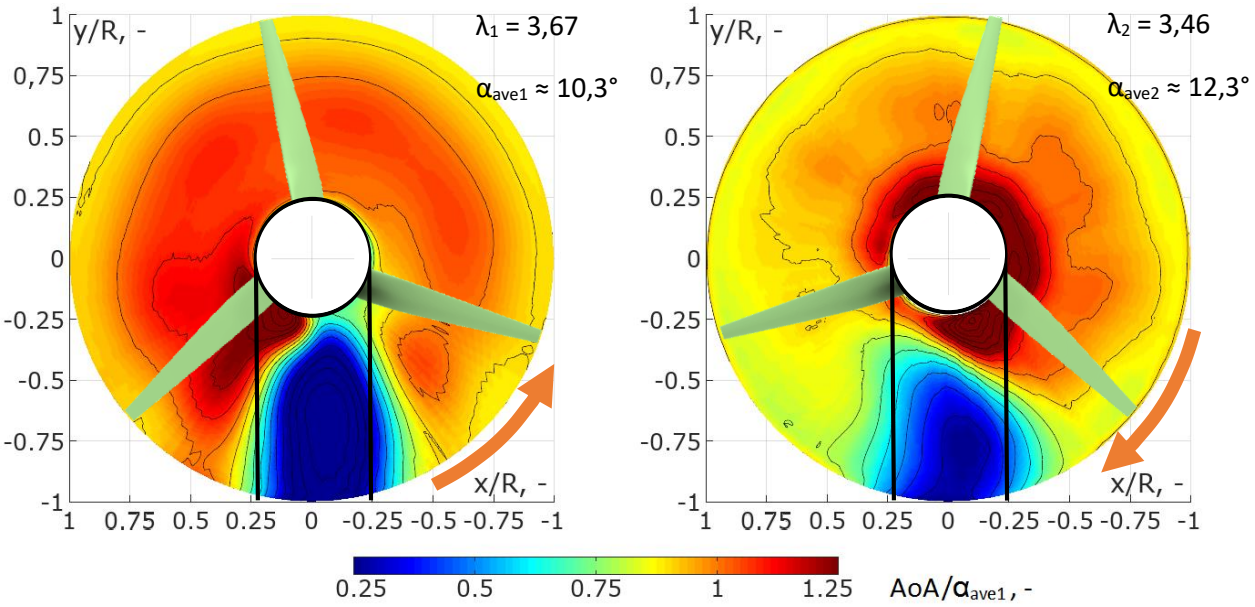

Rys. 4 La répartition de l'angle d'attaque normalisé dans la surface de rotation de rotor R1 (gauche) et R2 (droite) ; vue vers l'entrée de la soufflerie ; système avec carénage ; TSR1 = 3,67, TSR2 = 3,46; le lignes noires dénotent la position du pôle de fixation de banc d'essais T1

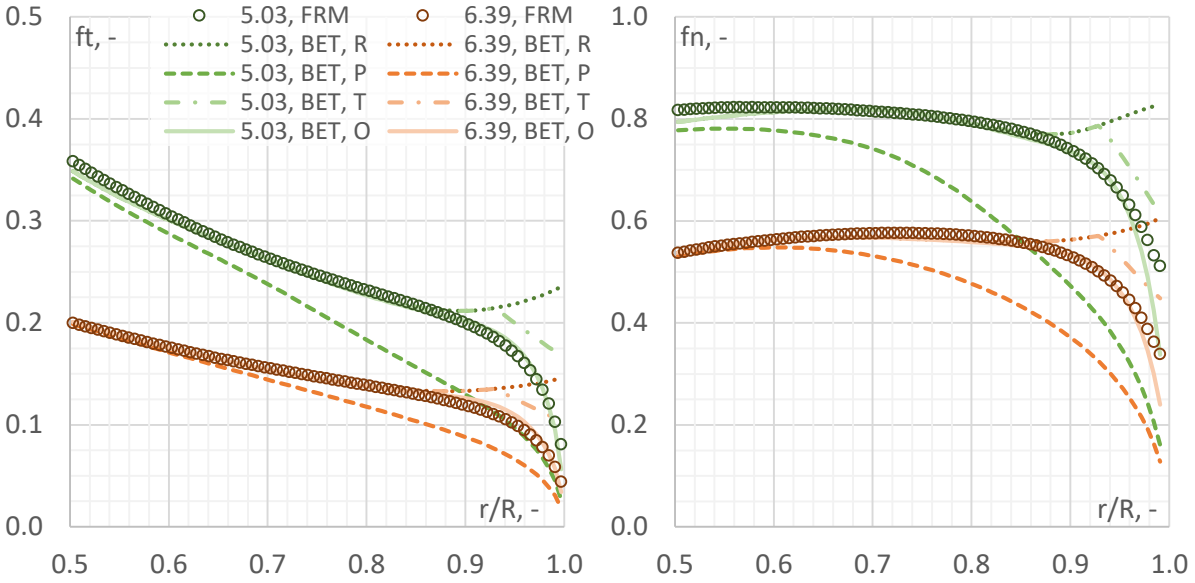

Fig. 5 Distribution radiale de coefficients de couple (gauche) et force de trainee (droite) pour TSR 5,03 (vert) et 6,39 (rouge) – resultats numeriques FRM et CFD-BET pour des corrections de la perte d'extrémité de la pale differentes : sans correction (R), modele de Prandtl (P [10]), Takahashi (T [11]), propre (O)

La recherche a également révélé le principal inconvénient de la méthode FRM: la complexité du modèle numérique entraîne une très forte demande en ressources numériques et en temps de calcul. Pour cette raison, son utilisation est justifiée en particulier dans le cas d'analyses détaillées de l'écoulement. Dans le but d'évaluer les performances d'une éolienne, la deuxième des méthodes testées est plus appropriée, le modèle hybride CFD-BET (dont le principe est présenté sur Fig. 6). Le modèle est basé sur le solveur classique CFD des équations de Navier-Stokes. Le rotor de l'éolienne est représenté par des termes sources, déterminés par le code propriétaire BET, attaché au modèle CFD sous la forme de l'User-Defined Function (UDF). L'application d'une telle approche a permis de réduire significativement le temps de calcul. La comparaison des résultats avec les données expérimentales a confirmé que le modèle hybride donnait des résultats acceptables qualitativement et quantitativement. Cela permet d'affirmer qu'il peut être utilisé, par exemple, pour des tests d'optimisation de systèmes éoliens considérés.

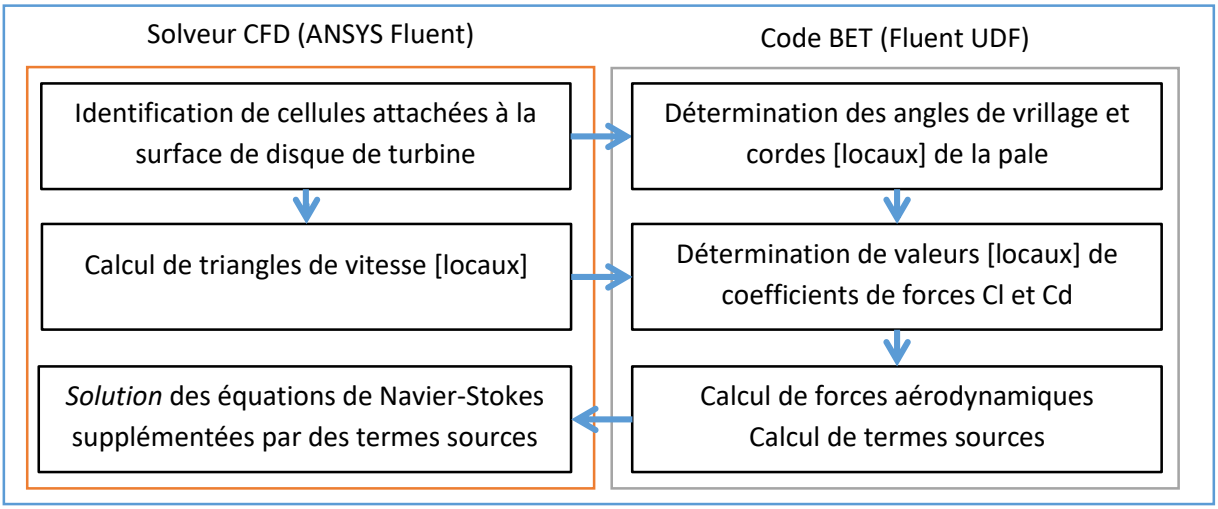

Fig. 6 L'algorithme de calculs d'un modèle hybride CFD-BET

Les remarques les plus importantes concernant les simulations effectuées incluent:

- Les deux modèles ont été validés expérimentalement et vérifiés numériquement. Le modèle FRM a montré une convergence des calculs supérieure à celle d'ADM, résultant des schémas de calcul utilisés et des maillages plus denses. Dans le même temps, le temps et les ressources de calcul nécessaires pour FRM sont considérablement plus importants (plusieurs jours pour un point de travail, contre 36 heures pour l'ensemble des caractéristiques des deux turbines).
- Dans le cas des deux modèles numériques, l'effet négatif du pôle de fixation de banc d'essais T1 sur la stabilisation de l'écoulement et la convergence des calculs est très important;
- Les méthodes existantes de modélisation du phénomène de la perte d'extrémité de la pale ne fonctionnent pas bien pour les éoliennes carénées. Sur la base des données numériques obtenues à partir du modèle FRM, la correction propre pour les forces aérodynamiques déterminées par l'algorithme BET dans la zone de l'extrémité de la pale a été formulée. Son bon fonctionnement a été confirmé par la confrontation des résultats (distributions de vitesses) obtenus avec un modèle hybride avec les résultats de simulations FRM;
- Le choix correct des coefficients de portance Cl et de traînée Cd des profils considérés pour le modèle hybride est très difficile en raison des faibles nombres de Reynolds et de la forte intensité de turbulence dans le sillage du rotor R1. Les données expérimentales sont insuffisantes à cet regard. Ainsi, les estimations obtenues avec le code de panneau XFoil ont été utilisées.

4 Etude de cas: éolienne carénée à double rotor

Fig. 7 présente les résultats des points de fonctionnement (c'est-à-dire lorsque la somme Cp1 + Cp2 atteint sa valeur maximale) du système CRSR pour différentes distances de séparation des rotors. Les valeurs de TSR (à gauche) et Cp (à droite) de différents rotors sont présentés pour modèle hybride (vert/rouge) et pour l'expérience (bleu/jaune). Le TSR1 optimal reste généralement à un niveau stable, de 5,1 à 5,3, quelle que soit la distance entre les rotors. La seule différence est à la distance de séparation la plus basse. Une évaluation plus précise du fonctionnement du rotor en amont dans ce cas a révélé que la plage TSR1 pour laquelle le Cp total du système reste proche au maximum est relativement large (environ 3 à 6). À son tour, le TSR2 optimal diminue lorsque l/D augmente. Il s'agit là d'une observation rationnelle: à mesure que le rotor en aval s'éloigne de l'entrée du diffuseur, la composante de vitesse axiale diminue. En conséquence, la vitesse de rotation optimale doit également être plus faible, ce qui influence TSR2.

À un faible distance de séparation entre les rotors, les deux éoliennes ont un Cp très similaire (de l'ordre de grandeur de 0,2 à 0,3). La différence devient d'autant plus importante que le rotor en aval est poussé vers la sortie du diffuseur. Le taux d'augmentation optimal de Cp1 est très similaire au taux de diminution de Cp2. En conséquence, la somme Cp1 + Cp2 reste à peu près constante dans la plage de l/D considérée. Des valeurs inférieures sont repérées lorsque le rotor en aval est placé à peu près à mi-chemin du diffuseur.

Bien que les résultats de l'ADM suivent les tendances générales observées dans l'expérience, des différences quantitatives significatives peuvent être repérées. Ceci est particulièrement visible pour les valeurs de Cp. Ils sont relativement bien décrits à faible distance de séparation, mais la simulation sous-estime les performances du rotor en amont et, par conséquent, sur-prédite les performances du rotor en aval à mesure que la distance de séparation augmente. La complexité croissante du caractère d'écoulement à l'approche de la sortie du diffuseur peut expliquer ce comportement. Certains exemples incluent l'influence du sillage hélicoïdal et de la zone de basse pression en aval du diffuseur/bride. Ces facteurs affectent la stabilité de l'écoulement, mais augmentent également l'intensité de turbulences, modifiant les caractéristiques de profil aérodynamique. Un remède à cette situation pourrait consister en une correction supplémentaire des coefficients Cl et Cd, tenant compte de l'intensité de turbulence locale, en particulier au niveau du rotor en aval.

Fig. 8 présente les valeurs de Ct dans les points de fonctionnement de système CRSR, et les rapports Cp1/Cp2, Ct1/Ct2 correspondants. En ce qui concerne le Ct, on peut à peu près répéter le même commentaire que pour les valeurs de Cp. Les relations Cp1/Cp2 et Ct1/Ct2 pour lesquelles la valeur totale de Cp du système atteint sa valeur maximale permettent d'évaluer comment sont répartis les charges entre les deux rotors de l'éolienne, afin d'optimiser les performances du système. On voit que, lorsque la distance entre les deux rotors augmente, la majorité de l'effort aérodynamique est pris par le rotor en amont. C'est un phénomène indésirable du point de vue mécanique, car les deux rotors subiraient des déformations différentes en fonctionnement.

Pour conclure, on peut dire que le meilleur emplacement pour le rotor en aval parmi toutes les alternatives testées est près de l'entrée du diffuseur. Ceci assure une distribution relativement uniforme de Cp et de Ct entre les deux rotors et préserve un Cp total élevé du système.

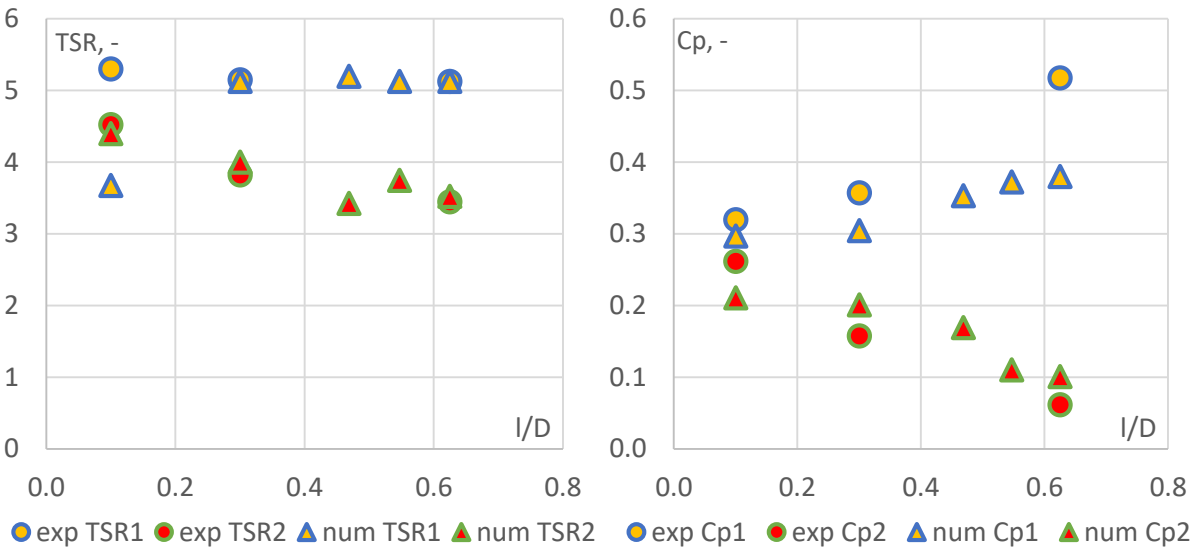

Fig. 7 TSR (gauche) et Cp (droite) de deux rotors achevées pour coefficient de puissance Cp totale de système est maximal, en fonction de distance entre rotors l/D : expérience vs. simulation CFD-BET

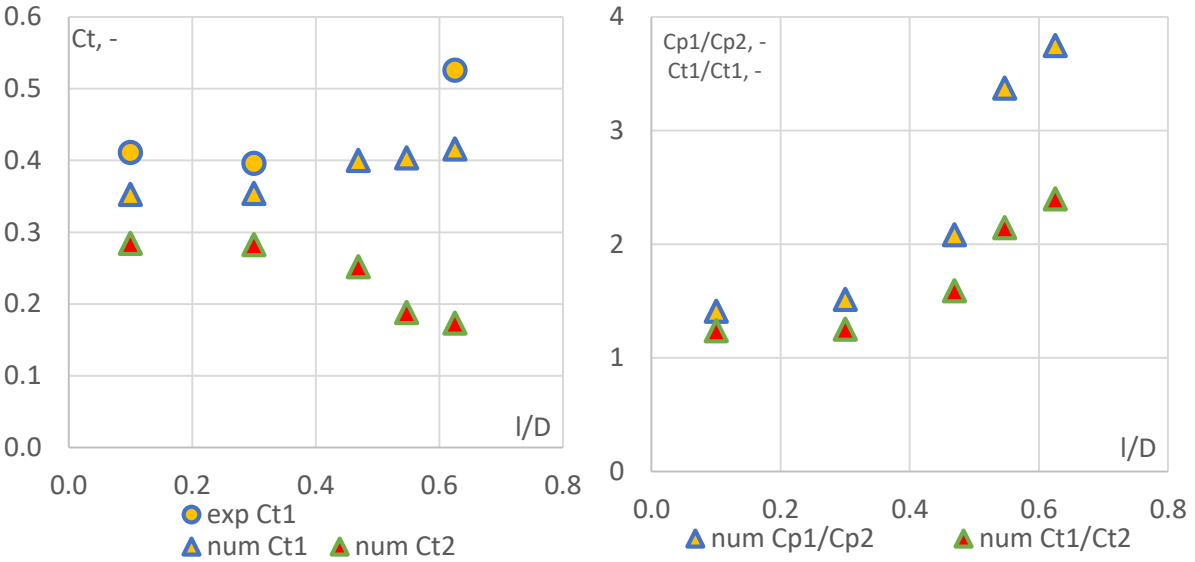

Fig. 8 Ct de deux rotors (gauche) et Cp1/Cp2, Ct1/Ct2 (droite) achevées quand le coefficient de puissance totale de système est maximal, en fonction de distance entre rotors l/D : expérience vs. simulation CFD-BET

Une analyse (qualitative) des champs d'écoulement instantanés (d'URANS FRM) a été effectuée. Fig. 9 présente les résultats pour les surfaces situées a la position angulaire égale a celle de deux pales. Des distributions pour plusieurs positions angulaires sont disponibles dans le partie anglais de la thèse. Présentées sont la vitesse axiale normalisée, coefficient de pression cp, vitesse circonférentielle normalisée et la vorticité circonférentielle. Les schémas de couleurs sont choisis en général de manière à représenter le déficit (bleu) ou l'augmentation (rouge) du paramètre par rapport aux conditions ambiantes (blanc). Le cas considéré est pour TSR1 = 3,67 et TSR2 = 3,45 (la différence entre TSR1 et TSR2 est d'environ 6%). Les pales des deux rotors sont visibles comme des régions blancs à l'entrée de diffuseur.

L'augmentation de la vitesse axiale du vent à l'entrée du diffuseur est suivie d'un déclin plus profond à l'intérieur du diffuseur. Ce phénomène n'est pas uniforme dans le sens radial: le déficit de vitesse le plus profond se produit au voisinage de la pale. Ceci est lié à la séparation de la couche limite et à la

recirculation, provenant probablement de l'interaction des zones de basse pression dans la couche limite et en aval du rotor. Cet effet est en outre amplifié par le gradient de pression défavorable de l'écoulement turbulent, comme suggéré par [12].

La composante de vitesse axiale supplémentaire est créée par le tourbillon attaché à la pale. La direction de cette vitesse supplémentaire est positive (par rapport à la direction du vent) devant la pale et négative devant celle-ci, augmentant ou diminuant par conséquent la vitesse axiale. Le phénomène de la perte d'extrémité de la pale est visible sous la forme de valeurs de vitesse axiale accrues près de la fin de la pale.

Les champs de coefficient de pression révèlent des zones de dépression de forme circulaire regroupées de manière régulière à l'intérieur du diffuseur, près de sa limite. Une comparaison avec les autres données présentés permet d'indiquer qu'il s'agit des sections de la structure du vortex hélicoïdal. La circulation associée à ces sommets induit des composantes de vitesse radiale et axiale supplémentaires. De là, les zones d'augmentation de la vitesse axiale locale et régulière à l'intérieur du diffuseur, près de sa limite.

La structure hélicoïdale tourbillonnaire est visible dans le sillage. La comparaison des images pour différentes positions angulaires a révélé que la vorticité due aux deux rotors partage le même signe (positif) dans la repère cylindrique. Ceci est jugé correct, suivant le modèle tourbillonaire classique de rotor. Cependant, la structure générale du sillage diffère considérablement pour les différentes positions angulaires sur lesquels on étudie l'écoulement (voir dans la thèse). Ceci est dû au fait que les deux hélices ont une chiralité différente (celle associée au rotor en amont est droite, en aval - gauche). Suivant le premier théorème de Helmholtz, les structures de tourbillons descendantes de l'extrémité de pales distinctes ne peuvent pas se croiser, ce qui permet de préserver le système de double hélice visible le long du diffuseur.

Takahashi et al. [11], dans leur étude LES sur les tourbillons descendantes de l'extrémité de pales de rotor d'une éolienne DAWT, ont observé la présence d'un tourbillon induit, créé entre la pointe de pales et la surface du diffuseur. Il avait le direction opposée à celle du tourbillon descendant de l'extrémité de pales. Ce phénomène n'a pas été observé dans la présente étude, probablement en raison d'une clairance entre les pales et le diffuseur supérieure à celle étudiée par Takahashi. Cependant, les images de tourbillon présentées confirment que l'interaction du vortex d'extrémité avec la couche limite du diffuseur conduit à l'amincissement de cette dernière.

Au vortex de la fin de pale correspond un vortex du pied de pale, de direction opposée, située près de moyeu. Ce système tourbillonnaire est visible, mais est plus faible que celui correspondant aux vortex de la fin de pale, comme il est éclipsé par la structure tourbillonnaire dans la couche limite de moyeu.

Les remarques les plus importantes concernant les simulations effectuées incluent :

- Le modèle hybride RANS CFD-BET a été utilisé, entre autres, pour étudier l'influence de la distance entre les rotors sur les paramètres de fonctionnement du système d'une éolienne carénée à deux rotors. Selon les résultats obtenus, la valeur optimale du TSR1 reste approximativement inchangée et le TSR2 diminue à mesure que la distance entre les rotors augmente. La diminution de la distance entre R1 et R2 entraîne une augmentation de Cp2 et une diminution de Cp1 ;
- L'utilisation du modèle URANS FRM a permis de collecter un vaste ensemble de données de l'écoulement instantané, telles que les champs de vitesse et les pressions. Cela nous a permis d'observer des éléments tels que l'interaction des structures de vortex hélicoïdales sortant des

pales du rotor, une séparation relativement rapide de la couche limite de moyeu ou l'impact du phénomène de la perte d'extrémité de la pale.

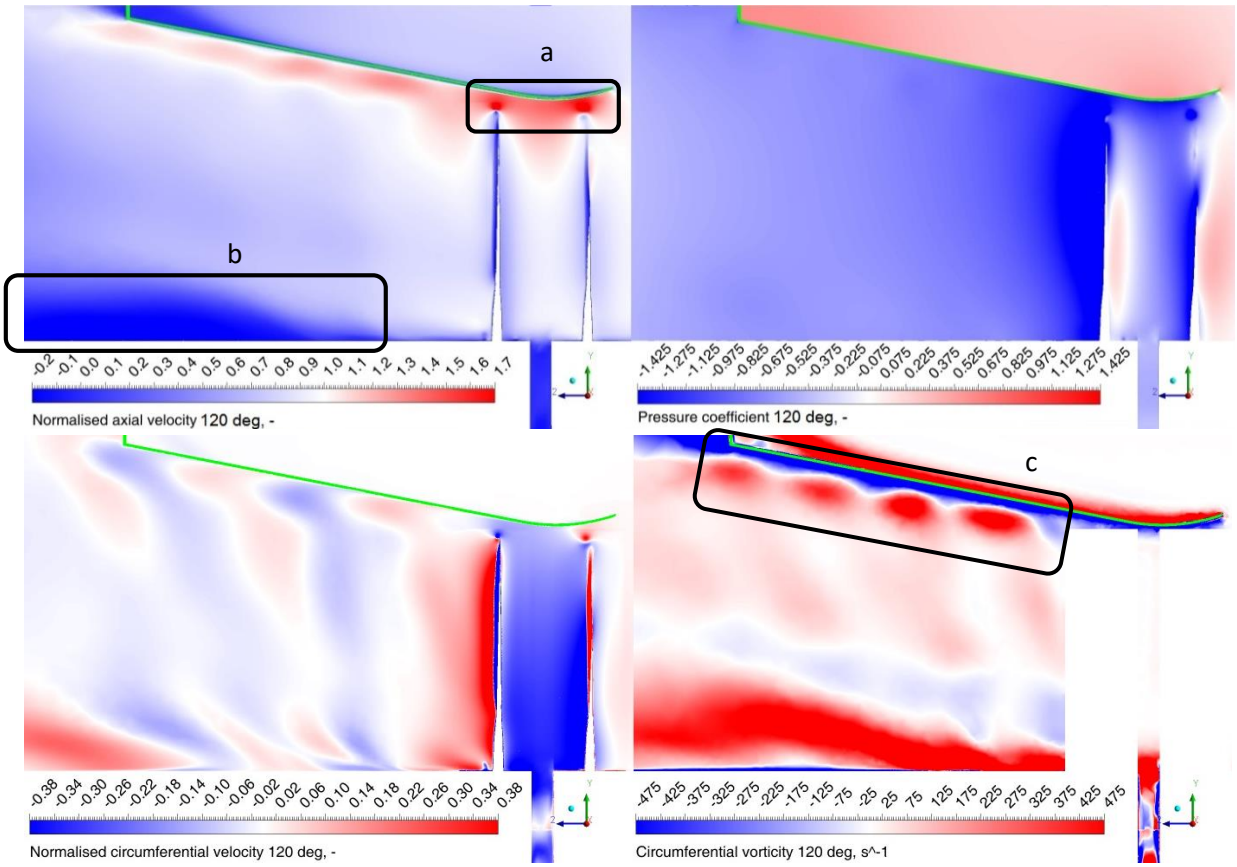

Fig. 9 Les champs instantanées de la vitesse axiale normalisée, coefficient de pression cp, vitesse circonférentielle normalisée et la vorticité circonférentielle (CRSR, TSR1 = 3,67, TSR2 = 3,46) ; à noter sont l'augmentation de la vitesse axiale associée au phénomène de la perte d'extrémité de la pale (a), la séparation de la couche limite proche de moyeu (b), les structures tourbillonnaires hélicoïdales R1 et R2 (c)

5 Les études environnementales

La valeur ajoutée supplémentaire a été établie en forme de la recherche environnementale, c'est-à-dire l'évaluation des ressources de vent. Ceci a été fait dans l'emplacement typique pour une petite éolienne considéré : une zone urbaine/suburbaine. Les mesures ont été effectuées à l'aide de 2 anémomètres à ultrasons Gill Windobserver II. Les résultats développés couvrent une période de 24 mois. Etant donné que les résultats de recherche obtenus ne constituent pas le sujet principal de la thèse de doctorat, leur développement a été limité au stade actuel au minimum nécessaire. Le développement supplémentaire est prévu pour le futur. Les résultats des mesures des ressources éoliennes ont été présentés à la conférence Small Wind Conference 2018 [13].

Fig. 10 montre la rose des vents crée sur la base des résultats moyennés sur l'ensemble du cycle de mesure. Les principales directions de l'afflux de vents sont également indiquées, de même que les facteurs environnementaux ayant une incidence sur leur formation. Les espaces vides (comme les champs) du côté ouest constituent un espace propice au développement des courants éoliens, d'où vient l'augmentation de la vitesse de vent venant de cette direction. Les obstacles, à la fois naturels (forêts) et artificiels (bâtiments), réduisent la vitesse du vent. Dans le même temps, on a observé une augmentation de la vitesse du vent en provenance du sud-est. Ce phénomène est attribué au « couloir aérien » formé entre deux zones boisées.

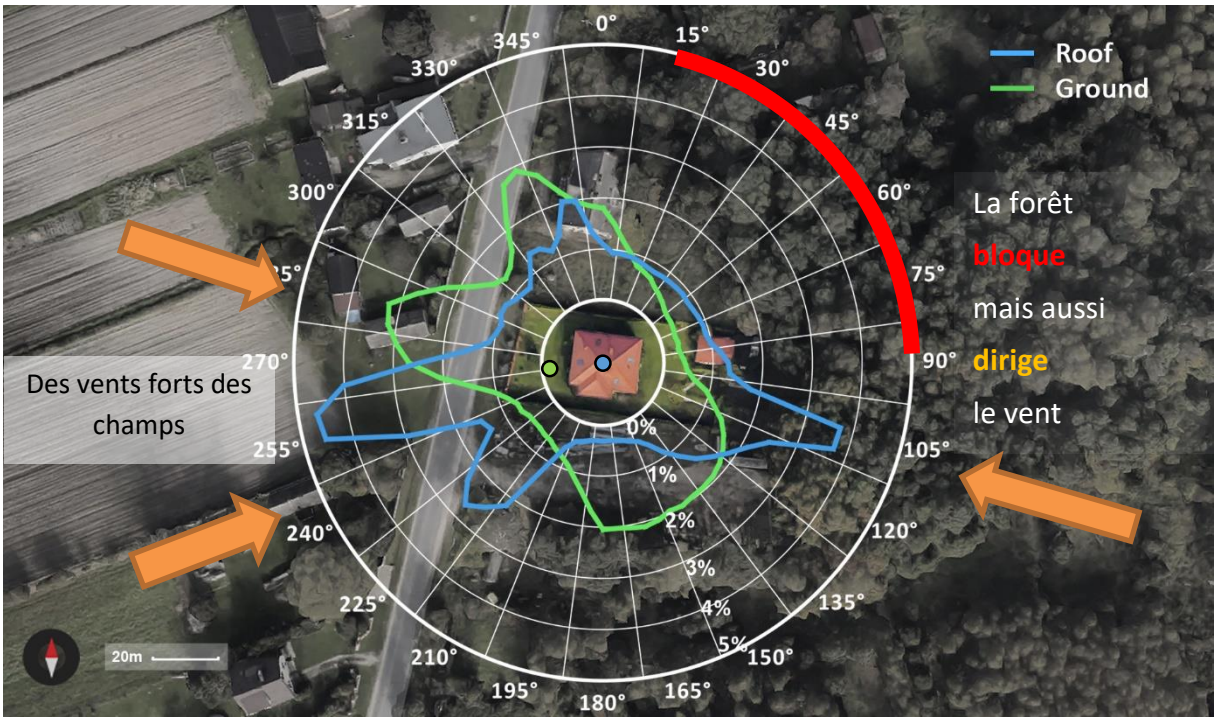

Fig. 10 La rose des vents préparée pour le site étudié: zone suburbaine (Brójce, près de Łódź); mesures à 2 hauteurs (repérées par des points): 2,25 m (« Ground », vert) et 10 m (« Roof », bleu)

Les résultats recueillis ont également permis d'étudier l'évolution de la vitesse du vent dans le temps (Fig. 11). La vitesse du vent varie quotidiennement, atteignant les vitesses les plus élevées vers midi et l'après-midi, car les effets des différents taux de réchauffement du sol à différents endroits sont plus visibles à ce moment-là. Dans le cycle annuel, les changements de la vitesse du vent sont dictés par l'intensité de l'ensoleillement au fil des saisons. L'intensité de ces changements dépend fortement de l'emplacement (par exemple, la distance de l'équateur). Selon les résultats présentés, les vitesses de

vent les plus faibles sont observées en été et les plus élevées en hiver. Ceci est cohérent avec les données de la littérature pour l'emplacement sélectionné.

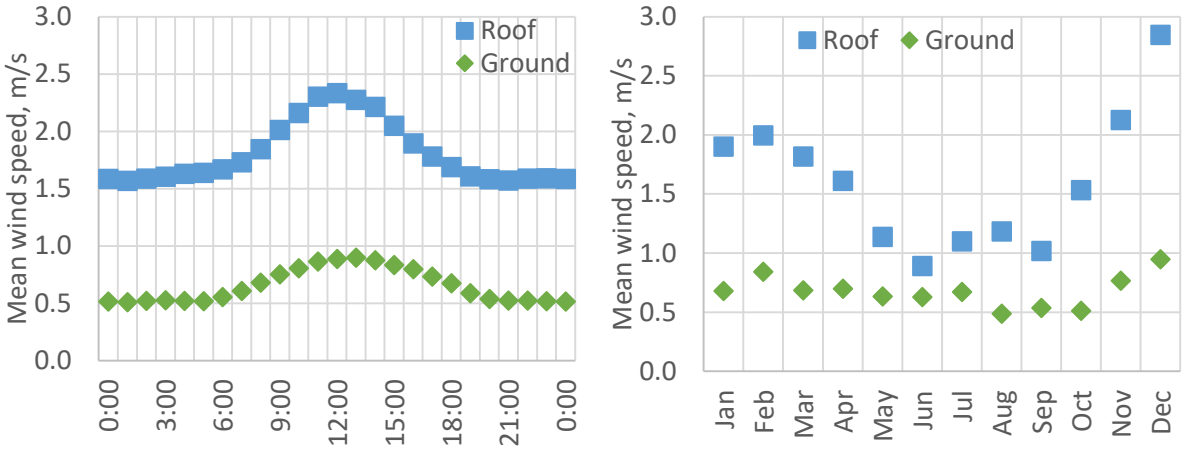

Rys. 11 Evolution quotidienne (gauche) et annuelle (droite) de la vitesse du vent dans la région analysée; mesures à 2 hauteurs: 2,25 m (« Ground », vert) et 10 m (« Roof », bleu)

En résumé, il convient de noter que l'emplacement choisi ne peut pas être considéré comme idéal pour l'installation d'une petite éolienne à l'axe horizontale. Les vitesses de vent annuelles moyennes à une hauteur de 10 m au-dessus du sol ne répondent pas aux exigences de la plupart des machines de ce type actuellement disponibles sur le marché.

6 Sommaire et remarques finales

La thèse *The hybrid simulation model for a twin-rotor diffuser-augmented wind turbine and its experimental validation* étudie deux solutions pour augmenter la puissance d'une éolienne: l'éolienne carénée (DAWT) et l'éolienne à deux rotors contra-rotatifs (CRR). La recherche menée a été fait en utilisant l'approche de l'intégration essai-simulation.

Au cours de la première étape de l'enquête, des expériences ont été réalisées dans la soufflerie subsonique d'IMP TUL. Les tests ont été précédés de l'étude de l'écoulement et du diagnostic des appareils de mesure. La campagne expérimentale était principalement basée sur des mesures pneumatiques et de forces/puissance mécanique. Pour effectuer les tests, un nouvel ensemble de banc d'essais a été développé. Les spécimens de rotors ont été fabriqués en utilisant l'approche « fast track » (basée sur le prototypage rapide), développée par IMP TUL.

Au cours de la deuxième étape de l'enquête, une recherche numérique a été réalisée dans le logiciel ANSYS. Cela a commencé par une évaluation plus profonde de l'écoulement dans la soufflerie, qui a permis de déterminer la taille et les conditions du domaine de simulation. L'étude a ensuite porté sur le développement des modèles réels de simulation d'éoliennes. Les méthodes de simulation 3D suivantes ont été retenues :

- Modèle rotor complet (*Fully-resolved Rotor Model*, FRM): modèle URANS dans ANSYS CFX, basé sur la discrétisation de la géométrie complète du rotor,
- Modèle hybride CFD-BET (théorie de l'élément de pale): modèle RANS dans ANSYS Fluent, dans lequel le rotor est représenté par les termes source dans les équations de Navier-Stokes.

En se basant sur le matériel présenté dans la thèse, il est justifié d'affirmer que les objectifs de la thèse ont été atteints et que l'hypothèse a été confirmée.

Les travaux réalisés dans le cadre de cette thèse peuvent servir de base à des études ultérieures. Les conseils et perspectives suivants peuvent être énoncés:

- Le principe général d'utilisation du modèle hybride pour le cas considéré a été prouvé. Il peut être encore développé pour répondre aux exigences encore plus sophistiquées. Celles-ci pourraient inclure l'ajout de termes sources de quantités turbulentes pour prendre en compte la production d'énergie cinétique turbulente des deux rotors et observer sa influence sur les performances des éoliennes (notamment le rotor en aval). Un autre développement possible serait l'utilisation du modèle hybride URANS basé sur l'approche de la ligne active et/ou les théorèmes tourbillonnaires ;
- La simulation du modèle FRM pourrait être répétée à l'aide d'approches de modélisation plus précises, notamment LES/DES. Cela permettrait de mieux comprendre les phénomènes tels que l'interaction entre la couche limite du diffuseur et le sillage hélicoïdal des rotors ;
- La thèse s'est concentrée sur l'évaluation de la performance du rotor. La campagne expérimentale a donc été limitée à l'évaluation de la puissance et de la force de trainée des éoliennes. Une campagne orientée vers l'évaluation de l'écoulement pourrait être réalisée dans l'avenir, comprenant par exemple la détermination des champs de l'écoulement par PIV et/ou CTA ;
- Le modèle hybride numérique validé peut être utilisé dans les études d'optimisation d'éoliennes. Parmi les cibles d'optimisation possibles, on peut citer la maximisation des performances du système et/ou la meilleure décomposition des charges aérodynamiques. Cette tâche est

particulièrement difficile en raison d'une multitude de variables d'optimisation, telles que le diamètre des rotors, la géométrie de pales et du diffuseur, le placement du rotor, etc.

Bibliographie

[1] European Comission, *Communication from the Commission to the European Parliament, the Council, the European Economic and Social Committee and the Committee of the Regions - 20 20 by 2020 - Europe's climate change opportunity /* COM/2008/0030 final */,* Brussels, 2008.

[2] EWEA, "Wind in power - 2015 European statistics," 2016.

[3] Energy Regulatory Office (URE), "Potencjał krajowy OZE w liczbach - moc zainstalowana," 2018.

[4] Kancelaria Sejmu RP, „Ustawa z dnia 20 lutego 2015 r. o odnawialnych źródłach energii," *Dziennik ustaw Rzeczpospolitej Polskiej,* nr 1148, pp. 1 - 115, 06 2017.

[5] H. Lorenc, Atlas klimatu Polski, Warszawa: Instytut Meteorologii i gospodarki Wodnej, 2005.

[6] RTE (Réseau de Transport d'Electricité), „Bilan électrique 2017," 2018.

[7] ADEME (L'Agence de l'Environnement et de la Maîtrise de l'Energie), „Le petit éolien," 2015.

[8] K. Olasek, M. Karczewski, M. Lipian, P. Wiklak and K. Jóźwik, "Wind tunnel experimental investigations of a diffuser augmented wind turbine model," *Int. J. Numerical Methods for Heat & Fluid Flow,* vol. 26, no. 7, 2016.

[9] M. Lipian, M. Karczewski i K. Jozwik, „Analysis and comparison of numerical methods for design and development of small Diffuser-Augmented Wind Turbine (DAWT)," w *IECON 2016 - 42nd Annual Conference of the IEEE Industrial Electronics Society*, 2016.

[10] W. F. Durand, Aerodynamic Theory vol. 4, Berlin: Springer Berlin Heidelberg, 1935, p. 453.

[11] S. Takahashi, Y. Hata, Y. Ohya, T. Karasudani and T. Uchida, "Behavior of the Blade Tip Vortices of a Wind Turbine Equipped with a Brimmed-Diffuser Shroud," *J. Energies,* no. 5, pp. 5229-5242, 2012.

[12] F. Massouh i I. Dobrev, „Exploration of the vortex wake behind of wind turbine rotor," *Journal of Physics: Conference Series,* nr 75, 2007.

[13] Lipian et al., *Sombrero or Logarithm? Scientific Look on the Wind Resource Assessment,* Small Wind Conference 2018, Minneapolis, MN, USA, 9 – 10 April 2018.

Modèle hybride pour simuler l'écoulement à travers un birotor éolien caréné et sa validation expérimentale

La thèse résume la recherche sur le fonctionnement et l'écoulement autour d'une éolienne caréné à deux rotors. Le placement d'une turbine à l'entrée d'un canal divergent permet d'augmenter le débit massique à travers le rotor. Afin de mieux tirer parti de l'augmentation de la vitesse du vent à l'entrée du diffuseur, il a été décidé d'examiner la possibilité de placer un deuxième rotor, tournant dans le sens opposé, dans cette zone.

L'étude menée combinait plusieurs voies de recherche différentes, y compris les méthodes de la mécanique des fluides numérique (CFD) et des études expérimentales. Cela a permis de mieux comprendre la nature de l'écoulement et du fonctionnement d'une éolienne à deux rotors. Des recherches expérimentales ont été menées dans la soufflerie de l'Institut de Turbomachinerie de l'Ecole Polytechnique de Lodz (Pologne). Une série de mesures de systèmes d'éoliennes divers, avec et sans carénage, à un et deux rotors, a été réalisée. Les résultats recueillis ont permis de confirmer que le carénage pouvait augmenter considérablement (même deux fois) l'efficacité du rotor. Cependant, les forces aérodynamiques et la vitesse de rotation augmentent également. Cet inconvénient peut être partiellement résolu en utilisant un deuxième rotor et en répartissant les charges aérodynamiques sur deux étages de turbine.

Une partie importante de l'étude était les simulations numériques. Ils ont permis de préciser la nature et les paramètres de l'écoulement et d'estimer leur impact sur les performances de l'éolienne. Deux modèles numériques différents ont été développés:

- Modèle rotor complet (anglais : Fully-resolved Rotor Model, FRM): modèle URANS dans ANSYS CFX, base sur la discrétisation de la géométrie complète du rotor; ce modèle a été utilisé pour l'analyse de l'écoulement,
- Modèle hybride CFD-BET (théorie de l'élément de pâle): modèle RANS dans ANSYS Fluent, dans lequel le rotor est représenté par les termes source dans les équations de Navier-Stokes, déterminés par un code interne; ce modèle a été utilisé pour évaluer les performances de différentes configurations d'éoliennes.

Au cours de la recherche, une correction empirique interne de la perte d'extrémité de la pâle (anglais : tip loss correction) a été proposée, en tenant compte de l'influence du diffuseur. L'étude réalisée a permis d'observer, entre autres, que le déplacement du rotor en aval vers la sortie du diffuseur pouvait entraîner une réduction de la vitesse du vent à travers le rotor en amont, placé à l'entrée du diffuseur, et une diminution de la puissance globale du système.

Mots clés : Eolienne DAWT, Eolienne double rotor, Intégration simulation-expérience

The hybrid simulation model for a twin-rotor diffuser-augmented wind turbine and its experimental validation

Doctoral dissertation summarizes the research on the functioning and flow around a two-stage, shrouded wind turbine. Placing the turbine at the inlet of a diverging channel allows to increase the mass flow rate of the flow through the rotor. To better take advantage of the increase in wind speed at the diffuser inlet, it was decided to examine the possibility of placing a second rotor in this area, with the opposite direction of rotation.

The conducted study combined several different research paths, including Computational Fluid Dynamics (CFD) methods and experimental studies. This allowed for a more refined understanding of the nature of the flow and operation of a wind turbine with two rotors. Experimental research was carried out in the IMP TUL wind tunnel. A series of measurements of various turbine systems with and without shroud, with single- and double-rotor wind turbine were made. The collected results allowed to confirm that the shrouding can significantly (even twice) increase the efficiency of the rotor. However, aerodynamic forces and rotational speed also increase. This disadvantage can be partially addressed by using a second rotor and distributing aerodynamic loads to two turbine stages.

An important part of the study were numerical simulations. They allowed to specify in more detail the nature and parameters of the flow and to estimate their impact on the performance of the wind turbine. Two different numerical models were developed:

- Fully-resolved Rotor Model: URANS model in ANSYS CFX, based on discretising the entire geometry of the rotor, used for the flow analysis,
- Hybrid model CFD-BET (Blade-Element Theory): RANS model in ANSYS Fluent, in which the rotor is represented by source terms in the Navier-Stokes equations, determined by an in-house code; the model was used to evaluate the performance of different wind turbine configurations.

In the course of the research an in-house, empirical tip loss correction was proposed, taking into account the influence of the diffuser. The performed study permitted to observe, among others, that moving the rear rotor towards the outlet of the diffuser may result in a reduction of the wind speed through the front rotor, placed at the inlet to the diffuser, and a decrease in the overall system power.

Keywords : Diffuser-Augmented Wind Turbine (DAWT), Twin rotor wind turbine, CFD-experiment integration

ARTS ET MÉTIERS ParisTech

ParisTech
INSTITUT DES SCIENCES ET TECHNOLOGIES
PARIS INSTITUTE OF TECHNOLOGY